



# **Bioactive Papers: Printing, Activity and Stability**

**Thesis in the fulfillment of the requirement for the degree of  
Doctor of Philosophy in Chemical Engineering**

**by**

**Mohammad Mohidus Samad Khan**

*B.Sc. Engg. (Chem.)*

**Department of Chemical Engineering**

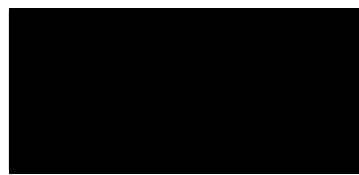
**Faculty of Engineering**

**MONASH UNIVERSITY**

**December 2009**

Under the Copyright Act 1968, this thesis must be used only under the normal conditions of scholarly fair dealing. In particular no results or conclusions should be extracted from it, nor should it be copied or closely paraphrased in whole or in part without the written consent of the author. Proper written acknowledgement should be made for any assistance obtained from the thesis.

I certify that I have made all reasonable efforts to secure copyright permissions for third-party content included in this thesis and have not knowingly added copyright content to my work without the owner's permission.



-----  
Mohammad Mohidus Samad Khan

## TABLE OF CONTENTS

	<i>Page</i>
<b>Title Page</b>	i
<b>Table of Contents</b>	ii
<b>Declaration of Publication and Authorship</b>	iv
<b>Dedication</b>	v
<b>Acknowledgements</b>	vii
<b>Abstract</b>	viii
<b>List of Publications and Awards</b>	x
<b>List of Figures</b>	xiv
<b>List of Tables</b>	xxi
<b>Glossary</b>	xxii
<b>Nomenclature</b>	xxiv
<b>Greek Letters and Symbols</b>	xxv
<b>Chapter 1</b> Introduction and Literature Review	1
<b>Chapter 2</b> Reaction Kinetics of Alkaline Phosphatase Immobilized on Paper	41
<b>Chapter 3</b> Thermal Stability of Bioactive Enzymatic Papers	67
<b>Chapter 4</b> Effect of Polymers on Retention and Aging of Enzymatic Bioactive Papers	92
<b>Chapter 5</b> Paper Diagnostic for Instantaneous Blood Typing	123
<b>Chapter 6</b> Isothermal Non-Coalescence of Liquid Droplets at the Air-Liquid Interface	155
<b>Chapter 7</b> Wicking of a Liquid Droplet in a Surface Groove	175
<b>Chapter 8</b> Effect of Liquid Droplet Impact Velocity on Its Wicking Kinetics in a Surface V-Groove	213
<b>Chapter 9</b> Wetting and Wicking Kinetics of a Sessile Droplet Impinging a Narrow Groove	233
<b>Chapter 10</b> Biosurface Engineering through Ink Jet Printing	261
<b>Chapter 11</b> Conclusions	285

<b>Appendix</b>		A1
<b>Appendix A</b>	<i>Modelling of a Liquid Droplet Wicking in a Surface Groove</i>	A3
<b>Appendix B</b>	<i>Patent: Testing Device for Identifying Antigens and Antibodies in Biofluids.</i>	A19
<b>Appendix C</b>	<i>Patent: Methods for Fabricating Microfluidic Systems.</i>	A43
<b>Appendix D</b>	<i>Awards</i>	A65
<b>Appendix E</b>	<i>Manuscript: Enzymatic Papers: Effect of Paper Structure and Composition</i>	A71

**Monash University**  
**Monash Research Graduate School**

**Declaration for thesis based or partially based on conjointly published or unpublished work**

**General Declaration**

In accordance with Monash University Doctorate Regulation 17 / Doctor of Philosophy and Master of Philosophy (MPhil) regulations the following declarations are made:

I hereby declare that this thesis contains no material which has been accepted for the award of any other degree or diploma at any university or equivalent institution and that, to the best of my knowledge and belief, this thesis contains no material previously published or written by another person, except where due reference is made in the text of the thesis.

This thesis includes three original papers published, four papers submitted and three manuscripts in preparation and to be submitted in different peer reviewed journals. The core theme of the thesis is to investigate the fundamental and applied issues to develop stable and functional bioactive papers and paper fluidic devices for health and environmental diagnostics. The ideas, development and writing up of all the papers in the thesis were the principal responsibility of myself, the candidate, working within the Department of Chemical Engineering, Monash University under the supervision of Prof. Gil Garnier and Assoc. Prof. Wei Shen.

The inclusion of co-authors reflects the fact that the work came from active collaboration between researchers and acknowledges input into team-based research.

In the case of all the chapters listed below, my contribution to the work involved the following:

Thesis chapter	Publication title	Publication status	Nature and extent of candidate's contribution
2	Reaction Kinetics of Alkaline Phosphatase Immobilized on Paper	Submitted	Initiation, Key ideas,
3	Thermal Stability of Bioactive Enzymatic Papers	Published	
4	Effect of Polymers on Retention and Aging of Enzymatic Bioactive Papers	Submitted	
5	Paper Diagnostic for Instantaneous Blood Typing	Submitted	Experimental works
6	Isothermal Non-Coalescence of Liquid Droplets at the Air-Liquid Interface	Published	
7	Wicking of a Liquid Droplet in a Surface Groove.	Submitted	Analysis works,
8	Effect of Impact Velocity on the Wicking of a Sessile Droplet on a V-Groove.	Manuscript in Preparation	
9	Wetting and Wicking Kinetics of a Sessile Droplet Impinging a Narrow Groove at Low Impact Velocity.	Submitted	Development and writing up
10	Biosurface Engineering Through Ink Jet Printing.	Published	

**Signed:** .....

**Date:** .....

*To my parents*

A man's dreams are an index to his greatness.

- Zadok Rabinwiz

There is one thing stronger than all the armies in the world and that is an idea whose time has come.

- Victor Hugo

## ACKNOWLEDGEMENTS

First of all I would like to thank Allah (the God almighty) for giving me the patience, strength and determination during the course of this work.

The work presented in this thesis was carried out under the supervisor of Prof. Gil Garnier and Assoc. Prof. Wei Shen. I don't think words are enough to express my gratitude and appreciation to Prof. Gil Garnier. His guidance throughout my PhD tenure was just wonderful. He eased me with his soothing words when I was in stress; encouraged me to think critically and explore new ideas; trained me to write in a better structure, especially in the top level of journals; congratulated me even for a small success; when needed, he didn't hesitate to push me hard to the limit to ensure I meet all the deadlines. He taught me an important lesson: in research failure is a part of success. He also taught me not to make any issue bigger than it is. From the very first day I met him, I found him highly energetic and efficient. I am still learning from him how to work hard day-in-day-out maintaining the same level of efficiency. I really enjoyed his supervision.

I also would like to acknowledge my co-supervisor Assoc. Prof. Wei Shen. He is one of the most creative persons I have ever worked with. He was been a safety net for me. I always knew, if I can't make out any of the experiments, I can consult this genius with magic hands. He taught me how to mix science with arts and make the science more aesthetic. I will carry this lesson for rest of my life.

I would like to thank the academic staff members at APPI and Department of Chemical Engineering at Monash University, for their assistance and discussions. Special thanks to Dr. Warren Bachelor from APPI for helping me with different pulp and paper samples. I would like to take the opportunity to acknowledge the academics from my high school and undergraduate university, especially Dr. Rana Chowdhury, Mr. Jauhar-Lal Sarkar and Mr. Sharif Mahtab, who taught me to be inquisitive, self-motivated and self-confident.

I would like to acknowledge three special ladies in the department: Janette Anthony, Jill Crisfield and Lilyanne Price. They made the administrative works so easy for me. Janette is the power house of the Australian Pulp and Paper Institute (APPI) and Jill is for the Department of Chemical Engineering. Special thanks to them for organizing exciting trips, postgraduate lunches and different other occasions throughout my PhD duration. Lilyanne was the Postgraduate programs administrator. Appreciation is also extended to the other administrative staff members, including Garry Thunder, Wren Schoppe, Kate Malcom and cleaning staff Anna. I also acknowledge the support of the technical staff of the department, particularly Ron Graham, Roy Harrip, Gamini Ganegoda, Ross Ellingham, Catherine Buckley and Kim Phu for their assistance for the experimental work.

I would like to thank and acknowledge Rokon, Sumaiya, Noman, Lubna, Muniz, Obayed, Dr. George, Eva, Debadi Chakraborti, Parama Chakraborty, Dr. Sajal Islam, Dr. Farzana Mazid, Dr. Nawshad and his family for their help and support. They are my friends and family in Australia.

I acknowledge my good friends Dr. Firas Ridha and Dr. Dushmantha Kannangara. With Firas I shared accommodation for more than three years. In those years his wisdom and guidance helped me a lot in different occasions. With Dushmantha, I worked in the lab in my PhD first year. He not only helped me in the lab but also guided me on different issues. Special thanks to Dr. Nathan Cowieson, Dr. George Thouas, Deniece Fon, Li Xu, Sharon and Alison for helping me in different parts of my PhD work.

I also would like to thank Thanh Nguyen, Kay Abd Rasid, Kostuhb Joshi, Roland Lee, Thao Nguyen, Yuan, Echo and Vinh for their friendship and providing a supportive environment for research and education.

Monash University is acknowledged for the opportunity provided to me and for the award of scholarships which were essential for my work.

Last but not the least, I would like to acknowledge Prof. R. Pelton and Dr. K Stack for reviewing my thesis. Their comments and corrections were judicious and much appreciated.

Some people don't require any formal acknowledgement. They are my parents. I am dedicating my PhD thesis to them.

## ABSTRACT

The fundamental and applied engineering knowledge required issues to develop stable and functional bioactive papers and paper fluidic devices for health and environmental diagnostics were investigated.

Bioactive papers are designed to be wetted by a biofluid or some solution of interest; biomolecule retention and behaviour on paper must be maximized. Two enzymes, alkaline phosphatase (ALP) and horseradish peroxidase (HRP) were directly physisorbed on paper or retained on paper with a polymer. Three model polymers were investigated: a high molecular weight cationic polyacrylamide (CPAM), an anionic polyacrylic acid (PAA) or a high molecular weight polyethylene oxide (PEO). The reactivity and the thermal stability of enzymatic bioactive papers were quantified using an advanced colorimetric technique. The enzymes adsorbed on paper retained their functionality and selectivity. Adsorption on paper increased the enzyme thermal stability by 2 to 3 orders of magnitude compared to the same enzyme in solution. The thermal degradation of the adsorbed enzyme follows two sequential first order reactions, indication of a reaction system.

The model polymers used as retention aids were efficient at increasing the enzyme concentration on paper (by 50%) and to prevent enzyme desorption/leaching upon the rewetting of the paper. The polymers affect the thermal stability and the aging of ALP enzyme on paper; the rapid initial deactivation becomes predominant, while it was negligible for the enzyme simply physisorbed on paper. As a result, the thermal stability significantly decreases. A mathematical model predicting the enzymatic paper's half-life time was developed.

The reaction kinetics of ALP enzymatic paper reacting with its substrate was measured and shown to follow a first order reaction with respect to the enzyme concentration. ALP immobilized on paper has a reaction rate 2 to 3 orders of magnitude lower than the free ALP in buffer solution. No increase in reaction rate was achieved by immobilizing ALP on paper with polymer as retention aids; this suggests that enzyme orientation was not significantly affected through preferentially linking with its anionic or cationic groups.

Paper bioassays to identify antigens and antibodies in a biofluid, such as blood, were investigated. Two series of experiments were performed. In the first, blood samples were mixed with different amounts of antibodies and a droplet of the mixture was deposited onto a paper strip. Agglutinated blood phase separated, with the red blood cells forming a distinct

spot upon contact with paper while the serum wicked; in contrast, stable blood wicked uniformly. In the second series, blood droplets were deposited onto the paper strips pretreated with solutions of antibodies. The wicking of blood droplets on paper strips was characterized. Blood agglutination by interaction with a specific antibody caused a chromatographic separation. The concept of blood typing using a paper diagnostic was demonstrated with a prototype.

The feasibility of thermal ink jet printing was demonstrated for the precise deposition of biomolecules on paper and poly( $\epsilon$ -caprolactone) (PCL) with a protein (albumin-FITC) and an enzyme (HRP) as model biomolecules. Complex patterns of HRP and albumin-FITC were ink jet printed on paper. Microfluidic channels were also printed on paper to demonstrate the concept of paper based bioassays as diagnostic devices. Discreet and continuous concentration gradients of proteins on PCL scaffolds were achieved by ink jet printing; these protein concentration gradients can serve as potential guidance cues for cell growth generation in tissue engineering.

Ink jet printing of biomolecules onto paper involves liquid-liquid interaction; acceptance of biomolecules on the porous surface is rather affected by the solid-liquid interaction. Both phenomena reduce print resolution. The liquid-liquid and solid-liquid interaction were quantified and modelled for sessile droplets. Satellite drops from the ink jet nozzle can form non-coalescence droplets (NCD), due to liquid-liquid interaction, and roll from their target. The Weber number ( $We$ ) of falling liquid drops was used to quantify the NCD generation. To quantify the solid-liquid interaction, the liquid wicking of a droplet impacting an open V-groove at different velocities (groove angle,  $\beta= 60^\circ, 90^\circ, 120^\circ$ ) was studied. A new mathematical model was developed to calculate liquid wicking distance in V-groove. The dynamics of wetting of sessile liquid droplets impinging, at different impact velocities, a groove surface ( $120^\circ$ ) was investigated experimentally. The dynamics of V-groove wicking and wetting is important to optimize paper for ink jet printing and microfluidic devices.

## LIST OF PUBLICATIONS AND AWARDS

### Peer-Reviewed Journal Papers

The following publications are included in this thesis as individual chapters:

1. **Khan, M. S.** and Garnier, G., ‘Reaction Kinetics of Alkaline Phosphatase Immobilized on Paper.’ *Submitted to Langmuir*.
2. **Khan, M. S.**, Xu, L., Shen, W. and Garnier, G., ‘Thermal Stability of Bioactive Enzymatic Papers.’ *Colloids and Surfaces B: Biointerfaces* **2009**, 75, (1), 239-246.
3. **Khan, M. S.**, Haniffa, S. B. M., Slater, A. and Garnier, G., ‘Effect of Polymers on the Retention and Aging of Enzymatic Bioactive Papers.’ *Submitted to Colloids and Surfaces B: Biointerfaces*.
4. **Khan, M. S.**, Thouas, G., Shen, W., and Garnier, G., ‘Bioactive Paper Assay for Blood Type Identification.’ *Submitted to Analytical Chemistry*.
5. **Khan, M. S.**, Kannangara, D., Shen, W. and Garnier, G., ‘Isothermal Noncoalescence of Liquid Droplets at the Air-Liquid Interface.’ *Langmuir* **2008**, 24, (7), 3199-3204.
6. Kannangara, D., **Khan, M. S.** and Shen, W., ‘Wicking of a Droplet in a Surface Groove.’ *Submitted to Langmuir*.
7. **Khan, M. S.**, Kannangara, D., Garnier, G., and Shen, W., ‘Wetting and Wicking Kinetics of a Sessile Droplets Impinging on a Narrow Groove.’ *Submitted to Colloids and Surfaces A: Physicochemical and Engineering Aspects*.
8. **Khan, M. S.**, Fon, D., Li, X., Tian, J., Forsythe, J., Garnier, G. and Shen, W., ‘Biosurface Engineering Through Ink Jet Printing.’ *Colloids and Surfaces B: Biointerfaces*, **2009**, 75, (2), 441-447.

### Manuscript(s) in Preparation

The following publications are in preparation. Manuscript 1 and 2 are included in this thesis as individual chapters. Manuscript 3 is included in *Appendix E*.

1. **Khan, M. S.**, Kannangara, D., Garnier, G. and Shen, W., ‘Effect of Impact Velocity on the Wicking of a Sessile Droplet on a V-groove.’ *Manuscript in preparation and to be submitted to Chemical Engineering Science*.

2. **Khan, M. S.**, Slater, A., Haniffa, S. B. M. and Garnier, G., ‘Effect of Paper Structure and Composition on the Bioactivity of Enzymatic Papers.’ *Manuscript in preparation and to be submitted to APPITA Journal*.

## **Book Chapter**

Following book chapter is published during this research which is not included in the thesis.

1. **Khan, M. S.**, Tian, J., Xu, L., Shen, W., and Garnier, G. ‘Bioactive Enzymatic Papers’. 14th Fundamental Research Symposium, "*Advances in Pulp and Paper Research, Oxford 2009*." St. Anne's College, Oxford. September 13-18, 2009, pp. 1149-1166.

## **Patents**

Following patent applications were made during this doctoral study, which are included in *Appendix B* and *Appendix C*.

1. **Khan, M.**, Li, X., Thuas, G., Shen, W. and Garnier, G. “Testing Device for Identifying Antigens and Antibodies in Biofluids”, Australian Provisional Patent, 2009904643, 24 Sept, 2009.
2. Shen, W., Tian, J., Li, X., **Khan, M.S.** and Garnier, G. “Methods for Fabricating Microfluidic Systems', PCT/AU2009/000889, 10 July, 2009.

## Conference Papers

Following conference papers were presented in international conferences during this research but not included in the thesis.

1. Khan, M. S., Shen, W. and Garnier, G. (2009) "Stability and Reactivity of Enzymatic Papers." *2009 AIChE Annual Meeting*, Nashville, TN, USA, Paper165800.
2. **Khan, M. S.**, Shen, W. and Garnier, G. (2009). "Thermal Stability of Horseradish Peroxidase Enzymatic Papers." *63rd Appita Annual Conference and Exhibition*, APPITA, Melbourne, Australia, pp. 273-280.
3. Kannangara, D., **Khan, M. S.** and Shen, W. (2009). "An Analysis of Effects of Internal and Surface Sizing on Ink Jet Printing Quality." *63rd Appita Annual Conference and Exhibition*, APPITA, Melbourne, Australia, pp. 195-200.
4. **Khan, M. S.**, Fon, D., Li, X., Forsythe, J., Thouas, G., Garnier, G., and Shen, W. (2008). "Printing Biomolecules Part-1: Achieving Total Control of Biomolecule Delivery Using Ink Jet Printing." *Chemeca 2008*, Engineers Australia, IChemE in Australia, City Hall, Newcastle, NSW, pp. 744-753.
5. **Khan, M. S.**, Fon, D., Li, X., Forsythe, J. S., Garnier, G., and Shen, W. (2008). "Ink Jet Printing of Biomolecules on Porous Surfaces." In: Ahmed, N. (Ed.), *International Conference on Chemical Engineering (ICChE) 2008*. Bangladesh University of Engineering and Technology (BUET), Dhaka, Bangladesh, pp. 171-176.
6. Kannangara, D., **Khan, M. S.**, and Shen, W. (2008). "The Inertial Effects on the Capillary Flow in Surface Grooves." *Chemeca 2008*, Engineers Australia, IChemE in Australia, City Hall, Newcastle, NSW, pp. 865-875.
7. **Khan, M. S.**, Kannangara, D., Shen, W., and Garnier, G. (2007). "Mechanism of Non-Coalescence for Liquid Droplets at the Air-Liquid Interface." *Chemeca 2007*, Engineers Australia, Melbourne, pp. 101-109.

## Awards

- State Winner (Victoria) in the **AusBiotech-GSK Student Excellence Awards** presented at the *AusBiotech 2009, Australia's Biotechnology Conference*, Melbourne, 26<sup>th</sup> -30<sup>th</sup> Oct, 2009 for the PhD project: Bioactive Papers.

This national award program aims to encourage and recognize Australia's promising student life-scientists and bio-entrepreneurs. This award is co-sponsored by AusBiotech and GlaxosmithKline (GSK). AusBiotech Ltd. (Australian Biotechnology Organization) is the national body of the biotechnology and life science industry in Australia. The award is documented in *Appendix D*.

- **Postgraduate Publications Award (PPA)**, Round 3/2009, Monash Research Graduate School (MRGS).

The Postgraduate Publications Award financially supports research students to prepare and write papers during the thesis examination period.

## LIST OF FIGURES

### *Chapter 1*

- Figure 1:** Use of biomolecules for different functional purposes <sup>28</sup>.
- Figure 2:** Three dimensional representation of enzyme. (a) Alkaline phosphatase (ALP) <sup>34</sup>, (b) horseradish peroxidase (HRP) <sup>35</sup>.
- Figure 3:** Structural diagrams representing antibody molecules <sup>53</sup>.
- Figure 4:** A range of immobilization strategies for biomolecules <sup>75</sup>.
- Figure 5:** Four approaches of biomolecular immobilization onto dry or wet cellulose; figure inspired from reference <sup>29, 70</sup>.
- Figure 6:** Biomolecular printing techniques; figure inspired from reference <sup>1, 82</sup>.
- Figure 7:** Contact printing with pin. (a) Solid pin printing process. (b) Split pin printing process <sup>1</sup>.
- Figure 8:** (a) Schematic of AFM dip-pen lithography. (b) Schematic of AFM grafting <sup>88</sup>.
- Figure 9:** (a) Scheme of fabrication of a microstamp. (b) Use of microstamp in  $\mu$ CP <sup>2</sup>.
- Figure 10:** Schematic illustrations of photochemistry based manufacturing procedures <sup>1</sup>; (a) Photolithography applied to silane self-assembled monolayers (SAMs), (b) Direct photochemical protein patterning by activation of a photochemical coupling species.
- Figure 11:** Thermal ink-jet printing. (a) A cross-section view of a generic bubble-jet cartridge <sup>4</sup>, (b) droplet dispensing using solenoid inkjet technique <sup>100</sup>, (c) droplet ejection sequence in a thermal bubble-jet <sup>101</sup>.
- Figure 12:** Drop formation with continuous ink jet and effect on printing: (a) Constriction of the ink jet to form a drop <sup>5</sup>, (b) A stream of drops with satellite drops combining with the subsequent main drop in flight, (c) A magnified image of printed vertical line <sup>101</sup>.
- Figure 13:** Non-coalescence behaviour of a satellite droplet <sup>109, 110</sup>.
- Figure 14:** Thesis research components and chapter lists.

### *Chapter 2*

- Figure 1:** Experimental system to prepare ALP enzymatic papers.
- Figure 2:** Experimental setup to measure enzymatic reaction kinetics on paper. (1) Video camera, (2) light box, (3)-(6) lights, (7) platform for the ALP enzymatic papers.
- Figure 3:** Kinetic scheme of the indoxyl tetrazolium method for the histochemical demonstration of non-specific ALP <sup>28, 33</sup>.
- Figure 4:** Mechanism of the ALP reaction <sup>23, 24, 33, 38</sup>.

- Figure 5:** Product formation on ALP enzymatic paper at different times. (a) ALP on paper; (b) ALP on CPAM Paper. The blue purple colour reveals the enzyme (ALP) - substrates (BCIP/NBT) reaction.
- Figure 6:** E-S product formation on ALP enzymatic papers as a function of time. (a) ALP on paper, (b) ALP on CPAM paper, (c) ALP on PAA paper and (d) ALP on PEO paper, n= 6, at 23°C.
- Figure 7:** Reactant concentration (a-x) on ALP enzymatic papers as a function of time. (a) ALP on paper, (b) ALP on CPAM paper, (c) ALP on PAA paper and (d) ALP on PEO paper, n= 6, at 23°C.
- Figure 8:** ALP reaction kinetics on enzymatic papers. (a) ALP on paper, (b) ALP on CPAM paper, (c) ALP on PAA paper and (d) ALP on PEO paper, n= 6, at 23°C.
- Figure 9:** Reaction rate constant of ALP reacting with BCIP/NBT on paper.

### *Chapter 3*

- Figure 1:** Dye concentration distribution on paper measured by image analysis (ImageJ 1.41o). (a) Surface profile, (b) Histogram of gray values.
- Figure 2:** Calibration curve of gray values of the enzymatic products resulting from enzyme-substrate reaction on paper. (a) ALP enzymatic paper, (b) HRP enzymatic paper.
- Figure 3:** Aging of ALP-enzymatic paper treated at 60°C and 90°C for various periods. The blue purple colour reveals the enzyme (ALP) - substrates (BCIP/NBT) reaction.
- Figure 4:** Aging of HRP-enzymatic paper treated at 23°C for various periods. The brownish colour reveals the enzyme (HRP) - substrates (DAB) reaction.
- Figure 5:** Effect of time and temperature on the activity of enzymatic paper: (a) ALP paper, (b) HRP paper; ( $I_0$  = gray value at 0 hr and  $I$  = gray value at 't' hr).
- Figure 6:** APPI Surface Engineering Group photo (14.5 cm × 10.5 cm) inkjet printed using HRP enzyme ink solution onto Whatman #4 and exposed to its liquid substrate (DAB).
- Figure 7:** Relative activity curve of alkaline phosphatase (ALP) heated at 50°C in a buffer solution for various periods [27].
- Figure 8:** Residual activity of peroxidase in 0.05 M phosphate buffer (pH 7.0,  $A_0$ : initial activity,  $A$ : residual activity) [25] (with permission).
- Figure 9:** Residual activity of enzyme active papers heated at different temperatures. (a) ALP enzymatic paper, (b) HRP enzymatic paper; ( $I_0$  = gray value at 0 hr and  $I$  = gray value at 't' hr).
- Figure 10:** Residual activity of alkaline phosphatase heated in buffer at 50°C for various periods (calculated from [27]).
- Figure 11:** Arrhenius plot for the thermal deactivation of bioactive enzymatic papers.

**Figure 12:** Activation energy of enzymatic deactivation: (a) Enzymes adsorbed on paper, (b) Enzymes in buffer solution [26, 40] ; ( $E_1$  and  $E_2$  are the activation energies of enzyme deactivation for phase-1 and 2, respectively).

#### *Chapter 4*

**Figure 1:** Experimental system to prepare ALP enzymatic papers.

**Figure 2:** Enzyme-Substrate product formation on paper samples. Substrate effect on: (a) paper without ALP, (b) ALP active paper samples before leaching ( $t = 0$ hr) and (c) Leached ALP papers aged at  $t = 24$ hrs.

**Figure 3:** Enzyme adsorption on different paper samples.

**Figure 4:** Aging of ALP enzymatic paper treated at  $23^\circ\text{C}$ ,  $60^\circ\text{C}$  and  $90^\circ\text{C}$  for various periods: (a) ALP on CPAM paper, (b) ALP on PAA paper. The blue purple colour reveals the enzyme (ALP) - substrates (BCIP/NBT) reaction.

**Figure 5:** Effect of time and temperature on the activity of enzymatic papers. ALP stabilized on paper using: (a) CPAM, (b) PAA, (c) PEO, (d) without polymer [2]; ( $I_0 =$  gray value at 0 hr and  $I =$  gray value at 't' hr).

**Figure 6:** Residual activity of enzyme active papers heated at different temperatures. ALP stabilized on paper using: (a) CPAM, (b) PAA, (c) PEO, (d) without polymer [2]; ( $I_0 =$  gray value at 0 hr and  $I =$  gray value at 't' hr).

**Figure 8:** Arrhenius plot for the thermal deactivation of ALP enzymatic papers. (a) ALP paper without polymer, (b) – (d) ALP CPAM, PAA and PEO papers.

**Figure 7:** Variation of  $t^*$  as a function of temperature.

**Figure 9:** Schematic of half-life model of ALP enzymatic papers. (a)  $RA^* < 50\%$ , (b)  $RA^* > 50\%$ .

**Figure 10:** Half-lives of ALP enzymatic papers predicted at  $0^\circ\text{C}$ .

#### *Chapter 5*

**Figure 1:** Paper strips for blood type detection; (a) treated with antibody-A (Anti-A of 1.0x concentration), (b) treated with PBS buffer.

**Figure 2:** Wicking on paper of blood previously agglutinated from antigen-antibody interaction; (a) 'B+' blood with (a) specific antibody (Anti-B), (b) non-specific antibody (Anti-A).

**Figure 3:** Blood wicking on Anti-A treated paper: 10mins after blood drop dispensing. Sample blood drops: (a) AB+ and (b) B+, were dispensed on papers treated with different concentrations of antibody-A. 'X' represents the dilution fraction.

- Figure 4:** Schematic representation of the wicking of blood on paper treated with a specific and a non-specific antibody (A). (a) AB+ blood interact with antibody-A on paper and create separate layer of RBC and serum, (b) B+ blood wick on paper without any distinctive separation.
- Figure 5:** Blood wicking on paper treated with different concentrations of antibody-A. AB+ blood wicking after (a) 4min, (b) 10 min, (c) B+ blood wicking after 4 min; n = 6. 'X' represents the dilution factor.
- Figure 6:** Evolution of blood wicking on antibody-A active paper; paper strips soaked in Anti-A of 1.0x. (a) AB+ blood, (b) B+ blood.
- Figure 7:** Blood wicking dynamics on paper treated with antibody-A. (a) AB+ blood, (b) B+ blood; n = 6.
- Figure 8:** Schematic of blood wicking on antibody treated paper. (a) ABO blood type antigens, antibodies and antibody active papers. Blue, orange and black colours are used for A, B and D antibody/antigen, respectively; (b) Antibody-A active paper (Anti-A, 1.0x); (c) antibody-B active paper (Anti-D, 1.0x). Blood wicking behavior varies for antibody interaction with non-specific (b (II, III), c (I, II)) and specific (b (I), c (III)) antigens.
- Figure 9:** Blood group detection using wicking of agglutinated colloids from specific antigen/antibody interaction on dry paper strips; Blood typing: (a) B+, (b) O+.
- Figure 10:** Blood group detection using RBC/blood serum separation on antibody active paper fluidic device; (a) schematic of colorimetric indication of phase separation on paper fluidic channels; (b) and (c) are two trials of same blood samples confirm A+ blood typing; for better resolution RGB images of b(I) and c(I) are converted into BRG images: b(II) and c(II), respectively.

## *Chapter 6*

- Figure 1:** Drop formation with continuous inkjet and effect on printing: (a) Constriction of the inkjet to form a drop, (b) A stream of inkjet drops with satellite droplets behind the main drops in flight, (c) A magnified image of printed vertical line; (a) and (b) are taken from<sup>8</sup> and c from<sup>6</sup> (with permission).
- Figure 2:** Non-coalescence behaviour of a satellite droplet.
- Figure 3:** Schematic diagram of formation of secondary Non-Coalescent Droplets.
- Figure 4:** Pendant droplet: coalescing mechanism at the air-liquid interface of a surfactant solution. (Video 1 on the web)
- Figure 5:** Sessile droplet: coalescing mechanism at the air-liquid interface of AKD. (Video 2 on the web)
- Figure 6:** Formation of non-coalescent droplets of NaOH [0.22M] in a TritonX-100 solution (0.8 mM) on air-liquid interfaces (H<sub>2</sub>SO<sub>4</sub>, 0.095M in the same surfactant solution with phenolphthalein dye). The non-coalescent

droplets and the interface showed no colour change. (Video 3 on the web)

- Figure 7:** Probability of forming secondary non-coalescent droplets as a function of the impinging height.
- Figure 8:** Probability of forming secondary non-coalescent droplets as a function of the Weber Number.
- Figure 9:** Schematic presentation of droplet coalescence as triggered by the Laplace Pressure.

### *Chapter 7*

- Figure 1:** Details of a V-groove made on quartz surface (all dimensions in mm). (a) top-view, (b) front-view, (c) cross-section of V-groove.
- Figure 2:** SEM micrograph and optical microscopic image of a 0.5 mm ( $\theta = 60^\circ$ ) groove.
- Figure 3:** Schematic diagram of the experimental setup.
- Figure 4:** Schematic representation of the V-groove wicking. Liquid wicks through a distance  $z$  into a wettable V-groove. V-groove of apex angle  $\beta$ , width  $w_0$  and height  $h_0$  creates  $\alpha$  angle with the horizontal surface. Wicking threshold creates  $\phi$  angle along the wicking direction.
- Figure 5:** Dynamics of a sessile water droplet when introduced on a flat, smooth quartz surface.
- Figure 6:** Dynamics of a sessile water droplet when introduced on a quartz surface with a V-groove ( $\beta = 60^\circ, 90^\circ, 120^\circ$ ;  $w_0 = 0.5$  mm). Images were taken at different magnifications.
- Figure 7:** Laplace driving force on wicking threshold. (a) Laplace driving force working perpendicular to the threshold, (b) planes (EFG and EFG') perpendicular or inclined ( $\pi/2 - \phi$ ) with respect to z-axis, (c) threshold geometry: for plane EFG and EFG', (d) threshold geometry: y-z plane.
- Figure 8:** Laplace driving force of the threshold.
- Figure 9:** Water wicking distance ( $z$ ) as a function of time in V-grooves on quartz surface of different geometry ( $\beta = 60^\circ, 90^\circ, 120^\circ$ ;  $w_0 = 0.2, 0.5$  mm).
- Figure 10:** Water wicking distance as a function of square root of  $t$  ( $\text{ms}^{1/2}$ ) in V-groove on a quartz surface of different geometry ( $\beta = 60^\circ, 90^\circ, 120^\circ$ ;  $w_0 = 0.2, 0.5$  mm).
- Figure 11:** Vectors representations of the threshold region; vector normal to the groove wall ( $\mathbf{F}_w$ ) and the vector normal to the flat liquid surface in the threshold region ( $\mathbf{F}_T$ ).
- Figure 12:** Percentage of droplet volume into the V-groove.
- Figure 13:** Schematic of liquid drop hydraulic head estimation using equal volume cylinder.

**Figure 14:** Theoretical prediction of wicking dynamics on V-groove surfaces in contrast with the experimental results. (a)  $\beta = 60^\circ$ ;  $w_0 = 0.2, 0.5$  mm, (b)  $\beta = 90^\circ$ ;  $w_0 = 0.2, 0.5$  mm, (c)  $\beta = 120^\circ$ ;  $w_0 = 0.2, 0.5$  mm.

### Chapter 8

**Figure 1:** Schematic diagram of the experimental setup.

**Figure 2:** Dynamics of a sessile water droplet impinging, with different impact velocities, a flat quartz surface; images were taken at different magnifications.

**Figure 3:** Dynamics of a sessile water droplet impinging, with different impact velocities, a V-groove ( $\beta = 90^\circ$ ,  $w_0 = 0.5$ mm) quartz surface; images were taken at different magnifications.

**Figure 4:** Effect of the impact velocity on the wicking dynamic; water wicking distance as a function of square root of  $t$  ( $\text{ms}^{1/2}$ ), V-groove on a quartz surface ( $v = 0.00\text{m/s}, 0.31\text{m/s}, 0.44\text{m/s}, 0.54$  m/s). (a)  $\beta = 60^\circ$ ;  $w_0 = 0.2, 0.5$  mm, (b)  $\beta = 90^\circ$ ;  $w_0 = 0.2, 0.5$  mm, (c)  $\beta = 120^\circ$ ;  $w_0 = 0.2, 0.5$  mm.

**Figure 5:** Effect of the groove geometry and inertia on the instantaneous wicking velocity ( $dz/dt$ ). (a)  $\beta = 60^\circ$ ,  $w_0 = 0.2$  mm, (b)  $\beta = 60^\circ$ ,  $w_0 = 0.5$  mm, (c)  $\beta = 90^\circ$ ,  $w_0 = 0.2$  mm, (d)  $\beta = 90^\circ$ ,  $w_0 = 0.5$  mm, (e)  $\beta = 120^\circ$ ,  $w_0 = 0.2$  mm, (f)  $\beta = 120^\circ$ ,  $w_0 = 0.5$  mm.

### Chapter 9

**Figure 1:** Schematic representation of wetting [ $r(t)$ ] and wicking [ $z(t)$ ] of a sessile droplet impinging the middle of a V-groove. (a) Isometric view, (b) threshold region, (c) top view.

**Figure 2:** Schematic representation of the V-groove.

**Figure 3:** Schematic of surface profile of V-groove ( $\beta=120^\circ$ ,  $w_0 = 0.2$  mm) measured using Talysurf Series; measurement: Slope =  $\alpha = 90 - \beta/2 = 30$  deg.

**Figure 4:** Experimental system to measure wicking and wetting.

**Figure 5:** Dynamics of a sessile water droplet impinging, with and without initial velocity, a flat quartz surface or a V-groove ( $\beta = 120^\circ$ ,  $w_0 = 0.5$  mm; quartz surface) on a quartz surface.

**Figure 6:** Dynamics of a sessile water droplet impinging, with initial velocity  $0.54$  m/s, a V-groove ( $\beta = 120^\circ$ ,  $w_0 = 0.2, 0.5$  mm) on a quartz surface.

**Figure 7:** Effect of groove width and droplet inertia on the wicking dynamic. (a)  $\beta = 120^\circ$ ,  $w_0 = 0.5$  mm, (b)  $\beta = 120^\circ$ ,  $w_0 = 0.2$  mm.

**Figure 8:** Effect of groove width and droplet inertia on the wetting dynamic. (a)  $\beta = 120^\circ$ ,  $w_0 = 0.5$  mm, (b)  $\beta=120^\circ$ ,  $w_0 = 0.2$  mm.

**Figure 9:** Percentage of droplet volume into the V-groove.

- Figure 10:** Effect of groove width and droplet inertia on the instantaneous wicking velocity ( $dz/dt$ ). (a)  $\beta=120^\circ$ ,  $w_0 = 0.5 \text{ mm}$ , (b)  $\beta=120^\circ$ ,  $w_0 = 0.2 \text{ mm}$ .
- Figure 11:** Effect of the groove width and droplet inertia on the instantaneous wetting velocity ( $dr/dt$ ). (a)  $\beta = 120^\circ$ ,  $w_0 = 0.5 \text{ mm}$ , (b)  $\beta = 120^\circ$ ,  $w_0 = 0.2 \text{ mm}$ .
- Figure 12:** Maximum Wicking ( $V_{\text{wick max}}$ ) and Wetting ( $V_{\text{wet max}}$ ) velocities for different drop impact velocities.
- Figure 13:** Comparison of average liquid wetting and wicking distance on V-groove geometry: (a)  $\beta = 120^\circ$ ,  $w_0 = 0.5 \text{ mm}$ , (b)  $\beta=120^\circ$ ,  $w_0 = 0.2 \text{ mm}$ .
- Figure 14:** Theoretical prediction of wicking dynamics on V-groove surfaces compared with experimental results; Washburn model:  $z \propto t^{1/2}$ , for  $\alpha > \theta$  and  $\alpha = \theta$ .

### *Chapter 10*

- Figure 1:** Scanning electron microscopic (SEM) image of the electrospun PCL nanofibres scaffold.
- Figure 2:** Text printed using albumin-FITC on paper (Times New Roman, 5pt and 10pt); (a) printing from two different cartridges (UV-light), (b) a confocal microscopy (Krypton, 5x).
- Figure 3:** (a) Printed digital photo using albumin-FITC on paper surface. (b) Negative image of the photo.
- Figure 4:** Text printed with of HRP enzyme on paper (Times New Roman, 14Bpt). The application of DAB liquid substrate reveals the characteristic brown-coloured precipitates of the oxidized DAB, indicating HRP enzyme activity.
- Figure 5:** Confocal Images (Krypton, 5x) of inkjet printed patterns on electrospun PCL Scaffold using albumin-FITC; biomolecules physically adsorbed on the surface (a) before, (b) after immersing into aqueous buffer (2 days in Phosphate Buffer Solution, PBS); (bar length = 200  $\mu\text{m}$ ).
- Figure 6:** Confocal Images (Krypton, 5x) of albumin-FITC concentration gradient; (a) concentration gradient printed using mono-bio-ink (protein solution), (b) concentration gradient printed using two bio-inks printed from two cartridges (protein solution and buffer solution).
- Figure 7:** Paper-based microfluidic devices. (a) Microfluidic paper with three different designs of biomolecular patterns (magenta shades represent intended printing patterns); (b)-(d) the three different printed patterns. The scales are in mm.

## LIST OF TABLES

### *Chapter 2*

**Table I:** ALP rate constants on different treated papers at 23°C

### *Chapter 3*

**Table I:** Concentration distribution parameters of gray values for adsorbed ink on paper

**Table II:** Deactivation rate constants for bioactive enzymatic papers

### *Chapter 4*

**Table I:** Enzyme retention on paper: before and after leaching; n = 8

**Table II:** Relative activity of ALP enzymatic papers at 23°C: with and without leaching

**Table III:** Deactivation Rate Constants for ALP enzymatic papers: Phase -1

**Table IV:** Deactivation Rate Constants for ALP enzymatic papers: Phase -2

**Table V:** Activation Energy of Deactivation Process of ALP Enzymatic Papers

### *Chapter 5*

**Table I:** Molecular weight and blood concentration of the various immunoglobins (Ig) (16, 19-20)

### *Chapter 6*

**Table I:** Physical properties of liquid droplets at 23°C <sup>19</sup>

### *Chapter 7*

**Table I:** V-groove geometrical parameters.

**Table II:** Critical Parameters of Liquid Wicking along V-groove

### *Chapter 8*

**Table 1:** V-groove geometry from different techniques.

### *Chapter 10*

**Table I:** Physical Properties of Commercial Ink Jet Inks and Bio-inks at 23°C

## GLOSSARY

<i>AFM</i>	Atomic force microscope
<i>AKD</i>	Alkyl Ketene Dimer
<i>ALP</i>	Alkaline Phosphatase
<i>AOD</i>	Alkaline oxidase
<i>BCIP</i>	5-bromo-4-chloro-3-indolyl phosphate
<i>CALB</i>	Candida antarctica lipase B
<i>CMYK</i>	Cyan-Magenta-Yellow-Black
<i>CMC</i>	Critical Micelle Concentration
<i>CPAM</i>	Cationic polyacrylamide
<i>DAB</i>	3,3'-Diaminobenzidine
<i>DOD</i>	Drop-on-demand
<i>DNA</i>	Deoxyribonucleic Acid
<i>dpi</i>	Dot per inches
<i>DTAB</i>	Dodecyltrimethylammonium bromide
<i>E<sub>a</sub></i>	Active enzyme
<i>E<sub>i</sub><sup>*</sup></i>	Inactive Enzyme
<i>E-S</i>	Enzyme-substrate
<i>FITC</i>	Fluorescein isothiocyanate
<i>fps</i>	frames per second
<i>GSM</i>	Gram per square meter
<i>H<sub>2</sub>O<sub>2</sub></i>	Hydrogen-per-oxide
<i>HRP</i>	Horseradish Peroxidase
<i>Ig</i>	Immunoglobulins
<i>KD</i>	Kilodalton ( $1.6605 \times 10^{-27}$ kg)
<i>LED</i>	Light Emitting Diode
<i>M<sub>w</sub></i>	Molecular weight
<i>NBT</i>	3,3'-(3,3'-dimethoxy-4,4'-biphenylene)-bis-(2-p-nitrophenyl-5-phenyl-2H-tetrazolium chloride)
<i>N-C-D</i>	Non-coalescent droplets
<i>NGF</i>	Nerve growth factor

<i>PAA</i>	Polyacrylic Acid
<i>PCL</i>	Poly( $\epsilon$ -caprolactone)
<i>PBS</i>	Phosphate buffer saline
<i>PDMS</i>	Poly-dimethylsiloxane
<i>PEO</i>	Polyethylene oxide
<i>PMMA</i>	Poly-methyl methacrylate
<i>RA</i>	Relative activity
<i>RBC</i>	Red Blood Cell
<i>RGB</i>	Red-Green-Blue
<i>RH</i>	Relative humidity
<i>SEM</i>	Scanning electron microscope
<i>TAPPI</i>	Technical Association of the Pulp and Paper Industry
<i>UV</i>	Ultra-Violet
$\Delta P$	Laplace pressure

## NOMENCLATURE

$Bo$	Bond number
$Bw$	Basis weight
$Ca$	Capillary number
$D, Da$	Dalton
$^{\circ}C$	Degree Celsius
$E$	Enzyme
$F_{\gamma}$	surface tension force
$F_{\mu}$	viscous resistance force
$F_T$	total driving force in the direction of wicking
$g$	Gravitational acceleration
$h_0$	V-groove height
$I$	Colour intensity
$ID$	Internal diameter
$k$	Rate constant
$k_d$	Deactivation rate constants
$M$	Molar concentration
$n$	Number of replicates
$P$	Poise
$P$	probability
$pt$	Point
$S$	Substrate
$t$	Time
$t^*$	Inflection time in Chapter 4
$t_{1/2}$	Half-life
$T$	Temperature
$t_{impact}$	Time of a droplet impact on surface
$w_0$	V-groove width
$We$	Weber number
$z$	Wicking distance

## GREEK LETTERS AND SYMBOLS

$\Omega$	Ohm
$\rho$	Density
$\gamma$	Surface tension
$\mu$	Viscosity of a liquid
$\zeta$	Zeta potential
$\eta$	Viscosity
$\theta$	Contact angle of air-liquid-solid interface
$\beta$	Apex angle of a V-groove
$\gamma$	Interfacial energy
$\varphi$	Slope of the threshold region as defined in chapter 5
$\alpha$	$90^\circ - \beta/2$
$\Delta$	change

---

# Chapter 1

---

Introduction and  
Literature Review

---

Chapter 1	1
Introduction and Literature Review	1
1. General	2
2. Literature Review	6
2.1. Functional Biomolecules	6
2.1.1. Enzymes	7
2.1.2. Antibody	8
2.2. Paper as a Substrate	9
2.3. Biomolecular Immobilization	11
2.4. Biomolecular Printing	14
2.4.1. Contact Printing Techniques	15
2.4.1.1. Pin Printing:	15
2.4.1.2. Nano-Tip Printing:	15
2.4.1.3. Micro-stamping:	16
2.4.2. Non-Contact Printing Techniques	17
2.4.2.1. Laser Writing:	18
2.4.2.2. Photochemistry-Based Printing:	18
2.4.2.3. Electro-Printing:	19
2.4.2.4. Electro-spray Deposition (ESD):	19
2.4.2.5. Ink jet Printing:	20
2.5. Liquid-Liquid interaction: Isothermal Non-Coalescence of Liquid Droplets at the Air-Liquid Interface	21
2.6. Solid-Liquid Interaction: Liquid Wicking Kinetics in Open Capillaries	23
3. Research Challenges	25
4. Scope of Thesis	26
5. Organization of Chapters	28
6. References	32

## 1. GENERAL

**B**iosurface engineering consists of optimizing the biomolecular activity on a surface in terms of biofunctionality and biocompatibility. Biomolecule immobilization on porous surface is of special interest to manufacture bioassays and functional surfaces. There is a need for low cost bioassays, in health and environmental diagnostics. Bioassays made of disposable materials can be used for the daily tests to monitor diabetes, and to detect blood typing, cancers and genetic conditions. They can also be used to identify and filter heavy metals, chemical compounds and microbial activity in water. Successful commercialization requires bioassays to be low cost, which is best achieved through a high volume manufacturing

process and with commodity materials. Paper and printing are two technologies meeting these criteria.

Printing is a high speed technology, highly adaptive and able to deliver controlled patterns of functional fluids at an exceptional accuracy and high lateral resolution. Biomolecular printing on porous surface/paper can be broadly classified as ‘contact’ and ‘non-contact’ techniques. Though contact printing is a widely used technology because of the reproducibility of printed spots and facile maintenance, it has limited flexibility and presents high risks of cross contamination<sup>1, 2</sup>. Non-contact printing techniques, such as ink jet printing, are newer and more varied. Ink jet printing is a digital technique which delivers functional fluids at high resolution, improved through-put and reduced cross contamination; it can be an interesting technology for large scale fabrication of bioassays<sup>1, 3, 4</sup>. However, two phenomena are of concern to the engineer when an ink jet drop comes into contact with a surface<sup>1, 5-8</sup>. The first is the formation of satellite drops from the ink jet nozzle, which may form non-coalescence droplets due to liquid-liquid interaction, and may roll from their target. The second is the solid-liquid interaction, and especially the wicking of the delivered droplet into the long surface grooves, fibres, or surface imperfections driven by capillary forces. These two phenomena would decrease print definitions and increase the biomolecular loss.

Paper, a non-woven material made of cellulosic fibres, is highly wettable when untreated, easy to functionalise, biodegradable, sterilisable, biocompatible and cheap. It is also chemically stable, porous, light weight and strong. It has long been used for analysis in chromatography<sup>9, 10</sup>. Thin coatings of polymers and inorganics can be achieved through wet-end addition, surface sizing, coating and other surface treatments. This suggests that paper is an ideal composite for biosurface engineering and is a renewable natural material of choice for the production of disposable bioassay devices.

However, the biotechnology industry has a limited understanding of the effect of the paper structure and chemical composition on the fluid transport; biomolecule functionalization of paper is also little known.

The concept of paper bioassays is to rely on paper for the transport of fluids which is achieved through capillary flow of the analyte within the porous paper structure. Hydrophobic barriers can be printed onto paper to control the directionality of the flow. Microfluidic systems for paper diagnostics have been pioneered by Whitesides at Harvard University<sup>11-13</sup>. A first generation system was achieved by flexographic printing of a rigid photoresist polymer onto filter paper to provide channels. A second

generation was made by plotting circuits with a pen filled with a polydimethylsiloxane/hexane solution<sup>13</sup>. Low resolution, low manufacturing speed, and low ink volume are three major limitations for these systems.

Peptides, enzymes and cells have already been printed under laboratory conditions using a variety of technologies including ink jet printing<sup>3, 4, 14-22</sup>. However, most trials have been limited to low volumes/areas and to very simple patterns. Little understanding is available on the ink jet printing defects caused by liquid-liquid and solid-liquid interactions during the delivery of the droplets of biomolecular solution. Also, no strong fundamental understanding has been developed on the effect of the surface on the biofunctionality. Few studies have investigated paper as a substrate for bio-printing and bioactive paper. Among those are paper strips to test fish freshness using two enzymes (xantine oxidase and nucleoside phosphoribosyltransferase)<sup>23</sup>, and bioactive paper to monitor alcohol content in the breath using alkaline oxidase (AOD)<sup>24</sup>.

Enzymes are model biomolecules of choice for a fundamental study because of their stereospecificity, wide range and availability. While enzyme engineering and enzyme immobilization are well understood<sup>24, 25</sup>, there is little knowledge on the effect of the biomolecule spatial orientation, surface property and interaction biomolecule-surface on the functionality of the immobilized enzymes and peptides. Voss et al. reported that the stability of Horseradish Peroxidase (HRP) immobilized within porous silica nanoparticle increases by over an order of magnitude compared to the molecule in solution<sup>26</sup>.

The first requirement of a bioactive paper is to retain the functionality, reactivity and selectivity of its immobilized biomolecule. The second is to provide good biomolecule stability. We hypothesize the biomolecules would be less stable on paper than in solution due to the harsh dry environment. Biomolecules physisorbed on paper can show less retention and higher desorption once rewetted. Covalent immobilization can reduce the problem, however, it would be unfavourable for the ink jet printing condition. Using polymers is hypothesized to improve the enzyme fixation and retention on paper<sup>27</sup>. However, little is known on the effect of retention polymers on the thermal stability and the aging of bioactive papers. An objective of this study is to evaluate the potential of paper as a stable support for the immobilization of biomolecules for catalytic and diagnostic applications. Another objective is to use ink jet print fine patterns of biomolecules on paper and other porous substrates.

The fundamental parts of this study are three fold. The first is to characterize the enzymatic papers in terms of activity, selectivity, stability and aging. The reactivity and stability of different enzymatic bioactive papers are modelled and quantified. Alkaline phosphatase (ALP) and Horseradish Peroxidase (HRP) were selected as model enzymes for their stability and wide range of applications. An image analysis technique was developed to quantify the enzymatic activity on paper. The selectivity of antibody deposited on paper was also investigated from the specific antibody-antigen interaction. The concept of bioassays to identify antigens and antibodies in biofluids was explored. The second objective of this study is to quantify the fixation and retention of biomolecules adsorbed on paper. Three different water soluble polymers: cationic, anionic and neutral, were used as retention aids to improve the adsorption and retention of enzymes on paper. The polymer effect on the activity and stability of enzymatic papers were quantified. The last objective is to engineer biosurface through ink jet printing. Different biomolecules were ink jet delivered in control patterns on two porous substrates. A protein (albumin-FITC) and an enzyme (HRP) were used as model biomolecules in bio inks. A commercial thermal ink jet printer was reconstructed to deliver biomolecules. Microfluidic systems and enzymatic papers were ink jet printed on paper. Discreet and continuous concentration gradients of proteins on polymeric scaffolds were achieved by ink jet printing; these protein concentration gradients can serve as potential guidance cues for cell growth generation for tissue engineering application. A novel strategy was developed to engineer very smooth, continuous concentration gradients of biomolecules by ink jet printing. The liquid-liquid and solid-liquid interaction of the droplets once ink jet printed on paper were quantified. It is the objective of the study to engineer stable bioactive papers for diagnostic and industrial surfaces.

This chapter consists of four sections. The first addresses the scientific and technological information required to develop for bioactive paper. Recent progresses on biomolecules, paper, biomolecular immobilization, printing techniques to deliver functional fluids are reviewed. The second is an analysis to identify the critical gaps in knowledge required to progress the development of bioactive papers. The third section presents how this doctoral study attempts to fulfill some of these gaps in knowledge. In the last section the organization of the thesis is presented.

## 2. LITERATURE REVIEW

### 2.1. Functional Biomolecules

Various biomolecules, particularly enzymes, growth factors for cells, antibodies and nucleic acids have been harnessed for analytical as well as different functional purposes<sup>28</sup>. Different research groups have deposited enzymes, antibodies and DNA (deoxyribonucleic acid) derivatives on various substrates to develop biosensors<sup>29</sup>. Different patterns of growth factors have been printed on polymer and hydrogel scaffolds to control cell positioning and outgrowth, which is essential for tissue engineering<sup>16-18, 30, 31</sup>. Biomolecules can be incorporated into paper or paper-like materials, enabling the mass-production of functional materials for multiple purposes.<sup>28, 29</sup>. Few scientific studies have described the immobilization of enzymes on paper. Among those, Masao investigated paper strips to test fish freshness using two enzymes<sup>23</sup>. Akahori et al demonstrated bioactive paper to monitor alcohol content in the breath using alkaline oxidase (AOD)<sup>24</sup>. Peptides and Enzyme immobilized on paper for the catalytic production of biofuels (diesel and ethanol), antibody immobilized on paper for the high selectivity separation of antigen in blood or fermentation streams, and antimicrobial papers are a few other potential applications<sup>32, 33</sup>. In an early review<sup>28</sup>, Aikio et al. summarized different types of biomolecules with their potential utilization for functional purposes, illustrated in Figure 1.

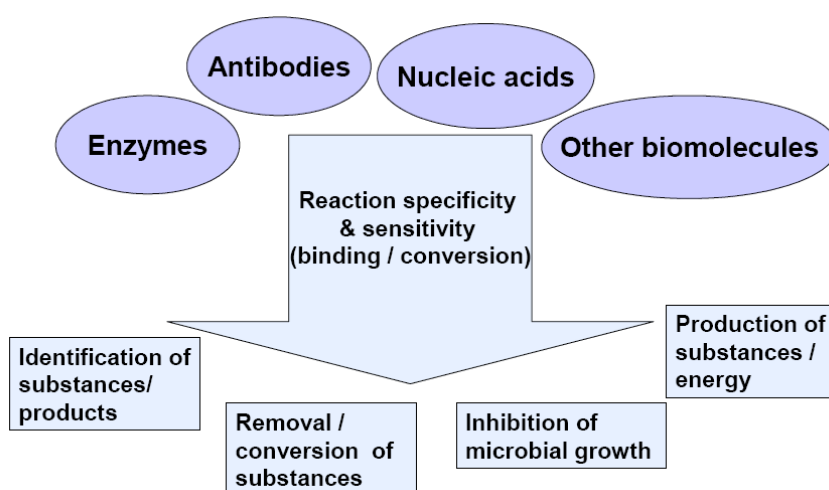
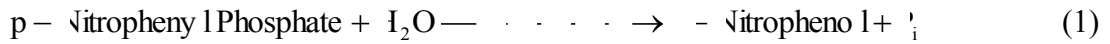


Figure 1: Use of biomolecules for different functional purposes<sup>28</sup>.

### 2.1.1. Enzymes

Enzymes are model biomolecules of choice for a fundamental study because of their stereospecificity, their wide range and availability. While enzyme engineering and enzyme immobilization are well understood<sup>24, 25</sup>, there is little knowledge on the effect of the biomolecule-paper interaction on the functionality, surface properties, orientation, reactivity and stability of immobilized enzymes and peptides.

Two enzymes: alkaline phosphatase (ALP) and horseradish peroxidase (HRP), are frequently selected for their stability and wide range of applications<sup>26, 34-49</sup>. The alkaline phosphatase enzyme is responsible for removing phosphate groups from different substrates including proteins and alkaloids. It is most effective in an alkaline environment. An example of the reaction can be described as<sup>50</sup>:



where  $\text{P}_i$  = inorganic phosphate.

ALP is present in the liver, intestine, placenta, bone, and kidney of mammals<sup>45</sup>. It can also be obtained from *Escherichia coli*, which has similar catalytic properties, similar pH-rate profile, and forms the same phosphoserine intermediate as the intestinal enzyme<sup>34</sup>. The molecular weight is 89 kDa for *E. coli* ALP<sup>51</sup> and 126-140 kDa for bovine intestinal ALP<sup>45, 48</sup>. ALP exists as a dimer comprising two very similar or identical subunits each containing 429 amino acids (Figure 2)<sup>34</sup>.

Horseradish peroxidase (HRP) is a single chain polypeptide enzyme containing four disulfide bridges (Figure 2). It is isolated from horseradish roots (*Amaracia rusticana*) and belongs to the ferroporphyrin group of peroxidase<sup>52</sup>. It has a molecular weight of 44 kDa and is reported to be very stable<sup>16</sup>. HRP readily combines with hydrogen peroxide ( $\text{H}_2\text{O}_2$ ) and the resultant, HRP- $\text{H}_2\text{O}_2$  complex, can oxidize a wide variety of chromogenic hydrogen donors<sup>52</sup>. Most reactions catalyzed by HRP can be expressed by the following equation<sup>35</sup>:



where,  $AH_2$  and  $AH^*$  represent the reducing substrate and its radical product, respectively.

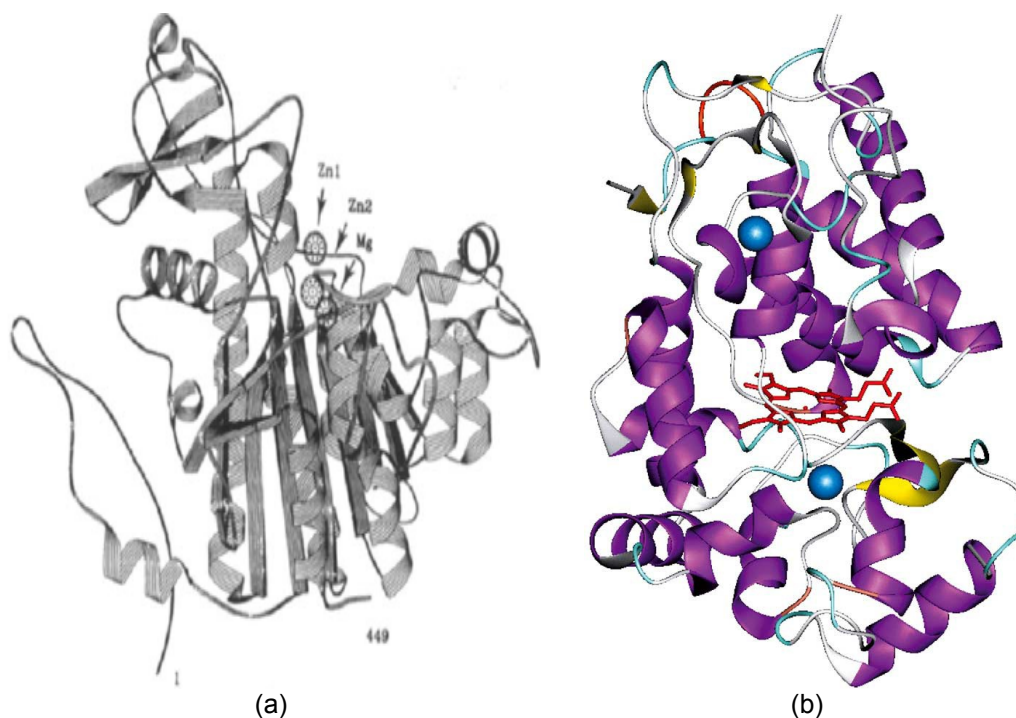


**Figure 2:** Three dimensional representation of enzyme. (a) Alkaline phosphatase (ALP)<sup>34</sup>, (b) horseradish peroxidase (HRP)<sup>35</sup>.

### 2.1.2. Antibody

Antibodies are large glycoproteins of molecular weight of around 150 kDa produced in living organisms (excluding plants) via the immune response<sup>53, 54</sup>. Contact with an immunogen triggers a chain of events that leads to the activation of lymphocytes (white blood cells) and the synthesis of antibodies that selectively binds the immunogen<sup>53</sup>. Antibodies are a subclass of serum globulins that possess selective binding properties. Antibodies are also known as immunoglobulins (Ig)<sup>55</sup>. Antibodies have common structural features<sup>56</sup>. They possess two small light polypeptide chains of Mw ~ 25 kDa each, and two large heavy polypeptide chains of Mw ~ 50 kDa each<sup>53, 56, 57</sup>. These four chains are bound together in a single antibody molecule by disulfide bonds, and form a distinctive Y-shaped molecule. The two halves are identical with a central axis of symmetry (Figure 3). The NH<sub>2</sub>-terminal ends of the light polypeptide chains, known as F<sub>ab</sub> fragments, act as the antigen-binding fragment of the antibody. It is the amino acid sequence of these N-terminal ends that determine the specific antigen-

binding properties of the antibody molecule. Although the general structure of all antibodies is similar, the  $F_{ab}$  fragment is extremely variable, which allows millions of different antigen binding sites to exist<sup>53, 58</sup>. The selectivity of antibody-antigen interactions is analogous to the selectivity of enzyme-substrate interactions. The structure of the antigen-binding site of an antibody allows a complementary fit with structural elements and functional groups on the antigen<sup>53</sup>.

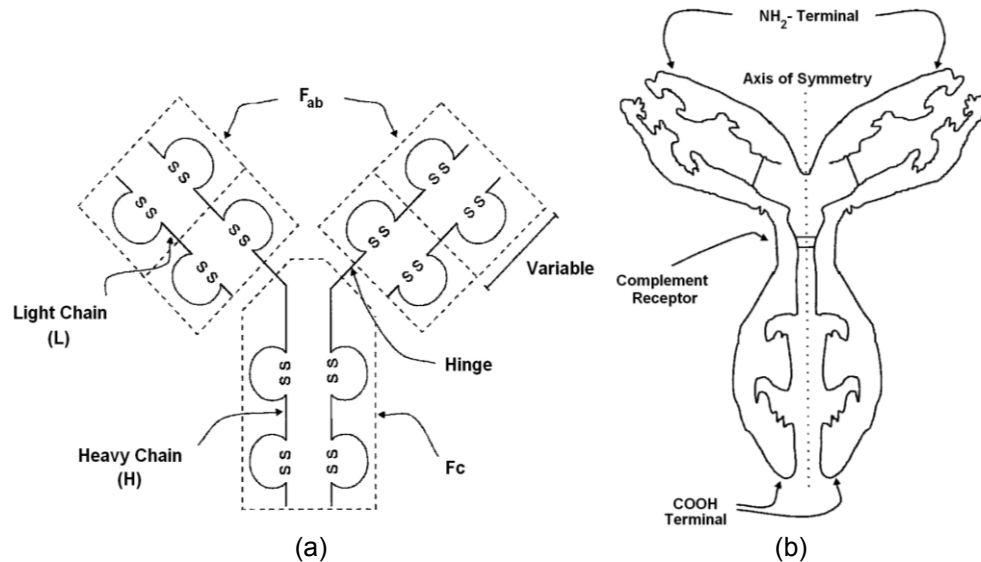


**Figure 3: Structural diagrams representing antibody molecules<sup>53</sup>.**

The antibodies are classified into five different isotypes on the basis of the different types of antibody heavy chains ( $F_c$ )<sup>56</sup>. The most abundant isotypes in mammals are called IgG, IgM, IgA, IgE and IgD<sup>59</sup>. They may have the same antigen-binding properties, but exhibit different functional properties. Their immune responses to the foreign objects they encounter are different<sup>57</sup>. IgM, immunoglobulin M, is the primary antibody against A and B antigens on red blood cells (RBC). It is a large antibody found in the human circulatory system<sup>59</sup>.

## 2.2. Paper as a Substrate

A wide range of substrates have been studied to immobilize biomolecules for different functional purposes. Poly-methyl methacrylate (PMMA), poly-dimethylsiloxane (PDMS), homogeneous fibrin films on glass slides have been investigated to immobilize growth factors for cell patterning and to guide cell growth and to develop biosensors<sup>19, 22, 60, 61</sup>. ‘Bio-papers’ made from soy agar and collagen gel

have been used to print mammalian cells<sup>3</sup>. Voss et al<sup>26</sup> reported the use of porous silica nanoparticles to immobilize enzymes and proteins to study denaturation. Different research teams have used papers to immobilize enzymes, deoxyribonucleic acid (DNA) derivatives, bacteriophages, antibodies, etc; this was in an effort to develop paper based bioassays and diagnostic devices<sup>11, 12, 33, 62-67</sup>. The ideal support properties of paper include physical resistance to compression, hydrophilicity, inertness toward biomolecules ease of derivatization, biocompatibility, resistance to microbial attack, low cost and availability<sup>25, 68, 69</sup>. Cellulose is particularly protein and biomolecule friendly<sup>29</sup>. The porous structure of paper facilitates lateral flow assays, chromatographic separations and inexpensive microfluidic devices<sup>11, 12, 29, 62</sup>. It can be manufactured from renewable and recyclable resources.

The cellulosic fibres made from wood are the major component of many papers, such as: filter paper, copy paper, newsprint, packaging, etc<sup>70</sup>. Clean cellulose is a hydrophilic, slightly anionic surface with a low negative surface charge density<sup>71</sup>. Cellulose fibres can be described as hollow tubes about 0.8 to 2.0 mm long, 10 to 20  $\mu\text{m}$  wide, with a wall thickness of  $\sim 2 \mu\text{m}$ <sup>29, 72</sup>. Different minerals, such as, calcium carbonate, titanium oxide and clay, can serve as fillers to improve printability and optical properties. Water soluble polymers are used as retention aid to improve the retention of filler and process colloids<sup>73</sup>. Optical brightening agents and dyes are often added to improve the optical properties of paper.

Paper results from the filtration of the furnish, a dilute ( $\sim 1 \text{ wt}\%$ ) aqueous suspension of fibres, colloidal filler particles and soluble polymers, over a moving wire. Papermaking consists of four basic unit operations: forming, pressing, drying and surface treatment. Forming consist of producing a wet-web of uniform basis weight and properties. The headbox forms a jet of furnish distributed across the width of the paper machine. The jet is impinged into a wire moving over a series of drainage elements (foils, vacuum boxes), which brings the web solid content to around 20%. The difference between the jet velocity ( $V_{\text{jet}}$ ) and the wire velocity ( $V_{\text{wire}}$ ) affects the fibre orientation. In ‘rushing’ the jet velocity is slightly higher than the wire velocity ( $V_{\text{jet}} > V_{\text{wire}}$ ) which preferentially aligns the fibres in the cross machine direction (CD). In ‘dragging’, the jet velocity is slightly lower than the wire velocity ( $V_{\text{jet}} < V_{\text{wire}}$ ) which orientates fibres more in the machine direction (MD). The wet web is then pressed by 3 roll nips placed in series. Pressing serves two functions. The first is to remove as much water by the economic mechanical action as possible without damaging the pulp fibres;

a solid content of 45% is typically reached. The second purpose is to consolidate the wet-web and to form strong fibre-fibre bonds. Drying removes all water and brings the paper to a solid content of 94% (fine paper) to 99% (tissue). Surface treatments, such as calendaring, surface sizing and coating, are then available to tailor make the properties of paper.

In the paper structure, the fibres are approximately layered into a x,y plane<sup>29, 74</sup>. Porosity, surface chemistry and optical properties are critical properties of paper to fabricate bioactive paper by printing or coating<sup>29, 70, 73</sup>. Thickness ( $\tau$ , m) and basis weight (Bw,  $\text{g/m}^2$ ) are two important macroscopic properties which determine absorption and liquid consumption. Paper surface chemistry can highly influence the biosensor immobilization<sup>70</sup>.

### 2.3. Biomolecular Immobilization

The immobilization strategies for biomolecules can be as simple as nonspecific adsorption or as complex as molecular imprinting<sup>25, 75</sup>. Printing and coating technologies allow the application of functional fluids onto porous surfaces<sup>29, 70</sup>. However, the biomolecular adsorption by coating or printing may show limited functionality as the molecules are randomly oriented<sup>75</sup>. The adsorbed biomolecules tend to desorb from the surface over time once immersed in a liquid solution<sup>66, 75</sup>. Covalent immobilization can eliminate problems associated with desorption. However, there is often little control over the conformation or the orientation and thus the activity of the biomolecules can be limited<sup>75</sup>. Gupta and Mattiasson classified the various approaches of biomolecular immobilization into two broad categories: irreversible and reversible methods<sup>25, 76</sup>. Brena and Batista-Viera described covalent binding, entrapment (beads or fibers), microencapsulation and cross linking techniques as the irreversible enzymatic immobilization approaches; whereas, adsorption, ionic binding, affinity binding, chelation or metal binding and disulfide bonds are the reversible techniques<sup>25</sup>. In the recent review, McArthur et al.<sup>75</sup> generalized different immobilization strategies for biomolecules at interfaces which are illustrated in Figure 4.

Pelton comprised a range of techniques to immobilize biomolecules on cellulose fibres in his recent reviews<sup>29, 70</sup>. He broadly classified the immobilization techniques into four major categories, shown in Figure 5. The first technique is the physical immobilization, which addresses the adsorption of antibodies, enzymes,

bacteriophages, DNA aptamer, etc. on cellulose. The use of polymers can improve the adsorption and retention of biomolecules on cellulosic fibres. Polymers can also be used to prevent non-specific adsorption<sup>25, 75</sup>. The second category is the chemical immobilization, which comprises the chemical coupling reactions of different biomolecules with the functional groups of pure cellulose. Most cellulose substrates need to be activated by reaction with a small molecule or a polymer to produce surface functional groups suitable for a subsequent bioconjugation reaction. More details of activation techniques can be found in Pelton's review articles<sup>29, 70</sup>. The third method, biochemical immobilization, consists of the techniques using one or more biomolecules to bind the target biomolecule to cellulose. Genetic engineering approaches have been used to couple cellulose binding modules (CBMs) to antibodies, enzymes, bacteriophages or cells which spontaneously adhere to cellulose and/or hemicellulose<sup>29, 70, 77, 78</sup>. In the fourth technique, carrier particles or target biomolecules are covalently coupled to colloidal sized particles which can be then printed, coated or even added during the papermaking process<sup>29, 70</sup>. Using carrier particles to attach biosensors is an established technique. Particles, such as: microgel, silica, TiO<sub>2</sub>, etc are used to conjugate biosensors<sup>26, 79, 80</sup>. Ouali et al. reported that when diluted suspension of latex particles, coated with antibodies, is exposed to antigen, antibody-antigen binding causes the latex dispersion to aggregate giving a visible response<sup>29, 70, 81</sup>.

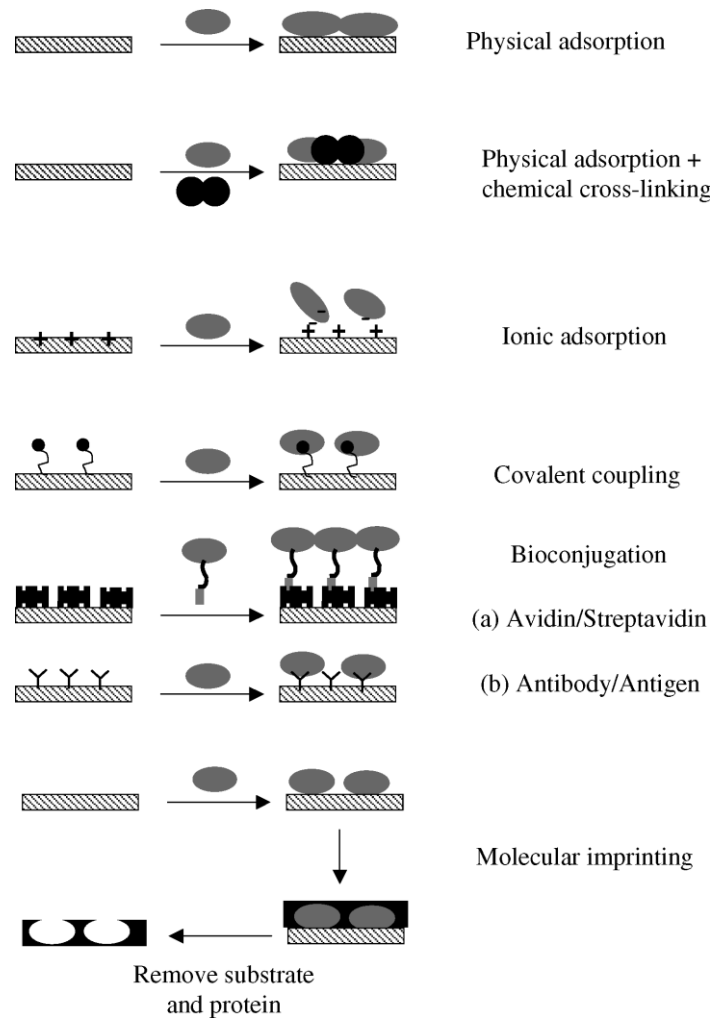


Figure 4: A range of immobilization strategies for biomolecules <sup>75</sup>.

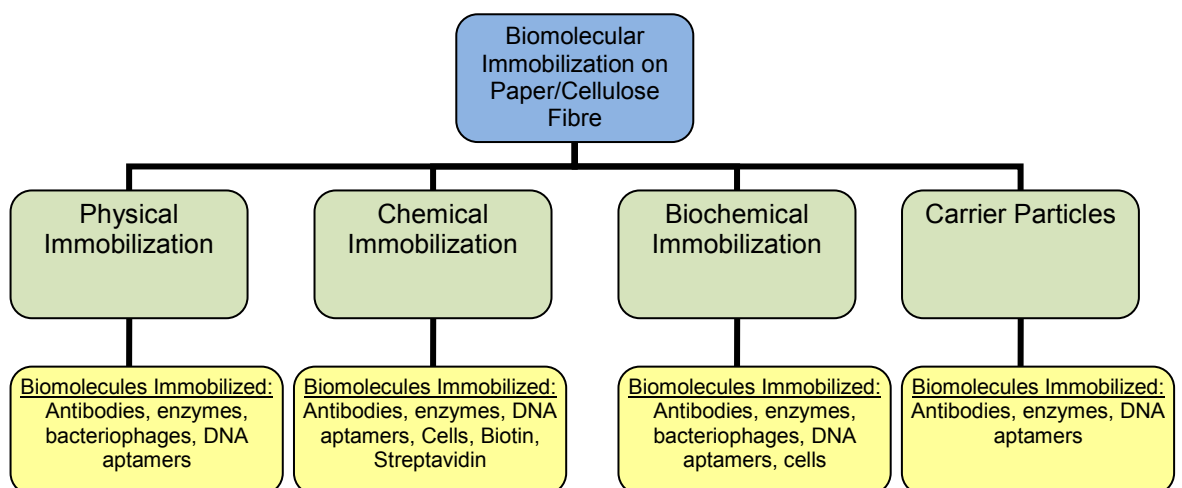
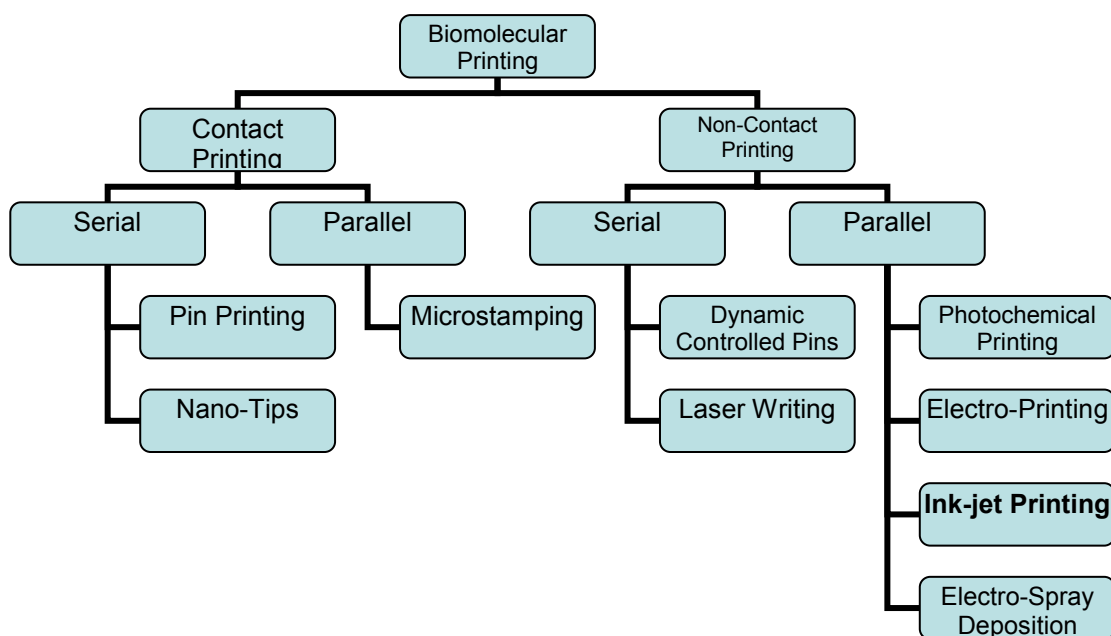


Figure 5 Four approaches of biomolecular immobilization onto dry or wet cellulose; figure inspired from reference <sup>29, 70</sup>.

## 2.4. Biomolecular Printing

Printing biomolecules on porous/solid substrates can be broadly categorized into ‘contact’ and ‘non-contact’ techniques<sup>1, 82</sup>. During contact printing, a roll comes into physical contact with the substrate to transfer fluid and deposit biomolecules. In contrast, non-contact printing involves no physical contact between the device and the substrate (e.g., photolithography, ink-jet printing, and laser writing). Each of these arrays of fabrication techniques can be sub-classified as serial or parallel. Fabrication throughput is limited in serial deposition due to serially repeated movements of the printing devices. Hence, parallel deposition techniques are a better choice for large-scale fabrication; however, most of the parallel techniques for depositing biomolecules are newer and thus, less developed than serial techniques<sup>1</sup>. Though contact printing is a widely used technology due to advantages like reproducibility of printed spots and facile maintenance, it has some major limitations, such as low-throughput and high contamination<sup>1, 2</sup>. Non-contact printing techniques are newer and more varied, comprising ink jet printing, which can be a better choice for large scale fabrication<sup>5, 67</sup>. Different printing techniques applied in biomolecule printing are summarised in Figure 6<sup>1, 82</sup>.



**Figure 6:** Biomolecular printing techniques; figure inspired from reference<sup>1, 82</sup>.

### 2.4.1. Contact Printing Techniques

Contact printing methods rely on the direct contact between the printing device and the substrate. Contact printing technologies employ solid pins, split pins, nano-tips, and microstamps<sup>1</sup>. Nano-tip printing is the most recent technology based on Scanning Probe Microscopy (SPM) and yields arrays with submicron spots.

#### 2.4.1.1. Pin Printing:

Pin printing is a widely used technique for microarray fabrication. Wang et al. reported that accurate quantitative analysis of printed microarrays is only possible with this method if spot uniformity and positional accuracy are achieved<sup>83</sup>. Spot uniformity is primarily determined by the sample viscosity, pin contact area, pin surface properties, substrate surface properties, substrate planarity, along with pin velocity, the precision of robotic controls, and the environmental control of humidity, temperature, and contamination. The technique of contact printing with pins is widely used for most non-commercial microarray fabrication. Figure 7 shows the basic principle behind contact printing with pin. When a pin is used to print multiple solutions, it must be washed and cleaned to avoid cross contamination. The load-print-wash process is repeated until the desired number of biological spots is printed on the substrate surface.

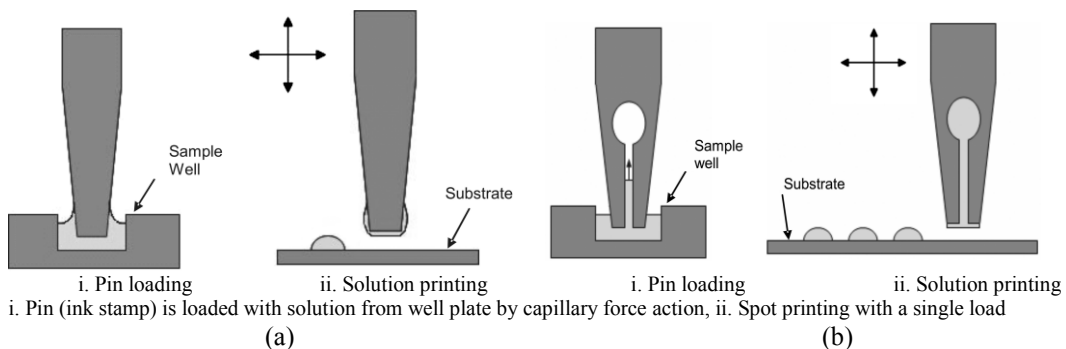


**Figure 7: Contact printing with pin. (a) Solid pin printing process. (b) Split pin printing process<sup>1</sup>.**

#### 2.4.1.2. Nano-Tip Printing:

The nano-tip printing technology developed for printing spots at the submicron scale are based on atomic force microscopy (AFM), which employs an AFM nano-tip for: (a) adding a sample or its binding molecules to the substrate (Figure 8a), known as dip-pen lithography<sup>84, 85</sup>; or (b) removing molecules (Figure 8b), known as AFM

grafting<sup>86, 87</sup>. When an AFM tip is brought into contact with a substrate, the solution flows from the coated tip to the substrate or vice versa by capillary action. AFM printing technology is a serial printing method, and is therefore slow compared to the parallel techniques such as, microstamping. Wadu-Mesthrige et al. reported the great advantage of AFM printing is the multiple use of same tip for both printing and reading (i.e., detection)<sup>1, 86</sup>.

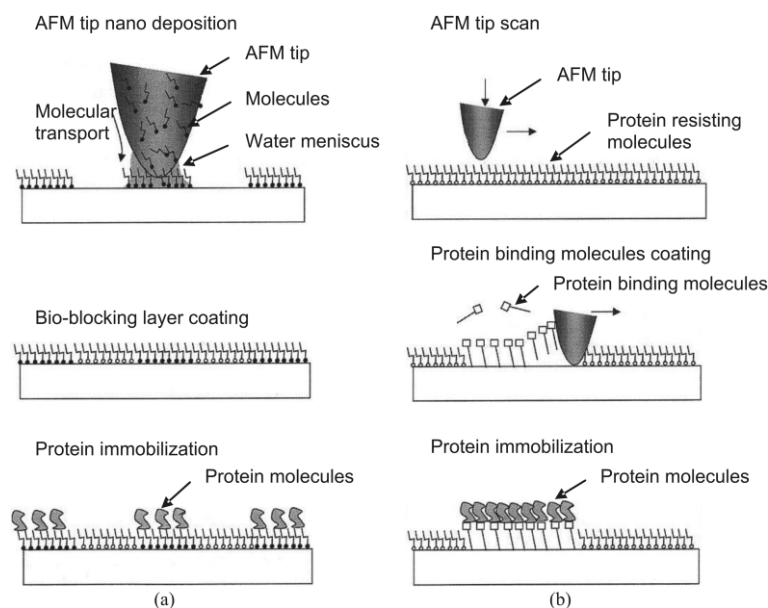


**Figure 8: (a) Schematic of AFM dip-pen lithography. (b) Schematic of AFM grafting<sup>88</sup>.**

#### 2.4.1.3. Micro-stamping:

As the micro-stamping process is simple and inexpensive, it is widely used in laboratory. Microcontact printing with elastomeric stamps, along with other soft lithographic microfabrication techniques, was first developed and demonstrated by Whitesides' group at Harvard University<sup>89, 90</sup>. Microstamping is an alternative to pin printing. In contrast to pin-printing, hundreds of spots are printed in parallel, enabling high-throughput microarray fabrication in microstamping. The mechanism of biomolecular microstamping is illustrated in Figure 9. Elastomeric stamps are manufactured by a micro-moulding technique that requires only a single photolithography step (Figure 9).

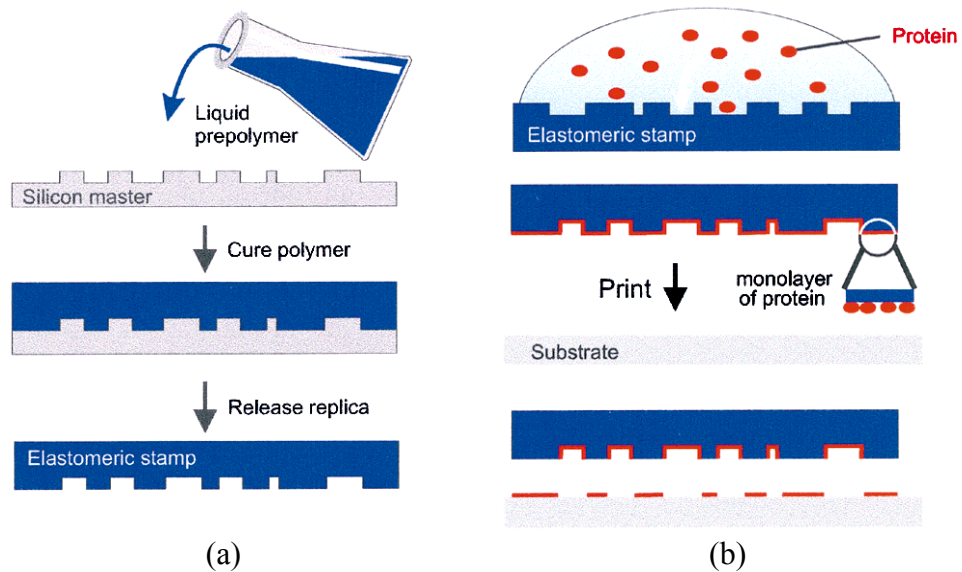


**Figure 9:** (a) Scheme of fabrication of a microstamp. (b) Use of microstamp in  $\mu\text{CP}$  <sup>2</sup>.

In Figure 9 a, a master, conventionally fabricated from a Si wafer, is replicated by pouring liquid pre-polymer of PDMS onto the master and curing. After its release, the stamp serves as the vehicle to transfer the “ink”, in this case proteins, to a substrate upon contact. Transfer occurs only at the sites of conformal contact between stamp and substrate <sup>2</sup>. This process enables reproducible, low-cost batch production, resulting in inexpensive and disposable micro-stamps. Using disposable stamps minimizes the problems of sample carry-over, cross-contamination, and the time consuming cleaning processes that are required for pin printing. One limitation of elastomeric microstamp fabrication procedure is the necessity of using photolithography and clean-room facilities to form the stamp molds.

#### 2.4.2. Non-Contact Printing Techniques

Non-contact printing techniques vary considerably from photochemistry methods, to laser writing and to fluid droplet dispensing. There are two main advantages to non-contact printing: reduced contamination and higher throughput. By keeping the printing devices and the substrates separated at all times, the likelihood of contamination is greatly reduced. Furthermore, non-contact printing methods hold the greatest potential for increasing micro-array fabrication throughput. Many non-contact methods deposit solutions in parallel, allowing entire arrays to be produced

simultaneously. Non-contact printing techniques comprise laser writing, photo-chemical printing, electro-spray deposition and ink jet printing.

#### **2.4.2.1. Laser Writing:**

Laser writing has recently been used to produce microarrays of protein solutions by means of direct and indirect spot deposition<sup>88</sup>. In indirect laser writing, a laminate or a photoresist is applied to a substrate and selectively removed with laser and a mask. A biological solution is then applied to the surface, and the remaining laminate is removed, leaving a patterned sample on the substrate<sup>91, 92</sup>. In direct laser printing, a pulsed laser is scanned across the surface of the disk, locally evaporating small regions of the coating. The sample evaporates and releases liquid droplets that accumulate on the substrate. Ringeisen et al. produced uniform 50  $\mu\text{m}$  spots and claimed that spots smaller than 10  $\mu\text{m}$  can be formed using this method<sup>91</sup>.

#### **2.4.2.2. Photochemistry-Based Printing:**

Photochemistry-based printing is based on the chemical treatment of the substrate and UV light exposure through photomasks. This technique is mainly categorized into photolithography and direct photochemical patterning<sup>93, 94</sup>. Figure 10 illustrates the mechanism of photochemistry-based printing. In photolithography, a positive photoresist layer is spin-coated onto the substrate, exposed to UV light through a photomask and then developed to form micrometer sized open regions where adhesion promoting molecules are bound (Figure 10a)<sup>1</sup>. The substrate is then immersed in solvent to remove the remaining photoresist, and adhesion-resistant molecules are bound to the exposed glass surfaces. In contrast, direct photochemical patterning does not require a photoresist layer. A substrate is coated with photochemical molecules and exposed to UV light through a photo mask (Figure 10b). UV-exposed molecules are either activated or deactivated to bind the biological molecules of interest. Photochemistry-based fabrication methods are mainly applied to protein and DNA arrays although cell adhesion regions can also be fabricated in this way<sup>1, 95</sup>. Photochemistry-based printing features high throughput. Tseng et al. reported that the major disadvantage of this method is the risk of biomolecule denaturation by photoresist solvents and the difficulty in patterning different samples in a single step<sup>88</sup>.

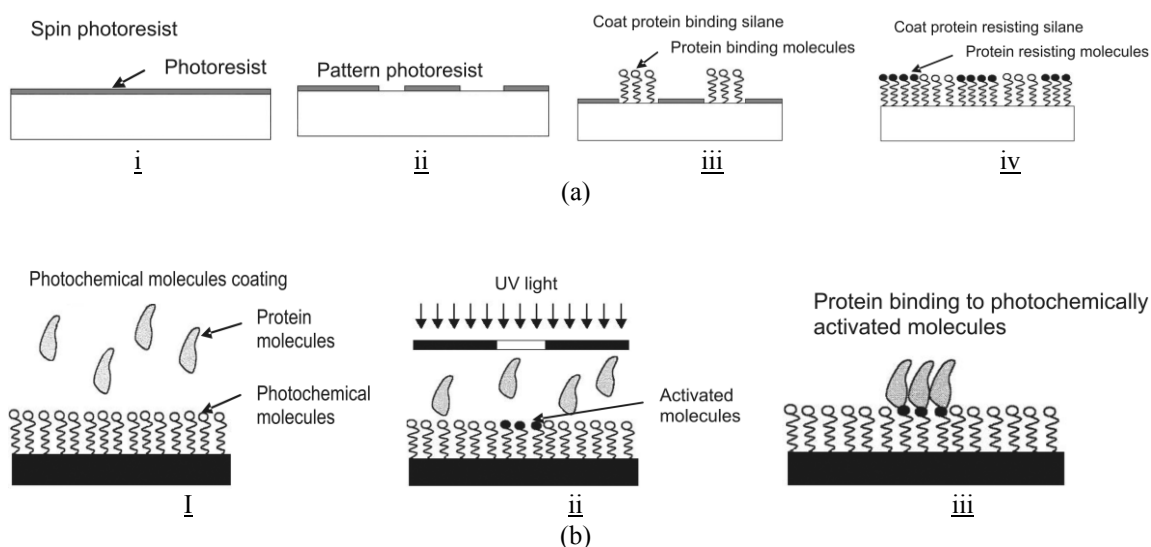


**Figure 10:** Schematic illustrations of photochemistry based manufacturing procedures <sup>1</sup>; (a) Photolithography applied to silane self-assembled monolayers (SAMs), (b) Direct photochemical protein patterning by activation of a photochemical coupling species.

#### 2.4.2.3. Electro-Printing:

The electro-printing technique is not widely used to fabricate biomolecule microarray. A few groups have been developing techniques that utilize electrochemistry and other on-chip electric field effects <sup>1</sup>. The NanoChip® (Nanogen, San Diego, CA) utilizes the negative charges of DNA and RNA molecules to immobilize them on a positively charged microelectrodes array <sup>96,97</sup>. Electrodes are coated with a streptavidin-agarose permeation layer and probes are biotinylated such that after the field is turned off, the probe molecules remain non-covalently bound to the surface. In addition, positive charge at individual test sites attracts target DNA molecules whose rapid concentration enables reduced hybridization times. The NanoChip® reported that the NanoChip® can have 25 to 10,000 test sites/electrodes, with dimensions of 80  $\mu\text{m}$  to 30  $\mu\text{m}$ , respectively <sup>1</sup>.

#### 2.4.2.4. Electro-spray Deposition (ESD):

Electro-spray deposition (ESD) is most commonly used to deposit thin films of polymers, semiconductive ceramics, and radioactive sources <sup>1,98</sup>. In ESD, numerous local deposits (dots, spots) can be produced under control of a local electrostatic field attracting charged ES products to specified substrate areas. One way to form such a field is to cover a conducting substrate with a dielectric mask containing an array of holes. Another way

to form a similar local electrostatic field is to locally increase conductivity of a photoconductive insulator layer (used as a substrate) by illuminating it through a photomask. This will result in deposition of the charged ES products into the illuminated areas. In addition to light, any other physical factor (temperature, radiation, injection of charges, etc.) capable of increasing a local electric conductivity of a dielectric film can be exploited<sup>98</sup>. ESD is a high efficiency technique and it also capable of producing very small spots<sup>1</sup>. To produce dots 2-6  $\mu\text{m}$  in diameter, mask openings need to be about 25  $\mu\text{m}$ <sup>98</sup>. The shortcoming of the ESD method is that the inter-spot distance (i.e., pitch) is inherently large because the mask holes are much larger than the spot sizes.

#### 2.4.2.5. Ink jet Printing:

In the recent years, ink jet printing technology has been investigated to print biomolecules on porous surface. In most cases, commercially available printers are modified to dispense a biomolecule solution instead of ink<sup>3, 4, 99</sup>. Xu et al. reported the successful conversion of HP550C bubble-jet printer and HP51626A ink cartridge to print Chinese Hamster Ovary (CHO) and embryonic motoneuron cells into pre-defined pattern<sup>3</sup>. Risio et al. printed Horseradish Peroxidase (HRP) using piezoelectric ink jet printer<sup>15</sup>. The computer-aided ink jet printing of viable mammalian cells holds potential for creating living tissue analogs, and may eventually lead to the construction of engineered human organs. Ink jet printing technology is advantageous due to its inexpensive operation and ability to deliver small droplets of reproducible volumes. These printers are often one or two orders of magnitude cheaper than robotic pin printing systems<sup>1</sup>.

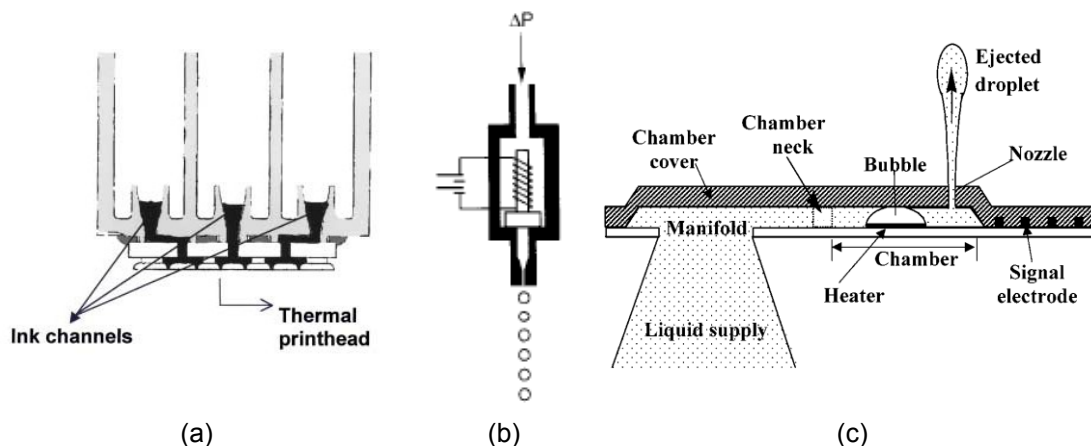


**Figure 11: Thermal ink-jet printing. (a) A cross-section view of a generic bubble-jet cartridge<sup>4</sup>, (b) droplet dispensing using solenoid ink jet technique<sup>100</sup>, (c) droplet ejection sequence in a thermal bubble-jet<sup>101</sup>.**

Ink jet printers used in biotechnology can be classified into three categories on basis of generating compressive force, which are thermal, solenoid and piezoelectric<sup>1, 100</sup>. In thermal ink jet printing, a heated plate (resistive heater) causes a vapour bubble to form and eject a droplet of ink through a nozzle. The current pulse lasts a few microseconds ( $\sim 10 \text{ ms}^{-1}$ ) and raises the plate temperature to about  $200\text{-}300^\circ\text{C}$ <sup>102</sup>. Solenoid ink jet technology uses gas or hydraulic pressure to compress the fluid against an ink jet valve<sup>100</sup>. In contrast, piezoelectric printing uses an array of piezoelectric plates, which drive the droplet in bend or push mode<sup>103, 104</sup>.

Different research groups reported that DNA can be spotted with ink jet printers and remain intact; however, proteins are more fragile and may be more sensitive to the extreme conditions of ink jet printing<sup>1, 4, 16</sup>. There are a few advantages of ink jet printing over the other printing techniques: it is a digital technique; it can reduce cross contamination; the printing results are highly reproducible and of high resolution; it can improve the through-put, etc. In spite of being very advantageous for biomolecular patterning, ink-jet printing has few significant drawbacks. Two phenomena are of concern to the engineer when an ink jet drop comes into contact with a surface. The first is the formation of satellite drops from the ink jet nozzle, which may form noncoalescent droplets (N-C-D) that roll from their target. The second is the wicking of the delivered droplet into the long surface grooves, fibres, or surface imperfections driven by capillary forces<sup>5</sup>. The dispensed droplets also experience high shear rates while passing through the nozzle and impacting the substrate surface<sup>1</sup>. Efforts have been made to analyze and overcome the drawbacks of ink jet printers to make them more suitable for microarray printing<sup>101, 105</sup>.

## **2.5. Liquid-Liquid interaction: Isothermal Non-Coalescence of Liquid Droplets at the Air-Liquid Interface**

The fluid mechanics of liquid drops impacting on liquid surfaces is of importance in a variety of applications, such as droplet combustions, separation of emulsion, pesticide delivery, fire fighting and ink-jet printing<sup>106-108</sup>.

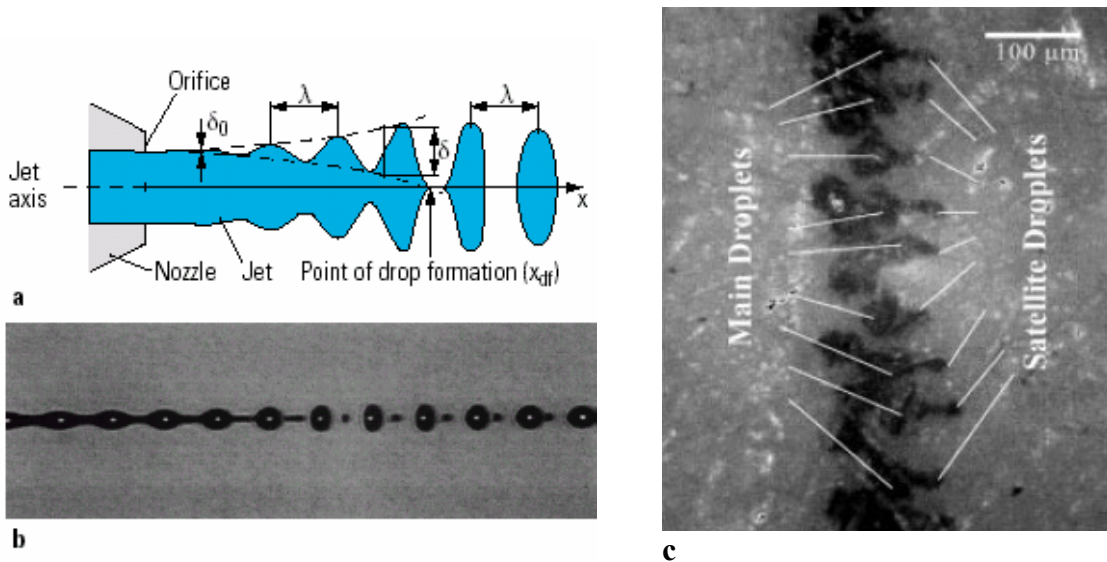


**Figure 12:** Drop formation with continuous ink jet and effect on printing: (a) Constriction of the ink jet to form a drop (Kipphan 2001), (b) A stream of drops with satellite drops combining with the subsequent main drop in flight, (c) A magnified image of printed vertical line<sup>101</sup>.

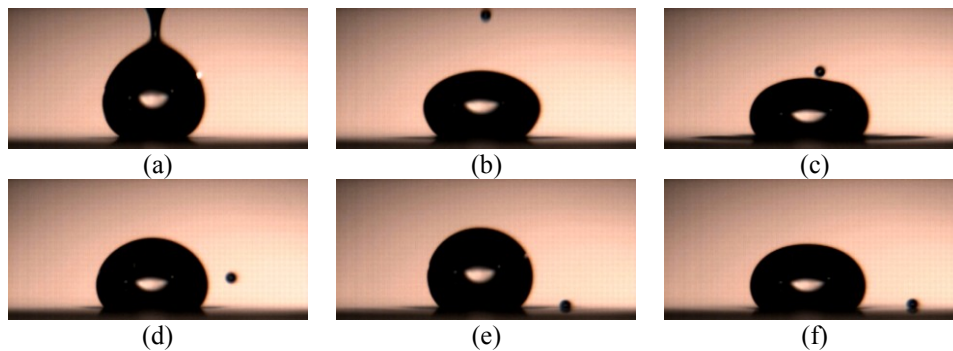


**Figure 13:** Non-coalescence behaviour of a satellite droplet<sup>109, 110</sup>.

Ink-jet printing offers potentials in bio-printing since it is a non-contact technique which can provide high printing resolution if the ink-substrate interaction can be understood and controlled. Satellite droplets formed from the ink-jet nozzle, which may form non-coalescent droplets (N-C-D) that rolls from their target and reduce the print definition (Figure 12, Figure 13).

A non-coalescent droplet is defined as a liquid droplet that retains its identity over a flat air-liquid interface<sup>111, 112</sup>. Droplet and flat liquid interface typically have the same bulk composition. We observe many manifestations of non-coalescent droplets in our daily life. An example is the rain splashing and rolling over a puddle before disappearing. There are three broad categories of non-coalescence mechanisms: (a) the Leidenfrost effect, (b) the thermo-capillary induction, and (c) the isothermal non-

coalescence<sup>113</sup>. In our daily life, we mostly observe the isothermal non-coalescence phenomena. Moreover, N-C-Ds can be primary or secondary<sup>114</sup>. Primary N-C-Ds form when the droplet is delivered from a height of one or two centimetres, whereas secondary N-C-Ds form when the droplets fall from a height sufficient to splash and send satellite droplets rolling in different directions.

The isothermal non-coalescence of droplets was first reported by Lord Rayleigh as early as 1879 and by Osborne Reynolds in 1881<sup>113, 115, 116</sup>. Despite the number of investigations recorded since the 19<sup>th</sup> century, scientists are yet to explain different facets of the isothermal non-coalescence phenomenon. It has been recognized that the droplet floats on a “cushion” of fluid (air in most cases) that must be drained to permit coalescence<sup>113</sup>; but there is still no direct evidence that supports the existence of the air cushion. There is a need to better understand the isothermal non-coalescence behaviour of liquids.

Non-coalescent droplets form when a liquid drop impinges on a planar air-liquid interface. The drop impingement can also result in the complete engulfment of the drop in the pool of liquid (splashing), or in bouncing off the free surface<sup>111, 112</sup>. The collision of a drop with a surface is governed by many parameters. An analysis using dimensionless numbers, such as the Bond number ( $Bo$ ), Capillary number ( $Ca$ ), and Weber number ( $We$ ), can shed light on the governing process<sup>108, 111-113, 117</sup>. The  $We$  is perhaps better suited to explain the non-coalescence behaviour of liquid droplets. The  $We$  links the fluid inertia to the fluid surface tension and is useful to analyse the formation of droplets and bubbles.

## **2.6. Solid-Liquid Interaction: Liquid Wicking Kinetics in Open Capillaries**

Understanding the kinetics of wetting and penetration of liquid on a rough and porous solid surface is critical in many industrial applications including printing technologies<sup>118, 119</sup>, textile and micro fluidic systems<sup>120, 121</sup>. The surface chemical composition and the topographical properties of the substrate, as well as the physical properties of the liquid, play different but equally important roles in controlling the wetting and penetration process.

Many liquid penetration systems involving porous solid media have been studied using the Washburn model <sup>122</sup>. This model predicts that the liquid penetration distance in a cylindrical capillary is linearly related to the square root of time. Many researchers, including Fisher and Lark, experimentally confirmed this relationship for cylindrical capillaries <sup>123</sup>.

A special case of liquid penetration in a porous medium is the liquid wicking in the open capillaries of a solid surface. Liquid wicking in open capillary channels is highly relevant to many applications including the management of spacecraft propellant under low-gravity conditions <sup>124</sup>, liquid penetration in biomedical chips <sup>125</sup>, wetting and penetration of water on human skin <sup>126</sup> and wicking and penetration of water-based ink on paper surface in printing applications <sup>119</sup>, to name just a few. However, Heimenz and Rajagopalan reported that liquid wicking in open capillaries cannot be explained by applying the Washburn model, which was derived and adapted for cylindrical pores <sup>127</sup>.

The development of ink jet printing technology has motivated further research on the wetting and penetration of water or water-based inks into paper <sup>128</sup>. Paper is a complex matrix of interconnected fibres. Roberts et al. showed that a wetting fluid on a paper surface has four potential flow paths <sup>128</sup>. These flow paths can be within the bulk pores, along the channels formed by inter fibre overlaps (or inter fibre gaps), along crevices formed by indentations and surface roughness of the intrafibre pores, and within intra fibre pores. It was observed that the capillary channels of inter fibre gaps in paper are the preferred flow path for liquids, since this flow path has fewer discontinuities that hinder the liquid flow.

The effect of paper surface chemical heterogeneity on paper and ink drop interaction was investigated by Kannangara et al. <sup>119</sup>. In this study, however, paper surface was taken to be a flat surface and no consideration was given to the capillary channels on its surface. Kannangara et al. showed that the liquid drop inertia significantly influences the ink drop spreading forced by the impact <sup>119</sup>. Asai et al. also reported the effect of ink jet ink drop inertia on ink drop impact on paper surface <sup>118</sup>.

Rye et al. proposed one of the first models for liquid wicking in V-groove capillary channels <sup>129</sup>. Their model was established on the principle of (interfacial) energy balance, and at the same time considered the balance of a capillary driving force and the Poiseuille type liquid flow resistance force in a V-groove channel. However, the Rye's model does not predict liquid wicking rate when liquid drop impacts on the V-groove with inertia. Model including inertia effect is critical for many industrial applications to model the liquid wicking kinetics in open capillary.

### 3. RESEARCH CHALLENGES

From the literature review the major scientific and engineering challenges to develop stable and functional bioactive papers or paper based fluidic devices for diagnostic and industrial applications are:

1. The biomolecular printing techniques currently available are limited by low resolution, low manufacturing speed and low ink volume. Contact printing technique presents high risk of cross contamination. Non-contact printing, such as ink jet, can be a better choice for fabrication. However, little understanding is available on the liquid-liquid and solid-liquid interaction once the droplets of biomolecules are delivered using ink jet technique.
2. The printed biomolecules must be able to sustain the heat and shear generated by ink jet printing.
3. For high printing resolution, the bio-ink needs to be compatible with the printing system. Understanding the effect of the fluid properties ( $\gamma$ ,  $\rho$ ,  $\mu$ ) on its ink jet printability is required. The ability to change the bio ink properties, without altering the biomolecule property is also needed.
4. Biomolecules physisorbed on paper typically demonstrates high desorption when used wet. Covalent immobilization can solve the problem but would drastically decrease the ink jet printing rate. Furthermore, the effect of biomolecule orientation on its activity is little known.
5. Polymers can be used as retention aid to improve the biomolecular adsorption on paper. However, there is little fundamental understanding available on the effect of polymer retention aids on the orientation of biomolecules during surface immobilization and their functionality.
6. There is limited understanding on:
  - a. The activity, selectivity and stability of biomolecules immobilized on paper;
  - b. The effect of paper structure and chemical composition on fluid transport or activity of bioactive papers;
  - c. The effect of paper morphology, wet strength and surface properties on activity of bioactive paper.
7. The scarcity of experimental methods to follow the kinetics of biomolecules on paper is a constraint to study the activity and stability of bioactive paper.

## 4. SCOPE OF THESIS

Understanding the fundamental and applied issues of bioactive paper and biomolecular deposition on paper are the aims of this research. From the literature review, the critical steps of this study have been identified and broadly classified as:

- 1) The delivery of biomolecules in a controlled pattern on paper using non-contact printing technique;
- 2) The fixation, retention and orientation of biomolecules on paper;
- 3) The reactivity, stability and selectivity of biomolecules on paper.

To address these issues, the objectives of this study are:

1. To quantify the reaction kinetics of enzymatic bioactive papers. An advanced analysis using a colorimetric technique and image analysis will be developed.
2. To develop a model to quantify the effect of time and temperature on the activity of enzymatic papers. This is to predict the half-life time and the ageing of bioactive papers. This knowledge is required to predict the shelf-life of bioactive papers.
3. To investigate water soluble polymers as retention aids to significantly improve the adsorption and retention of biomolecules on paper. To measure the effect of polymer on the activity and the stability of enzymatic papers.
4. To investigate the concept of specific antibody-antigen interaction to trigger coagulation and to quantify the transport of stable/unstable colloid suspensions on the wicking and the chromatographic separation on paper. Explore the concept for (ABO) blood typing paper test.
5. To deliver biomolecules on porous surfaces using an ink jet printing technique and to quantify the liquid-liquid interaction once the droplets of biomolecules are delivered.
6. To model the acceptance of biomolecules ink jet printed on paper and imperfect surfaces; this will address the solid-liquid interaction and quantify the wicking dynamics of a sessile droplet deposited or imprinted onto grooved surfaces.
7. To deposit precise and complex patterns of biomolecules on paper and porous surfaces by thermal ink jet.

The effect of paper morphology, wet strength and surface properties on bioactive paper performance are not addressed comprehensively in this study. An attempt was taken to quantify the effect on paper structure and chemical composition on the activity of enzymatic papers. Three different kinds of papers were used in that experimental study. The results are included in *Appendix B*.

The literature review suggests that the reactivity, stability and selectivity of biomolecules on paper are the least understood, followed by the fixation and retention of biomolecules on paper. Therefore, these phenomena are addressed in the first part of the thesis (Chapter 2 - 5). The critical issues of non-contact delivery and acceptance of biomolecules on paper are addressed in the second part of the thesis (Chapter 6 - 10).

The relationship between the objectives, the critical steps, the individual studies and the chapters of this thesis are illustrated in Figure 14.

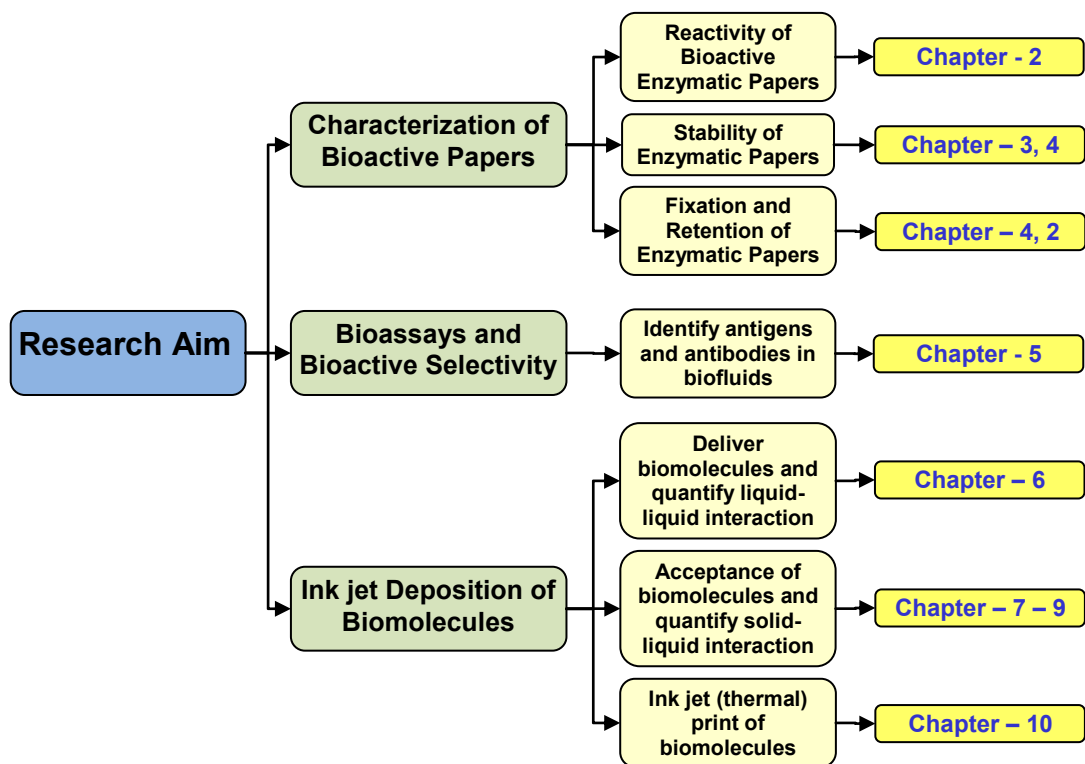


**Figure 14:** Thesis research components and chapter lists.

## 5. ORGANIZATION OF CHAPTERS

The thesis consists of three published, four submitted and two manuscripts in preparation. The objective and the contribution of each chapter are as followed:

- Chapter 2: Reaction Kinetics of Alkaline Phosphatase Immobilized on Paper.

*(Paper – 1, submitted to Langmuir)*

This chapter quantifies the reaction kinetics of a model enzyme, Alkaline Phosphatase (ALP), on paper using a colorimetric technique. The Effects of three different polymers: a cationic, an anionic and a neutral, on the reactivity of enzymatic papers are also quantified in this chapter. An advanced image analysis technique was developed to quantify the enzymatic activity on paper.

- Chapter 3: Thermal Stability of Bioactive Enzymatic Papers.

*(Paper – 2, published in Colloids and Surfaces B: Biointerfaces)*

This chapter quantifies the effect of temperature and aging on enzymatic bioactive papers using a colorimetric technique. Alkaline Phosphatase and Horseradish Peroxidase are used as model enzymes. The half-lives of the enzymatic papers are quantified from the deactivation kinetics.

- Chapter 4: Effect of Polymers on Retention and Aging of Enzymatic Bioactive Papers.

*(Paper – 3, published in Colloids and Surfaces B: Biointerfaces)*

The polymer effects on the fixation and the retention of biomolecules on paper is discussed in this chapter. Three different polymers: a cationic, an anionic and a neutral polymer, are used as model polymers. A deactivation model is developed to quantify the thermal stability and shelf life of enzymatic bioactive papers with and without polymers.

- Chapter 5: Paper Diagnostic for Instantaneous Blood Typing.

*(Manuscript – 1 submitted to Analytical Chemistry)*

This chapter investigates the critical issues to identify antigens and antibodies in a biofluid, such as blood, from the specific antibody-antigen interaction which triggers colloidal agglutination on paper. This agglutination

process enhances the chromatographic separation of the individual blood components, especially the red blood cell from the serum. This chapter explores the concept of paper based fluidic devices for ABO blood typing.

A provisional patent application resulted from the novel findings of this chapter, which is included in *Appendix B*.

- Chapter 6: Isothermal Non-Coalescence of Liquid Droplets at the Air-Liquid Interface.

*(Paper – 4, published in Langmuir)*

This chapter investigates the mechanism of generation and sustainability of non-coalescence droplets (N-C-D) on the liquid-air interface of the same liquids. The formation of N-C-D is likely to reduce the print quality, as the N-C-Ds can roll away from the print target. The Weber number ( $We$ ) of impinging liquid drops was used to correlate and to quantify the N-C-D generation. The  $We$  correlation suggest that any ink droplets larger than 4.0 pL can form N-C-Ds.

- Chapter 7: Wicking of a Liquid Droplet in a Surface Groove.

*(Paper – 5, submitted to Langmuir)*

This chapter addresses the liquid wicking dynamics of a sessile droplet during short contact time in V-shaped grooves (open capillaries). An experimental setup consisting of two cameras was established to measure liquid wicking in V-grooves. A kinetic model considering the driving force at the threshold region of the wicking front was developed to quantify liquid wicking along V-grooves at zero impact velocity. This understanding is important to design optimized uncoated papers for ink jet printing and to manufacture effective low-cost microfluidic devices by ink jet printing.

The complete calculation of the proposed kinetic model is included in *Appendix A*.

- Chapter 8: Effect of Impact Velocity on the Wicking of a Sessile Droplet on a V-Groove.

*(Manuscript – 2 in preparation, to be submitted to Chemical Engineering Science)*

The effect of droplet inertia on V-groove wicking flow is experimentally investigated in this chapter. The results show an increasing rate of wicking for droplet impacting a V-groove with. However, the inertia effect gradually decreases as the wicking front moves away from the point of impact. The V-groove wicking affects the ink wicking on the surface of uncoated paper as the size and the shape of the inter fibre gap can strongly influence the ink wicking. Understanding the liquid wicking kinetic in a V-groove geometry is required to control the liquid wicking rate for optimized ink jet printing.

- Chapter 9: Wetting and Wicking Kinetics of a Sessile Droplet Impinging a Narrow Groove at Low Impact Velocity.

*(Paper – 6, submitted to Colloids and Surfaces A: Physicochemical and Engineering Aspects)*

In this chapter, the dynamics of wicking and wetting of sessile droplets impinging a narrow groove of wide angle ( $120^\circ$ ) was investigated experimentally. Wicking and wetting velocities were measured by high speed image analysis. Wetting and wicking kinetics both increase with the initial droplet impact velocity. Wicking velocity decreases at a much slower rate than wetting and proceeds as long as there is a liquid reservoir. This explains the effect of surface grooves on ink jet printing resolution causing feathering defect.

- Chapter 10: Biosurface Engineering through Ink Jet Printing.

*(Paper – 7, published in Colloids and Surfaces B: Biointerfaces)*

This paper demonstrates the feasibility of thermal ink jet printing as a convenient and up-scalable process for biosurface engineering. High printing resolution was achieved by formulating bio-inks. Complex biomolecular patterns and microfluidic channels were printed on paper to demonstrate the concept of paper based bioassays and diagnostic devices. A novel strategy was developed to engineer smooth, continuous concentration gradient of biomolecules by ink jet printing.

A Patent Cooperation Treaty (PCT) patent application is resulted from the findings of this chapter (*Appendix C*).

A preliminary study investigated the effect of paper structure and chemical composition on the activity of enzymatic papers. Three different types of papers: newsprint paper, copy paper and filter paper, are investigated as substrate for enzyme deposition. A manuscript (Manuscript – 2) is in preparation for APPITA journal (*Appendix E*).

## 6. REFERENCES

1. Barbulovic-Nad, I.; Lucente, M.; Sun, Y.; Zhang, M.; Wheeler, A. R.; Bussmann, M., Bio-Microarray Fabrication Techniques - A Review. *Critical Reviews in Biotechnology* **2006**, 26, 237-259.
2. Bernard, A.; Renault, J. P.; Michel, B.; Bosshard, H. R.; Delamarche, E., Microcontact Printing of Proteins. *Advanced Materials* **2000**, 12, (14), 1067-1070.
3. Xu, T.; Jin, J.; Gregory, C.; Hickman, J. J.; Boland, T., Inkjet Printing of Viable Mammalian Cells. *Biomaterials* **2005**, 26, (1), 93-99.
4. Allain, L. R.; Askari, M.; Stokes, D. L.; Vo-Dinh, T., Microarray Sampling-Platform Fabrication Using Bubble-Jet Technology for a Biochip System. *Fresenius Journal of Analytical Chemistry* **2001**, 371, (2), 146-150.
5. Khan, M. S.; Kannangara, D.; Shen, W.; Garnier, G., Isothermal Noncoalescence of Liquid Droplets at the Air-Liquid Interface. *Langmuir* **2008**, 24, (7), 3199-3204.
6. Khan, M. S.; Kannangara, D.; Shen, W.; Garnier, G. In *Mechanism of Non-Coalescence for Liquid Droplets at the Air-Liquid Interface*, Chemeca 2007, Melbourne, 2007; Rhodes, M., Ed. Engineers Australia: Melbourne, 2007; pp 101-109.
7. Tseng, F.-G.; Kim, C.-J.; Ho, C.-M., A high-resolution high-frequency monolithic top-shooting microinjector free of satellite drops - Part II\_Concept, Design, and Model. *Journal of Microelectromechanical Systems* **2002**, 11, (5), 437-447.
8. Tseng, F.-G.; Kim, C.-J.; Ho, C.-M., A high-resolution high-frequency monolithic top-shooting microinjector free of satellite drops - Part I\_Concept, Design, and Model. *Journal of Microelectromechanical Systems* **2002**, 11, (5), 427-436.
9. Lepri, L.; Cincinelli, A., TLC Sorbents. In *Encyclopedia of Chromatography*, 2 ed.; Cazes, J., Ed. CRC Press: 2004; pp 1-5.
10. Macek, K., *Pharmaceutical Application of Thin-Layer and Paper Chromatography*. Elsevier: 1972; p 275-348.
11. Martinez, A. W.; Phillips, S. T.; Carrithe, E.; Thomas III, S. W.; Sindi, H.; Whitesides, G. M., Simple Telemedicine for Developing Regions: Camera Phones and Paper-Based Microfluidic Devices for Real-Time, Off-Site Diagnosis. *Analytical Chemistry* **2008**, 80, (10), 3699-3707.
12. Martinez, A. W.; Phillips, S. T.; Butte, M. J.; Whitesides, G. M., Patterned paper as a platform for inexpensive, low-volume, portable bioassays. *Angewandte Chemie International Edition* **2007**, 46, (8), 1318-1320.
13. Bruzewicz, D. A.; Reches, M.; Whitesides, G. M., Low-Cost Printing of Poly(dimethylsiloxane) Barriers To Define Microchannels in Paper. *Analytical Chemistry* **2008**, 80, (9), 3387-3392.
14. Keenan, T. M.; Folch, A., Biomolecular Gradients in Cell Culture Systems. *Lab on a Chip* **2008**, 8, 34-57.
15. Risio, S. D.; Yan, N., Piezoelectric Ink-Jet Printing of Horseradish Peroxidase: Effect of Ink Viscosity Modifiers on Activity. *Molecular Rapid Communications* **2007**, 28, (18-19), 1934-1940.

16. Ilkhanizadeh, S.; Teixeira, A. I.; Hermanson, O., Inkjet Printing of Macromolecules on Hydrogels to Steer Neural Stem Cell Differentiation. *Biomaterials* **2007**, *28*, (27), 3936-43.
17. Xu, T.; Gregory, C. A.; Molnar, P.; Cui, X.; Jalota, S.; Bhaduri, S. B.; Boland, T., Viability and Electrophysiology of Neural Cell Structures Generated by the Inkjet Printing Method. *Biomaterials* **2006**, *27*, (19), 3580-3588.
18. Ringeisen, B. R.; Othon, C. M.; Barron, J. A.; Young, D.; Spargo, B. J., Jet-based Methods to Print Living Cells. *Biotechnology Journal* **2006**, *1*, (9), 930-948.
19. Miller, E. D.; Fisher, G. W.; Weiss, L. E.; Walker, L. M.; Campbell, P. G., Dose-Dependent Cell Growth in Response to Concentration Modulated Patterns of FGF-2 Printed on Fibrin. *Biomaterials* **2006**, *27*, (10), 2213-2221.
20. Newman, J. D.; Turner, A. P. F., Ink-jet Printing For The Fabrication of Amperometric Glucose Biosensors. *Biosensors and Bioelectronics* **2005**, *20*, (10), 2019-2026.
21. Nakamura, M.; Kobayashi, A.; Takagi, F.; Watanabe, A.; Hiruma, Y.; Ohuchi, K.; Iwasaki, Y.; Horie, M.; Morita, I.; Takatani, S., Biocompatible Inkjet Printing Technique for Designed Seeding of Individual Living Cells. *Tissue Engineering* **2005**, *11*, (11-12), 1658-1666.
22. Roth, E. A.; Xu, T.; Das, M.; Gregory, C.; Hickman, J. J.; Boland, T., Inkjet Printing for High-Throughput Cell Patterning. *Biomaterials* **2004**, *25*, (17), 3707-3715.
23. Masao, G. Preparation of Enzyme-Immobilized Filter Paper for Determination of Freshness of Fish Meat. JP 87-157619, 1989.
24. Akahori, Y.; Yamazaki, H.; Nishio, G.; Matsunaga, H.; Mitsubayashi, K., An alcohol gas - sensor using an enzyme immobilized paper. *Chemical Sensors* **2004**, *20*, (Suppl. B), 468-469.
25. Brena, B. M.; Batista-Viera, F., Immobilization of Enzymes. In *Methods in Biotechnology: Immobilization of Enzymes and Cells*, 2nd ed.; Guisan, J. M., Ed. Human Press: Totowa, New Jersey, 2006; pp 15-30.
26. Voss, R.; Brook, M. A.; Thompson, J.; Chen, Y.; Pelton, R. H.; Brennan, J. D., Non-destructive Horseradish Peroxidase Immobilization in Porous Silica Nanoparticles. *Journal of Materials Chemistry* **2007**, *17*, 4854-4863.
27. Hiemenz, P. C.; Rajagopalan, R., *Principles of Colloid and Surface Chemistry, Third Edition, Revised and Expanded*. Marcel Dekker: New York, 1997; p 688.
28. Aikio, S.; Grönqvist, S.; Hakola, L.; Hurme, E.; Jussila, S.; Kaukonen, O.-V.; Kopola, H.; Käsäkoski, M.; Leinonen, M.; Lippo, S.; Mahlberg, R.; Peltonen, S.; Qvintus-Leino, P.; Rajamäki, T.; Ritschkoff, A.-C.; Smolander, M.; Vartiainen, J.; Viikari, L.; Vilkmann, M., Bioactive Paper and Fibre Products: Patent and Literature Survey. In 2006; pp 1-84.
29. Pelton, R., Bioactive Paper Provides a Low-Cost Platform for Diagnostics. *Trends in Analytical Chemistry* **2009**, *28*, (8), 925-942.
30. Flaim, C. J.; Chien, S.; Bhatia, S. N., An Extracellular Matrix Microarray for Probing Cellular Differentiation. *Nature Methods* **2005**, *2*, (2), 119-125.
31. Lauer, L.; Ingebrandt, S.; Scholl, M.; Offenhausser, A., Aligned Microcontact Printing of Biomolecules on Microelectronic Device Surfaces. *IEEE TRANSACTIONS ON BIOMEDICAL ENGINEERING* **2001**, *48*, (7), 838-842.
32. Khan, M. S.; Shen, W.; Garnier, G. In *Stability and Reactivity of Enzymatic Papers*, 2009 AIChE Annual Meeting, Nashville, TN, In Press; Nashville, TN, In Press.

33. Khan, M. S.; Tian, J.; Xu, L.; Shen, W.; Garnier, G., Bioactive Enzymatic Papers. In *Advances in Pulp and Paper Research, Oxford 2009*, I'Anson, S. J., Ed. The Pulp & Paper Fundamental Research Society: 2009; Vol. 2, pp 1149-1166.
34. Coleman, J. E., Structure and Mechanism of Alkaline Phosphatase. *Annual Review of Biophysics and Biomolecular Structure* **1992**, 21, 441-483.
35. Veitch, N. C., Horseradish Peroxidase: A Modern View Of A Classic Enzyme. *Phytochemistry* **2004**, 65, (3), 249-259.
36. Haifeng, L.; Yuwen, L.; Xiaomin, C.; Zhiyong, W.; Cunxin, W., Effect of Sodium Phosphate Buffer on Horseradish Peroxidase Thermal Stability. *Journal of Thermal Analysis and Calorimetry* **2008**, 93, (2), 569-574.
37. Fadiloglu, S.; Erkmen, O.; Sekeroglu, G., Thermal Inactivation Kinetics of Alkaline Phosphatase in Buffer and Milk. *Journal of Food Processing and Preservation* **2006**, 30, (3), 258-268.
38. Whitmore, D. H.; Goldberg, E., Trout Intestinal Alkaline Phosphatases. II. The Effect of Temperature upon Enzymatic Activity in vitro and in vivo. *Journal of Experimental Zoology* **2005**, 182, (1), 59-68.
39. Machado, M. F.; Saraiva, J. M., Thermal Stability and Activity Regain of Horseradish Peroxidase in Aqueous Mixtures of Imidazolium-Based Ionic Liquids *Biotechnology Letters* **2005**, 27, (16), 1233-1239.
40. Ingledew, W. J.; Rich, P. R., A Study of the Horseradish Peroxidase Catalytic Site by FTIR Spectroscopy. *Biochemical Society Transactions* **2005**, 33, (4), 886-889.
41. Smeller, L.; Fidy, J., The Enzyme Horseradish Peroxidase Is Less Compressible at Higher Pressures. *Biophysical Journal* **2002**, 82, (1), 426-436.
42. Kaposi, A. D.; Fidy, J.; Manas, E. S.; Vanderkooi, J. M.; Wright, W. W., Horseradish Peroxidase Monitored by Infrared Spectroscopy: Effect of Temperature, Substrate and Calcium. *Biochimica et Biophysica Acta* **1999**, 1435, (1), 41-50.
43. Gajhede, M.; Schuller, D. J.; Henriksen, A.; Smith, A. T.; Poulos, T. L., Crystal Structure of Horseradish Peroxidase C at 2.15 Å Resolution. *Nature Structural Biology* **1997**, 4, (12), 1032-1038.
44. Chang, B. S.; Park, K. H.; Lund, D. B., Thermal Inactivation Kinetics of Horseradish Peroxidase. *Journal of Food Science* **1988**, 53, (3), 920-923.
45. Besman, M.; Coleman, J. E., Isozymes of Bovine Intestinal Alkaline Phosphatase. *The Journal of Biological Chemistry* **1985**, 260, (20), 11190-11193.
46. Pittner, F., Temperature-Dependent Behavior of Immobilized Alkaline Phosphatase. I. Role of Working Conditions and pH During Coupling *Applied Biochemistry and Biotechnology* **1982**, 7, (3), 1599-0291.
47. Rej, R.; Bretauiere, J.-P., Effects of Metal Ions on the Measurement of Alkaline Phosphatase Activity. *Clinical Chemistry* **1980**, 26, (3), 423-428.
48. Fosset, M.; Chapelet-Tordo, D.; Lazdunski, M., Intestinal Alkaline Phosphatase. Physical Properties and Quaternary Structure. *Biochemistry* **1974**, 13, (9), 1783-1788.
49. Shannon, L. M.; Kay, E.; Lew, J. Y., Peroxidase Isozymes from Horseradish Roots I. Isolation and Physical Properties. *The Journal of Biological Chemistry* **1966**, 241, (9), 2166-2172.
50. Enzymatic Assay of Phosphatase, Alkaline. In *Product Information*, Sigma Aldrich (web: [www.sigmaaldrich.com](http://www.sigmaaldrich.com)).

51. Anderson, R. A.; Vallee, B. L., Cobal (III), a Probe of Metal Binding Sites of *Escherichia Coli* Alkaline Phosphatase. *Proceedings of the National Academy of Sciences of the United States of America* **1975**, 72, (1), 394-397.
52. Peroxidase from Horseradish (HRP). In *Product Information*, Sigma Aldrich (web: www.sigmaaldrich.com).
53. Mikkelsen, S. R.; Corton, E., *Bioanalytical Chemistry*. John Wiley & Sons, Inc., Publication: New Jersey, 2004; p 361.
54. Young, C. R., Structural Requirements for Immunogenicity and Antigenicity. In *Molecular Immunology*, Atassi, M. Z.; Oss, C. J. V.; Absolom, D. R., Eds. Marcel Dekker, Inc.: New York, 1984; pp 1-14.
55. Litman, G. W.; Rast, J. P.; Shamblott, M. J.; Haire, R. N.; Hulst, M.; Roess, W.; Litman, R. T.; Hinds-Frey, K. R.; Zilch, A.; Amemiya, C. T., Phylogenetic Diversification of Immunoglobulin Genes and the Antibody Repertoire. *molecular Biology and Evolution* **1993**, 10, (1), 60-72.
56. Benjamini, E.; Coico, R.; Sunshine, G., *Immunology: A Short Course*. 5th ed.; John Wiley & Sons, Inc.: New Jersey, 1996; p 361.
57. Market, E.; Papavasiliou, F. N., V(D)J Recombination and the Evolution of the Adaptive Immune System. *PLoS Biology* **2003**, 1, (1), 24-27.
58. Janeway, C. A.; Travers, P.; Walport, M.; Shlomchik, M., *Immunobiology*. Garland Science: New York and London, 2001.
59. Davies, D. R.; Metzger, H., Structural Basis of Antibody Function. *Annual Review of Immunology* **1983**, 1, 84-117.
60. Offenhausser, A.; Bocker-Meffert, S.; Decker, T.; Helpenstein, R.; Gasteier, P.; Groll, J.; Moller, M.; Reska, A.; Schafer, S.; Schultea, P.; Vogt-Eisele, A., Microcontact Printing of Proteins for Neuronal Cell Guidance. *Soft Matter* **2007**, 3, 290-298.
61. Schmalenberg, K. E.; Buettner, H. M.; Uhricha, K. E., Microcontact Printing of Proteins on Oxygen Plasma-Activated Poly(Methyl Methacrylate). *Biomaterials* **2004**, 25, (10), 1851-1857.
62. Hossain, S. M. Z.; Luckham, R. E.; Smith, A. M.; Lebert, J. M.; Davies, L. M.; Pelton, R. H.; Filipe, C. D. M.; Brennan, J. D., Development of a Bioactive Paper Sensor for Detection of Neurotoxins Using Piezoelectric Inkjet Printing of Sol-Gel-Derived Bioinks. *Analytical Chemistry* **2009**, 81, (13), 5474-5483.
63. Zhao, W.; Berg, A. v. d., Lab on Paper. *Lab on a Chip* **2008**, 8, (12), 1988-1991.
64. Shen, W.; Junfei, T.; Li, X.; Nguyen, T.; Garnier, G. Switches for Micro-Fluidic Systems. Australian Provisional Patent, 2008904179, August 14, 2008.
65. Pelton, R.; Geng, X.; Brook, M., Photocatalytic Paper from Colloidal TiO<sub>2</sub>-Fact or Fantasy. *Advances in Colloid and Interfaces Science* **2006**, 127, (1), 43-53.
66. Khan, M. S.; Xu, L.; Shen, W.; Garnier, G., Thermal Stability of Bioactive Enzymatic Papers. *Colloids and Surfaces B: Biointerfaces* **In Press**.
67. Khan, M. S.; Fon, D.; Li, X.; Tian, J.; Forsythe, J.; Garnier, G.; Shen, W., Biosurface Engineering Through Ink Jet Printing. *Colloids and Surfaces B: Biointerfaces* **In Press**.
68. Trevan, M. D., *Techniques of Immobilization*. Chichester : Wiley: New York, 1980; p 1-9.
69. Buchholz, K.; Klein, J., Characterization of Immobilized Biocatalysts. In *Methods in Enzymology*, Moshback, K., Ed. Academic Press: London, 1987; Vol. 135, pp 3-30.

70. Pelton, R., Bioactive Paper - A Paper Science Perspective. In *Advances in Pulp and Paper Research, Oxford 2009*, I'Anson, S. J., Ed. The Pulp & Paper Fundamental Research Society: 2009; Vol. 2, pp 1096-1145.
71. Pelton, R., A Model of the External Surface of Wood Pulp Fibers. *Nordic Pulp & Paper Research Journal* **1993**, 08, (1), 113-119.
72. Bristow, J. A.; Kolset, P., *Paper Structure and Properties*. Marcel Dekker, Inc.: New York, 1986; p 390.
73. Eklund, D.; Lindstrom, T., *Paper Chemistry An Introduction*. DT Paper Science Publication: Grankulla, Finland, 1991; p 305.
74. Roberts, J. C., *Paper Chemistry*. Blackie A & P, an imprint of Chapman & Hall: London, 1996; p 267.
75. McArthur, S. L.; Shard, A. G., Surface Properties of Biomaterials. In *Encyclopedia of Medical Devices and Instrumentation*, 2nd ed.; Webster, J. G., Ed. John Wiley & Sons, Inc.: New York, 2006; pp 342-354.
76. Gupta, M. N.; Mattiasson, B., *Unique Applications of Immobilized Proteins in Bioanalytical Systems*. John Wiley & Sons, Inc.: 1992; Vol. 36.
77. Craig, S. J.; Shu, A.; Xu, Y.; Foong, F. C.; Nordon, R., Chimeric Protein for Selective Cell Attachment onto Cellulosic Substrates *Protein Engineering, Design and Selection* **2007**, 20, (5), 235-241.
78. Cao, Y.; Zhang, Q.; Wang, C.; Zhu, Y.; Bai, G., Preparation of Novel Immunomagnetic Cellulose Microspheres via Cellulose Binding Domain-Protein a Linkage And its Use for the Isolation of Interferon a-2b. *Journal of Chromatography A* **2007**, 1149, (2), 228-235.
79. Ye, L.; Filipe, C. D. M.; Kavooosi, M.; Haynes, C. A.; Pelton, R.; Brook, M. A., Immobilization of TiO<sub>2</sub> Nanoparticles onto Paper Modification Through Bioconjugation. *Journal of Materials Chemistry* **2009**, 19, (5), 2189-2198.
80. Su, S.; Ali, M. M.; Filipe, C. D. M.; Li, Y.; Pelton, R., Microgel-Based Inks for Paper-Supported Biosensing Applications. *Biomacromolecules* **2008**, 9.
81. Ouali, L.; Stoil, S.; Pefferkorn, E.; Elaissari, A.; Lanet, V.; Pichot, C.; Mandrand, B., Coagulation of Antibody-sensitized Latexes in the Presence of Antigen. *Polymers for Advanced Technologies* **1995**, 6, (7), 541-546.
82. Morozov, V. N., Protein Microarrays: Principles and Limitations. In *Protein Microarrays*, Schena, M., Ed. Jones and Bartlett Publishers, Inc.: Sudbury, MA., 2005; pp 71-106.
83. Wang, X. H.; Istepanian, R. S. H.; Song, Y. H., Microarray Image Enhancement by Denoising Using Stationary Wavelet Transform. *IEE Transactions on Nanobioscience* **2003**, 2, 184-189.
84. Lee, K. B.; Park, S. J.; Mirkin, C. A.; Smith, J. C.; Mrksich, M., Protein Nanoarrays Generated by Dip-Pen Nanolithography. *Science* **2002**, 295, (5560), 1702-1705.
85. Piner, R. D.; Zhu, J.; Xu, F.; Hong, S. H.; Mirkin, C. A., "Dip-pen" Nanolithography. *Science* **1999**, 283, (5402), 661-663.
86. Wadu-Mesthrige, K.; Xu, S.; Amro, N. A.; Liu, G. Y., Fabrication and Imaging of Nanometer-Sized Protein Patterns. *Langmuir* **1999**, 15, (25), 8580-8583.
87. Xu, S.; Liu, G. Y., Nanometer-scale Fabrication by Simultaneous Nanoshaving and Molecular Self-Assembly. *Langmuir* **1997**, 13, (2), 127-129.
88. Tseng, F.-G.; Lin, S.-C.; Yao, D.-J.; Huang, H.; Chieng, C.-C., Technological Aspects of Protein Microarrays and Nanoarrays. In *Protein Microarrays*, Schena, M., Ed. Jones and Barlett Publishers, Inc.: Sudbury, MA, 2005; pp 305-338.

89. Xia, Y.; Whitesides, G. M., Soft Lithography. *Angewandte Chemie - International Edition* **1998**, 37, (5), 551-575.
90. Zhao, X.-M.; Xia, Y.; Whitesides, G. M., Soft Lithographic Methods for Nano-Fabrication. *Journal of Materials Chemistry* **1997**, 7, 1069-1074.
91. Ringeisen, B. R.; Wu, P. K.; Kim, H.; Pique', A.; Auyeung, R. Y. C.; Young, H. D.; Chrisey, D. B.; Krizman, D. B., Picoliter-Scale Protein Microarrays by Laser Direct Write. *Biotechnology Progress* **2002**, 18, (5), 1126-1129.
92. Schwarz, A.; Rossier, J. S.; Roulet, E.; Mermod, N.; Roberts, M. A.; Girault, H. H., Micropatterning of Biomolecules on Polymer Substrates. *Langmuir* **1998**, 14, 5526-5531.
93. Blawas, A. S.; Reichert, W. M., Protein Patterning. *Biomaterials* **1997**, 19, (7-9), 595-609.
94. Moore, S. K., Making Chips to Probe Genes. *IEEE Spectrum* **2001**, 38, (3), 54-60.
95. Lom, B.; Healy, K. E.; Hockberger, P. E., A Versatile Technique for Patterning Biomolecules onto Glass Coverslips. *Journal of Neuroscience Methods* **1993**, 50, 385-397.
96. Gilles, P. N.; Wu, D. J.; Foster, C. B.; Dillon, P. J.; Chanock, S. J., Single Nucleotide Polymorphic Discrimination by an Electronic Dot Blot Assay on Semiconductor microchips. *Nature Biotechnology* **1999**, 17, (4), 365-370.
97. Heller, M. J.; Forster, A. H.; Tu, E., Active Microelectronic Chip Devices which Utilize Controlled Electrophoretic Fields for Multiplex DNA Hybridization and Other Genomic Applications. *Electrophoresis* **2000**, 21, (1), 157-164.
98. Morozov, V. N.; Morozova, T. Y., Electrospray Deposition as a Method for Mass Fabrication of Mono- and Multicomponent Microarrays of Biological and Biologically Active Substances. *Analytical Chemistry* **1999**, 71, (15), 3110-3117.
99. Xu, T.; Jin, J.; Gregory, C.; Hickman, J. J.; Boland, T., Inkjet Printing of Viable Mammalian Cell. *Biomaterials* **2005**, 26, 93-99.
100. Lemmo, A. V.; Rose, D. J.; Tisone, T. C., Inkjet Dispensing Technology: Applications in Drug Discovery. *Current Opinion in Biotechnology* **1998**, 9, (6), 615-617.
101. Tseng, F.-G.; Kim, C.-J.; Ho, C.-M., A high-resolution high-frequency monolithic top-shooting microinjector free of satellite drops - Part I\_ Concept, Design, and Model. *Journal of Microelectromechanical Systems* **2002**, 11, (5).
102. Le, H. P., Progress and trends in ink-jet printing technology. *The Journal of imaging science and technology* **1998**, 42, (1), 49-62.
103. Calvert, P., Inkjet Printing for Materials and Devices. *Chemistry of Materials* **2001**, 13, 3299-3305.
104. Setti, L.; Piana, C.; Bonazzi, S.; Ballarin, B.; Frascaro, D.; Fraleoni-Morgera, A.; Giuliani, S., Thermal Inkjet Technology for the Microdeposition of Biological Molecules as a Viable Route for the Realization of Biosensors. *Analytical Letters* **2004**, 37, (8), 1559-1570.
105. Khan, M. S.; Kannangara, D.; Shen, W.; Garnier, G. In *Mechanism of non-coalescence for liquid droplets at the air-liquid interface*, Chemica Conference, Melbourne, Australia, 23-26, September, 2007; Rhodes, M., Ed. Melbourne, Australia, 2007; pp 101-109.
106. Rein, M., Phenomena of Liquid Drop Impact on Solid and Liquid Surfaces. *Fluid Dynamic Research* **1993**, 12, (1993), 61-93.

107. Savino, R.; Monti, R.; Nota, F.; Fortezza, R.; Carotenuto, L.; Piccolo, C., Preliminary Results of the Sounding Rocket Experiment on Wetting and Coalescence Prevention by Marangoin Effect. *Acta Astronautica* **2004**, *55*, 169-179.
108. Sikalo, S.; Ganic, E. N., Phenomena of Droplet-Surface Interactions. *Experimental Thermal and Fluid Science* **2006**, *31*, 97-110.
109. Khan, M. S.; Kannangara, D.; Shen, W.; Garnier, G., Isothermal non-coalescence of liquid droplets at the air-liquid interface. *Submitted to Langmuir* **2007**.
110. Khan, M. S.; Kannangara, D.; Shen, w.; Garnier, G. In *Mechanism of non-coalescence for liquid droplets at the air-liquid interface*, Chemica Conference 2007, Melbourne, Australia, 23-26, September, 2007; Rhodes, M., Ed. Melbourne, Australia, 2007; pp 101-109.
111. Fedorchenko, A. I.; Wang, A.-B., On some common features of drop impact on liquid surfaces. *PHYSICS OF FLUIDS* **2004**, *16*, (5), 1349-1365.
112. Honey, E. M.; Kavehpour, H. P., Astonishing life of a coalescing drop on a free surface. *Physical Review E* **2006**, *73*, (027301), 027301-1 - 027301-3.
113. Neitzel, G. P.; Dell'Aversana, P., Noncoalescence and Nonwetting Behavior of Liquids. *ProQuest Science Journals* **2002**, *34*, ProQuest Science Journals, 267-289.
114. Seth, J. B.; Anand, C.; Mahajan, L. D., Liquid Drops on the Same Liquid Surface. *Philosophical Magazine (1798-1977)* **1929**, *7*, 247-53.
115. Dell'Aversana, P.; Neitzel, G. P., When Liquids Stay Dry. *Physics Today* **1998**, *51*, (1), 38-41.
116. Sreenivas, K. R.; De, P. K.; Arakeri, J. H., Levitation of a Drop over a Film Flow. *Journal of Fluid Mech.* **1999**, *380*, 297-307.
117. Miura, K.; Miura, t.; Ohtani, S., Heat and Mass Transfer to and from Droplets. *AIChE Symposium Series* **1977**, *73*, (163), 95-102.
118. Asai, A.; Shioya, M.; Hirasawa, S.; Okazaki, T., Impact of an Ink Drop on Paper. *J. Imaging Sci. Technol.* **1993**, *37*, (2), 205-207.
119. Kannangara, D.; Zhang, H.; Shen, W., Liquid-paper interactions during liquid drop impact and recoil on paper surfaces. *Colloids and Surfaces, A: Physicochemical and Engineering Aspects* **2006**, *280*, (1-3), 203-215.
120. Baret, J. C.; Decre, M. M. J.; Herminghaus, S.; Seemann, R., Transport Dynamics in Open Microfluidic Grooves. *Langmuir* **2007**.
121. Seemann, R.; Brinkmann, M.; Kramer, E. J.; Lange, F. F.; Lipowsky, R., Wetting morphologies at microstructured surfaces. *Proceedings of the National Academy of Sciences of the United States of America* **2005**, *102*, (6), 1848-1852.
122. Washburn, E. W., Dynamics of capillary flow. *Phys. Rev.* **1921**, *17*, (3), 374-5.
123. Fisher, L. R.; Lark, P. D., Experimental-Study of the Washburn Equation for Liquid Flow in Very Fine Capillaries. *J. Colloid Interface Sci.* **1979**, *69*, (3), 486-492.
124. Rosendahl, U.; Ohlhoff, A.; Dreyer, M. E.; Rath, H. J., Investigation of forced liquid flows in open capillary channels. *Microgravity Sci. Technol.* **2002**, *13*, (4), 53-59.
125. Kim, W. S.; Kim, M. G.; Ahn, J. H.; Bae, B. S.; Park, C. B., Protein Micropatterning on Bifunctional Organic-Inorganic Sol-Gel Hybrid Materials. *Langmuir* **2007**.
126. Dussaud, A. D.; Adler, P. M.; Lips, A., Liquid transport in the networked microchannels of the skin surface. *Langmuir* **2003**, *19*, (18), 7341-7345.

127. Hiemenz, P. C.; Rajagopalan, R., *Principles of Colloid and Surface Chemistry, Third Edition, Revised and Expanded*. Marcel Dekker: New York, 1997; p 688 pp.
128. Roberts, R. J.; Senden, T. J.; Knackstedt, M. A. In *3D imaging of the spreading and penetration of aqueous liquids into unsized and sized papers*, 5th International Paper and Coating Chemistry Symposium, Montreal, June 16-19, 2003; Montreal, 2003; pp 303-311.
129. Rye, R. R.; Mann, J. A.; Yost, F. G., The flow of liquids in surface grooves. *Langmuir* **1996**, 12, (2), 555-565.

This page is intentionally blank

---

# Chapter 2

---

Reaction Kinetics of  
Alkaline Phosphatase  
Immobilized on Paper

---

This page is intentionally blank

# Monash University

## Declaration for Thesis Chapter 2

### Declaration by candidate

In the case of Chapter 2, the nature and extent of my contribution to the work was the following:

Nature of contribution	Extent of contribution (%)
Initiation, key ideas, experimental and analysis works, development and writing up of the paper	80

The following co-authors contributed to the work. Co-authors who are students at Monash University must also indicate the extent of their contribution in percentage terms:

Name	Nature of contribution	Extent of contribution (%) for student co-authors only
Gil Garnier	Initiation, key ideas, reviewing and editing of the paper	Supervisor

Candidate's  
Signature

	Date 17/12/09
--	------------------

### Declaration by co-authors

The undersigned hereby certify that:

- (1) the above declaration correctly reflects the nature and extent of the candidate's contribution to this work, and the nature of the contribution of each of the co-authors.
- (2) they meet the criteria for authorship in that they have participated in the conception, execution, or interpretation, of at least that part of the publication in their field of expertise;
- (3) they take public responsibility for their part of the publication, except for the responsible author who accepts overall responsibility for the publication;
- (4) there are no other authors of the publication according to these criteria;
- (5) potential conflicts of interest have been disclosed to (a) granting bodies, (b) the editor or publisher of journals or other publications, and (c) the head of the responsible academic unit; and
- (6) the original data are stored at the following location(s) and will be held for at least five years from the date indicated below:

Location(s)

Bioresource Processing Research Institute of Australia (BioPRIA),  
Department of Chemical Engineering, Monash University, Clayton, VIC  
3800, Australia.

Signature 1

	Date 17/12/09
---	------------------

# Reaction Kinetics of Alkaline Phosphatase Immobilized on Paper

Mohidus Samad Khan and Gil Garnier\*

Bioresource Processing Research Institute of Australia (BioPRIA),  
Department of Chemical Engineering,  
Monash University, Clayton, VIC 3800, Australia.

\*Corresponding author: Gil.Garnier@eng.monash.edu.au

Chapter 2	41
Reaction Kinetics of Alkaline Phosphatase Immobilized on Paper	41
Abstract	44
1. Introduction	45
2. Experimentals	47
2.1. Materials	47
2.2. Methods	47
3. Theory	50
3.1. Mechanism	50
3.2. Kinetic Model	52
4. Results	53
5. Discussion	57
5.1. Kinetic Model	57
5.2. Polymer Effect on Enzyme Adsorption and Reactivity	60
6. Conclusion	61
Acknowledgment	62
References	63

## ABSTRACT

The reaction kinetics of alkaline phosphatase (ALP) immobilized on paper was quantified by image analysis using a colorimetric technique. The colour intensity of the product complex was measured by image analysis as a function of time. ALP was either physisorbed directly on paper or adsorbed on paper treated with a monolayer of a high molecular weight cationic polyacrylamide (CPAM), an anionic polyacrylic acid (PAA) or a high molecular weight polyethylene oxide (PEO). The reaction rate of enzymatic paper follows a first order reaction with respect to the enzyme concentration. ALP immobilized on paper has a reaction rate 2 to 3 orders of magnitude lower than the free ALP enzyme in buffer solution. This might be due to a critical loss of enzyme flexibility upon adsorption. No

We choose to go to the moon, not because it is easy but because it is hard.

– John F. Kennedy

increase in reaction rate was achieved by immobilizing ALP on paper treated with a high molecular weight cationic polyacrylamide (CPAM) or a highly charged anionic polyacrylic acid oligomer (PAA), which suggests the enzyme orientation was not significantly affected. However, the reaction rate for ALP on PEO treated paper was lower than that on CPAM or PAA treated papers. That is probably due to some PEO-enzyme interaction affecting the tertiary structure of the ALP enzyme.

**Key Words:** Bioactive surfaces, paper, enzyme, polymer, reaction kinetics

## 1. INTRODUCTION

The potential of bioactive papers for medicine, environmental and industrial applications has recently captured wide attention<sup>1, 2</sup>. Disposable bioassays for routine health monitoring, instant water analysis of heavy metals or microbial activities, paper towels that signal bacterial contamination on the kitchen counter, medical masks that disable viruses are just a few of the potential applications. Bioactive papers can also have industrial applications. Enzymes immobilized on paper for the catalytic production of biofuels, food packaging to detect the presence of bacteria or the product ripeness and paper for the purification or separation of blood or fermentation streams are some examples<sup>1, 3, 4</sup>.

For bioactive papers to hold their promises, two major developments are required. The first, from a performance aspect, requires the immobilized biomolecules to retain their full functionality. This means that the reaction rate and the selectivity must be preserved upon immobilization. The second requirement is an economically attractive product, which requires a combination of low cost materials and high efficiency production process. Paper is certainly one of the cheapest substrates available. Since the biomolecule is often the most expensive component of the device, it is essential to maximize its life time and its retention on the surface. Retention is especially critical as most bioactive papers or devices are designed to be used wet, in contact with some biofluid or aqueous solution of interest; the biomolecules must remain on paper during cycles of wetting/drying or upon prolong exposure to aqueous solutions.

Printing is among the most efficient processes to consistently deliver well defined and complex patterns of fluids on a solid surface. The technology is widely

developed, very flexible and digital techniques allow printing one of a kind-pattern. Printing velocities of 1000 m/min are achievable by inkjet, and even higher by modern flexography and lithography. Lateral resolution of 20  $\mu\text{m}$  and decreasing has already been achieved<sup>5</sup>. Functional printing has recently been explored for manufacturing bio devices<sup>6-17</sup>. Many types of biomolecules have been printed<sup>18-21</sup>, and complex patterns of micro-fluidic systems have been created by printing hydrophobic barriers and channels<sup>2, 8, 18-21</sup>. However, the current printing technology has a major limitation: any covalent bond development between the surface and the printed biomolecule would drastically reduce the efficiency of the process. The challenge is therefore to permanently retain functional biomolecules on a surface without requiring one of the bio-affinity or coupling reaction methods widely used in the laboratory.

Polymer layers are promising to engineer biomolecules featuring on a surface<sup>22</sup>. This study investigates water soluble polymers as retention aids to immobilize biomolecules on paper. Polymers can easily be deposited prior to biomolecule deposition or even printed in any pattern immediately prior to printing the bio-system of interest. Three model polymers: a high molecular weight medium charge cationic polyacrylamide (CPAM), a highly charged low molecular weight anionic polyacrylic acid (PAA) and a high molecular weight neutral polyethylene oxide (PEO) were selected to investigate the effect of polymer charge and molecular weight on enzyme retention. An enzyme, alkaline phosphatase (ALP), was selected as model biomolecule. This is because enzymes are a family of biocatalysts able to perform a wide variety of selective biochemical reactions critical for life-science and many industrial applications. Among enzymes, ALP is robust, inexpensive and widely used and its behavior is predictable and well documented<sup>23-25</sup>. This study has two main objectives. The first is to quantify the reaction rate of an enzyme immobilized on paper in comparison to the free enzyme in solution. The second is to analyse the effect of retention polymer on the kinetics of immobilized enzyme. A secondary objective is to explore whether reaction rate can be increased through preferential biomolecule orientation on a surface by controlling the electrostatic interactions with polymers. The effect of these polymers on the stability, the aging and the retention of the immobilized enzymes is reported elsewhere<sup>26</sup>.

An image analysis technique quantifying the intensity of the colour product was developed to measure the enzymatic rate on paper. The kinetics of the enzymatic paper system was quantified, and the effect of model retention polymer on enzyme kinetic rate measured.

## 2. EXPERIMENTALS

### 2.1. Materials

Alkaline phosphatase (ALP) from bovine intestinal mucosa, was purchased from Aldrich and used as received. ALP was immobilized on paper using three different water soluble polymers. A cationic polyacrylamide (CPAM) of  $M_w = 5 \times 10^6$  and medium charge density (2.1 meq/g), Percol 1550\*, was provided by BASF, Ludwigshafen, Germany. Polyacrylic acid (PAA),  $M_w = 2,000$  and polyethylene oxide (PEO),  $M_w = 4 \times 10^6$ , were purchased from Aldrich. All polymers were dissolved to a concentration of 1g/L. Water (Millipore, 18M $\Omega$ ) was used for making all dilutions.

ALP was dissolved to a concentration of 0.5 mg/mL in 1 M diethanolamine buffer with 0.50 mM magnesium chloride and 5 M HCl to maintain pH at 9.7. Water (Millipore, 18M $\Omega$ ) was used for making all dilutions. The 5-bromo-4-chloro-3-indolyl phosphate and 3,3'-(3,3'-dimethoxy-4,4'-biphenylene)-bis-(2-p-nitrophenyl-5-phenyl-2H-tetrazolium chloride) liquid substrate system (BCIP/NBT), purchased from Aldrich, was selected to quantify the enzymatic activity of ALP on paper. The biochemical reaction of ALP with BCIP/NBT results in a blue-purple complex; its intense colour can be directly observed, is very stable and does not fade upon exposure to light<sup>3</sup>.

Whatman #4 filter paper was chosen as paper substrate to immobilize enzymes.

### 2.2. Methods

#### 2.2.1. Polymer on Paper

Paper samples (diameter of 16 cm) were soaked into polymer solutions contained in a glass tray for about 1 minute. To remove the extra polymer, the paper samples were then rinsed thoroughly in excess water for 1 minute (Figure 1). The samples were carefully kept horizontal while being removed from the polymer solutions to ensure uniform distribution on paper. This methodology aimed at depositing a consistent monolayer polymer on paper. The polymer treated samples were immediately soaked (wet) into the enzymatic solution.

### 2.2.2. Enzyme on Paper

Enzyme aqueous solutions were homogeneously applied onto paper following TAPPI standard (T 205 sp-95). Circular paper samples (d = 16 cm), with or without polymer, were immersed into the ALP enzymatic solution contained in a large Petri-dish (Figure 1). The well-soaked paper samples were then blotted and left to dry in a dark chamber at standard conditions: 23°C and 50% relative humidity (RH), for 24 hours. Additional experimental information on surface profile analysis and histogram distribution of gray values were described elsewhere<sup>3, 27</sup>. This system combines the enzyme-substrate (E-S) reaction upon formation of the product (blue-purple complex).

### 2.2.3. Reactivity of ALP Enzymatic Papers

The liquid substrate system BCIP/NBT was applied onto the enzymatic papers at the time defined as  $t=0$ . This was done as follow: small droplets of fresh liquid substrate were deposited onto the enzymatic papers using a 1.0 mL syringe equipped with a stainless steel flat-tipped needle (0.21 mm outer diameter). The E-S reaction was allowed to proceed under standard conditions: 23°C and 50% relative humidity (RH) for 30 minutes; this insures a complete enzymatic reaction<sup>3</sup>. The colour change due to the E-S reaction was captured using a standard imaging system. From the colour intensity of the E-S reaction on paper, the relative activity of the enzymatic paper was measured. Each measurement reported results from the average of 6 full replicates.

### 2.2.4. Image Capturing and Activity Measurement

The reaction kinetics images were captured using a standard video camera (JVC Camcorder Everio GZ-MG530) (Figure 2). Two sets of lighting systems (SCHOTT KL1500LCD, Germany and ELMO Visual Presenter, EV-2500AF PAL, Japan) were used for optimal resolution. The video clips were transferred to a computer and converted using Prism Video Converter v 1.27 and VirtualDub-1.8.8 software.

The converted images were analyzed using ImageJ software (ImageJ 1.41o). ImageJ calculates the gray values of RGB (red-green-blue) images. For any selected area, the ImageJ software calculates the weighted average gray value within the selection, which can be related to the activity of enzymatic paper.

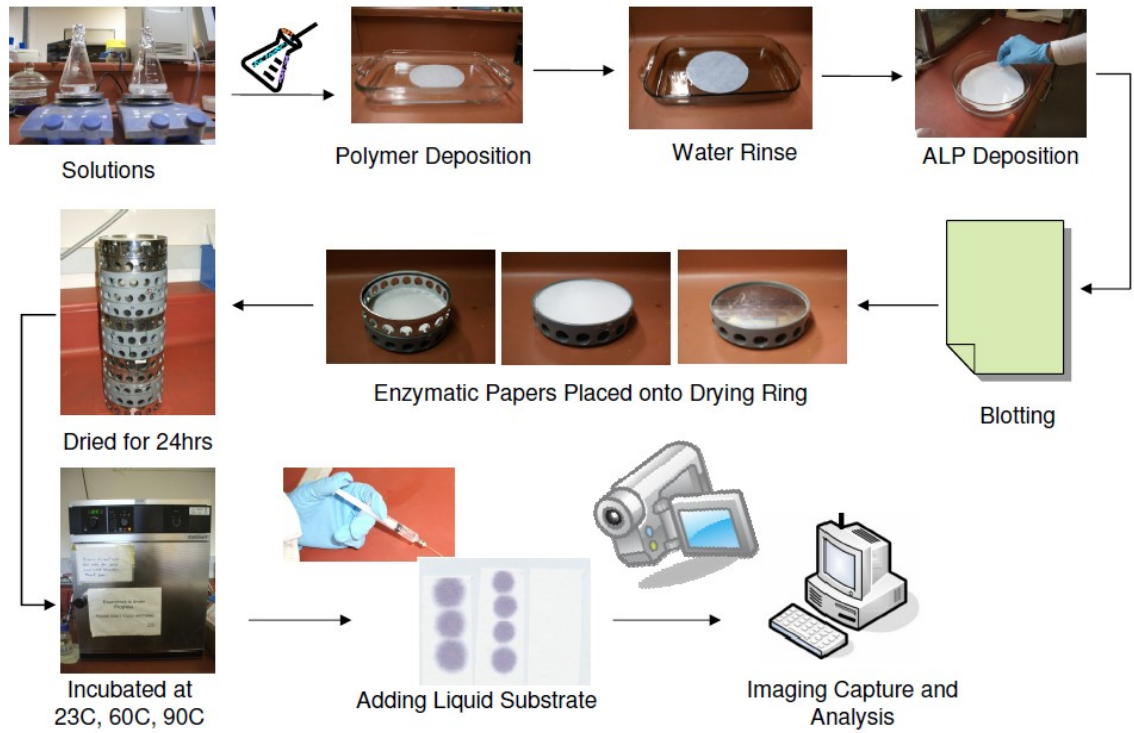


**Figure 1:** Experimental system to prepare the ALP enzymatic papers.

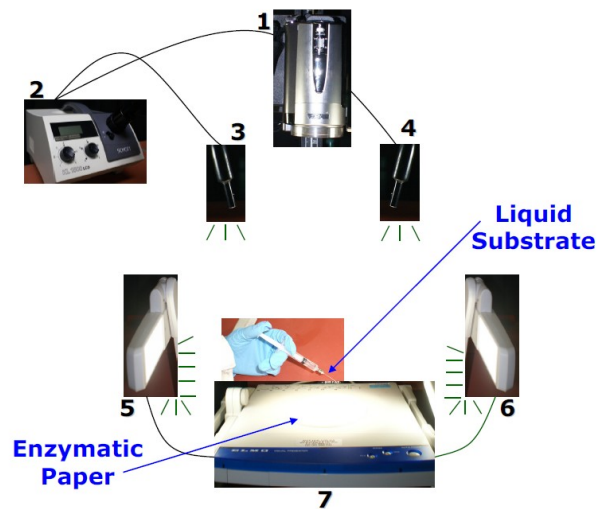


**Figure 2:** Experimental setup to measure the enzymatic reaction kinetics on paper. (1) Video camera, (2) light box, (3)-(6) lights, (7) platform for the ALP enzymatic papers.

### 3. THEORY

The indoxyl tetrazolium method<sup>28</sup> was selected to investigate the reaction kinetics of alkaline phosphatase (ALP). The standard combination of BCIP (5-bromo-4-chloroindoxyl phosphate) and NBT (3,3'-(3,3'-dimethoxy-4,4'-biphenylene)-bis-(2-p-nitrophenyl-5-phenyl-2H-tetrazolium chloride)) was used as the enzymatic substrate system. Together ALP and BCIP/NBT yield an intense, insoluble dark-purple precipitate when reacted with ALP under alkaline conditions. ALP has a molecular weight ranging from 89 to 140 KD<sup>24, 29-31</sup>. Its phosphate substrate is a much smaller molecule of molecular weight of 95 D. A fully active native ALP enzyme has two active sites; each active site contains three closely spaced metal binding sites identified as A, B and C. A and B contain zinc ions and C contains magnesium ion<sup>23,24</sup>. The enzymatic hydrolysis of the phosphate substrate from an ester to a secondary alcohol involves two sequential in-line nucleophilic attacks at the phosphorous atoms, which forms the intermediate products<sup>24,25</sup>. It is believed that the ALP enzyme renders the nucleophilic path more favourable by creating protein-binding sites reducing the negative charge of the phosphate group<sup>24</sup>. The complete reaction proceeds at a steady rate, allowing accurate control of the relative sensitivity and control of the development of the reaction<sup>32</sup>.

#### 3.1. Mechanism

With the indoxyl tetrazolium method, BCIP is hydrolyzed by the ALP enzyme into an intermediate, which under alkaline conditions dimerises to produce an indigo dye: 5,5'-dibromo-4,4' dichloro indigo white. Under alkaline conditions the dimerisation reaction involves the loss of two hydrogen atoms, used to reduce a tetrazolium salt Nitro B.T. into NBT-diformazan at the enzyme site (Figure 3)<sup>28,34</sup>. The diformazan is insoluble in alcohols and can be dehydrated, mounted in a synthetic medium and thus a permanent specimen can be obtained<sup>28</sup>. The second step illustrated on Figure 3 represents the tautomerism of the BCIP intermediate, which is a rapid reaction with a high rate constant of  $k \approx 3-5 \times 10^9 \text{ M}^{-1} \text{ s}^{-1}$ ,<sup>35</sup>. The redox reaction of NBT and BCIP intermediate to form NBT-formazan and the indigo white dye is also a fast reaction described by a high rate constant:  $k \approx 10^6-10^7 \text{ M}^{-1} \text{ s}^{-1}$ <sup>34,36</sup>. Therefore, the first step of the reaction scheme: hydrolysis of BCIP by ALP, is the rate limiting step of

the reaction scheme ( $k \approx 30 - 118 \text{ s}^{-1}$  <sup>23, 24, 37</sup>). The kinetic constant is 5 to 8 orders of magnitude lower than that of the other reactions involved.

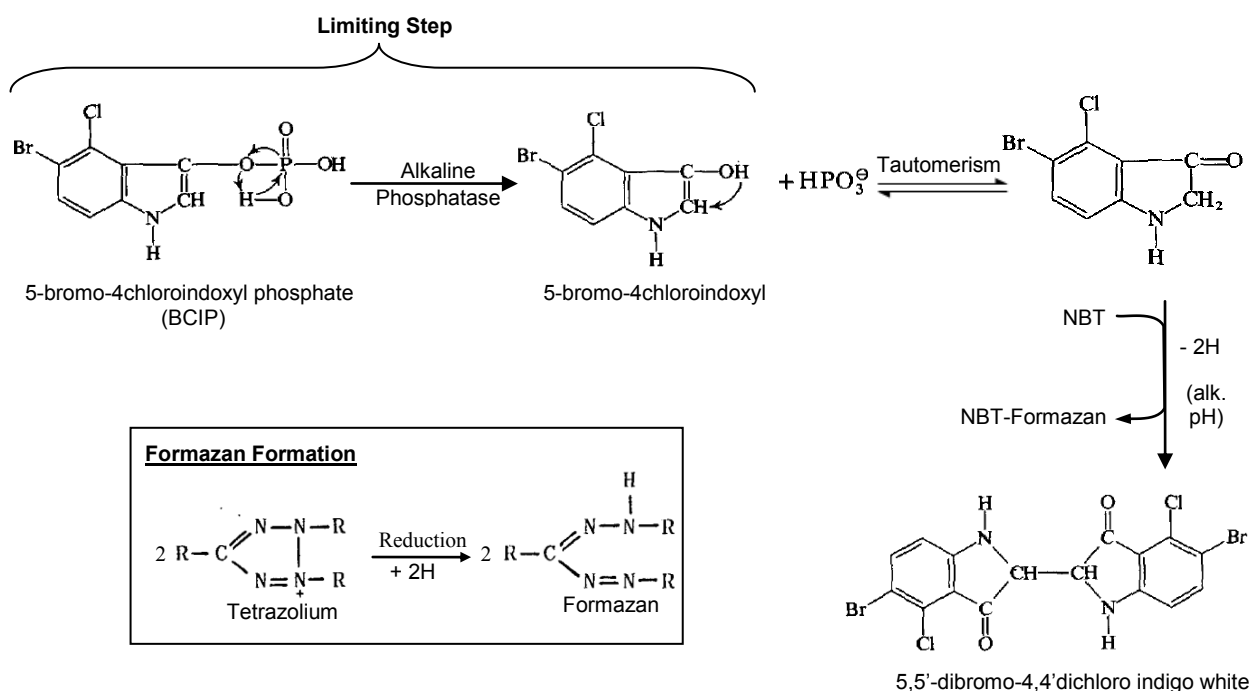


**Figure 3: Kinetic scheme of the indoxyl tetrazolium method for the histochemical demonstration of non-specific ALP** <sup>28, 33</sup>.

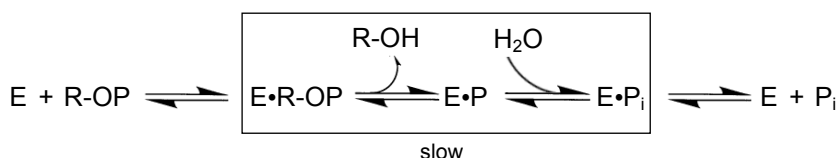


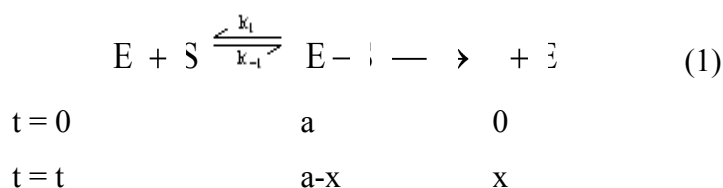
**Figure 4: Mechanism of the ALP reaction** <sup>23, 24, 33, 38</sup>.

The hydrolysis mechanism of phosphate monoesters by ALP is described by the kinetic scheme shown on Figure 4: E is the free enzyme, R-OP is the substrate, E•R-OP is the activated enzyme-substrate complex, E•P is the phosphorylated enzyme, and P<sub>i</sub> is the inorganic phosphate <sup>37</sup>. The first step represents ligand bonding <sup>38</sup>. The second step corresponds to the catalytic reaction. The covalent E-P intermediate is subsequently hydrolyzed to form a non-covalent enzyme-phosphate complex (E•P<sub>i</sub>). Wilson et al. <sup>33</sup>

and Hull et al.<sup>39</sup> demonstrated that the hydrolysis of the non-covalent E-P<sub>i</sub> is the rate limiting step under alkaline condition. Detailed discussion of ALP reaction mechanism can be found in Holtz and Kentrowitz<sup>23</sup>, Coleman<sup>24</sup>, Kim and Wyckoff<sup>25</sup> and Craig et al.<sup>37</sup>.

### 3.2. Kinetic Model

The simplest form of an enzyme reaction converting a substrate (S) into a product (P) via the formation of an enzyme-substrate (E-S) is represented by Eq.1:



where, 'a' is the initial enzyme-substrate concentration [E-S] and 'x' is the concentration of product at time 't'. Using an excess amount of substrate, the enzyme concentration will limit and govern the reaction rate; however, only the enzyme-substrate complex can yield the product. For a zero, first and second order reaction, the kinetic models of Eq.1 can be expressed by Eq. 2, 3 and 4, respectively<sup>37</sup>:

zero order:  $x = k t$  (2)

first order:  $\ln (a-x) = - k t + c$  (3)

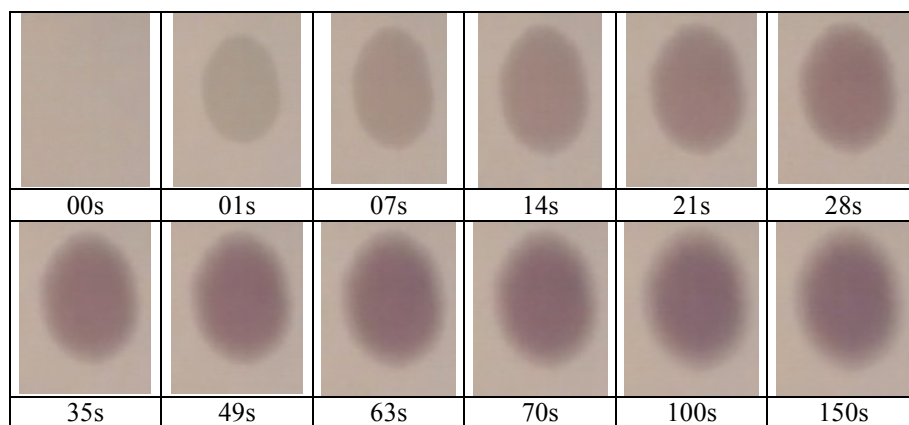
second order:  $1/(a-x) = k t + c$  (4)

## 4. RESULTS

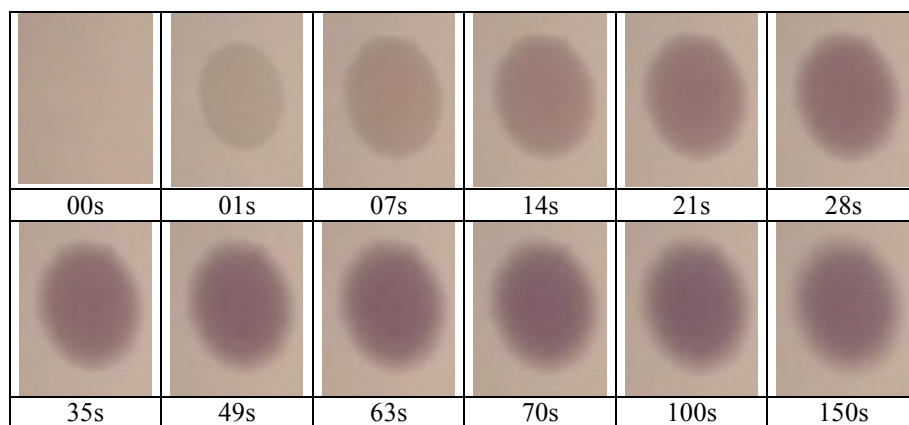
A monolayer of CPAM, PAA or PEO was created on the paper samples which were subsequently immersed in an enzyme solution (in excess) and dried. The liquid substrate system BCIP/NBT was applied onto the different ALP enzymatic papers and the E-S reaction was allowed to proceed to completion. The reaction converting the substrate system with ALP results in a blue-purple colour of product complex on paper. The colour formation on paper was video captured and the images were analyzed. The activities of the enzymatic papers were calculated from the weighted mean grey value measured from the captured images. The colorimetric evolution of the enzymatic reactivity of ALP enzymatic papers was analyzed as a function of time. Pictures of product colour formation on ALP enzymatic papers are shown in Figure 5. Two enzymatic papers are compared; in the first, ALP is directly physisorbed on paper (Figure 5 a); in the second, ALP is adsorbed on paper treated with a high molecular weight cationic polymer CPAM (Figure 5 b). The colour intensity of the product-complex increased non-linearly as a function of time. The evaluation of colour intensity also varied as a function of the paper used.

Figure 6 illustrates the product formation due to the E-S reaction on the four different ALP enzymatic papers as a function of time. The product colour intensity (x) on enzymatic paper increased rapidly for the first 35-40 sec. After that initial period, the colour change slows down and levels-off to a saturation value (Figure 6 a-d). Each line on Figure 6 represents the average of six replicates. The standard derivation is illustrated for each in curve. A narrow variance is observed, confirming the reproducibility and giving confidence in the methodology. Very low variance appears in the initial period, critical to quantify the reaction kinetics. The variance increases slightly with time, as the reaction progresses. The plateau representing final product concentration differs among the different enzymatic papers; this suggests some polymer-enzyme-substrate interaction. The time to reach saturation of the product formation also varies among the different enzymatic papers.

The gray values corresponding to the reactant concentration (a-x) on ALP enzymatic paper is represented on Figure 7 as a function of time.

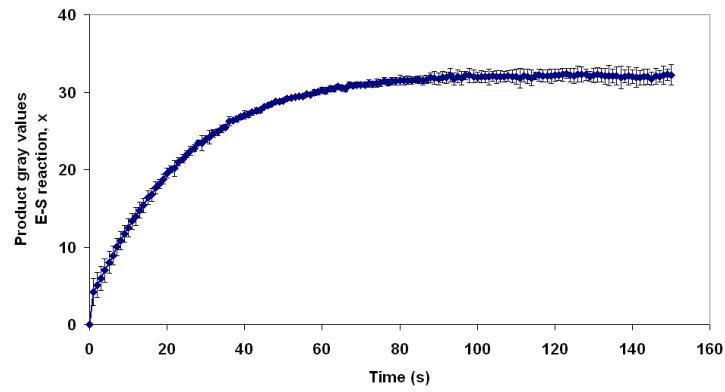


(a)

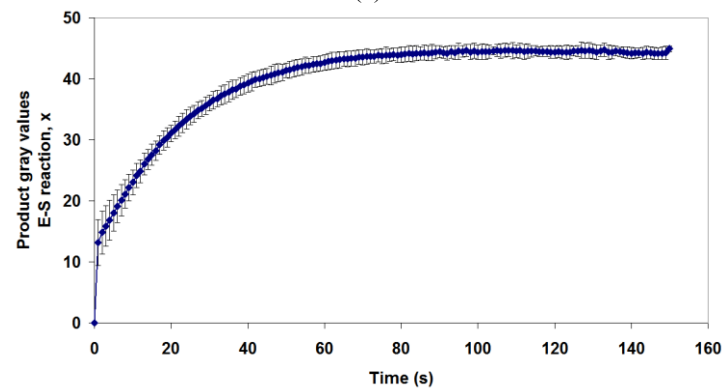


(b)

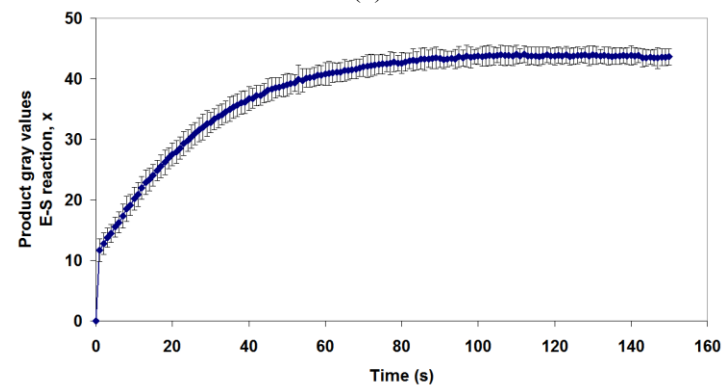
**Figure 5: Product formation on ALP enzymatic paper at different times. (a) ALP on paper; (b) ALP on CPAM Paper. The blue purple colour reveals the enzyme (ALP) - substrates (BCIP/NBT) reaction.**



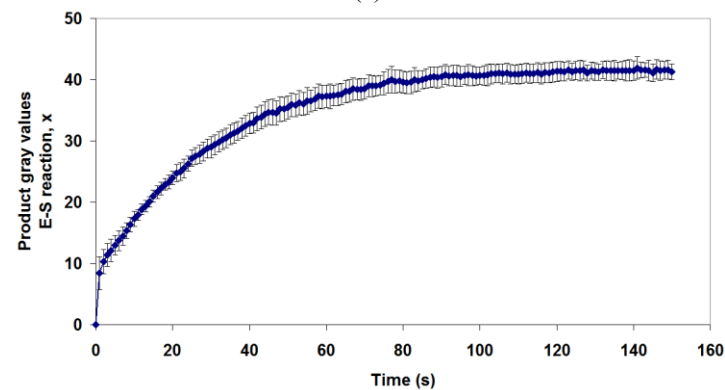
(a)



(b)



(c)



(d)

Figure 6: E-S product formation on ALP enzymatic papers as a function of time. (a) ALP on paper, (b) ALP on CPAM paper, (c) ALP on PAA paper and (d) ALP on PEO paper,  $n = 6$ , at  $23\text{ }^{\circ}\text{C}$ .

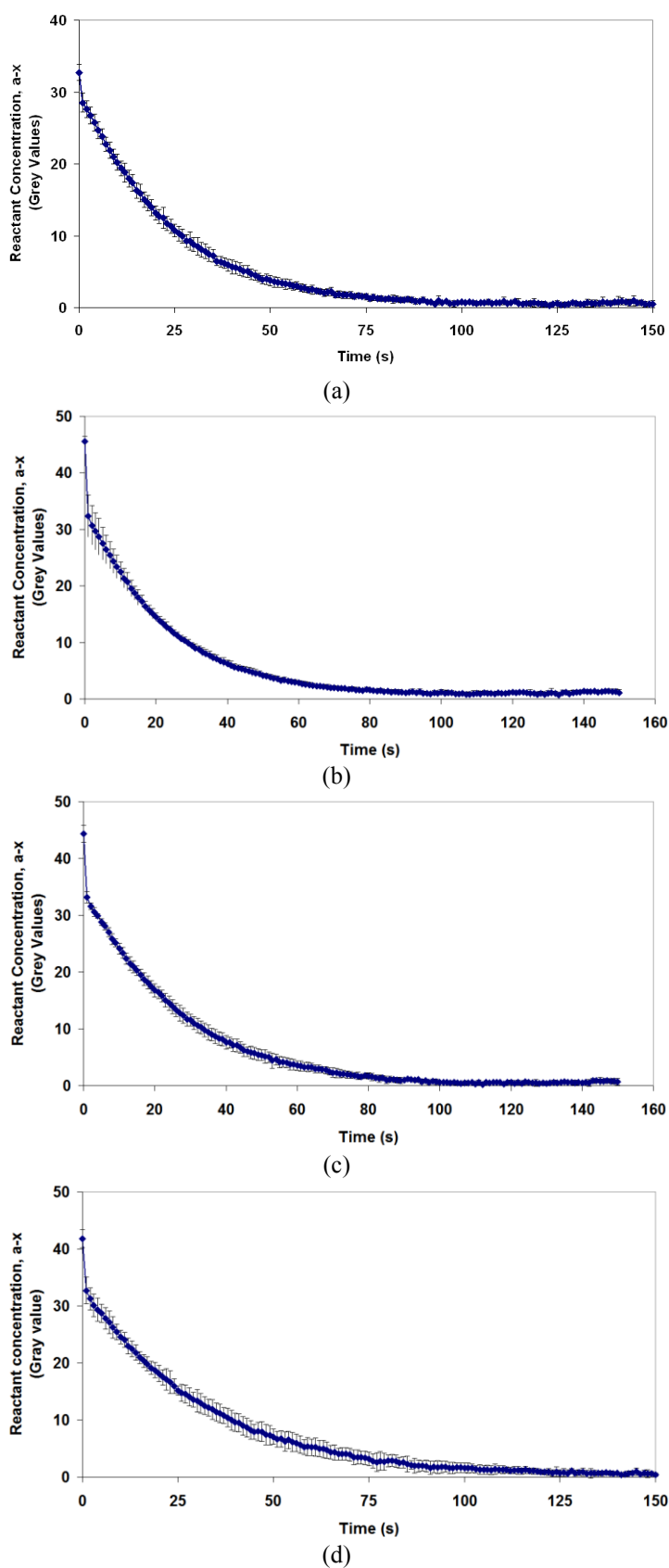


**Figure 7:** Reactant concentration (a-x) on ALP enzymatic papers as a function of time. (a) ALP on paper, (b) ALP on CPAM paper, (c) ALP on PAA paper and (d) ALP on PEO paper, n= 6, at 23 °C.

## 5. DISCUSSION

### 5.1. Kinetic Model

As substrate was used in large excess in all enzymatic papers, a pseudo first order reaction with respect to enzyme concentration is expected. Whether the enzyme preferentially exists as enzyme-substrate (E-S) complex or as free enzyme (E) depends on the values of the kinetic constants  $k_1$ ,  $k_{-1}$ ,  $k$  introduced in Eq.1. However, the product colour concentration is directly related to the E-S complex formation. The simplest model is a first order reaction with respect to the E-S complex formation, described by Eq.3, and expressed in the logarithmic form:

$$2.303 \times \log (a-x) = -k t + c \quad (5)$$

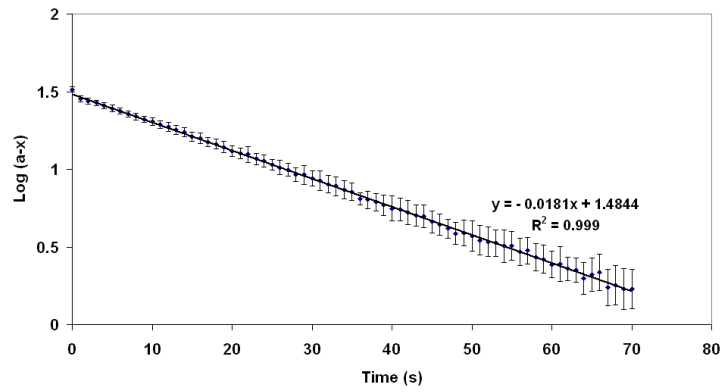
Assuming a first order reaction with respect to the E-S complex concentration, a linear relationship is expected between the  $\log(a-x)$  as a function of time, the slope of which indicating the reaction rate constant  $k$ . Figure 8 represents the relationship between  $\log(a-x)$  as a function of time for the four different enzymatic papers. Linear relationship suggesting a first order reaction kinetics is observed for all papers. The reaction kinetic constants,  $k$ , calculated from Eq. 5 are presented in Table I. The reaction kinetics of the substrate reacting onto the various enzymatic papers are compared in Figure 9.

**Table I: ALP rate constants on different treated papers at 23°C**

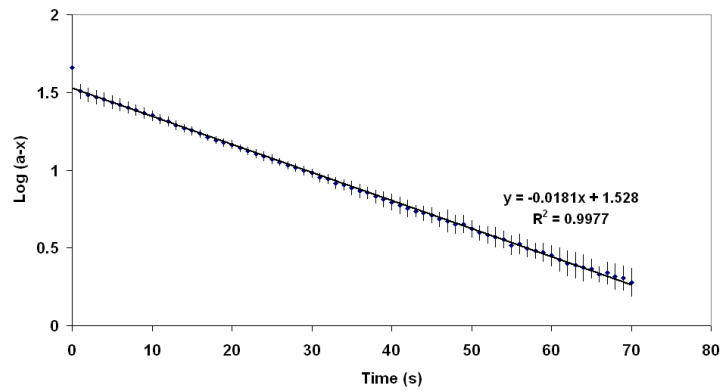
	Rate constant, $k$ (hr <sup>-1</sup> )
ALP on Paper	150.1
ALP on CPAM Paper	150.1
ALP on PAA Paper	143.5
ALP on PEO Paper	114.4
ALP in Buffer <sup>23, 24, 37</sup>	108 to 425 × 10 <sup>3</sup>

The reaction kinetics of ALP immobilized on paper is three orders of magnitude slower than that of the free enzymes in buffer solution (Table I). Rate constants of ALP

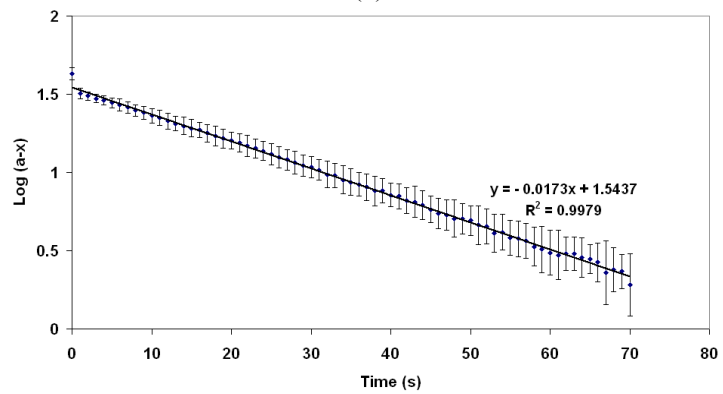
reaction in buffer ranging from 108 to  $425 \times 10^3 \text{ hr}^{-1}$  are reported in the literature<sup>23, 24, 37</sup>; this compares to  $k$  ranging from 114 to  $150 \text{ hr}^{-1}$  measured from our enzyme immobilized on paper. A decrease of enzyme reaction rate upon immobilization was also reported by Pelton et al. for the horseradish peroxidase (HRP) enzyme immobilized in nano-silica<sup>40</sup>. Four possible explanations are foreseen for this observation. First, a fraction of the enzymes might be locked by adsorption into a limiting configuration, which may prevent the substrate molecules to fully access all the enzyme active sites. Second, mass transport of the substrate to and from the surface might represent a delaying resistance. Third, the enzyme might require mobility of its active sites or of the molecule to optimize the reaction; enzyme immobilization would reduce this mobility. Fourth, immobilization might denature the enzyme; the last hypothesis can be rejected as separately investigated elsewhere<sup>26</sup>.



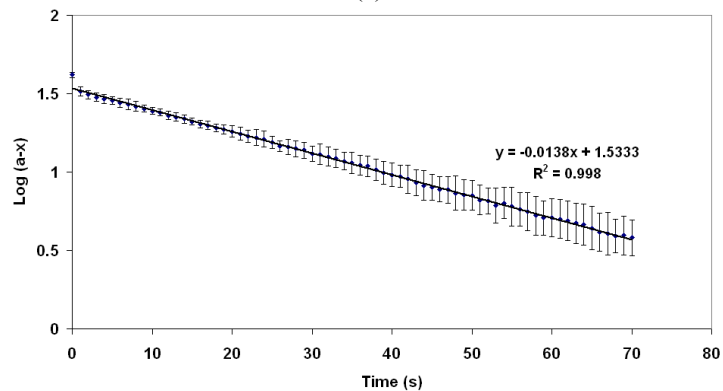
(a)



(b)



(c)



(d)

**Figure 8:** ALP reaction kinetics on enzymatic papers. (a) ALP on paper, (b) ALP on CPAM paper, (c) ALP on PAA paper and (d) ALP on PEO paper,  $n=6$ ,  $T = 23\text{ }^\circ\text{C}$ .

## 5.2. Polymer Effect on Enzyme Adsorption and Reactivity

The nature of immobilization can affect the kinetics of enzyme reaction. ALP simply physisorbed on paper, or CPAM and PAA treated papers, all have a similar reaction rate constant of  $k = 150 \text{ hr}^{-1}$  (Figure 9 and Table I). The cationic polyacrylamide (CPAM) is a high molecular weight linear polymer of medium charge density that can bridge colloids through electrostatic interaction with the anionic groups of the enzyme. The PAA is a highly charged polyacrylic oligomer able of electrostatic interaction with the cationic groups of ALP, but of insufficient molecular weight for bridging. The last is a high molecular weight neutral polyethylene oxide (PEO), known for its efficient bridging ability. The polymers are adsorbed such as to leave a full monolayer, but without any excess, on the cellulose fibres. Polymer molecules are also expected to be adsorbed flat under their equilibrium configuration and not as random coils because of the relatively long preparation time (2 minutes) before enzyme adsorption. Therefore, the different polymer molecules are not expected to act as spacers, increasing the distance enzyme-surface or extending the enzyme mobility. This is demonstrated by the similar reaction rate constants obtained by the high molecular weight CPAM and the PAA oligomer. However, all the polymers do increase the adhesion enzyme-paper as revealed by the higher initial colour concentration (blue-purple) seen on Figure 6, which was further investigated elsewhere <sup>26</sup>.

The similar reaction rates achieved by the ALP enzyme immobilized on the cationic paper (CPAM), or on the anionic paper (PAA) suggest that neither the accessibility nor the orientation of the enzyme was significantly improved by controlling the electrostatic forces between enzyme and paper. This can have a few explanations: the expected change of orientation of the enzyme active sites might have failed. The increase in enzyme reaction rate due to improved active site accessibility might be obscured by a corresponding reduction in reaction rate caused by a loss in enzyme molecule flexibility.

Interesting is the significant reduction in reaction rate of ALP immobilized on PEO paper (Figure 9). PEO is well known to prevent protein deposition on surfaces <sup>22, 41-43</sup>.

The reaction rate constant ranging from 114 to 150  $\text{hr}^{-1}$  for the enzymatic conversion of the BCIP/NBT substrate system into the blue-purple product is many orders of magnitude slower than either of the tautomerism or the electron transfer steps.

This confirms that the limiting step of the enzymatic reaction is measured by following the evolution of the intensity of the indigo dye.

No significant difference in enzyme kinetics was observed for ALP immobilized by CPAM, PAA or simply physisorbed on paper. No improvements were seen whether the enzyme was linked to paper by bridging, by charge reversal or by interacting with the enzyme cationic or anionic groups; this suggests similar enzyme morphology and orientation on the surface.

While ALP enzyme immobilized on paper has a lower reaction rate than the enzyme in solution, it also has a much higher stability<sup>3, 26</sup>. Considering the critical enzyme life-time, its higher surface density and retention upon wetting, enzymatic paper offers an attractive option for health and environmental applications.

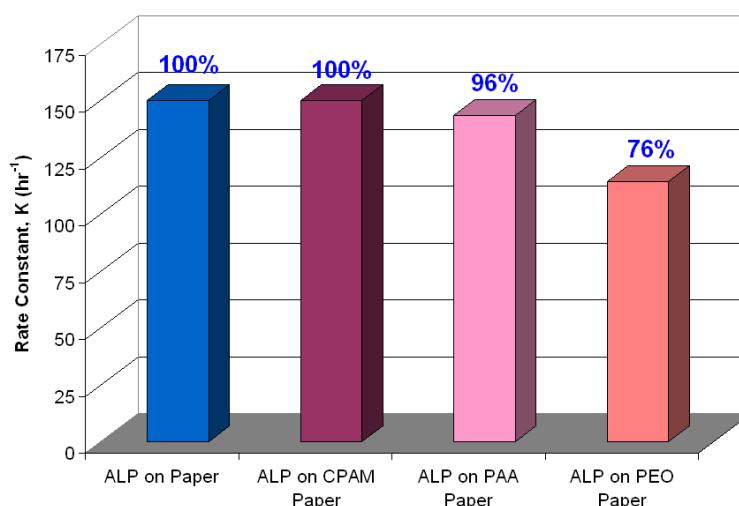


**Figure 9:** Reaction rate constant of ALP reacting with BCIP/NBT on paper at 23 °C.

## 6. CONCLUSION

The reaction kinetics of alkaline phosphatase (ALP) immobilized on paper was quantified by image analysis using a colorimetric technique. The colour intensity of the blue purple product complex was measured as a function of time. ALP was either directly physisorbed on paper or adsorbed on a paper treated with a monolayer of a high molecular weight cationic polyacrylamide (CPAM), an anionic polyacrylic acid (PAA) or a high molecular weight polyethylene oxide (PEO). ALP immobilized on paper has

reaction rate 2 to 3 orders of magnitude lower than the free ALP enzyme in buffer solution. This might be due to a critical loss of enzyme flexibility upon adsorption. No increase in reaction rate was achieved by immobilizing ALP on paper treated with a high molecular weight cationic polyacrylamide (CPAM) or a highly charged anionic polyacrylic acid oligomer (PAA). This suggests that enzyme orientation was not significantly affected through preferentially linking with its anionic or cationic groups. Polymers simply provide a strong adhesion of the biomolecule to paper which remains unaffected upon wetting. However, the reaction rate of ALP on PEO treated paper was lower than that on CPAM or PAA treated papers. That is probably due to some PEO-enzyme interaction affecting the tertiary structure of the enzyme molecules. PEO is a well known polymer preventing protein fouling on surfaces.

In spite of a lower reaction rate, enzymatic bioactive papers offer a great potential in biotechnology, medicine and environmental applications because of their significantly increased stability, aging, surface density and retention of the biomolecules in wet conditions.

## **ACKNOWLEDGMENT**

Many thanks to A. Slater and S. B. M. Haniffa for technical assistance and to Monash University for postgraduate scholarships (MSK).

## REFERENCES

1. Pelton, R., Bioactive Paper Provides a Low-Cost Platform for Diagnostics. *Trends in Analytical Chemistry* **2009**, 28, (8), 925-942.
2. Aikio, S.; Grönqvist, S.; Hakola, L.; Hurme, E.; Jussila, S.; Kaukonen, O.-V.; Kopola, H.; Känsäkoski, M.; Leinonen, M.; Lippo, S.; Mahlberg, R.; Peltonen, S.; Qvintus-Leino, P.; Rajamäki, T.; Ritschkoff, A.-C.; Smolander, M.; Vartiainen, J.; Viikari, L.; Vilkmann, M., Bioactive Paper and Fibre Products: Patent and Literature Survey. In 2006; pp 1-84.
3. Khan, M. S.; Xu, L.; Shen, W.; Garnier, G., Thermal Stability of Bioactive Enzymatic Papers. *Colloids and Surfaces B: Biointerfaces* **In Press (2009)**.
4. Pelton, R.; Geng, X.; Brook, M., Photocatalytic Paper from Colloidal TiO<sub>2</sub>-Fact of Fantasy. *Advances in Colloid and Interfaces Science* **2006**, 127, (1), 43-53.
5. Khan, M. S.; Fon, D.; Li, X.; Tian, J.; Forsythe, J.; Garnier, G.; Shen, W., Biosurface Engineering Through Ink Jet Printing. *Colloids and Surfaces B: Biointerfaces* **In Press (2009)**.
6. Hossain, S. M. Z.; Luckham, R. E.; Smith, A. M.; Lebert, J. M.; Davies, L. M.; Pelton, R. H.; Filipe, C. D. M.; Brennan, J. D., Development of a Bioactive Paper Sensor for Detection of Neurotoxins Using Piezoelectric Inkjet Printing of Sol-Gel-Derived Bioinks. *Analytical Chemistry* **2009**, 81, (13), 5474-5483.
7. Jabrane, T.; Jaïdi, J.; Dube, M.; Mangin, P. J. In *Gravure Printing of Enzymes and Phages*, Advances in Printing and Media Technology, 2008; Iarigai, Ed. 2008; pp 279-288.
8. Risio, S. D.; Yan, N., Piezoelectric Ink-Jet Printing of Horseradish Peroxidase: Effect of Ink Viscosity Modifiers on Activity. *Molecular Rapid Communications* **2007**, 28, (18-19), 1934-1940.
9. Ilkhanizadeh, S.; Teixeira, A. I.; Hermanson, O., Inkjet Printing of Macromolecules on Hydrogels to Steer Neural Stem Cell Differentiation. *Biomaterials* **2007**, 28, (27), 3936-43.
10. Newman, J. D.; Turner, A. P. F., Ink-jet Printing For The Fabrication of Amperometric Glucose Biosensors. *Biosensors and Bioelectronics* **2005**, 20, (10), 2019-2026.
11. Nakamura, M.; Kobayashi, A.; Takagi, F.; Watanabe, A.; Hiruma, Y.; Ohuchi, K.; Iwasaki, Y.; Horie, M.; Morita, I.; Takatani, S., Biocompatible Inkjet Printing Technique for Designed Seeding of Individual Living Cells. *Tissue Engineering* **2005**, 11, (11-12), 1658-1666.
12. Roth, E. A.; Xu, T.; Das, M.; Gregory, C.; Hickman, J. J.; Boland, T., Inkjet Printing for High-Throughput Cell Patterning. *Biomaterials* **2004**, 25, (17), 3707-3715.
13. Allain, L. R.; Askari, M.; Stokes, D. L.; Vo-Dinh, T., Microarray Sampling-Platform Fabrication Using Bubble-Jet Technology for a Biochip System. *Fresenius Journal of Analytical Chemistry* **2001**, 371, (2), 146-150.
14. Keenan, T. M.; Folch, A., Biomolecular Gradients in Cell Culture Systems. *Lab on a Chip* **2008**, 8, 34-57.
15. Miller, E. D.; Fisher, G. W.; Weiss, L. E.; Walker, L. M.; Campbell, P. G., Dose-Dependent Cell Growth in Response to Concentration Modulated Patterns of FGF-2 Printed on Fibrin. *Biomaterials* **2006**, 27, (10), 2213-2221.
16. Xu, T.; Jin, J.; Gregory, C.; Hickman, J. J.; Boland, T., Inkjet Printing of Viable Mammalian Cells. *Biomaterials* **2005**, 26, (1), 93-99.

17. Khan, M. S.; Kannangara, D.; Shen, W.; Garnier, G., Isothermal Noncoalescence of Liquid Droplets at the Air-Liquid Interface. *Langmuir* **2008**, 24, (7), 3199-3204.
18. Shen, W.; Junfei, T.; Li, X.; Khan, M.; Garnier, G. Method of Fabricating Paper-Based Microfluidic Systems by Printing. Australian Provisional Patent, 2008905776, November 7, 2008.
19. Martinez, A. W.; Phillips, S. T.; Carrithe, E.; Thomas III, S. W.; Sindi, H.; Whitesides, G. M., Simple Telemedicine for Developing Regions: Camera Phones and Paper-Based Microfluidic Devices for Real-Time, Off-Site Diagnosis. *Analytical Chemistry* **2008**, 80, (10), 3699-3707.
20. Li, X.; Tian, J.; Nguyen, T.; Shen, W., Paper-Based Microfluidic Devices by Plasma Treatment. *Analytical Chemistry* **2008**, 80, (23), 9131-9134.
21. Martinez, A. W.; Phillips, S. T.; Butte, M. J.; Whitesides, G. M., Patterned paper as a platform for inexpensive, low-volume, portable bioassays. *Angewandte Chemie International Edition* **2007**, 46, (8), 1318-1320.
22. McArthur, S. L.; Shard, A. G., Surface Properties of Biomaterials. In *Encyclopedia of Medical Devices and Instrumentation*, 2nd ed.; Webster, J. G., Ed. John Wiley & Sons, Inc.: New York, 2006; pp 342-354.
23. Holtz, K. M.; Kantrowitz, E. R., The Mechanism of the Alkaline Phosphatase Reaction: Insights from NMR, Crystallography and Site-Specific Mutagenesis. *FEBS Letters* **1999**, 462, 7-11.
24. Coleman, J. E., Structure and Mechanism of Alkaline Phosphatase. *Annual Review of Biophysics and Biomolecular Structure* **1992**, 21, 441-483.
25. Kim, E. E.; Wyckoff, H. W., Reaction Mechanism of Alkaline Phosphatase Based on Crystal Structures. *Journal of Molecular Biology* **1991**, 218, (2), 263-477.
26. Khan, M. S.; Haniffa, S. B. M.; Slater, A.; Garnier, G., Effect of Polymers on Retention and Aging of Enzymatic Bioactive Papers. *Colloids and Surfaces B: Biointerfaces* **2009**, Submitted.
27. Khan, M. S.; Tian, J.; Xu, L.; Shen, W.; Garnier, G., Bioactive Enzymatic Papers. In *Advances in Pulp and Paper Research, Oxford 2009*, I'Anson, S. J., Ed. The Pulp & Paper Fundamental Research Society: 2009; Vol. 2, pp 1149-1166.
28. McGadey, J., A Tetrazolium Method for Non-Specific Alkaline Phosphatase. *Histochemistry* **1970**, 23, 180-184.
29. Fosset, M.; Chappelet-Tordo, D.; Lazdunski, M., Intestinal Alkaline Phosphatase. Physical Properties and Quaternary Structure. *Biochemistry* **1974**, 13, (9), 1783-1788.
30. Anderson, R. A.; Vallee, B. L., Cobal (III), a Probe of Metal Binding Sites of *Escherichia Coli* Alkaline Phosphatase. *Proceedings of the National Academy of Sciences of the United States of America* **1975**, 72, (1), 394-397.
31. Besman, M.; Coleman, J. E., Isozymes of Bovine Intestinal Alkaline Phosphatase. *The Journal of Biological Chemistry* **1985**, 260, (20), 11190-11193.
32. NBT/BCIP Substrates. In *Pierce Protein Research Products*, Scientific, T., Ed. Rockford, USA, 2009.
33. Wilson, I. B.; Dayan, J., The Free Energy of Hydrolysis of Phosphoryl-Phosphatase. *Biochemistry* **1965**, 4, (4), 645-649.
34. Altman, F. P., Tetrazolium Salts and Formazans. *Progress in Histochemistry and Cytochemistry* **1976**, 9, (3).

35. Dodin, G.; Bensaude, O.; Dubois, J.-E., Tautomerism of Formycin. Mechanism of Interconversion. *Journal of The American Chemical Society* **1979**, 102, (11), 3879-3899.
36. Abugo, O.; Rifkind, J. M., Oxidation of Hemoglobin and the Enhancement Produced by Nitroblue Tetrazolium. *The Journal of Biological Chemistry* **1994**, 269, (40), 24845-24853.
37. Craig, D. B.; Arriaga, E. A.; Wong, J. C. Y.; Lu, H.; Dovichi, N. J., Studies on Single Alkaline Phosphatase Molecules: Reaction Rate and Activation Energy of a Reaction Catalyzed by a Single Molecule and the Effect of Thermal Denaturation The Death of an Enzyme. *Journal of The American Chemical Society* **1996**, 118, (22), 5245-5253.
38. Price, N. C.; Stevens, L., *Fundamentals of Enzymology*. Oxford University Press: New York, 1984.
39. Hull, W. E.; Halford, S. E.; Gutfreund, H.; Sykes, B. D., <sup>31</sup>P Nuclear Magnetic Resonance Study of Alkaline Phosphatase: The Role of Inorganic Phosphate in Limiting the Enzyme Turnover Rate at Alkaline pH. *Biochemistry* **1976**, 15, (7), 1547-1561.
40. Voss, R.; Brook, M. A.; Thompson, J.; Chen, Y.; Pelton, R. H.; Brennan, J. D., Non-destructive Horseradish Peroxidase Immobilization in Porous Silica Nanoparticles. *Journal of Materials Chemistry* **2007**, 17, 4854-4863.
41. Kang, S.; Asatekin, A.; Mayes, A. M.; Elimelech, M., Protein Antifouling Mechanisms of PAN UF Membranes Incorporating PAN-g-PEO Additive. *Journal of Membrane Science* **2007**, 296, (1-2), 42-50.
42. Cole, M. A.; Voelcker, N. H.; Thissen, H., Electro-Induced Protein Deposition on Low-Fouling Surfaces. *Smart Materials and Structures* **2007**, 16, (6), 2222-2228.
43. Szleifer, I., Protein Adsorption on Surfaces with Grafted Polymers: A Theoretical Approach. *Biophysical Journal* **1997**, 72, (2 Pt 1), 595-612.

This page is intentionally blank

---

# Chapter 3

---

Thermal Stability of  
Bioactive Enzymatic  
Papers

---

This page is intentionally blank

**Monash University**

**Declaration for Thesis Chapter 3**

**Declaration by candidate**

In the case of Chapter 3, the nature and extent of my contribution to the work was the following:

Nature of contribution	Extent of contribution (%)
Initiation, key ideas, experimental and analysis works, development and writing up of the paper	70

The following co-authors contributed to the work. Co-authors who are students at Monash University must also indicate the extent of their contribution in percentage terms:

Name	Nature of contribution	Extent of contribution (%) for student co-authors only
<b>Gil Garnier</b>	Initiation, key ideas, reviewing and editing of the paper	Co-supervisor
<b>Wei Shen</b>	Initiation, key ideas, reviewing and editing of the paper	Co-supervisor
<b>Xu Li</b>	Initiation and experimental work	20

Candidate's Signature



Date

16/12/09

**Declaration by co-authors**

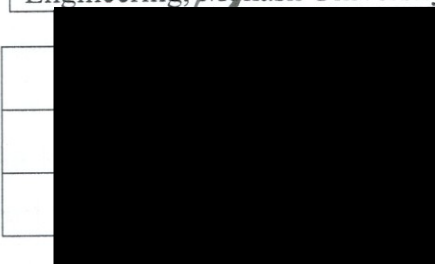
The undersigned hereby certify that:

- (1) the above declaration correctly reflects the nature and extent of the candidate's contribution to this work, and the nature of the contribution of each of the co-authors.
- (2) they meet the criteria for authorship in that they have participated in the conception, execution, or interpretation, of at least that part of the publication in their field of expertise;
- (3) they take public responsibility for their part of the publication, except for the responsible author who accepts overall responsibility for the publication;
- (4) there are no other authors of the publication according to these criteria;
- (5) potential conflicts of interest have been disclosed to (a) granting bodies, (b) the editor or publisher of journals or other publications, and (c) the head of the responsible academic unit; and
- (6) the original data are stored at the following location(s) and will be held for at least five years from the date indicated below:

**Location(s)**

Australian Pulp and Paper Institute (APPI), Department of Chemical Engineering, Monash University, Clayton, VIC 3800, Australia.

Signature 1



Date

17/12/09

Signature 2

Date

17/12/09

Signature 3

Date

16/12/2009

# Thermal Stability of Bioactive Enzymatic Papers

Mohidus Samad Khan, Xu Li, Wei Shen and Gil Garnier\*

Australian Pulp and Paper Institute,  
Department of Chemical Engineering,  
Monash University, Clayton, VIC 3800, Australia.

\*Corresponding author: Gil.Garnier@eng.monash.edu.au

Chapter 3	67
Thermal Stability of Bioactive Enzymatic Papers	67
Abstract	70
1. Introduction	71
2. Experimentals	73
2.1. Materials	73
2.2. Methods	73
3. Theory	78
3.1. Kinetics	78
3.2. Enzymes	79
4. Results	80
4.1. Thermal Stability of Enzymatic Papers	80
4.2. Bio-Printing	82
5. Discussion	83
5.1. Immobilized Enzymes on Paper	83
5.2. Enzymatic Activity Measurement	83
5.3. Deactivation of Enzymes Adsorbed on Paper	84
5.4. Deactivation Kinetics of Enzymatic Paper	86
5.5. Bioactive Enzymatic Papers	89
6. Conclusion	90
Acknowledgment	91
References	91

## ABSTRACT

The thermal stability of two enzymes adsorbed on paper, alkaline phosphatase (ALP) and horseradish peroxidase (HRP), was measured using a colorimetric technique quantifying the intensity of the product complex. The enzymes adsorbed on paper retained their functionality and selectivity. Adsorption on paper increased the enzyme thermal stability by 2 to 3 orders of magnitude compared to the same enzyme in solution. ALP and HRP enzymatic papers

had half-lives of 533 hrs and 239 hrs at 23°C, respectively. The thermal degradation of adsorbed enzyme was found to follow two sequential first order reactions, indication of a reaction system. A complex pattern of enzyme was printed on paper using a thermal inkjet printer. Paper and inkjet printing are ideal material and process to manufacture low cost – high volume bioactive surfaces.

**Key Words:** Bioactive papers, thermal stability, enzyme, deactivation, kinetics.

## **1. INTRODUCTION**

The benefits of many breakthroughs in biotechnology, medicine and environmental science have often been restricted by the high cost and the limited availability of tests and application devices. Most methods developed in the laboratory are difficult to scale up for mass production. There is a need for low cost bioassays for health and environmental diagnostics. Disposable routine bioassays for the early detection of cancers and genetic conditions, for daily tests to monitor diabetes, and for instant water analyses of heavy metals and microbial activity are a few of the potential applications. Bioactive papers can also have industrial applications. Enzymes immobilized on paper for the catalytic production of biofuels, antibody immobilized on paper for the high selectivity separation of antigen in blood or fermentation streams, and antimicrobial papers are some examples.

Low cost is a critical requirement for the successful commercialization of bioassays and bioactive surfaces; this is best achieved through high volume manufacturing and with commodity materials. Printing is a high speed technology, highly adaptive and able to deliver patterns of materials such as functional fluids at an exceptional accuracy. Paper, a non-woven material made of cellulosic fibres, is highly wettable when untreated, easy to functionalise and engineer, biodegradable, sterilisable, biocompatible and cheap. It has long been used for analysis in chromatography [1, 2]. Liquid flow in paper proceeds through capillarity action which is affected by paper structure and chemical treatment. Also, thin coatings of polymers and inorganics can easily be achieved through standard wet-end addition, surface sizing, coating and other surface treatments common to the industries. This suggests that paper is a natural material of choice for the production of disposable bioassay devices and bioactive surfaces.

However, the biotechnology industry has a limited understanding of the effect of paper structure and chemical composition on fluid transport or biomolecule functionality.

The concept of paper bioassays is to rely on paper for the transport of fluids samples, biomolecule detection/reaction, and the communication of the event in a single step process. Whitesides pioneered paper microfluidic systems by developing hydrophobic barriers on paper with photolithography technique or using a x,y-plotter [3-5]. The pattern accuracy and manufacturing efficiency of microfluidic papers can be improved with plasma treatments or inkjet printing [6]. Peptides, enzymes and cells have also been printed under laboratory conditions using a variety of technologies including inkjet printing [7-20].

Few scientific studies have described the immobilization of enzymes on paper. Among those are paper strips indicators for sea food freshness using two enzymes (xantine oxidase and nucleoside phosphorase) [21], and bioactive paper to monitor alcohol content in the breath using alkaline oxidase (AOD) [22]. However, there is little fundamental understanding on the effect of surface property on biofunctionality. Chen et al. investigated by AFM the effect of surface wettability on enzyme loading (candida antarctica lipase B CALB) [23]. As surface wettability increased, the number of immobilized CALB molecules decreased, and enzyme aggregation increased. Changes in protein conformation and orientation were attributed to the protein-surface and protein-protein interactions. The enzyme activity was found to decrease with the surface hydrophobicity.

The first requirement of a bioactive paper is to retain the functionality, reaction rate and selectivity of its immobilized biomolecules. The second is to provide good biomolecule stability. Bioactive paper must not only uphold the shear and temperature of the printing and roll to roll manufacturing process, but also sustain the transport and storage conditions while insuring a reasonable shelf-life. The objective of this study is to measure the potential of paper as stable support for the immobilization of enzymes required for catalytic and diagnostic applications. Alkaline phosphatase (ALP) and horseradish peroxidase (HRP) were the enzymes selected for their stability and their wide range of applications.

In the first part of the study, the thermal stability of ALP and HRP adsorbed on paper is measured and modelled. In the second, a complete enzymatic pattern is printed by ink jet printing on paper. Last, the requirements and potentials of bioactive paper for diagnostic and industrial surfaces are analysed. It is the objective of the study to engineer fully bioactive and stable enzymatic papers.

## **2. EXPERIMENTALS**

### **2.1. Materials**

The two enzymes, Horseradish peroxidase (HRP) and alkaline phosphatase (ALP, from bovine intestinal mucosa), were purchased from Aldrich and used as received. HRP and ALP were immobilized on paper to study deactivation of enzymatic papers. HRP was also used to formulate bio ink deposited on paper by inkjet printing. HRP was dissolved in 100mM sodium-phosphate buffer solution (pH 6) to a concentration of 1.0 mg/mL to print on paper. A liquid substrate system, 3,3'-Diaminobenzidine (DAB), from Aldrich, was used to identify the enzymatic activity of HRP. The biochemical reaction of HRP and DAB generates the brown stain on paper.

ALP was dissolved to a concentration of 0.1 mg/mL in 1 M diethanolamine buffer with 0.50 mM magnesium chloride and 5 M HCl to maintain pH at 9.7. Water (Millipore, 18M $\Omega$ ) was used for making all dilutions. The 5-bromo-4-chloro-3-indolyl phosphate/nitroblue tetrazolium (BCIP/NBT) liquid substrate system, purchased from Aldrich, was selected to quantify the enzymatic activity of ALP on paper. The biochemical reaction of ALP with BCIP/NBT results in a blue-purple complex; it is very stable and does not fade upon exposure to light [24].

A filter paper (Whatman #4) was chosen as paper substrate for printing and to immobilize biomolecules.

### **2.2. Methods**

#### **2.2.1. Printing HRP-enzyme on Paper**

A basic Canon inkjet printer (Pixma ip4500) and ink cartridges (CLI, Y-M-C-BK, PGBK model) were reconstructed to print the hydrophobization solution and the HRP-enzyme solution on paper. This bubble jet printer offers a resolution of 9600 $\times$ 2400 dpi and is controlled by a personal computer which supplies page-data using MS Office 2003 software.

### 2.2.2. Immobilization of Enzyme on Paper

Enzyme aqueous solutions were homogeneously applied onto paper following TAPPI standard (T 205 sp-95). Basically, circular paper samples (16 cm) were immersed into the enzymatic solution contained in a large Petri-dish. To ensure uniform enzyme concentration on paper, the samples were carefully kept horizontal while being removed from the stock solution. The well-soaked paper samples were then blotted using one set of standard blotting papers (Drink Coster Blotting, 280 GSM) to remove any extra solution. A polyethylene sheet (3M, PP2500) (d = 16 cm) was placed underneath each blotted sample. Paper and polyethylene sheet were placed into a drying ring assembled so that each sample bioactive paper-sheet is uppermost and in contact with the rubber seat of the next ring. The samples were left to dry in a dark chamber at 23°C and 50% relative humidity for 24 hours. The enzymatic paper samples were then used for further deactivation experiment and this time was set as  $t = 0$ .

To visualize the uniformity of enzyme distribution on paper, a diluted ink jet solution (cyan) was applied on the paper surface using the same procedure. Analyses of the surface profiles (Figure 1a) and histogram distribution of gray values (Figure 1b) of 5 replicates of dyed papers revealed a uniform distribution of ink on paper. The statistics of these tests are summarized in Table I.

**Table I: Concentration distribution parameters of gray values for adsorbed ink on paper**

Reading	Area (pixels)	Mean	Standard Deviation
1	87132	125.4	12.5
2	87132	122.6	12.4
3	87132	124.1	11.4
4	87132	127.3	11.6
5	87132	128.4	11.8

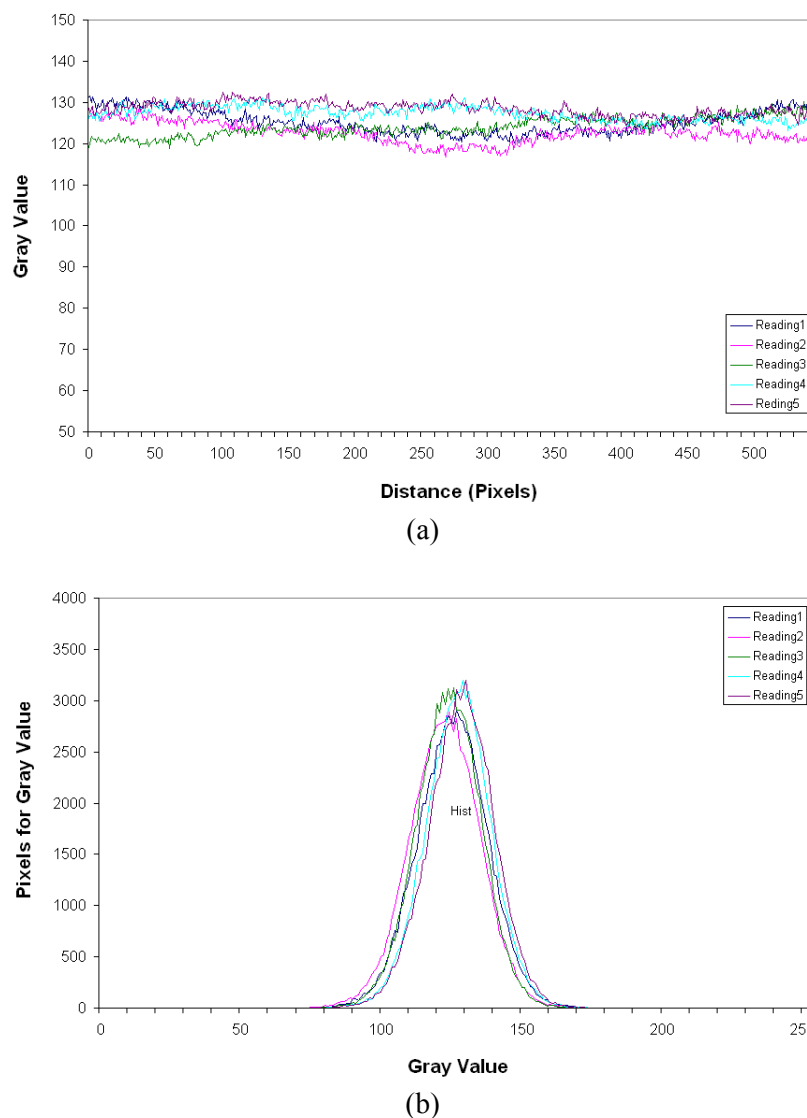


**Figure 1** Dye concentration distribution on paper measured by image analysis (ImageJ 1.41o). (a) Surface profile, (b) Histogram of gray values.

### 2.2.3. Thermal Stability of Enzymatic Papers

The enzymatic papers were cut into small samples (6 cm × 2 cm) and aged at different temperatures in an oven. The ALP and HRP enzymatic paper samples were treated at three different temperatures: 23°C, 60°C or 90°C for various periods. For 23°C, the samples were treated in a temperature and humidity controlled lab (23°C and 50% relative humidity). Two ovens (Memmert Universal Oven, Schwabach, Germany) were used to treat samples at 60°C and 90°C. A digital humidity and temperature indicator (VAISALA Humidity and Temperature Indicator, Finland; operating range: -20°C to +60°C) was used to measure the relative humidity (RH) in the ovens. At 60°C, the RH

was in range of 6.5-7.0%. For the second oven, the limiting RH reading was 5-5.5% for 65°C, which indicates even dryer condition at 90°C.

Each enzymatic paper was exposed to its specific liquid substrate after the aging treatment. This was done as follow: small droplets of freshly prepared liquid substrate were applied onto the aged enzymatic papers using a 1.0 mL syringe equipped with a stainless steel flat-tipped needle (0.21 mm outer diameter). The enzyme-substrate reaction was allowed to proceed in a dark chamber for 2 hours at 23°C and 50% relative humidity; this treatment insures complete enzymatic reaction [25-27]. From the colour intensity of enzyme-substrate reaction, the relative activity of the enzymatic paper was measured. Each measurement reported results from the average of 6 to 8 full replicates.

#### 2.2.4. Image Analysis and Activity Measurement

The colour intensity resulting from the enzyme-substrate reaction of enzymatic papers was measured at 1200 dpi using a standard scanner (EPSON PERFECTION 2450 PHOTO). The scanned images were analyzed using ImageJ software (ImageJ 1.41o). ImageJ calculates the gray values of RGB images. RGB pixels are converted to gray values using the built in formula ( $gray = (red + green + blue) / 3$ ). For any selected area, the ImageJ software calculates the weighted average gray value within the selection, which can be related to the enzymatic activity of enzymatic paper. Thus the average gray value is the sum of the gray values of all the pixels in the selection divided by the number of pixels. From the gray value analysis, the relative activity of enzymatic papers was measured. Activity corresponding to the gray value at  $t = 0$  hr was considered as 100%. The relative activity at different time intervals was measured and normalized by the activity at  $t = 0$  hr, i.e. relative activity,  $[Ea]_t / [Ea]_0 = I / I_0$ . The  $\log$  value of relative activity is defined as the residual activity,  $\log(I * 100 / I_0) = \log([Ea]_t * 100 / [Ea]_0)$ .

#### 2.2.5. Calibration Curve

Two calibration curves, one for ALP (Figure 2a) and the other for HRP (Figure 2b), were built to qualify the extent of enzymatic reaction on paper from the intensity colorimetric sample produced. The colour intensity increases non-linearly with enzyme concentration on paper. Colour results from the product of the enzyme-substrate reaction on papers using different enzyme concentrations.

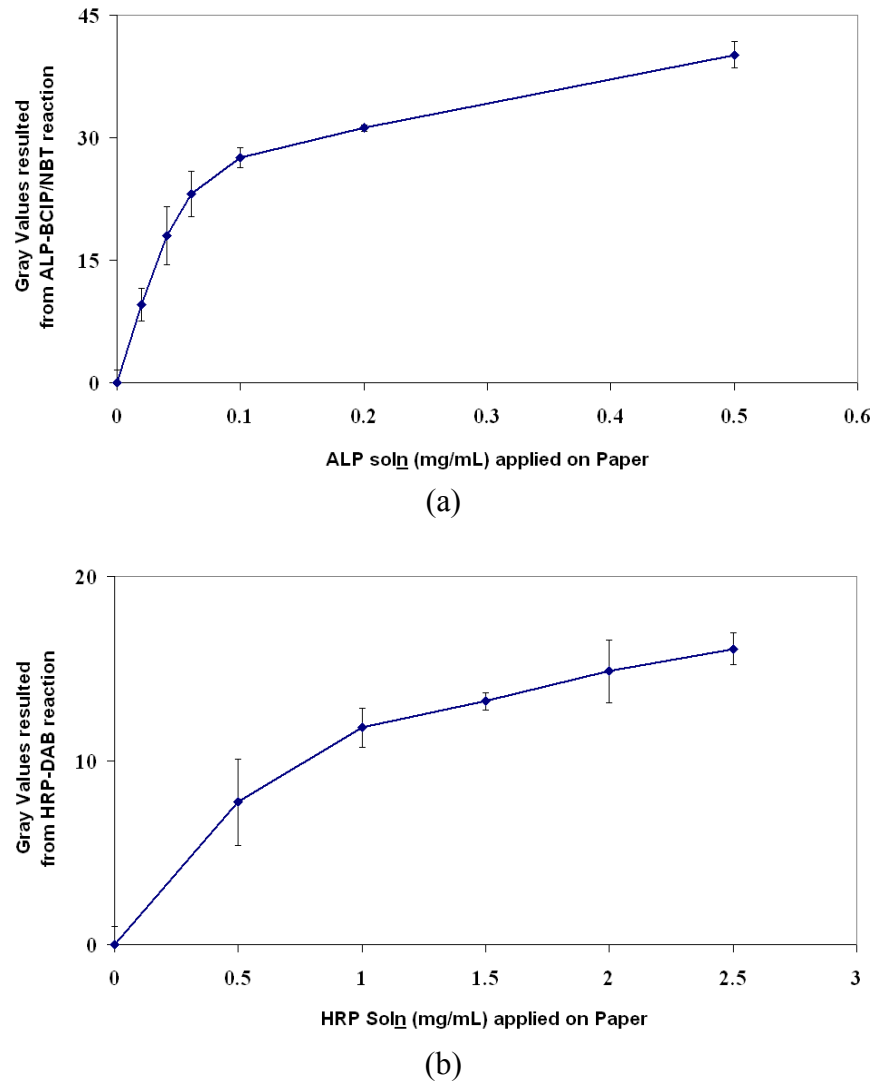


**Figure 2** Calibration curve of gray values of the enzymatic products resulting from enzyme-substrate reaction on paper. (a) ALP enzymatic paper, (b) HRP enzymatic paper.

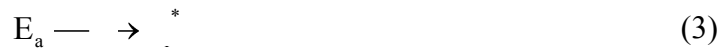
### 3. THEORY

#### 3.1. Kinetics

The kinetics of enzyme-substrate reaction can be expressed with the two-steps Michaelis-Menten model [28]:



where  $E_a$ ,  $S$ ,  $P$  and  $ES$  represent the enzyme, substrate, product and enzyme complex concentration, respectively. However, enzyme activity is known to decrease as a function of time as some enzyme molecules become inactive when removed from their native environment [28]. The simplest enzymatic deactivation model consists of an active enzyme ( $E_a$ ) molecule undergoing an irreversible structural or chemical change to some inactive form ( $E_i^*$ ) [28].



The enzyme deactivation rate ( $r_d$ ) can be written as being proportional to the active enzyme concentration:

$$r_d = - \frac{d[E_a]}{dt} = k_d [E_a] \quad (4)$$

where,  $k_d$  is the deactivation rate constant. By integrating,

$$\ln \frac{[E_a]_{t=}}{[E_a]_{t=}} = - k_d t \quad (5)$$

From which the half-life ( $t_{1/2}$ ) of enzymatic deactivation can be calculated. At time  $t_{1/2}$ , the residual enzymatic activity decreases to half of its initial value:

$$[E_a]_{t=1/2} = 0.5 [E_a]_{t=}, \text{ or:}$$

$$t_{1/2} = \frac{0.693}{k_d} \quad (6)$$

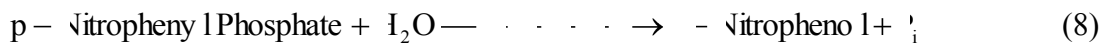
The temperature dependency of rate constant  $k_d$  can be correlated using Arrhenius equation [29]:

$$\log k_d = \log A - \frac{E}{2.303R} \left( \frac{1}{T} \right) \quad (7)$$

where, A, E, R and T represent the pre-exponential factor, activation energy of the deactivation process (kJ/mol), gas constant (8.314 J/mol·K) and absolute temperature (K), respectively. Reactions with high activation energies are rather temperature sensitive, whereas, reactions with low activation energies are relatively temperature insensitive [30].

### 3.2. Enzymes

The alkaline phosphatase (ALP) enzyme is responsible for removing phosphate groups from different substrates including proteins and alkaloids. It is most effective in an alkaline environment. An example of the reaction can be described as [31]:



where  $\text{P}_i$  = inorganic phosphate.

ALP is present in the liver, intestine, placenta, bone, and kidney of mammals [32]. It can also be obtained from *Escherichia coli*, which has similar catalytic properties, similar pH-rate profile, and forms the same phosphoserine intermediate as the intestinal enzyme [33]. The molecular weight is 89 kDa for *E. coli* ALP [34] and 126-140 kDa for bovine intestinal ALP [32-35]. ALP exists as a dimer comprising two very similar or identical subunits each containing 429 amino acids [33].

Horseradish peroxidase (HRP) is a single chain polypeptide enzyme containing four disulfide bridges. It is isolated from horseradish roots (*Amaracia rusticana*) and belongs to the ferroporphyrin group of peroxidase [36]. It has a molecular weight

of 44 kDa and is reported to be very stable [11]. HRP readily combines with hydrogen peroxide ( $H_2O_2$ ) and the resultant, HRP- $H_2O_2$  complex, can oxidize a wide variety of chromogenic hydrogen donors [36]. Most reactions catalyzed by HRP can be expressed by [37]:



where,  $AH_2$  and  $AH^*$  represent the reducing substrate and its radical product, respectively.

## 4. RESULTS

### 4.1. Thermal Stability of Enzymatic Papers

Enzymatic paper samples were aged at different temperatures for various periods. After applying the liquid substrate to the aged enzymatic paper and letting the enzyme-substrate reaction proceed to completion, the paper samples were scanned. The relative activities of enzymatic papers were calculated from the weighted mean gray value of the scan images. Figure 3 and 4 show the colorimetric evolution of the two types of enzymatic paper aged at different temperatures as a function of time. Pictures of ALP enzymatic papers heated at 60°C and 90°C for periods up to 24 hrs are shown in Figure 3. Figure 4 illustrates the effect of aging HRP enzymatic papers up to 4 days at room temperature on their bioactivity. Paper yellowing is becoming visible for papers treated at the higher temperature and longer periods ( $\geq 4$  hr).

The effect of aging temperature and time on the relative activity of bioactive enzymatic papers is illustrated in Figure 5. The enzymatic activity quickly fell within the initial hours of thermal treatment and then gradually decreased at a slower rate. The deactivation of enzymatic papers is faster at the higher temperatures. ALP enzymatic papers nicely retain their activity at 23°C and exhibit only a moderate loss of activity when exposed at 60°C (Figure 5a). For HRP papers, the enzyme activity strongly decreased at 90°C. For lower temperature (23°C), the HRP enzymatic activity quickly fell within the first hours of thermal treatment and gradually decreased at a slower rate thereafter.

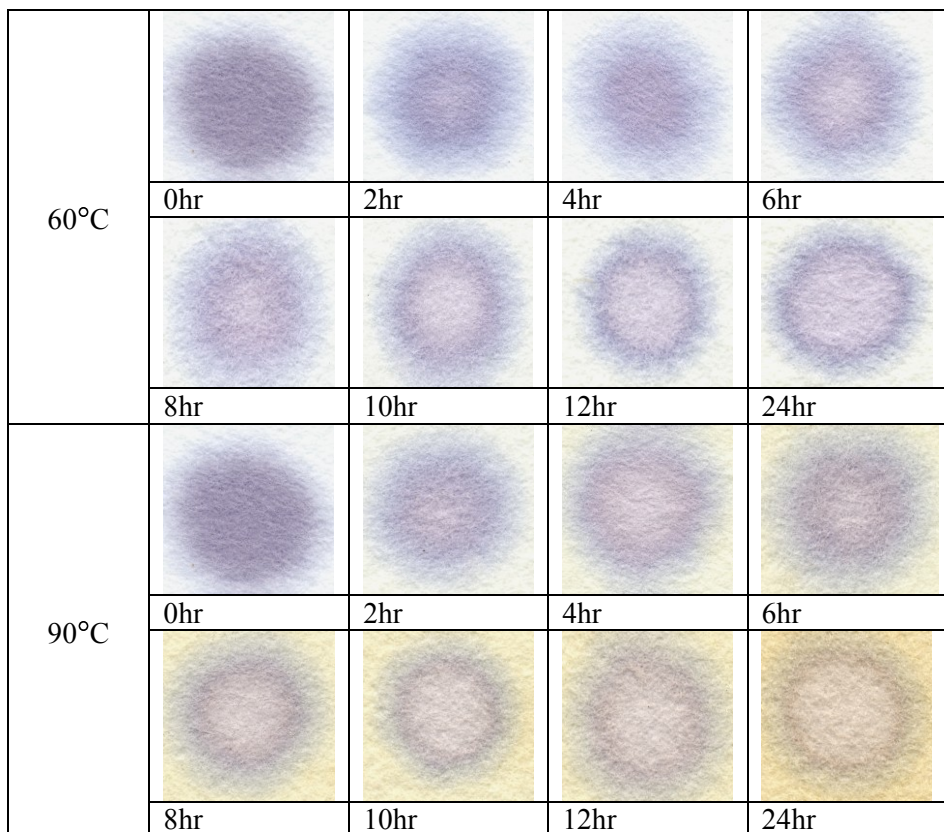


**Figure 3:** Aging of ALP-enzymatic paper treated at 60°C and 90°C for various periods. The blue purple colour reveals the enzyme (ALP) - substrates (BCIP/NBT) reaction.

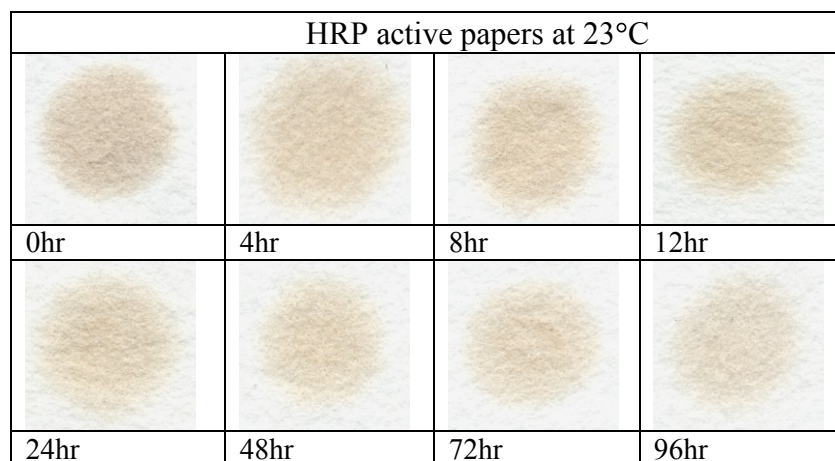


**Figure 4:** Aging of HRP-enzymatic paper treated at 23°C for various periods. The brownish colour reveals the enzyme (HRP) - substrates (DAB) reaction.

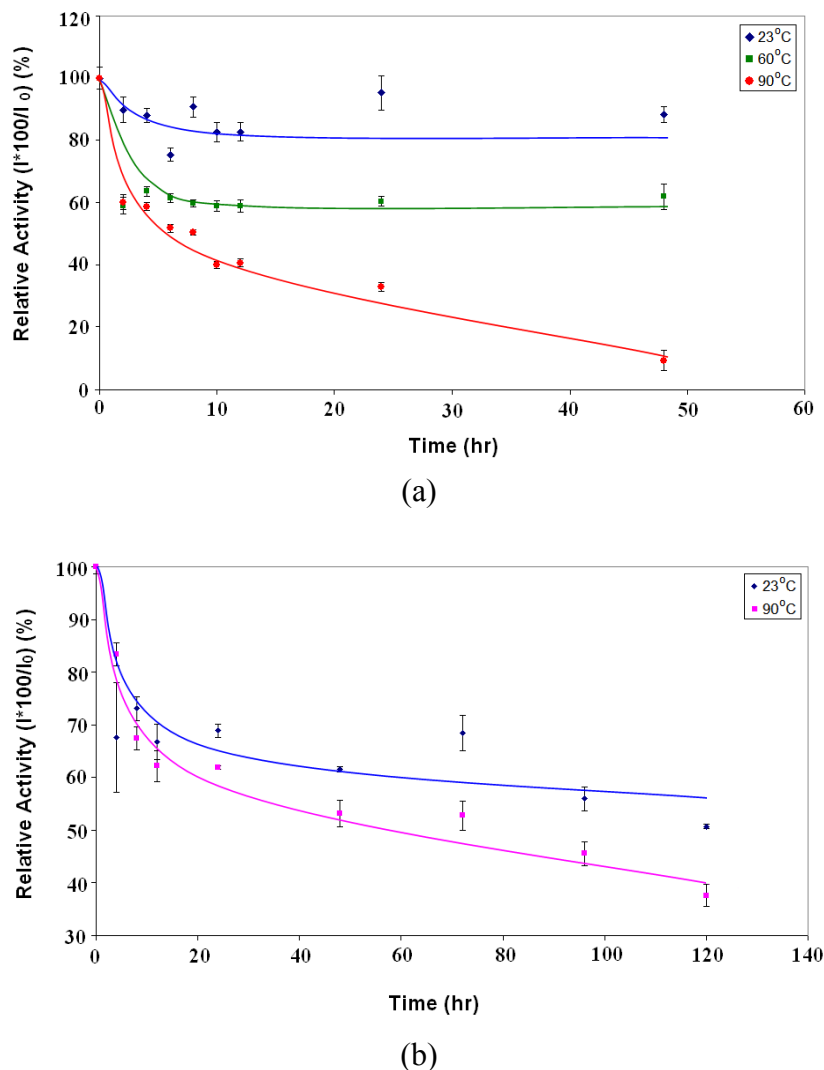


**Figure 5:** Effect of time and temperature on the activity of enzymatic paper: (a) ALP paper, (b) HRP paper; ( $I_0$  = gray value at 0 hr and  $I$  = gray value at 't' hr).

## 4.2. Bio-Printing

The HRP enzyme solution was ink jet printed on paper. The enzymatic paper was exposed, under standard conditions (23°C, 50% relative humidity), to a solution containing its specific liquid substrate 3,3'-Diaminobenzidine (DAB). The enzyme-substrate reaction yielded a brownish colour. The colour intensity was proportional to the concentration of the product resulting from the enzymatic activity. Figure 6 is a picture of our research group obtained by inkjet printing the HRP enzyme followed by reaction with DAB. Nice concentration profiles were achieved.



**Figure 6:** APPI Surface Engineering Group photo (14.5 cm × 10.5 cm) inkjet printed using HRP enzyme ink solution onto Whatman #4 and exposed to its liquid substrate (DAB).

## 5. DISCUSSION

### 5.1. Immobilized Enzymes on Paper

Enzymes randomly adsorbed from solution on paper retained their activities and selectivity upon immobilization on paper. This means that the active sites retained their structural integrity and remained available to the substrate. This was expected because of the low molecular weight of the substrates: phosphate (Mw =95 D) for ALP and peroxide (Mw=36 D) for HRP. These small molecules can easily diffuse through the cellulosic fibres of paper. The reaction rate of these adsorbed enzymes was not measured in this study. Mass transfer limitations and potential steric hindrance due to the orientation of the immobilized enzyme deserve further attention.

### 5.2. Enzymatic Activity Measurement

The intensity of the colour complex was found to vary with the enzymatic product concentration for the range studied; simple measurement of colour intensity can therefore quantify relative enzymatic activity.

The paper substrate was initially white and its background did not contribute any gray value to the enzymatic activity measurement. After prolonged exposure to high

temperatures, paper can turn yellow, which adds an extra gray value to the image analysis intensity measurement. This is especially catalysed by the alkaline conditions required for the ALP enzyme. To normalize the yellowing of paper from its enzymatic activity, the gray value of the paper control was measured and subtracted from the gray value of enzyme-substrate paper.

### **5.3. Deactivation of Enzymes Adsorbed on Paper**

Protein and enzyme are known to denature and become deactivated once removed from their biological surroundings and exposed to perturbations such as temperature, mechanical forces, radiation, chemicals and transition metals [28]. It is of interest to quantify the effect of enzyme immobilization on paper on its stability.

Yang and Kim [27] quantified the aging of ALP enzyme in aqueous medium; at 50°C the activity of ALP reduced to around 10% of its initial rate within 30 mins (Figure 7). Chang et al. [25] and Machado & Saraiva [26] measured the aging of HRP enzyme in aqueous medium at different temperatures. They reported that in water the activity of HRP reduced to around 5% of its initial rate within 30 mins at 90<sup>0</sup>C (Figure 8) [25]. The increased stability of the HRP and ALP enzymes adsorbed on paper is not exclusive to paper as substrate; Pelton et al. also reported that the stability of HRP immobilized in porous silica nanoparticle increases by over an order of magnitude compared to the molecule in solution [38]. OH containing molecules, such as alcohol, were also reported to stabilize HRP in solution [16, 25].

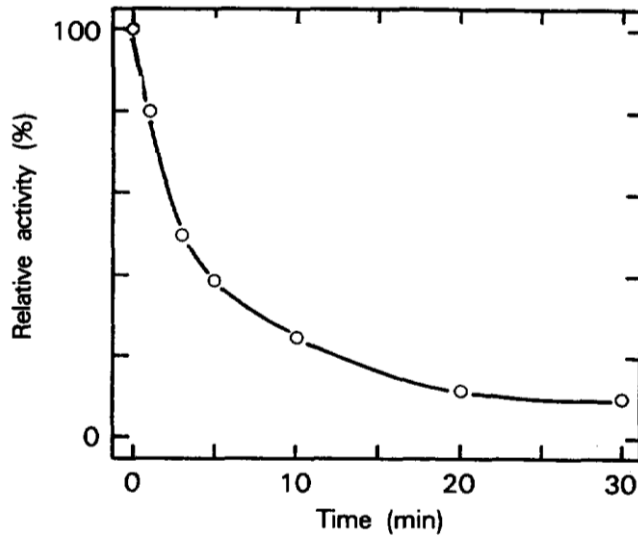


**Figure 7:** Relative activity curve of alkaline phosphatase (ALP) heated at 50°C in a buffer solution for various periods [27].

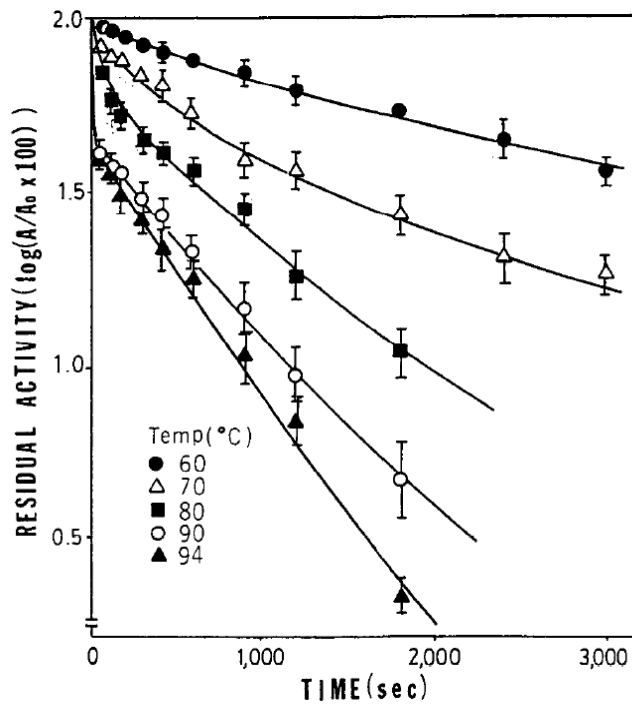


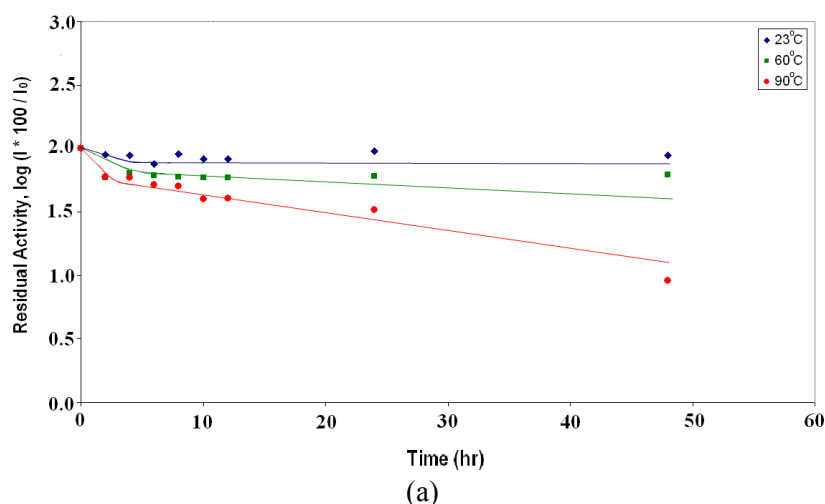
**Figure 8:** Residual activity of peroxidase in 0.05 M phosphate buffer (pH 7.0,  $A_0$ : initial activity,  $A$ : residual activity) [25] (with permission).

Heat deactivates and denatures enzymes by modifying their conformation due to increased thermal movement and decreased solvent stabilization [28, 39]. Proteins can also aggregate when heated which can restrict accessibility of their active sites. We

believe that immobilization of enzyme on paper prevents protein aggregation and retards the conformation disorder by stabilizing the secondary and tertiary structures of enzyme through the establishment of a network of hydrogen bonds protein-cellulose. The effect of surface chemistry and morphology on enzyme stability deserves further investigation.

#### 5.4. Deactivation Kinetics of Enzymatic Paper

In its simplest form, enzyme deactivation can follow a first order kinetics with respect to enzyme concentration (Eqn. (5)). Enzyme activity plotted on a logarithmic scale is expected to vary linearly with time. That was not the case for enzymes immobilized on paper (Figure 9), where two first order kinetic regimes were observed (Table II). Bailey and Ollis [28] also reported that the decay of enzyme activity with time does not always follow the first-order model; kinetics with two distinct rates have been reported. Machado and Saravia [26] also described that enzymatic deactivation pattern in aqueous medium comprised two distinct first-order phases (semi-logarithmic plot of the activity vs. time). Two sequential first order reactions might be an indication of a reaction system in which different enzyme molecules denatures by two distinct reaction pathways during different time frames. Subscript 1 refers to the deactivation rate constant of the steeper region and subscript 2 describes the pseudo-plateau.



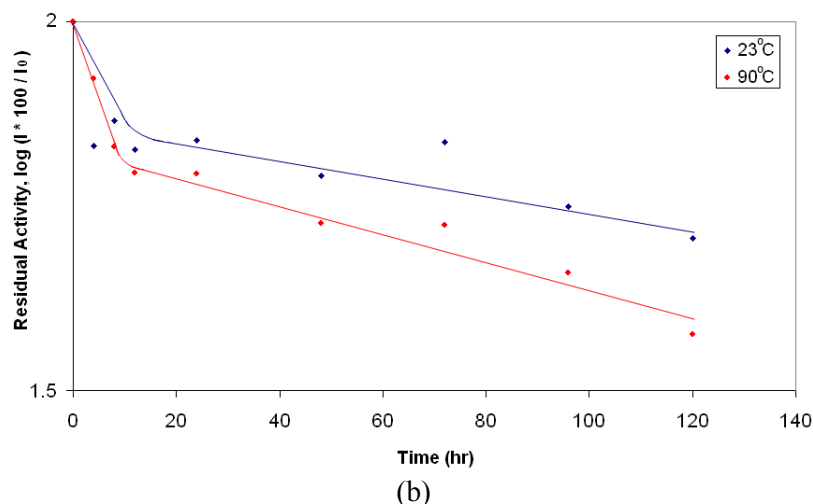


**Figure 9:** Residual activity of enzyme active papers heated at different temperatures. (a) ALP enzymatic paper, (b) HRP enzymatic paper; ( $I_0$  = gray value at 0 hr and  $I$  = gray value at 't'hr).

Replotting Figure 7 in logarithmic scale shows that the deactivation of ALP in aqueous medium projects two different linear regions (Figure 10). Figure 8 also indicates two different regions for HRP deactivation in aqueous medium.

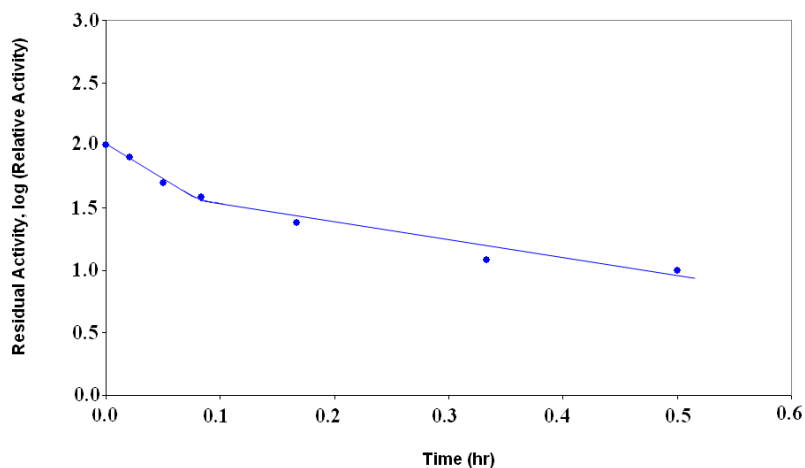


**Figure 10:** Residual activity of alkaline phosphatase heated in buffer at 50°C for various periods (calculated from [27]).

The deactivation rate constants for the two regions of ALP deactivation in water (buffer) were calculated at 50°C, to be  $12.9 \text{ hr}^{-1}$  and  $3.4 \text{ hr}^{-1}$ , respectively (Figure 10). In contrast, the deactivation rate constants of ALP on paper varied from  $229.5 \times 10^{-3} \text{ hr}^{-1}$

(phase-1, at 90°C) to  $1.3 \times 10^{-3} \text{ hr}^{-1}$  (phase-2, at 23°C), which are 2-3 orders of magnitude smaller than in water. The activation energies of ALP deactivation process on paper surface were found to be 16.74 kJ/mol for phase-1 and 42.09 kJ/mol for phase-2, respectively (Table II).

Machado and Saraiva [26] reported that at 85°C the deactivation rate constants for both phases of HRP deactivation in solution were  $48 \text{ h}^{-1}$  and  $2.52 \text{ h}^{-1}$ , respectively. Whereas, at 90°C, the deactivation rate constants of HRP on paper varied from  $92 \times 10^{-3} \text{ hr}^{-1}$  to  $4 \times 10^{-3} \text{ hr}^{-1}$ , respectively for phase-1 and 2 (Figure 9, Table II), which are 2-3 orders of magnitude smaller than that in aqueous medium.

Fadiloglu et al [40] reported the activation energy of ALP deactivation in buffer is 97.2 kJ/mol. The activation energies for HRP deactivation in buffer found by Machado and Saraiva [26] were 177 kJ/mol for phase-1 and 146 kJ/mol for phase-2. The activation energy (E) for the denaturation of enzymatic papers was calculated with the Arrhenius plot (Figure 11). 'E' of enzyme deactivation on paper is much smaller than in buffer: 2-5 times smaller for ALP and 30-35 times smaller for HRP (Figure 12, Table II). This indicates that enzyme deactivation in solution is more temperature sensitive than that on paper.

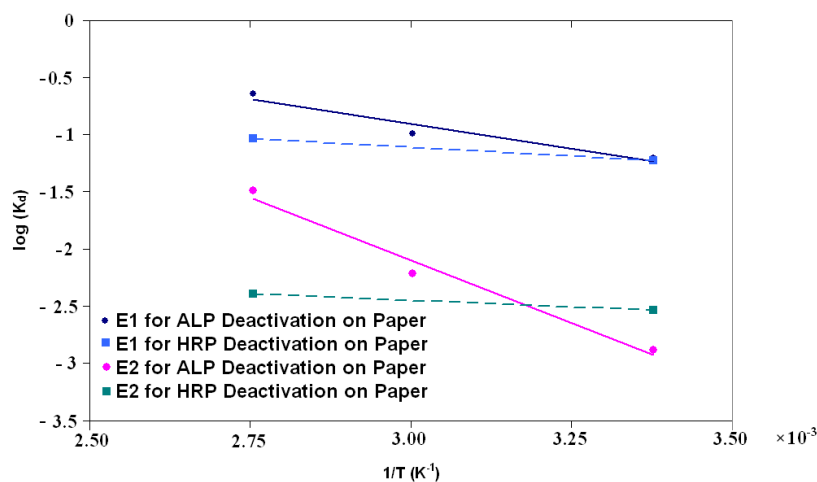


**Figure 11:** Arrhenius plot for the thermal deactivation of bioactive enzymatic papers.

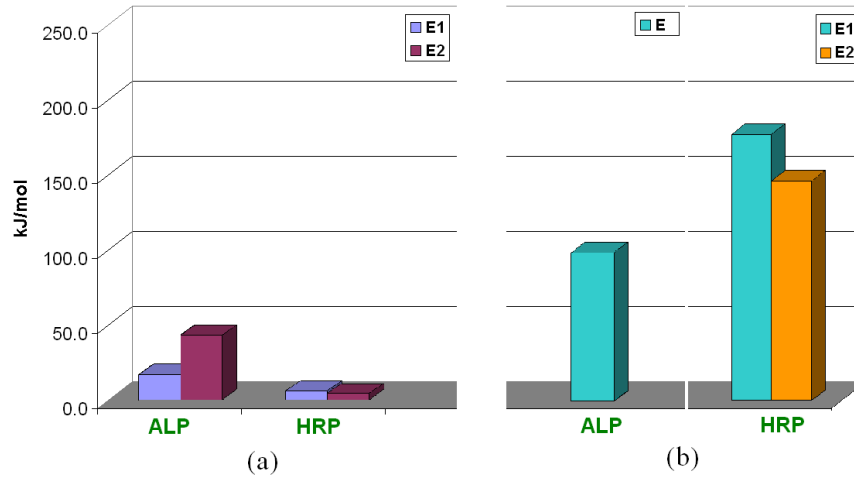


**Figure 12:** Activation energy of enzymatic deactivation: (a) Enzymes adsorbed on paper, (b) Enzymes in buffer solution [26, 40]; (E<sub>1</sub> and E<sub>2</sub> are the activation energies of enzyme deactivation for phase-1 and 2, respectively).

**Table II: Deactivation rate constants for bioactive enzymatic papers**

		ALP active paper			HRP active paper		
Temperature	k <sub>d1</sub> (hr <sup>-1</sup> )	k <sub>d2</sub> (hr <sup>-1</sup> )	t <sub>1/2</sub> (hr)	k <sub>d1</sub> (hr <sup>-1</sup> )	k <sub>d2</sub> (hr <sup>-1</sup> )	t <sub>1/2</sub> (hr)	
23°C	62.8 × 10 <sup>-3</sup>	1.3 × 10 <sup>-3</sup>	533	59.8 × 10 <sup>-3</sup>	2.9 × 10 <sup>-3</sup>	239	
60°C	102.1 × 10 <sup>-3</sup>	6.05 × 10 <sup>-3</sup>	114.5				
90°C	229.5 × 10 <sup>-3</sup>	32.2 × 10 <sup>-3</sup>	21.5	92 × 10 <sup>-3</sup>	4 × 10 <sup>-3</sup>	173	

Activation energy of enzyme deactivation, E

Environment	E <sub>1</sub> (kJ/mol)	E <sub>2</sub> (kJ/mol)	E <sub>1</sub> (kJ/mol)	E <sub>2</sub> (kJ/mol)
on paper	16.74	42.09	5.74 <sup>§</sup>	4.29 <sup>§</sup>
in buffer [28, 41]	E (kJ/mol)		E <sub>1</sub> (KJ/mol)	E <sub>2</sub> (KJ/mol)
	97.2 ± 7.2		177	146

<sup>§</sup> values are calculated from the slope of two points

### 5.5. Bioactive Enzymatic Papers

The deactivation half-life (t<sub>1/2</sub>) of enzymatic papers can be calculated from the corresponding deactivation rate constants (Eqn. (6)). For both enzymatic papers, the phase-1 ended within a few hours (2-12hrs) and half-life is considered as a constant

negligible compared to phase-2. Phase-2 is more stable; its half-life is rather significant and dominates the process. As an approximation, we therefore neglect phase-1 and assume that thermal deactivation is solely described by phase-2. ALP enzymatic paper had a half-life of 533 hrs, 114.5 hrs and 21.5 hrs, at 23°C, 60°C and 90°C, respectively. HRP enzymatic papers half-lives are 239 hrs at 23°C and 173 hrs at 90°C. From the model, we calculate the deactivation rate constant ( $k_d$ ) and the half-life of ALP enzymatic paper at 0°C, to be  $0.24 \times 10^{-3} \text{ hr}^{-1}$  and 2932 hrs, respectively. This means that ALP enzymatic paper remains bioactive 22 days at room temperature or 4 months refrigerated. After 14 days at 23°C, the kinetic model predicts the ALP enzymatic paper to retain 65% of its initial activity; 63% was measured experimentally. This confirms the validity of the model.

## 6. CONCLUSION

The activity and thermal stability of two enzymatic papers were quantified using a colorimetric technique measuring the colour intensity of the product complex. Enzymes such as Alkaline phosphatase (ALP) and horseradish peroxidase (HRP) adsorbed from solution onto paper and dried remain functional and exhibit strong activity and selectivity. Adsorption onto paper increases the enzyme thermal stability by two to three orders of magnitude compared to the enzyme in solution. As an example, ALP enzymatic paper retained 60% of its initial activity after 48 hours at 60°C; this compares to less than 20% activity after 30 minutes at 50°C for ALP enzyme in its buffer. The thermal degradation of ALP and HRP adsorbed enzymes follows two sequential first order reactions, this might indicate two distinct enzyme degradation reactions having different time frames. From the Arrhenius plot, the energies of enzyme deactivation on paper were much smaller than in solution. This simply means that enzyme deactivation on paper is much less temperature sensitive than in solution. From the model, we calculated that ALP enzymatic paper remains bioactive for 22 days if stored at room temperature and 4 months if refrigerated.

A complex pattern of HRP-enzyme was printed on paper by modifying a common thermal inkjet printer. Enzyme sustained the printing thermal and shear stress and remained bioactive. This demonstrates that bioactive paper has exceptional potential for low cost, high flexibility diagnostic and industrial application.

## ACKNOWLEDGMENT

Many thanks to Dr. Nathan Cowieson for discussion and Monash University for postgraduate scholarships (MSK, XL).

## REFERENCES

- [1] M.S. Khan, L. Xu, W. Shen, G. Garnier, *Colloids and Surfaces B: Biointerfaces* (In Press).
- [2] M.S. Khan, D. Fon, X. Li, J. Tian, J. Forsythe, G. Garnier, W. Shen, *Colloids and Surfaces B: Biointerfaces* (In Press).
- [3] M.S. Khan, J. Tian, L. Xu, W. Shen, G. Garnier, *Bioactive Enzymatic Papers*, in: I'Anson, S.J. (Ed.), *Advances in Pulp and Paper Research*, Oxford 2009, The Pulp & Paper Fundamental Research Society, 2009, pp. 1149-1166.
- [4] A.W. Martinez, S.T. Phillips, E. Carrithe, S.W. Thomas III, H. Sindi, G.M. Whitesides, *Analytical Chemistry* 80 (2008) 3699-3707.
- [5] A.W. Martinez, S.T. Phillips, M.J. Butte, G.M. Whitesides, *Angewandte Chemie International Edition* 46 (2007) 1318-1320.
- [6] R. Pelton, *Bioactive Paper - A Paper Science Perspective*, in: I'Anson, S.J. (Ed.), *Advances in Pulp and Paper Research*, Oxford 2009, The Pulp & Paper Fundamental Research Society, 2009, pp. 1096-1145.
- [7] R. Pelton, *Trends in Analytical Chemistry* 28 (2009) 925-942.
- [8] S. Aikio, S. Grönqvist, L. Hakola, E. Hurme, S. Jussila, O.-V. Kaukonieni, H. Kopola, M. Käsäkoski, M. Leinonen, S. Lippo, R. Mahlberg, S. Peltonen, P. Qvintus-Leino, T. Rajamäki, A.-C. Ritschkoff, M. Smolander, J. Vartiainen, L. Viikari, M. Vilkmán, *Bioactive Paper and Fibre Products: Patent and Literature Survey*, 2006, pp. 1-84.
- [9] S.M.Z. Hossain, R.E. Luckham, A.M. Smith, J.M. Lebert, L.M. Davies, R.H. Pelton, C.D.M. Filipe, J.D. Brennan, *Analytical Chemistry* 81 (2009) 5474-5483.
- [10] X. Li, J. Tian, T. Nguyen, W. Shen, *Analytical Chemistry* 80 (2008) 9131-9134.
- [11] R. Voss, M.A. Brook, J. Thompson, Y. Chen, R.H. Pelton, J.D. Brennan, *Journal of Materials Chemistry* 17 (2007) 4854-4863.
- [12] M.S. Khan, A. Slater, S.B.M. Haniffa, G. Garnier, *Langmuir* Submitted (2009).
- [13] K.M. Holtz, E.R. Kantrowitz, *FEBS Letters* 462 (1999) 7-11.
- [14] D.B. Craig, E.A. Arriaga, J.C.Y. Wong, H. Lu, N.J. Dovichi, *Journal of The American Chemical Society* 118 (1996) 5245-5253.
- [15] J.E. Coleman, *Annual Review of Biophysics and Biomolecular Structure* 21 (1992) 441-483.
- [16] C.J.F. VanNoorden, G.N. Jonges, *Histochemical Journal* 19 (1987) 94-102.
- [17] P. Sinha, *Journal of Biochemical and Biophysical Methods* 11 (1985) 327-340.
- [18] P. Gettins, M. Metzler, J.E. Coleman, *The Journal of Biological Chemistry* 260 (1985) 2875-2883.
- [19] J. McGadey, *Histochemie* 23 (1970) 180-184.
- [20] G. Masao, JP 87-157619. Jpn Kokai Tokkyo Koho 1989.

- [21] Y. Akahori, H. Yamazaki, G. Nishio, H. Matsunaga, K. Mitsubayashi, *Chemical Sensors* 20 (2004) 468-469.
- [22] B. Chen, N. Pernodet, M.H. Rafailovich, A. Bakhtina, R.A. Gross, *Langmuir* 24 (2008) 13457-13464.
- [23] P.C. Hiemenz, R. Rajagopalan, *Principles of Colloid and Surface Chemistry*, Third Edition, Revised and Expanded, Marcel Dekker, New York, 1997, Chapter.
- [24] BCIP/NBT Liquid Substrate System, Product Information, Sigma Aldrich (web: [www.sigmaaldrich.com](http://www.sigmaaldrich.com)), 2009.
- [25] M.S. Khan, W. Shen, G. Garnier, in: Coghill, R. (Ed.), 63rd Appita Annual Conference and Exhibition, Melbourne, Australia, 19-22 April, 2009, APPITA, 2009, pp. 273-280.
- [26] J.E. Bailey, D.F. Ollis, *Biochemical Engineering Fundamentals*, 2nd ed., McGraw-Hill, New York, 1986, Chapter.
- [27] H.S. Fogler, *Elements of Chemical Reaction Engineering*, Prentice-Hall, Englewood Cliffs, New Jersey, 1986, Chapter.
- [28] O. Levenspiel, *Chemical Reaction Engineering*, 3rd ed., John Wiley & Sons, New York, USA, 1999, Chapter.
- [29] R.A. Anderson, B.L. Vallee, *Proceedings of the National Academy of Sciences of the United States of America* 72 (1975) 394-397.
- [30] M. Besman, J.E. Coleman, *The Journal of Biological Chemistry* 260 (1985) 11190-11193.
- [31] M. Fosset, D. Chappelet-Tordo, M. Lazdunski, *Biochemistry* 13 (1974) 1783-1788.
- [32] E.E. Kim, H.W. Wyckoff, *Journal of Molecular Biology* 218 (1991) 263-477.
- [33] M.F. Machado, J.M. Saraiva, *Biotechnology Letters* 27 (2005) 1233-1239.

---

# Chapter 4

---

Effect of Polymers on the  
Retention and Aging of  
Enzymatic Bioactive  
Papers

---

This page is intentionally blank

## Monash University

### Declaration for Thesis Chapter 4

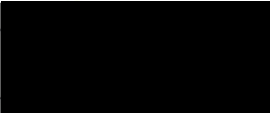
**Declaration by candidate**

In the case of Chapter 4, the nature and extent of my contribution to the work was the following:

Nature of contribution	Extent of contribution (%)
Initiation, key ideas, experimental and analysis works, development and writing up of the paper	70

The following co-authors contributed to the work. Co-authors who are students at Monash University must also indicate the extent of their contribution in percentage terms:

Name	Nature of contribution	Extent of contribution (%) for student co-authors only
Gil Garnier	Initiation, key ideas, reviewing and editing of the paper	Supervisor
Sharon B. M. Haniffa	Initiation and experimental work	10
Alison Slater	Initiation and experimental work	10

<b>Candidate's Signature</b>		<b>Date</b> 17/12/09
------------------------------	--	-------------------------

**Declaration by co-authors**

The undersigned hereby certify that:

- (1) the above declaration correctly reflects the nature and extent of the candidate's contribution to this work, and the nature of the contribution of each of the co-authors.
- (2) they meet the criteria for authorship in that they have participated in the conception, execution, or interpretation, of at least that part of the publication in their field of expertise;
- (3) they take public responsibility for their part of the publication, except for the responsible author who accepts overall responsibility for the publication;
- (4) there are no other authors of the publication according to these criteria;
- (5) potential conflicts of interest have been disclosed to (a) granting bodies, (b) the editor or publisher of journals or other publications, and (c) the head of the responsible academic unit; and
- (6) the original data are stored at the following location(s) and will be held for at least five years from the date indicated below:

<b>Location(s)</b>	Bioresource Processing Research Institute of Australia (BioPRIA), Department of Chemical Engineering, Monash University, Clayton, VIC 3800, Australia.
--------------------	--

<b>Signature 1</b>		<b>Date</b> 17/12/09
<b>Signature 2</b>	<i>undergraduate student</i>	<b>Date</b>
<b>Signature 3</b>	" " "	<b>Date</b>

# Effect of Polymers on the Retention and Aging of Enzymatic Bioactive Papers

Mohidus Samad Khan, Sharon B. M. Haniffa, Alison Slater and Gil Garnier\*

Bioresource Processing Research Institute of Australia (BioPRIA),  
Department of Chemical Engineering,  
Monash University, Clayton, VIC 3800, Australia.

\*Corresponding author: Gil.Garnier@eng.monash.edu.au

Chapter 4	93
Effect of Polymers on the Retention and Aging of Enzymatic Bioactive Papers	93
Abstract	96
1. Introduction	97
2. Experimentals	99
2.1. Materials	99
2.2. Methods	100
3. Theory	103
3.1. Enzymatic Deactivation Kinetics	103
4. Results	104
4.1. Enzymes Adsorption and Retention	104
4.2. Thermal Stability and Aging of Enzymatic Papers	106
5. Discussion	109
5.1. Enzyme Adsorption on Polymer Papers	109
5.2. Enzymatic Activity Measurement	110
5.3. Enzyme Retention	110
5.4. Deactivation Kinetics of Enzymatic Paper	111
5.5. Bioactive Enzymatic Papers	116
6. Conclusion	119
Acknowledgment	120
References	121

## ABSTRACT

The effect of polymer on the retention and the thermal stability of bioactive enzymatic papers was measured using a colorimetric technique quantifying the intensity of the enzyme-substrate product complex. Alkaline phosphatase (ALP) was used as model enzyme. Three water soluble polymers: a cationic polyacrylamide (CPAM), an anionic polyacrylic acid (PAA) and a neutral polyethylene oxide (PEO) were selected as retention aids. The model polymers

efficiently increased the enzyme adsorption on paper by around 50% and also prevented enzyme desorption or leaching upon rewetting of the papers. The thermal deactivation of ALP retained on paper with polymers follows two sequential first order reactions. This was also observed for ALP simply physisorbed on paper. The retention aid polymers instigated a rapid initial deactivation which significantly decreased the longevity of the enzymatic papers. This suggests some enzyme-polymer interaction probably affecting the enzyme tertiary structure. A deactivation mathematical model predicting the enzymatic paper half-life was also developed.

**Key Words:** Bioactive papers, enzyme, aging, thermal stability, deactivation kinetics, polyelectrolytes.

## **1. INTRODUCTION**

A bioactive paper can be defined as a paper based substrate supporting some biomolecules or an agent reacting with a biological system. Bioactive paper is emerging as a promising technology offering many new applications for health, environmental and industrial activities long deemed not economically feasible [1-5]. Pelton and Aikio recently provided enlightening reviews of the emerging applications and the current status of this technology [6-8]. Two of the fundamental aspects of bioactive papers are their interaction with fluids, and their low cost. The former aspect has lead to the development of microfluidic bioactive papers pioneered by Whitesides and further refined by other groups [4, 5, 9-11]. Paper allows, through capillarity, the controlled transport of liquids and offers a substrate retaining biomolecules. As bioactive papers are used wet, the retention of their biomolecules during use is critical. The second aspect, low cost, is insured by the choice of inexpensive materials (cellulosic fibers) and efficient processes such as papermaking and printing [2, 3, 8].

Product life time is another critical requirement of bioactive papers as they must sustain the often harsh conditions of shipping and provide a reasonable shelf-life. Immobilizing enzyme on paper by simple physisorption was shown to decrease the enzyme reaction rate by two to three orders of magnitude [12], but also to increase its thermal resistance and aging performance by two to three orders of magnitude [1].

However, important desorption of the enzyme was recorded when the bioactive paper was rewetted [1].

In this study, an enzyme, Alkaline Phosphatase (ALP), was selected as model biomolecule. Enzymes are model biomolecules of choice because of their stereospecificity, wide range and availability [13-19]. Understanding the effect of adsorption on the secondary and tertiary structure of the enzyme, its functionality, stability and the selectivity of substrate recognition is critical for engineering biocatalysis. Few studies have described the immobilization of enzymes on paper. Among those are paper strips indicators for sea food freshness using two enzymes: xantine oxidase and nucleoside phosphorylase [20], and bioactive paper to monitor alcohol content in the breath using alkaline oxidase (AOD) [21]. Chen et al. investigated by AFM the effect of surface wettability on enzyme loading (candida antarctica lipase B CALB) [22]. The enzyme activity was found to decrease with the surface hydrophobicity. However, there is little fundamental understanding available on the effect of polymer retention aids on the orientation of bioactive molecules during surface immobilization and their biofunctionality.

This study investigates water soluble polymers as retention aids to immobilize and retain the enzyme on paper. Three model polymers were selected: a high molecular weight medium charged cationic polyacrylamide (CPAM), a highly charged low molecular weight anionic polyacrylic acid (PAA) and a high molecular weight neutral polyethylene oxide (PEO). The first hypothesis investigated is that the high molecular weight polymers can retain a biomolecule on a surface by bridging, should their radius of gyration be higher than the electrical double layer of the biomolecules [23]. The second hypothesis tested is that a charged polymer can adsorb the biomolecules through charge neutralization. Anionic and cationic polymers were selected in an effort to modify the enzymatic reaction rate through preferential orientation of the active site on the surface. A random orientation is expected from the neutral polymers.

This study has three objectives. The first is to analyze the effect of model polymers on the retention of immobilized enzyme during wet application. The second is to quantify the effect of polymers on the aging and stability of immobilized enzyme on paper in comparison to the free enzyme in solution. The last objective is to develop a kinetic model predicting the life time of enzymatic papers as a function of temperature. This is in an effort to model product efficiency and aging. The kinetics of enzymatic

papers and the effect of these polymers on the reaction rate of the immobilized enzymes are reported elsewhere [12].

An image analysis technique quantifying the intensity of the enzyme-substrate colour product was developed to measure the enzymatic rate on paper. Paper samples were successively immersed into a polymer solution (rinsed) and an excess solution of ALP enzyme to create a monolayer of polymer/enzyme. The enzymatic papers were aged at different temperatures for different periods, and their residual enzymatic activities were measured by depositing an excess of liquid substrate system, allowing the reaction to proceed to completion, and measuring the resulting product concentration.

## **2. EXPERIMENTALS**

### **2.1. Materials**

Alkaline phosphatase (ALP) from bovine intestinal mucosa, was purchased from Aldrich and used as received. ALP was immobilized on paper using three different water soluble polymers. A cationic polyacrylamide (CPAM) Percol 1550\* provided by BASF, Ludwigshafen, Germany, of  $M_w = 5 \times 10^6$  and medium charge density (2.1 meq/g), was used as cationic polymer. Polyacrylic acid (PAA), Aldrich,  $M_w = 2,000$  and polyethylene oxide (PEO), Aldrich,  $M_w = 4 \times 10^6$ , were used as anionic and non-ionic polymers, respectively. All the polymers were dissolved to a concentration of 1g/L. Water (Millipore, 18M $\Omega$ ) was used for making all dilutions. The pH of CPAM, PAA and PEO polymer solutions were 3.6, 2.63 and 7.70, respectively.

ALP was dissolved to a concentration of 0.5 mg/mL in 1 M diethanolamine buffer with 0.50 mM magnesium chloride and 5 M HCl to maintain pH at 9.7. The 5-bromo-4-chloro-3-indolyl phosphate/nitroblue tetrazolium (BCIP/NBT) liquid substrate system, purchased from Aldrich, was selected to quantify the enzymatic activity of ALP on paper. The biochemical reaction of ALP with BCIP/NBT results in a blue-purple complex; its intense colour can be observed visually, is very stable and does not fade upon exposure to light [24].

Whatman #4 filter paper was chosen as paper substrate to immobilize the biomolecules.

## **2.2. Methods**

### **2.2.1. Polymer on Paper**

Paper samples (diameter of 16 cm) were soaked into the polymer solutions contained in a glass tray for about 1 minute. To remove the extra polymer, the paper samples were then rinsed thoroughly in excess water for 1 minute (Figure 1). The samples were carefully kept horizontal while being removed from the polymer solutions to ensure uniform distribution on paper. This methodology aimed at depositing a consistent monolayer of polymer on paper. The polymer treated samples were immediately soaked (wet) into the enzymatic solution.

### **2.2.2. Enzyme on Paper**

Enzyme aqueous solutions were homogeneously applied onto paper following TAPPI (T 205 sp-95) standard. Paper samples ( $d = 16$  cm), with and without polymer, were immersed into the ALP enzymatic solution contained in a large Petri-dish (Figure 1). The well-soaked paper samples were then blotted using standard blotting papers (Drink Coster Blotting, 280 GSM) to remove any extra solution. A polyethylene sheet (3M, PP2500,  $d = 16$  cm) was deposited underneath each blotted sample. Paper and polyethylene sheet were placed into a drying ring assembled so that each sample is uppermost and in contact with the rubber seat of the next ring. The paper samples were kept horizontal while been removed from the stock solutions and placed into drying ring to ensure a uniform enzyme concentration on paper. The samples were left to dry in a dark chamber at 23°C and 50% relative humidity (RH), for 24 hours. The enzymatic paper samples were then used for further deactivation experiment and this time was defined as  $t = 0$ . Analyses of the surface profiles and histogram distribution of gray values are described elsewhere [1].

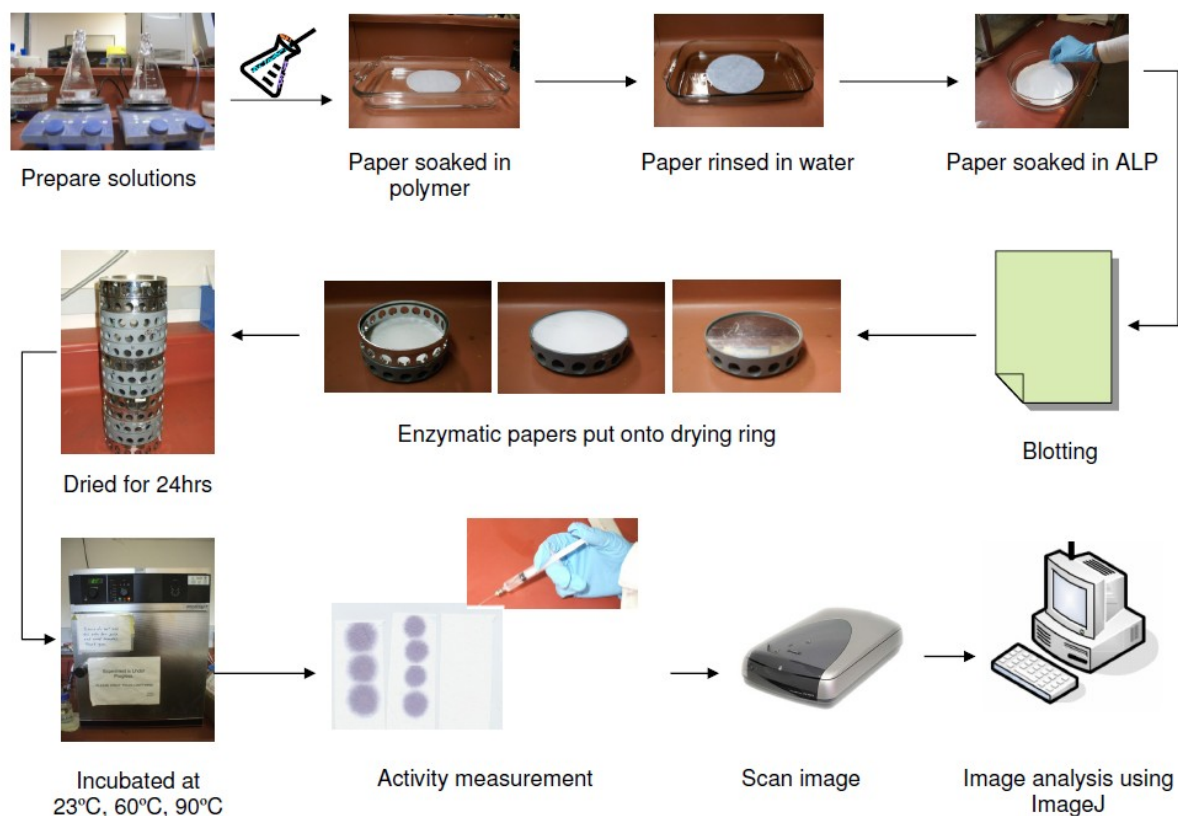


**Figure 1: Experimental system to prepare ALP enzymatic papers.**

### 2.2.3. Thermal Treatment of Enzymatic Papers

The enzymatic papers were cut into small samples (6 cm × 2 cm) and aged at different temperatures. The ALP enzymatic paper samples were treated at 23°C, 60°C or 90°C for various periods. For 23°C, the samples were treated in a temperature and humidity controlled lab (23°C and 50% RH). Two ovens (Memmert Universal Oven, Schwabach, Germany) were used to treat samples at 60°C and 90°C. A digital humidity and temperature indicator (VAISALA Humidity and Temperature Indicator, Finland; operating range: -20°C to +60°C) were used to measure the relative humidity (RH) in the ovens. At 60°C, the RH was in range of 6.5-7.0%. For the second oven, the limiting RH reading was 5-5.5% for 65°C, which indicates even dryer conditions at 90°C.

After the aging treatment, the liquid substrate was applied onto the enzymatic papers. This was done as follow: small droplets of fresh liquid substrates were applied onto the aged enzymatic papers using a 1.0 mL syringe equipped with a stainless steel flat-tipped needle (0.21 mm outer diameter). The enzyme-substrate (E-S) reaction was

allowed to proceed in a dark chamber for half an hour at standard condition, 23°C and 50% RH; this insures complete enzymatic reaction [1, 12, 25]. From the colour intensity of enzyme-substrate reaction, the relative activity of the enzymatic paper was measured. Each measurement reported results from the average of 6 to 8 full replicates.

#### 2.2.4. Activity Measurement:

The colour resulting from the E-S reaction on enzymatic papers was measured at 1200 dpi using a standard scanner (EPSON PERFECTION 2450 PHOTO) (Figure 1). The scanned images were analyzed using ImageJ software (ImageJ 1.41o). ImageJ calculates the gray values of RGB (red-green-blue) images. For any selected area, the ImageJ software calculates the weighted average gray value within the selection, which can be related to the activity of enzymatic paper. From the gray value analysis, the relative activity of enzymatic papers was measured as described elsewhere [1, 25]. Activity corresponding to the gray value at  $t = 0$  hr was considered as 100%. The relative activity at different time intervals was measured and normalized by the activity at  $t = 0$  hr, i.e. relative activity,  $[Ea]_t/[Ea]_0 = I/I_0$ . The  $\log$  value of relative activity is defined as the residual activity,  $\log(I*100/I_0) = \log([Ea]_t*100/[Ea]_0)$ . The colour intensity increases with enzyme concentration on paper is described elsewhere [1].

#### 2.2.5. Leaching of Enzymatic Papers

The enzymatic paper samples deposited in a glass tray were thoroughly leached in excess water for 1 minute. The paper samples were then dried and aged at controlled condition (23°C, 50% RH). For each sample, the enzymatic activity was measured before and after performing leaching test.

### 3. THEORY

#### 3.1. Enzymatic Deactivation Kinetics

The enzyme activity decreases as a function of time when removed from its native environment. The simplest deactivation model consists of an active enzyme ( $E_a$ ) undergoing an irreversible structural or chemical change to some inactive form ( $E_i^*$ ) following a first order reaction [26]. The enzyme deactivation rate,  $r_d$ , can be expressed as:



$$r_d = - \frac{d[E_a]}{dt} = k_d [E_a] \quad (2)$$

where,  $k_d$  is the deactivation rate constant. From integration,

$$\ln \frac{[E_a]_{t_2}}{[E_a]_{t_1}} = - k_d t \quad (3)$$

The half-life ( $t_{1/2}$ ) of enzymatic deactivation becomes:

$$t_{1/2} = \frac{0.693}{k_d} \quad (4)$$

The temperature dependency of rate constant  $k_d$  can be correlated using Arrhenius equation [27]:

$$\log k_d = \log A - \frac{E}{2.303R} \left( \frac{1}{T} \right) \quad (5)$$

where, A, E, R and T represent the pre-exponential factor, activation energy of the deactivation process (kJ/mol), gas constant (8.314 J/mol·K) and absolute temperature (K), respectively.

A high activation energy implies a temperature sensitive process, whereas, a low activation energy indicates a relatively temperature insensitive reaction [28].

## **4. RESULTS**

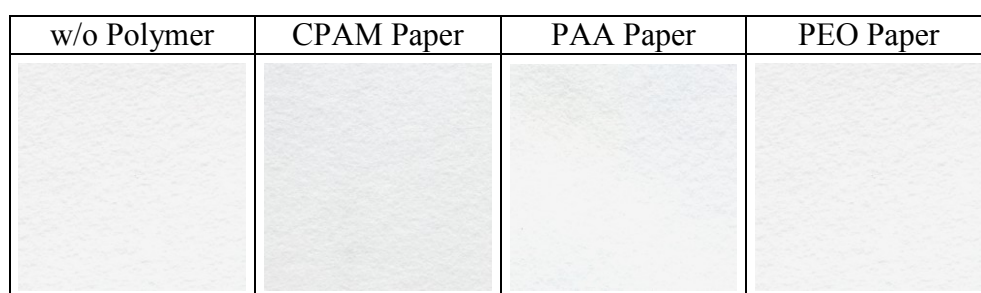
### **4.1. Enzymes Adsorption and Retention**

Polymers were investigated to improve enzyme retention on paper. Three linear polymers were selected: a high molecular weight medium charged cationic polyacrylamide (CPAM), a high charge anionic polyacrylic acid oligomer (PAA) and a high molecular weight neutral polyethylene oxide (PEO). A full monolayer of polymer was adsorbed by immersing paper in an excess polymer solution. Any unbounded polymer excess was washed off. The polymer treated papers were immediately immersed wet in an enzymatic solution. After the papers were dried ( $t=0$  hr) and aged, liquid substrate was deposited on the various enzymatic papers and the product colour intensity was quantified by image analysis. The effect of the different polymer treatments on the activity of the enzyme immobilized on paper can be visualized on Figure 2. Polymer treatment does not affect the image analysis technique (Figure 2a). The higher colour intensity observed for enzymatic papers treated with polymers indicates a higher product concentration caused by a higher initial enzyme density on paper (Figure 2b). To investigate enzyme desorption, enzymatic paper samples were leached thoroughly in excess water. A fraction of the enzyme molecules desorbed from the enzymatic paper (Figure 2c). The leached samples were dried at standard conditions ( $23^{\circ}\text{C}$ , 50% RH). The relative activity of the leached samples at  $t = 24$  hrs can be quantified from the product colour intensity. Figure 3 and Table I show that the initial enzyme activity of paper treated with a monolayer of CPAM, PAA and PEO are higher by 52%, 56% and 49%, respectively, than that of the untreated paper. However, it is not clear whether the enzyme activity is directly correlated to the initial enzyme concentration. Polymers used as retention aids increased the initial enzyme concentration on paper and their retention upon immersion in water. The enzyme retention efficiency of the three polymers investigated is similar.

**Table I: Enzyme retention on paper: before and after leaching; n = 8**

	Product Gray Value (Pixel)	
	Before Leaching, (t = 0hr)	Leached and Dry samples, (t = 24hr)
ALP on Paper	31.56 ± 2.40	18.29 ± 1.53
ALP on CPAM Paper	48.14 ± 3.19	28.84 ± 1.58
ALP on PAA Paper	49.30 ± 1.97	26.24 ± 1.18
ALP on PEO Paper	46.98 ± 2.19	19.27 ± 2.00*

\* t = 48 hrs



(a)



(b)



(c)

\* (t = 48hrs)

**Figure 2: Enzyme-substrate product formation on paper samples. Substrate effect on: (a) paper without ALP, (b) ALP active paper samples before leaching (t = 0 hr) and (c) Leached ALP enzymatic papers aged at t = 24 hrs.**

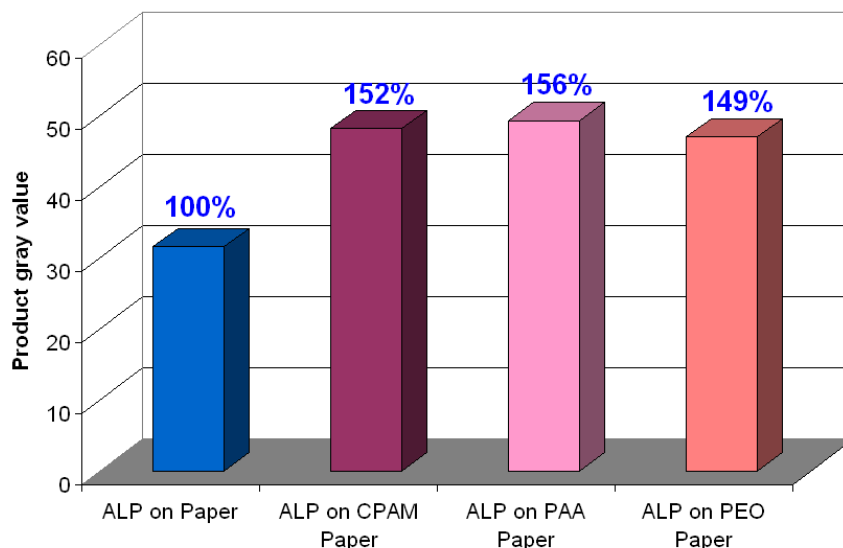
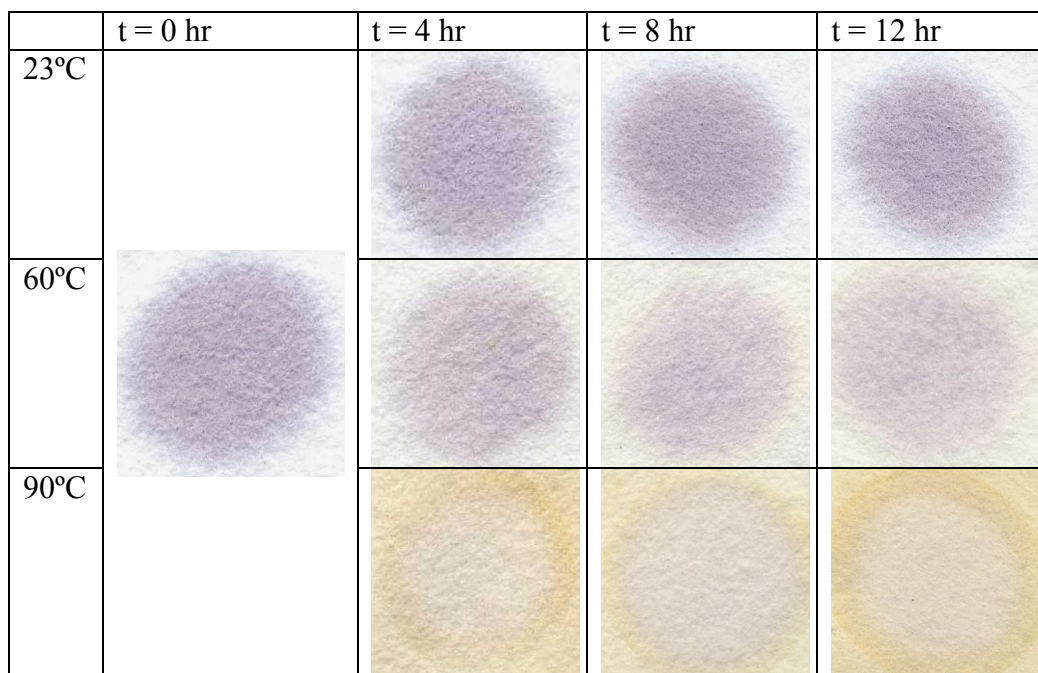


**Figure 3: Enzyme adsorption on different paper samples.**

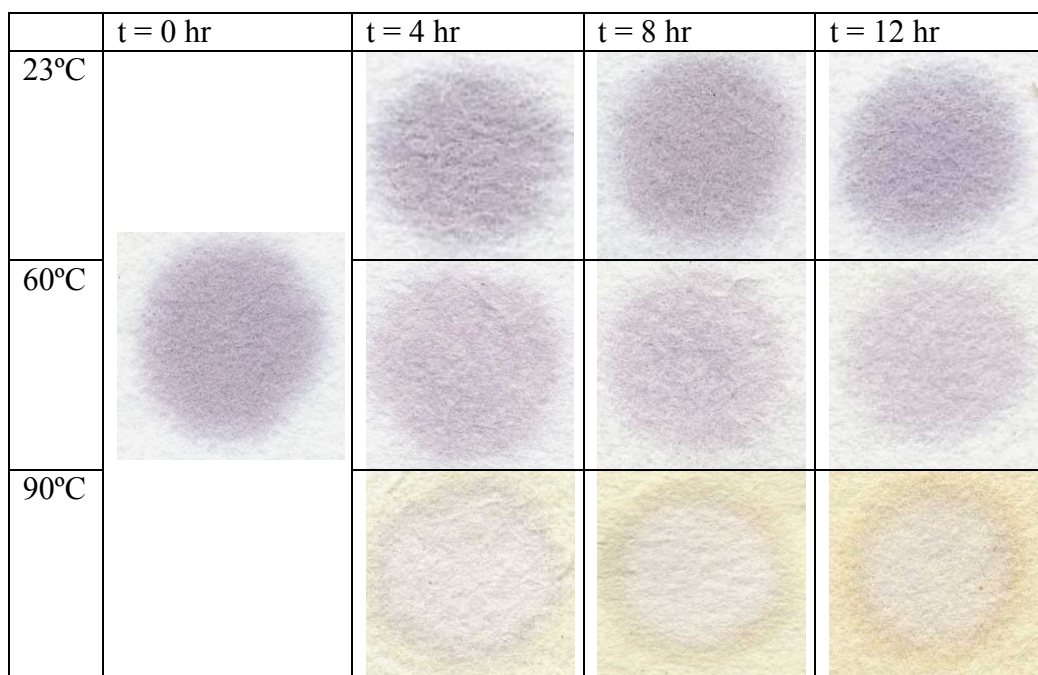
## 4.2. Thermal Stability and Aging of Enzymatic Papers

Enzymatic paper samples were aged at different temperatures for various periods. After applying the liquid substrate to the aged enzymatic paper and letting the E-S reaction proceed to completion, the paper samples were scanned. The relative activities of the different enzymatic papers were calculated from the weighted mean gray value of the images. Figure 4 shows images of ALP polymer (CPAM and PAA) papers heated at 23°C, 60°C and 90°C for periods of up to 12 hrs. The product colour intensity decreased with the aging of enzymatic paper at different temperatures. Paper yellowing becomes visible for papers treated at the higher temperature and longer periods ( $\geq 4$  hr) catalyzed by the alkalinity of the enzyme buffer (pH 9.7).

The effect of aging temperature and time on the relative activity of polymer treated enzymatic papers is illustrated and compared with that of enzyme physisorbed on paper in Figure 5. The deactivation rates of ALP enzymatic papers treated with polymers were much faster in the early hours of thermal treatment (60°C and 90°C) than that of the untreated paper. At high temperatures the ALP polymer papers lost 50% or more of their activity within the first 4 hrs (Figure 4). The deactivation rates slow down after the quick fall. By contrast, at 23°C the deactivation rates of the ALP enzymatic papers with polymers were much slower and they retained their activities for longer times (Figure 5a – c).

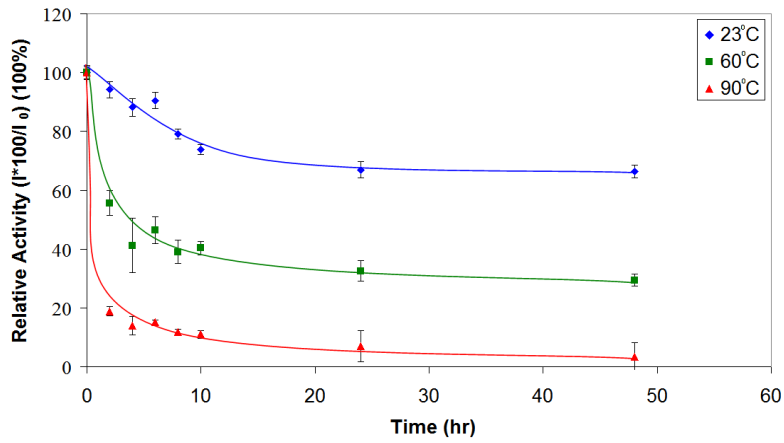


(a)

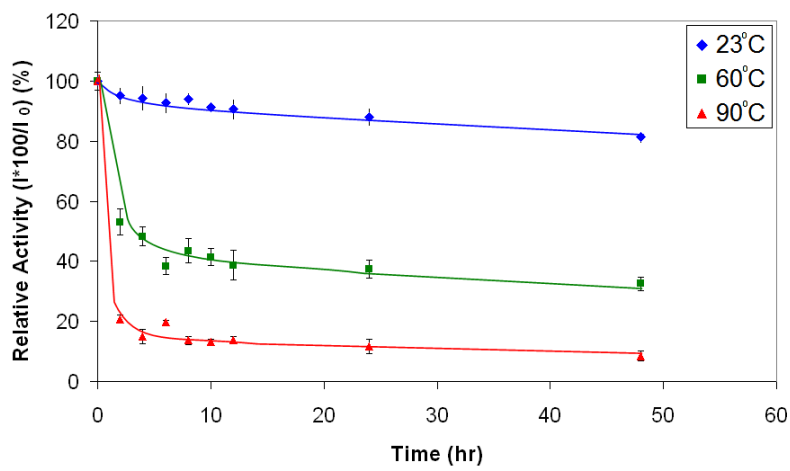


(b)

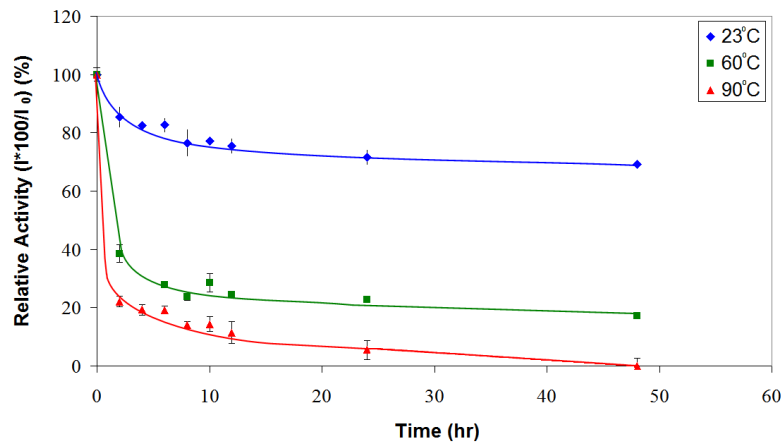
**Figure 4:** Aging of ALP enzymatic paper treated at 23°C, 60°C and 90°C for various periods: (a) ALP on CPAM paper, (b) ALP on PAA paper. The blue purple colour reveals the enzyme (ALP) - substrates (BCIP/NBT) reaction.



(a)



(b)



(c)

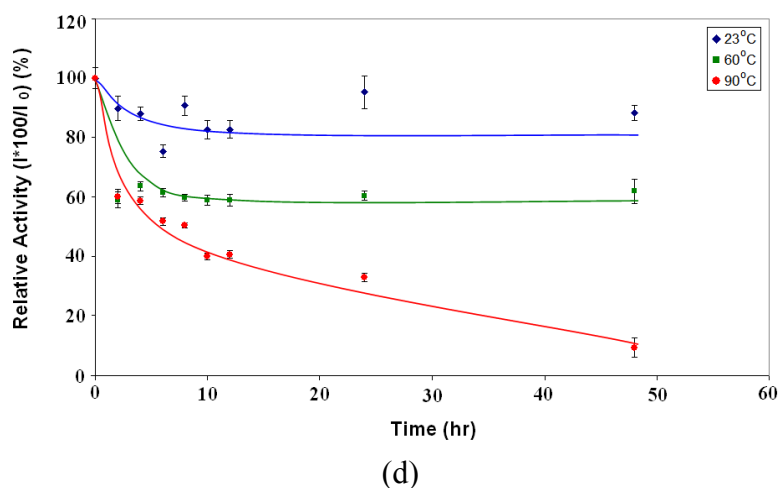


**Figure 5:** Effect of time and temperature on the activity of enzymatic papers. ALP stabilized on paper using: (a) CPAM, (b) PAA, (c) PEO, (d) without polymer [1]; ( $I_0$  = gray value at 0 hr and  $I$  = gray value at ‘t’ hr).

## 5. DISCUSSION

### 5.1. Enzyme Adsorption on Polymer Papers

Three water soluble polymers were selected as model. The cationic polyacrylamide (CPAM) is a high molecular weight linear polymer ( $M_w = 5 \times 10^6$  D) of medium charge density able to bridge colloids and to weakly interact with the ALP enzyme by electrostatic interactions. The polyacrylic acid (PAA) is a highly charged anionic oligomer ( $M_w = 2000$  D) that can retain colloids by electrostatic interaction and charge neutralization. The neutral polyethylene oxide ( $M_w = 4 \times 10^6$  D) is efficient at bridging colloids.

The purposes of the polymers were two fold. First, to increase the initial enzyme concentration on paper; second, to retain the enzyme upon rewetting of the enzymatic paper. ALP has a molecular weight ranging from 89 to 140 KD [15, 29-31]. A fully active native ALP enzyme has two active sites; each active site contains three closely spaced metal binding sites identified as A, B and C. A and B contain zinc ions and C contains magnesium ion [13, 15, 32]. Its phosphate substrate is a much smaller molecule of molecular weight of 95 D.

By soaking paper in a large volume of weak polymer solution (1 min) followed by rinsing in excess water, the formation of a full polymer monolayer is predicted. This layer is expected to adsorb in a flat train-loop-tail configuration much thinner than the hydrodynamic radius of gyration of the free polymer coil. Therefore, the polymers are expected to increase the strength of the adhesion of enzyme on paper, but not to be able to act as spacers retaining enzyme away from the surface.

## **5.2. Enzymatic Activity Measurement**

The intensity of the colour complex varies with the E-S product concentration; the relative enzymatic activity can be quantified from simple measurement of colour intensity.

Paper was initially white and did not contribute any gray value to the enzymatic activity measurement. After prolonged exposure to high temperatures, paper can turn yellow, which adds an extra gray value to the image analysis intensity measurement. This is especially catalysed by the alkaline conditions required for the ALP enzyme. To normalize the yellowing of paper from its enzymatic activity, the gray value of the paper control was measured and subtracted from the gray value of enzyme-substrate product colour formation on paper.

## **5.3. Enzyme Retention**

After 24 hrs aging, the relative activity of ALP enzymatic paper without polymer was 81%. The relative activity reduced to 58% for the leached sample aged for 24 hrs. ALP enzymatic paper without polymer lost 23% of its relative activity by enzyme leaching. Enzyme desorption was also significant for PAA and PEO treated ALP enzymatic papers (Table II). Enzyme retention was relatively higher for the leached ALP CPAM paper. The relative activities of 24 hrs aged ALP CPAM paper samples reduced from 67% to 60% due to enzyme desorption. However, the absolute amount of retained ALP for the leached polymer papers was higher than that of non-leached non-polymer papers (Table I).

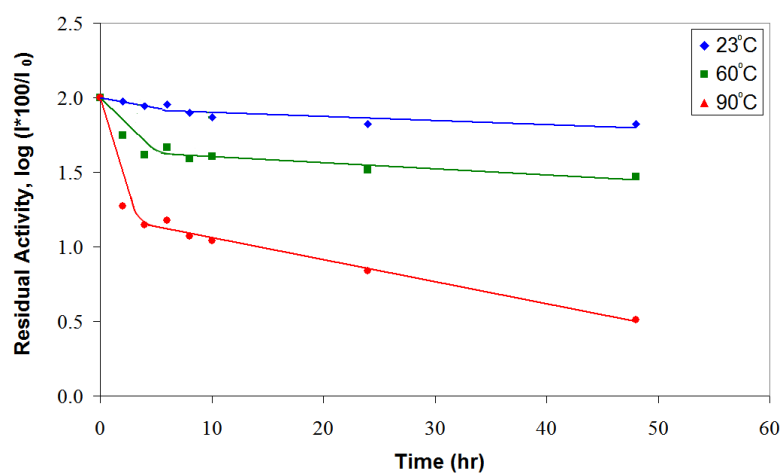
**Table II: Relative activity of ALP enzymatic papers at 23°C: with and without leaching**

	t = 0hr	Aging at t = 24hr	
		w/o leaching	with leaching
ALP on Paper	100%	81%	58%
ALP on CPAM Paper	100%	67%	60%
ALP on PAA Paper	100%	88%	53%
ALP on PEO Paper	100%	69%*	41%*

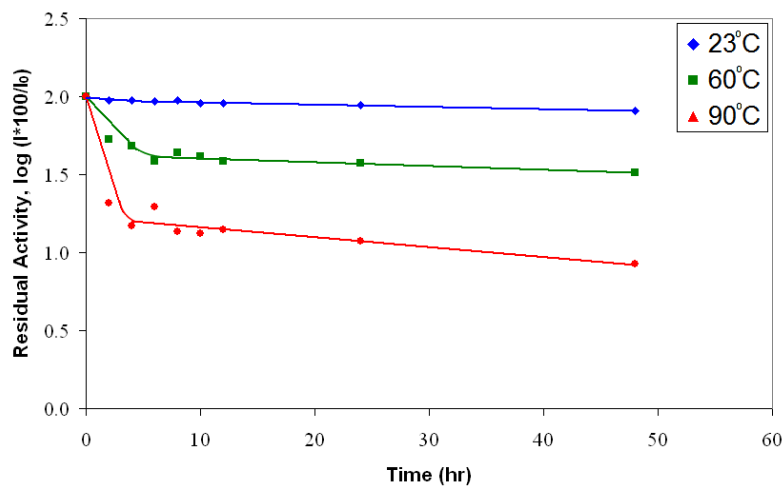
\*samples aged for t = 48 hrs

#### 5.4. Deactivation Kinetics of Enzymatic Paper

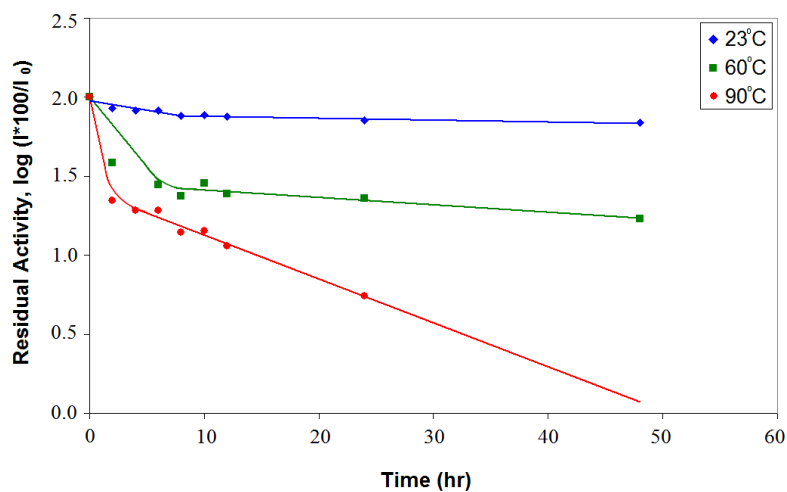
In its simplest form, enzyme deactivation can be expected to follow a first order kinetics with respect to enzyme concentration (Eq. 3). Enzyme activity plotted on a logarithmic scale will then vary linearly with time. Figure 6 presents the evolution of the residual activity on a log scale, as a function of time. The enzyme deactivation behaviour is described by two linear regimes in series: phase-1 and phase-2. In phase-1, the enzyme activity steeply drops over a short period of aging. This is followed by a slower deactivation regime which lasted at least 40 hrs. The slope of the first regime, representing the reaction constant, is a strong function of temperature.



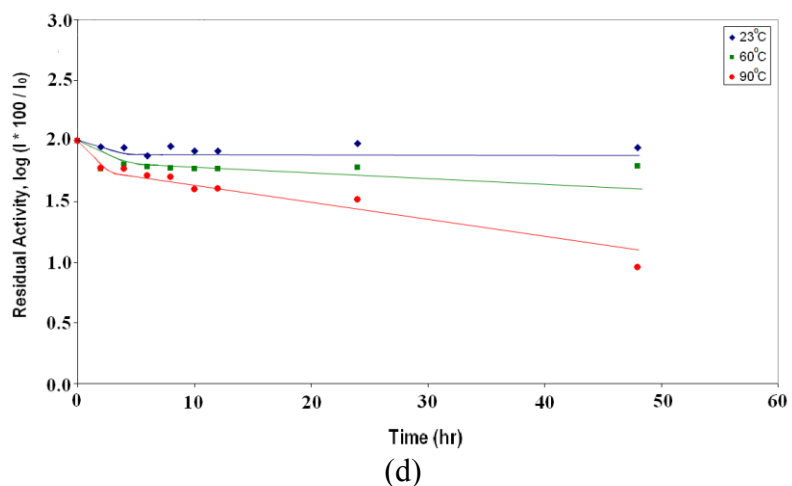
(a)



(b)



(c)



(d)

**Figure 6:** Residual activity of enzyme active papers heated at different temperatures. ALP stabilized on paper using: (a) CPAM, (b) PAA, (c) PEO, (d) without polymer [1] ( $I_0$  = gray value at 0 hr and  $I$  = gray value at 't' hr).

The duration of the phase-1 is short and varies with temperature. Lets define  $t^*$  as the inflection time defining the transition from phase-1 to phase-2 which represents the time at when enzymatic degradation slows down to phase-2. For the different enzymatic papers,  $t^*$  varied from 2.5 to 4 hours at 90°C, 4 to 6 hours at 60°C and 6 to 8 hours at 23°C (Figure 6). The variation of  $t^*$  as a function of temperature is illustrated on Figure 7. For simplicity we can consider  $t^*$  of ALP enzymatic papers as a linear function of temperature (Figure 7).

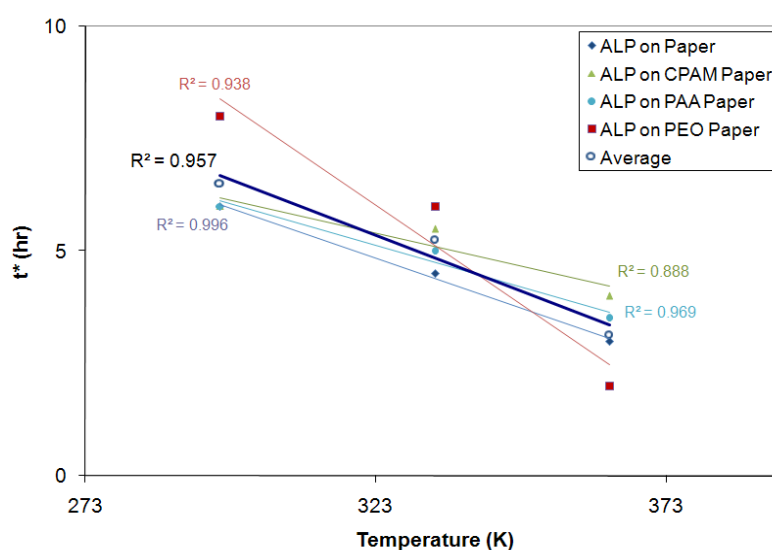


**Figure 7: Variation of  $t^*$  as a function of temperature.**

The slope of the second regime is a much weaker function of temperature. From the slopes of Figure 6, it can be appreciated that the type of polymers influences the kinetics of enzyme deactivation. As we showed previously [1], the deactivation of enzyme simply physisorbed on paper follow two first order kinetics (Figure 6). Bailey et al. [26] and Machado et al. [33] also reported that the decay of enzyme activity with time does not always follow the first-order kinetic model; kinetics with two distinct rates have been reported [26, 33]. A few explanations could account for this sequential first order kinetic deactivation. First, two different active sites on the ALP molecules could denature following two different kinetics. ALP has three different types of metal binding sites: site A and B involve Zn ions, and site C contains Mg ions. Second, the enzyme deactivation could proceed through two different mechanisms, each having a different time frame. Third, the equilibrium moisture content of the enzymatic papers

might play an important role in enzyme deactivation. The quick fall of the first deactivation regime might imply the transient moisture content of the enzymatic paper, whereas, during the second regime the deactivation might be slower at the paper equilibrium moisture content. This deserves further attention. Subscript 1 refers to the deactivation rate constant of the steeper region and subscript 2 describes the pseudo-plateau. In phase-1, at high temperature (60°C and 90°C) the enzymatic activities of ALP polymer papers dropped to 50% or less within first few hours. After the drastic initial reduction, the deactivation rate was slower in phase-2.

The rate constants for the two regions of ALP deactivation on paper calculated from Figure 6 are shown in Table III and Table IV. For phase-1, the deactivation rate constants ( $k_{d_1}$ ) of ALP enzymatic papers with polymers were higher than those without polymer at high temperatures, but lower at low temperature. The activation energy of enzymatic deactivation (E) on paper surfaces were calculated using Arrhenius plots (Eq. 5, Figure 7). The 'E<sub>1</sub>' values were 2 to 3 times higher for ALP enzymatic papers with polymers than that without (Table V, Figure 7), which indicates a higher temperature sensitivity of ALP polymer paper deactivation.

**Table III: Deactivation Rate Constants,  $k_{d_1}$  (hr<sup>-1</sup>) for ALP enzymatic papers: Phase -1**

Temp	ALP on paper	ALP on CPAM paper	ALP on PAA paper	ALP on PEO paper
23°C	$62.8 \times 10^{-3}$	$31.6 \times 10^{-3}$	$14.3 \times 10^{-3}$	$28.3 \times 10^{-3}$
60°C	$102.1 \times 10^{-3}$	$166.7 \times 10^{-3}$	$177.1 \times 10^{-3}$	$202.4 \times 10^{-3}$
90°C	$229.5 \times 10^{-3}$	$560.6 \times 10^{-3}$	$538.4 \times 10^{-3}$	$755.2 \times 10^{-3}$
0°C	$32.77 \times 10^{-3}$	$8.37 \times 10^{-3}$	$2.91 \times 10^{-3}$	$6.32 \times 10^{-3}$

**Table IV: Deactivation Rate Constants,  $k_{d_2}$  (hr<sup>-1</sup>) for ALP enzymatic papers: Phase -2**

Temp	ALP on paper	ALP on CPAM paper	ALP on PAA paper	ALP on PEO paper
23°C	$1.3 \times 10^{-3}$	$6.45 \times 10^{-3}$	$3.22 \times 10^{-3}$	$2.76 \times 10^{-3}$
60°C	$6.05 \times 10^{-3}$	$9.44 \times 10^{-3}$	$5.53 \times 10^{-3}$	$10.6 \times 10^{-3}$
90°C	$32.2 \times 10^{-3}$	$34.1 \times 10^{-3}$	$14.5 \times 10^{-3}$	$67.5 \times 10^{-3}$
0°C	$2.42 \times 10^{-4}$	$2.66 \times 10^{-3}$	$1.51 \times 10^{-3}$	$0.57 \times 10^{-3}$

In phase-2, the deactivation rate constants ( $k_{d_2}$ ) of ALP enzymatic papers exhibit a different trend than for phase-1 (Table III).  $E_2$  for phase-2 were 42.09 kJ/mol, 21.09 kJ/mol, 19.41 kJ/mol and 41.57 kJ/mol respectively for ALP paper without polymer and for CPAM, PAA and PEO ALP papers (Table V, Figure 7). The lower  $E_2$  indicates that the deactivation of ALP enzymatic papers with PEO and CPAM are less temperature sensitive.

**Table V: Activation Energy of Deactivation Process of ALP Enzymatic Papers**

	Activation energy of enzyme deactivation, E	
	$E_1$ (kJ/mol)	$E_2$ (kJ/mol)
ALP on paper	16.74	42.09
ALP on CPAM paper	38.25	21.09
ALP on PAA paper	49.00	19.41
ALP on PEO paper	43.76	41.57

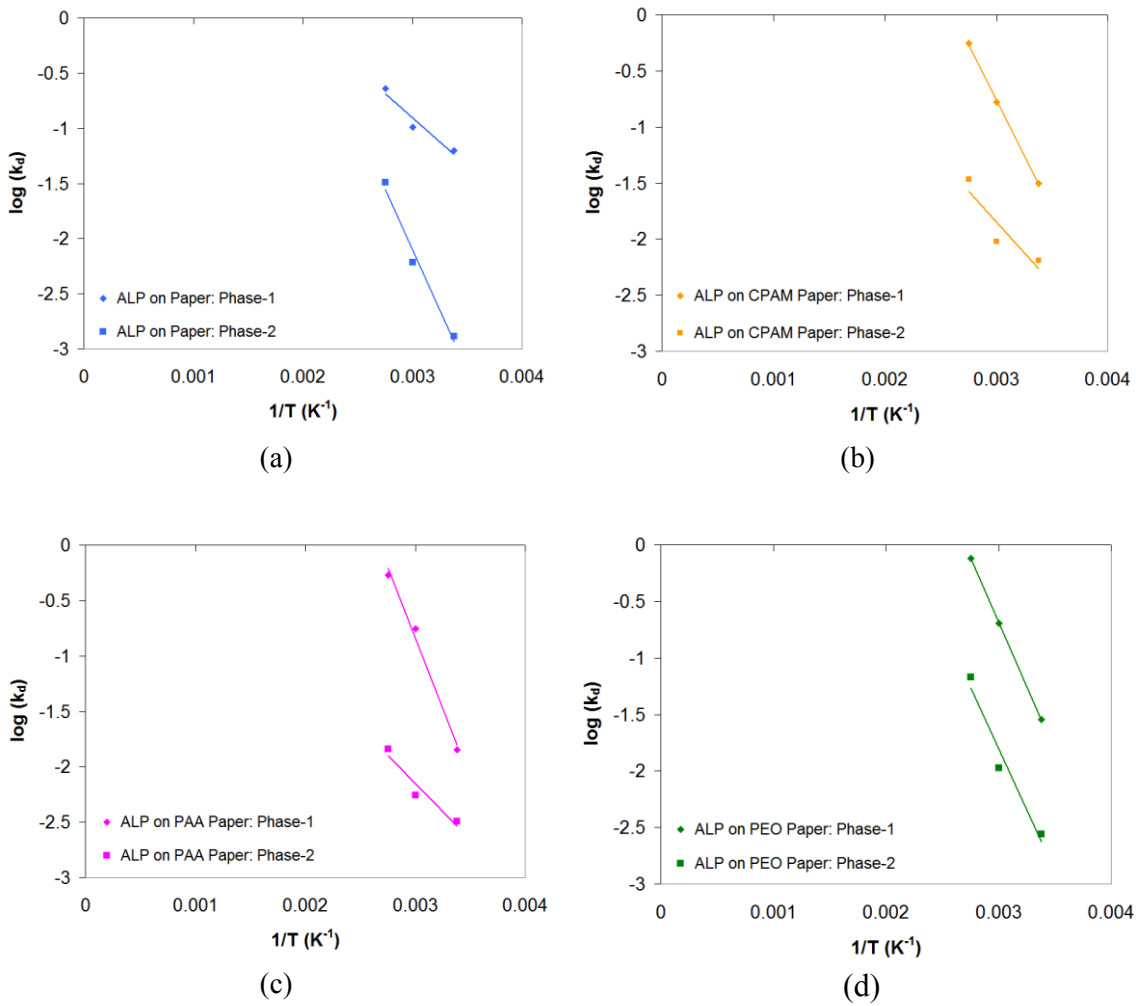


**Figure 8:** Arrhenius plot for the thermal deactivation of ALP enzymatic papers. (a) ALP enzymatic paper without polymer, (b) – (d) ALP CPAM, PAA and PEO papers.

### 5.5. Bioactive Enzymatic Papers

It is critical to predict the shelf-life of enzymatic paper and to model the affect of temperature on the enzymatic paper performance. The half-life time, defined as the time at which enzymes retain half of their original activity, is a convenient metric. The half-life ( $t_{1/2}$ ) of enzymatic papers can be modelled from the deactivation kinetics (Eq. 3 – 5). For enzymatic papers with the enzyme physisorbed, phase-1 was shown to be short and negligible compared to phase-2 [1]. However, the behaviour of ALP enzymatic papers with the enzyme retained by polymer is different, as both phases are significant and must be considered. The sharp decrease in enzymatic activity defined by phase-1 lasts

for a short time ( $t^*$ ) for the various ALP enzymatic papers treated at different temperatures (Figure 6 and 7). Let's define the relative activity corresponding to the transition time  $t^*$  as  $RA^*$ , which can be calculated from Eq. 3:

$$RA_{t=t^*}^- = RA^* = RA_{t=0}^- e^{-k_{d1}t^*} \quad (6)$$

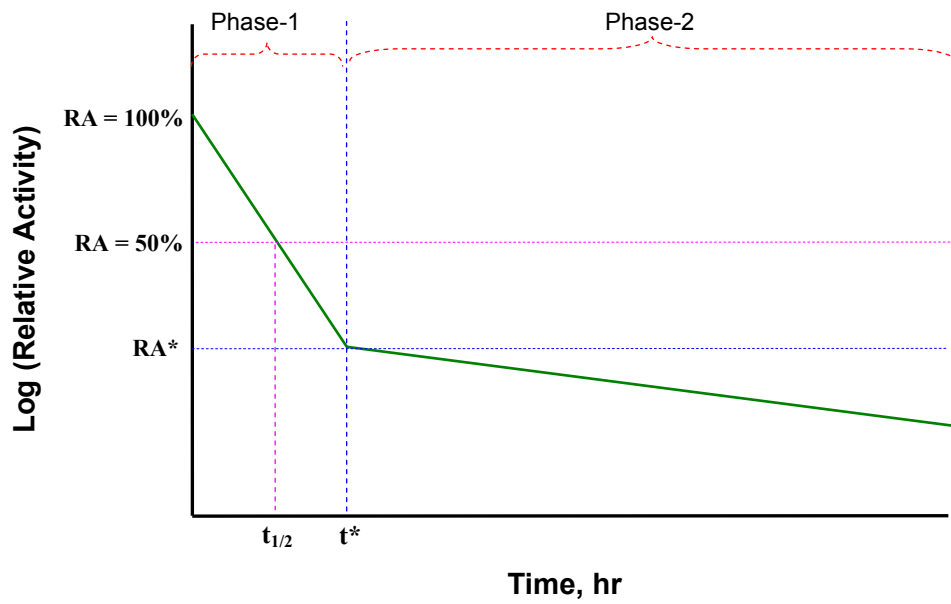
The two deactivation conditions of enzymatic papers are schematically represented in Figure 9 for a)  $RA^* \leq 50\%$  and b)  $RA^* > 50\%$ . The half-life time ( $t_{1/2}$ ) at any temperature can then be modelled with Equations 7 and 8:

$$\text{Condition-1: } RA^* \leq 50\%, \quad t_{1/2} = \frac{0.693}{k_{d1}} \quad (7)$$

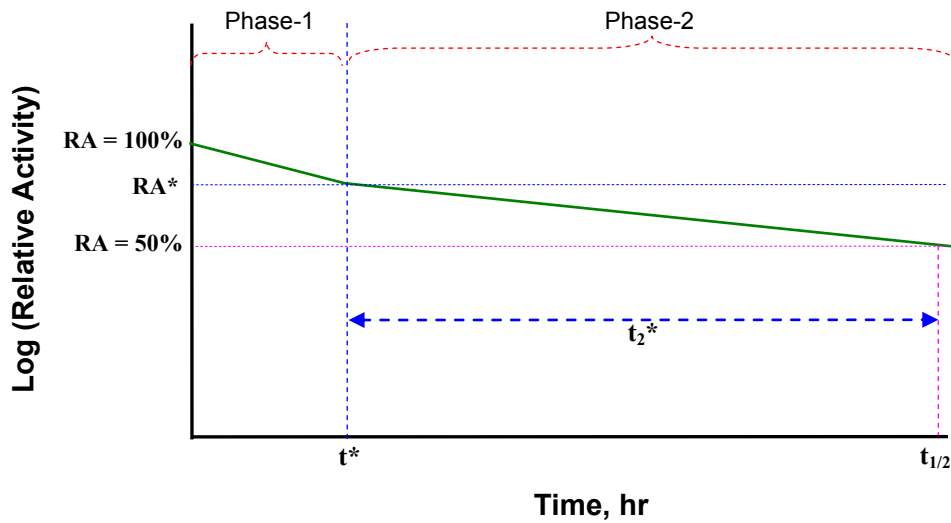
$$\text{Condition-2: } RA^* > 50\%, \quad t_{1/2} = t^* + \frac{\ln \frac{RA_{t=t^*}^-}{RA_{t=t^*}^-}}{k_{d2}} \quad (8)$$

$t^*$  and  $RA^*$  are functions of temperature and define the duration of phase-1 deactivation. If  $RA^* \leq 50\%$ , the enzymatic paper half-life time is solely defined by phase-1 (Figure 9a); if  $RA^* > 50\%$ , phase-1 and phase-2 are both required to model  $t_{1/2}$ . At high temperature the enzymatic deactivation is significant in phase-1; consequently  $RA^*$  is low and often less than 50%. In contrast, at low temperature, the enzymatic deactivation rate in phase-1 is slow and the corresponding  $RA^*$  is higher than 50%. At low temperature,  $t^*$  becomes negligible compared to  $t_{1/2}$ ;  $t_{1/2}$  can be expressed as  $t_{1/2} \approx t_{1/2}$ , which is a modified form of Eq. 8. For any specific temperature, the kinetic properties:  $k_{d1}$ ,  $k_{d2}$ ,  $t^*$ ,  $RA^*$  and the corresponding  $t_{1/2}$  can be calculated from the kinetic model.

At 0°C, the half-lives for the different ALP enzymatic papers: without polymer, with CPAM, PAA and PEO are respectively 2932 hrs, 260.2 hrs, 495.5 hrs and 1211.2 hrs (Figure 10). ALP enzymatic paper without polymer remains bioactive 4 months refrigerated which is much higher than the ALP polymer papers. The polymer treatment required to increase enzyme retention is decreasing the longevity of enzymes immobilized on paper. One possible hypothesis is that the polymer interferes with the tertiary structure of the enzyme. Another hypothesis is that the enzyme is immobilized on paper in a more rigid configuration which affects its ability of reconfiguration.



(a)



(b)

Figure 9: Schematic of half-life model of ALP enzymatic papers. (a)  $t^*$  as a function of temperature, (b)  $RA^* < 50\%$ , (c)  $RA^* > 50\%$ .

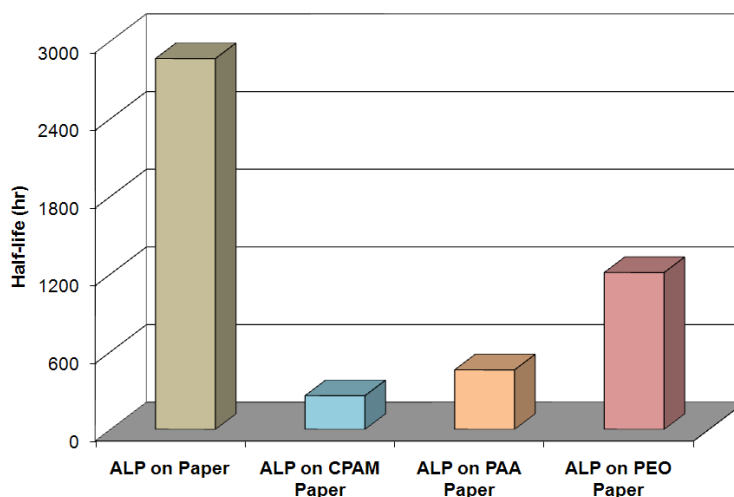


**Figure 10:** Half-lives of ALP enzymatic papers predicted at 0°C.

## 6. CONCLUSION

Bioactive papers are designed to be wetted by biofluids or solutions of interest. It is therefore critical to maximize the retention and behaviour of the biomolecules on paper. This study investigated the retention, aging and the thermal deactivation of alkaline phosphatase (ALP) immobilized on paper. Three model polymers were studied as retention aids: a high molecular weight medium charge cationic polyacrylamide (CPAM), a highly charged polyacrylic acid anionic oligomer (PAA) and a high molecular weight neutral polyethylene oxide (PEO). An enzyme (ALP) was selected as a model biomolecule because of the potential of enzymatic papers for industrial and diagnostic applications. A fresh monolayer of polymer was deposited on paper immediately prior to enzyme adsorption from solution; the paper was dried, aged and treated by depositing a liquid substrate system with a colorimetric dye detecting product formation. The enzymatic paper performance was quantified by image analysis.

All the model polymers studied were efficient at increasing the enzyme concentration on paper (by around 50%) and to prevent enzyme desorption/leaching upon rewetting of the paper. Interestingly, all polymers performed similarly in spite of their different mechanism for adhering the enzyme on paper. However, the type of polymers affects the thermal stability and the aging of ALP enzyme on paper. Thermal deactivation of ALP bridged with polymers on paper follows two sequential first order

reactions. This was also observed for ALP simply physisorbed on paper. Two explanations are favoured: either the enzyme thermal reaction follows two sequential reactions, or the three different metal binding sites forming the two active sites of the enzyme have two different thermal degradation kinetics. However, when polymers are used as enzyme retention aid, the rapid initial deactivation becomes predominant, while it was negligible for the enzyme simply physisorbed on paper. As a result, the thermal stability significantly decreases. PAA affects enzyme stability the least; CPAM and PEO strongly decreased immobilized enzyme stability, especially at high temperature. This suggests some interaction between the polymer and ALP probably affecting the tertiary structure of the enzyme. A mathematical model predicting the enzymatic paper's half-life time was developed.

## **ACKNOWLEDGMENT**

Many thanks to R. Lee for useful discussion, and to Monash University for postgraduate scholarships (MSK).

## REFERENCES

- [1] M.S. Khan, L. Xu, W. Shen, G. Garnier, *Colloids and Surfaces B: Biointerfaces* (In Press).
- [2] M.S. Khan, D. Fon, X. Li, J. Tian, J. Forsythe, G. Garnier, W. Shen, *Colloids and Surfaces B: Biointerfaces* (In Press).
- [3] M.S. Khan, J. Tian, L. Xu, W. Shen, G. Garnier, *Bioactive Enzymatic Papers*, in: I'Anson, S.J. (Ed.), *Advances in Pulp and Paper Research*, Oxford 2009, The Pulp & Paper Fundamental Research Society, 2009, pp. 1149-1166.
- [4] A.W. Martinez, S.T. Phillips, E. Carrihe, S.W. Thomas III, H. Sindi, G.M. Whitesides, *Analytical Chemistry* 80 (2008) 3699-3707.
- [5] A.W. Martinez, S.T. Phillips, M.J. Butte, G.M. Whitesides, *Angewandte Chemie International Edition* 46 (2007) 1318-1320.
- [6] R. Pelton, *Bioactive Paper - A Paper Science Perspective*, in: I'Anson, S.J. (Ed.), *Advances in Pulp and Paper Research*, Oxford 2009, The Pulp & Paper Fundamental Research Society, 2009, pp. 1096-1145.
- [7] R. Pelton, *Trends in Analytical Chemistry* 28 (2009) 925-942.
- [8] S. Aikio, S. Grönqvist, L. Hakola, E. Hurme, S. Jussila, O.-V. Kaukonen, H. Kopola, M. Käsäkoski, M. Leinonen, S. Lippo, R. Mahlberg, S. Peltonen, P. Qvintus-Leino, T. Rajamäki, A.-C. Ritschkoff, M. Smolander, J. Vartiainen, L. Viikari, M. Vilkmann, *Bioactive Paper and Fibre Products: Patent and Literature Survey*, 2006, pp. 1-84.
- [9] S.M.Z. Hossain, R.E. Luckham, A.M. Smith, J.M. Lebert, L.M. Davies, R.H. Pelton, C.D.M. Filipe, J.D. Brennan, *Analytical Chemistry* 81 (2009) 5474-5483.
- [10] X. Li, J. Tian, T. Nguyen, W. Shen, *Analytical Chemistry* 80 (2008) 9131-9134.
- [11] R. Voss, M.A. Brook, J. Thompson, Y. Chen, R.H. Pelton, J.D. Brennan, *Journal of Materials Chemistry* 17 (2007) 4854-4863.
- [12] M.S. Khan, A. Slater, S.B.M. Haniffa, G. Garnier, *Langmuir* Submitted (2009).
- [13] K.M. Holtz, E.R. Kantrowitz, *FEBS Letters* 462 (1999) 7-11.
- [14] D.B. Craig, E.A. Arriaga, J.C.Y. Wong, H. Lu, N.J. Dovichi, *Journal of The American Chemical Society* 118 (1996) 5245-5253.
- [15] J.E. Coleman, *Annual Review of Biophysics and Biomolecular Structure* 21 (1992) 441-483.
- [16] C.J.F. VanNoorden, G.N. Jonges, *Histochemical Journal* 19 (1987) 94-102.
- [17] P. Sinha, *Journal of Biochemical and Biophysical Methods* 11 (1985) 327-340.
- [18] P. Gettins, M. Metzler, J.E. Coleman, *The Journal of Biological Chemistry* 260 (1985) 2875-2883.
- [19] J. McGadey, *Histochemie* 23 (1970) 180-184.
- [20] G. Masao, JP 87-157619. *Jpn Kokai Tokkyo Koho* 1989.
- [21] Y. Akahori, H. Yamazaki, G. Nishio, H. Matsunaga, K. Mitsubayashi, *Chemical Sensors* 20 (2004) 468-469.
- [22] B. Chen, N. Pernodet, M.H. Rafailovich, A. Bakhtina, R.A. Gross, *Langmuir* 24 (2008) 13457-13464.
- [23] P.C. Hiemenz, R. Rajagopalan, *Principles of Colloid and Surface Chemistry*, Third Edition, Revised and Expanded, Marcel Dekker, New York, 1997, Chapter.
- [24] BCIP/NBT Liquid Substrate System, Product Information, Sigma Aldrich (web: [www.sigmaaldrich.com](http://www.sigmaaldrich.com)), 2009.

- [25] M.S. Khan, W. Shen, G. Garnier, in: Coghill, R. (Ed.), 63rd Appita Annual Conference and Exhibition, Melbourne, Australia, 19-22 April, 2009, APPITA, 2009, pp. 273-280.
- [26] J.E. Bailey, D.F. Ollis, *Biochemical Engineering Fundamentals*, 2nd ed., McGraw-Hill, New York, 1986, Chapter.
- [27] H.S. Fogler, *Elements of Chemical Reaction Engineering*, Prentice-Hall, Englewood Cliffs, New Jersey, 1986, Chapter.
- [28] O. Levenspiel, *Chemical Reaction Engineering*, 3rd ed., John Wiley & Sons, New York, USA, 1999, Chapter.
- [29] R.A. Anderson, B.L. Vallee, *Proceedings of the National Academy of Sciences of the United States of America* 72 (1975) 394-397.
- [30] M. Besman, J.E. Coleman, *The Journal of Biological Chemistry* 260 (1985) 11190-11193.
- [31] M. Fosset, D. Chappelet-Tordo, M. Lazdunski, *Biochemistry* 13 (1974) 1783-1788.
- [32] E.E. Kim, H.W. Wyckoff, *Journal of Molecular Biology* 218 (1991) 263-477.
- [33] M.F. Machado, J.M. Saraiva, *Biotechnology Letters* 27 (2005) 1233-1239.

---

# Chapter 5

---

Paper Diagnostic for  
Instantaneous Blood  
Typing

---

This page is intentionally blank

**Monash University**

**Declaration for Thesis Chapter 5**

**Declaration by candidate**

In the case of Chapter 5, the nature and extent of my contribution to the work was the following:

Nature of contribution	Extent of contribution (%)
Initiation, key ideas, experimental and analysis works, development and writing up of the paper	70

The following co-authors contributed to the work. Co-authors who are students at Monash University must also indicate the extent of their contribution in percentage terms:

Name	Nature of contribution	Extent of contribution (%) for student co-authors only
<b>Gil Garnier</b>	Initiation, key ideas, reviewing and editing of the paper	Co-supervisor
<b>George Thouas</b>	Initiation, key ideas, reviewing and editing of the paper	Co-supervisor
<b>Wei Shen</b>	Initiation, key ideas, reviewing and editing of the paper	Co-supervisor
<b>Gordon Whyte</b>	Initiation, key ideas, reviewing and editing of the paper	Co-supervisor

**Candidate's Signature**

[Redacted Signature]

**Date**

17/12/09

**Declaration by co-authors**

The undersigned hereby certify that:

- (1) the above declaration correctly reflects the nature and extent of the candidate's contribution to this work, and the nature of the contribution of each of the co-authors.
- (2) they meet the criteria for authorship in that they have participated in the conception, execution, or interpretation, of at least that part of the publication in their field of expertise;
- (3) they take public responsibility for their part of the publication, except for the responsible author who accepts overall responsibility for the publication;
- (4) there are no other authors of the publication according to these criteria;
- (5) potential conflicts of interest have been disclosed to (a) granting bodies, (b) the editor or publisher of journals or other publications, and (c) the head of the responsible academic unit; and
- (6) the original data are stored at the following location(s) and will be held for at least five years from the date indicated below:

**Location(s)**

Bioresource Processing Research Institute of Australia (BioPRIA), Department of Chemical Engineering, Monash University, Clayton, VIC 3800, Australia.

**Signature 1**

[Redacted Signature]

**Date**

22/12/09

**Signature 2**

[Redacted Signature]

**Date**

For Dr. Thouas

**Signature 3**

[Redacted Signature]

**Date**

17/02/10

**Signature 4**

[Redacted Signature]

**Date**

For Prof. G. Whyte

# Paper Diagnostic for Instantaneous Blood Typing

Mohidus Samad Khan<sup>1</sup>, George Thouas<sup>2,3,4</sup>, Wei Shen<sup>1</sup>, Gordon Whyte<sup>5</sup> and Gil Garnier<sup>1\*</sup>

<sup>1</sup>Bioresource Processing Research Institute of Australia (BioPRIA),  
Department of Chemical Engineering,  
Monash University, Clayton, Victoria 3800, Australia.

<sup>2</sup>Division of Biological Engineering, Monash University.

<sup>3</sup>Monash Immunology and Stem Cell Laboratories (MISCL), Monash University.

<sup>4</sup>Now: Department of Zoology, The University of Melbourne, Victoria 3010, Australia.

<sup>5</sup>School of Rural Health, Faculty of Medicine,  
Nursing & Health Science, Monash University.

\*Corresponding author: Gil.Garnier@eng.monash.edu.au

Chapter 5	123
Paper Diagnostic for Instantaneous Blood Typing	123
Abstract	126
1. Introduction	127
2. Experimental	129
2.1. Materials	129
2.2. Methods	129
3. Results	131
3.1. Transport of blood/antibody solution on Paper	131
3.2. Transport of blood on Antibody treated Paper	132
3.3. Wicking Kinetics of blood on Antibody treated Paper	137
4. Discussion	140
4.1. Mechanism of Blood coagulation	140
4.2. Mechanism of blood transport on paper	141
4.3. Paper diagnostic for blood typing	146
5. Conclusion	149
Acknowledgment	150
References	151

## ABSTRACT

**A**gglutinated blood transports differently onto than stable blood with well dispersed red cells. This difference was investigated to develop instantaneous blood typing tests using specific antibody-antigen interactions to trigger blood agglutination. Two series of experiments were performed. The first related the level of agglutination and the fluidic properties of blood on its

Nothing great was ever achieved without enthusiasm.

– Ralph Waldo Emerson

transport in paper. Blood samples were mixed at different ratios with specific and non-specific antibodies; a droplet of each mixture was deposited onto a filter paper strip and the kinetics of wicking and red cell separation were measured. Agglutinated blood phase separated, with the red blood cells (RBC) forming a distinct spot upon contact with paper while the serum wicked; in contrast, stable blood suspensions wicked uniformly. The second study analyzed the wicking and the chromatographic separation of droplets of blood deposited onto paper strips pretreated with specific and non-specific antibodies. Drastic differences in transport occurred. Blood agglutinated by interaction with one of its specific antibodies phase separated, causing a chromatographic separation. The red cells wicked very little while the serum wicked at a faster rate than the original blood sample.

Blood agglutination and wicking in paper followed the concepts of colloids chemistry. The immunoglobulin M antibodies agglutinated the red blood cells by polymer bridging, upon selective adsorption on the specific antigen at their surface. The transport kinetics was viscosity controlled, with the viscosity of red cells drastically increasing upon blood agglutination. 3 arms prototypes were developed for single-step blood typing.

**Key Words:** Paper diagnostics, bioactive surfaces, blood typing, agglutination, antibody, antigen.

## 1. INTRODUCTION

Detecting blood type (ABO) is critical for many medical procedures. Different blood typing techniques are available: gel column <sup>1-3</sup>, TLC-immunostaining <sup>4</sup>, fiber optic-microfluidic device <sup>5</sup>, spin tube method <sup>2</sup>. Among those, the identification and automation of red blood cell (RBC) agglutination by antigen-antibody interaction often requires optical or microfluidic analytical instruments not available in many parts of the world <sup>6-11</sup>. Cheap paper based diagnostics offer an attractive alternative. We have observed that the transport of blood in a porous media such as paper widely varies whether its red cells are agglutinated or not. This study explores this observation for developing low cost paper-based tests for blood typing.

Blood is essential for sustaining living tissue by supplying oxygen and other soluble nutrients to provide immune protection and metabolic turnover<sup>12</sup>. Blood is a concentrated stable colloid suspension made of red blood cells (erythrocytes, 4-6 million/mL, 6-8  $\mu\text{m}$ ), white cells (leukocytes, 4000-6000 /mL, 10-21 $\mu\text{m}$ ) and platelets (150,000-400,000 /mL, 2-5  $\mu\text{m}$ ) dispersed in an aqueous solution (serum) containing a host of biomolecules (albumins, fatty acids, hormones)<sup>13-16</sup>. Some of these biomolecules, such as the glycoproteins and carbohydrates, responsible for blood type and tissue immunity (antigens), are directly adsorbed onto the surface of the blood cells<sup>17</sup>. Common portable testing methods for blood include analysis of glucose content, cholesterol, metabolic panel (sodium, potassium, bicarbonate, blood urea nitrogen, magnesium, creatine, calcium, triglycerides), microbial and disease markers and protein molecular profile (liver, prostate)<sup>14</sup>. Surprisingly, there are no robust and convenient low cost disposable tests available for “on the spot” analysis of blood type. Blood samples are typically outsourced to an analytical laboratory. Reliable tests to instantaneously provide critical blood analysis, without requiring sophisticated laboratory analytical instrumentation such as chromatographic and spectroscopic methods, would be invaluable for improving health in developing countries. Blood analysis is also important in veterinary medicine, also requiring low cost and versatile devices designed for field use.

This study investigates a blood testing platform based on the principle that red cell agglutination, triggered by specific antigen interaction, drastically decreases blood wicking and transport on paper or chromatographic media. The agglutination process also considerably enhances the chromatographic separation (elution) of the blood components, especially the red cells from the serum.

## 2. EXPERIMENTAL

### 2.1. Materials

Antibody solutions of red cell antigens A, B and D (Epiclone™ Anti-A, Anti-B and Anti-D) were purchased from CSL, Australia. Anti-A and B come as blue and yellow colour reagents, respectively, and Anti-D is a clear solution. Anti-D can agglutinate any blood (A, B, O) with the rhesus factor (D). These antibodies are made of immunoglobulin M (IgM)<sup>18, 19</sup>. Phosphate buffer saline (PBS) (Invitrogen, Australia) was used as diluent for all antibody solutions. 2 mm wide paper strips (Whatman filter paper #4) were used as porous substrate for antibody. To measure the wicking distance, 2 mm units were laser printed with a HP LaserJet 4250n on each paper strip. Standard blotting papers (Drink Coster Blotting, 280 g/m<sup>2</sup>) were used to remove the excess of antibody solution from the treated paper strips. Reflex paper (80 g/m<sup>2</sup>) served as semi-hydrophobic surface. Blood samples (AB+, A+, B+ and O+) were collected from adult volunteers (3 males and 2 females). Blood samples were kept in standard plastic vials containing the standard citrate anti-coagulant. All the antibody and blood samples were stored below 4°C. Blood samples were used within 5 days. Plastic tubes (Microtubes, 1.7mL; Axygen, USA) were used to mix the blood with the antibody (200 µL). A calibrated micro-pipette served to dispense standard (20 µL) droplets on the paper strips.

### 2.2. Methods

#### 2.2.1. Blood Chromatographic Separation

Paper strips were soaked into antibody solutions of different concentrations (Anti-A@1.0x, 0.8x, 0.6x, 0.4x, 0.2x and 0.0x); PBS was used as diluent (Figure 1). Excess antibody was removed from the paper strips with blotting papers. The antibody (Anti-A) active paper strips were then placed on Reflex Paper. Blood droplets of 20µL were dispensed at the center of the paper strip using a calibrated micro-pipette. The wicking distance was measured from centre to either direction.

### 2.2.2. Agglutinated Blood on Paper

Blood samples and antibody solutions were mixed into plastic vials at different ratios (25:75, 50:50 and 75:25) to prepare 200 $\mu$ L solutions. The plastic vials were manually shaken gently for 20 sec and left to rest for 2-3 minutes. The paper strips were soaked into PBS and the excess PBS was removed with blotting papers. The paper strips were then placed on Reflex Paper. For each different ratio blood-antibody investigated, 20  $\mu$ L of the premixed blood/antibody solution was dispensed at the center of a fresh paper strip.

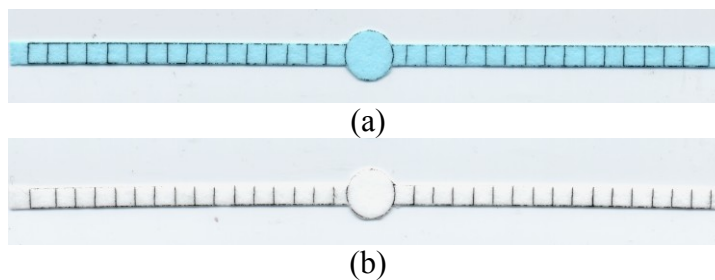


**Figure 1:** Paper strips for blood type detection; (a) treated with antibody-A (Anti-A of 1.0x concentration), (b) treated with PBS buffer.

### 2.2.3. Image Capture and Analysis

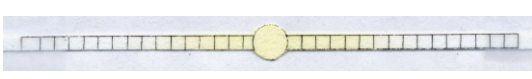
The wicking kinetics images were captured using a standard video camera (JVC Camcorder Everio GZ-MG530) and a digital SLR camera (SONY-DSLR-A100) with additional close-up lenses. The video clips were transferred to a computer and converted using Prism Video Converter v 1.27 and VirtualDub-1.8.8 software. The still and video images were analyzed using Image-Pro Plus 5.0 software.

### 3. RESULTS

We observed that the transport of blood droplets deposited on paper widely varies whether blood agglutinates or not. This difference was investigated to develop blood typing tests. Two complementary studies are presented. The first aims at quantifying the level of blood agglutination and fluidic properties on its transport in paper. Various blood samples were mixed at different ratio with specific and non-specific antibodies. A droplet of the mixture was deposited onto a filter paper strip and the kinetics of wicking and red cell separation were recorded using image analysis. In the second study, specific and non-specific antibodies were adsorbed onto paper and a droplet of blood was deposited; the transport by wicking and the chromatographic separation of the blood components on the treated paper were measured.

#### 3.1. Transport of blood/antibody solution on Paper

In the first study, B+ blood was mixed at different ratios with solutions of antibody-A and antibody-B. A 20  $\mu\text{L}$  droplet of the mixture was gently deposited in the middle of a paper strip soaked in buffer (PBS) and the blood separation and wicking kinetics were quantified by image analysis. Pictures of the paper strips after 10 minutes wicking are presented on Figures 2. A few observations are of interest. The blood B+/antibody-B mixtures undergo phase separation once deposited on paper (Figure 2A); the blood serum readily wicks paper while the agglutinated red cells do not. The agglutinated red cells show no ability to wick paper; instead they readily adsorb upon contact with the porous structure of paper, forming a very distinct red dot. The extent of red blood cell (RBC) separation decreases as increases the ratio blood/antibody. Drastic separation of the RBCs occurs until a ratio blood/antibody up to around 50:50. The behavior of blood mixed with a non-specific antibody on paper widely differs. For mixtures of blood B+/antibody-A deposited on paper (Figure 2B), no separation of red cells from the serum occur and the extent of wicking is mostly independent of the ratio blood/antibody.

Blood Antibody Ratio	Anti-B
0 : 100	
25 : 75	
50 : 50	
75 : 25	
100 : 0	

(a)

Blood Antibody Ratio	Anti-A
0 : 100	
25 : 75	
50 : 50	
75 : 25	
100 : 0	

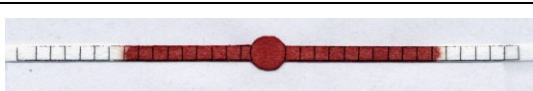
(b)

**Figure 2:** Wicking on paper of blood previously agglutinated from antigen-antibody interaction; (a) ‘B+’ blood with (a) specific antibody (Anti-B), (b) non-specific antibody (Anti-A).

### 3.2. Transport of blood on Antibody treated Paper

In the second study, paper strips were impregnated with solutions containing different concentrations of antibody-A. A 20  $\mu$ L droplet of blood was deposited in the middle of a wet paper strip, and the blood transport and the separation dynamics were measured by image analysis. Two types of blood were investigated: AB+ and B+. The interaction of AB+ and B+ blood droplets with antibody-A treated paper is shown after 10 minutes on Figure 3a and 3b, respectively. There are three observations. First, for

AB+ blood deposited on antibody-A treated paper, the red blood cells (RBCs) separate from the blood and adsorb on paper while the serum wicks. The extent of RBC adsorption, and therefore their reduction in wicking ability, tends to increase with the concentration of antibody-A deposited on paper. Second, blood B+ transports differently on antibody-A treated paper; no red blood cells separation from the serum is observed. However, the extent of blood wicking decreases as increases the concentration of antibody A on paper. This observation suggests that some type of weak non-specific, non-agglutination related interaction between blood B and antibody A exists. A third observation is that some blood was observed to flow over the layer of blood agglutinated on the paper surface; this is especially prevalent at the center of the paper strip, where the blood is introduced (Figure 3). A fraction of the blood dispensed did not come into contact with the antibody in the first instance of contact and was allowed to flow over a layer of immobilized blood, therefore decreasing the sharpness of detection. A higher paper surface/blood volume ratio is required to minimize this side effect.

Anti-A concentration on Paper	'AB+' blood on paper-A
0.0 x	
0.2 x	
0.6 x	
0.8 x	
1.0 x	

(a)

Anti-A concentration on Paper	'B+' blood on paper-A
0.0 x	
0.2 x	
0.6 x	
0.8 x	
1.0 x	

(b)

**Figure 3:** Blood wicking on Anti-A treated paper: 10mins after blood drop dispensing. Sample blood drops: (a) AB+ and (b) B+, were dispensed on papers treated with different concentrations of antibody-A. 'X' represents the dilution fraction.

The effect of RBC agglutination through specific antibody-antigen interaction on paper wicking can be quantified. In absence of agglutination, blood wicking on paper showed a faint gradient at the wicking threshold due to some component separated by paper chromatography. When RBC agglutination occurs by antigen-antibody interaction, two distinct layers are formed on paper: RBC and blood serum. The blood serum separated from RBC produced a white contrast on the blue paper surface. Figure 4 is a schematic representation of the phenomena with ' $z_1$ ' defining the wicking length of blood (serum with red blood cells) and ' $z_2$ ' the wicking distance of serum (no red cells). The total wicking length is simply  $z = z_1 + z_2$ .

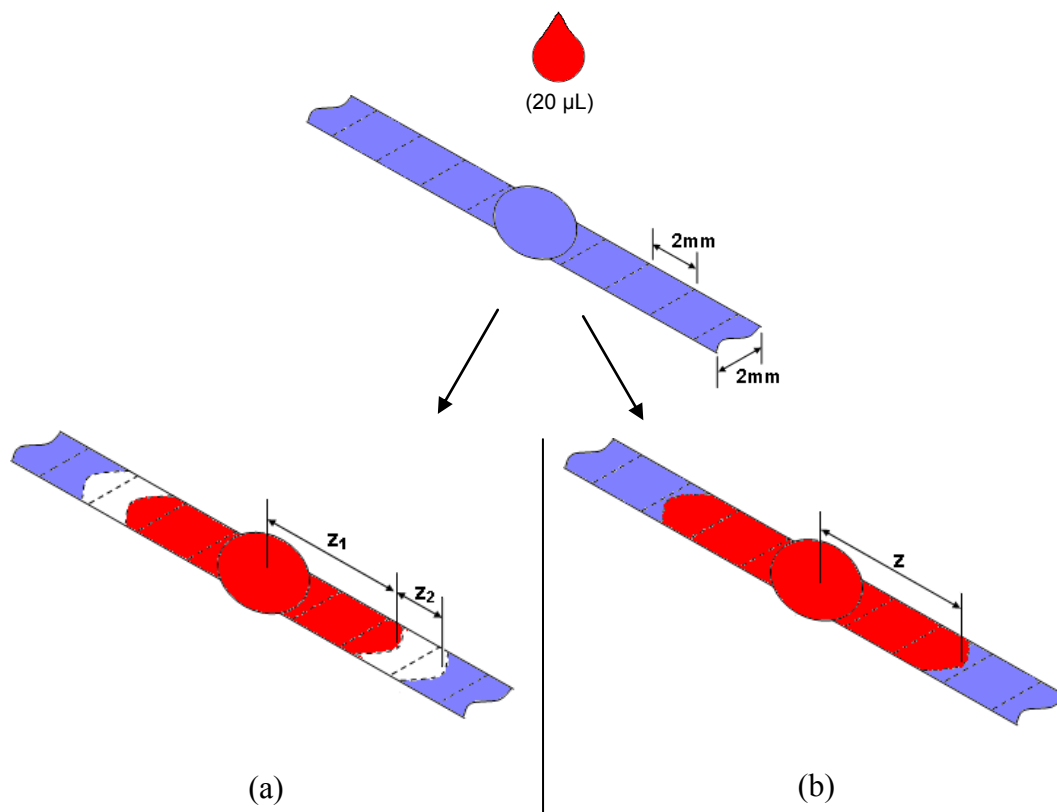
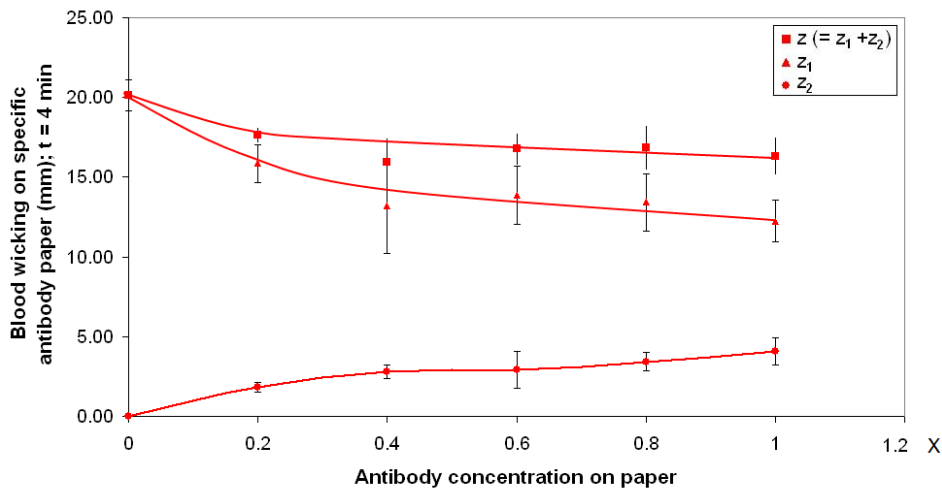


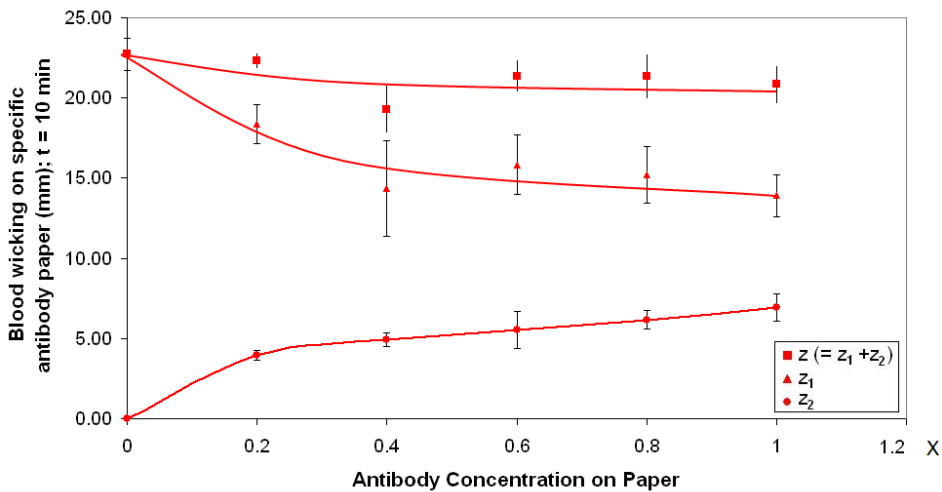
**Figure 4:** Schematic representation of the wicking of blood on paper treated with a specific and a non-specific antibody (A). (a) AB+ blood interact with antibody-A on paper and create separate layer of RBC and serum, (b) B+ blood wick on paper without any distinctive separation.

The extent of blood wicking as a function of antibody concentration is shown on Figure 5 for paper strips treated with antibody A. Two types of blood (AB+ and B+) and two wicking periods (4 min and 10 min) were compared. Figure 5a and 5b quantify the RBC/blood serum separation for AB+ blood on treated paper strips (antibody-A) after 4 min and 10 min wicking, respectively. Six replicates were used and the average and standard deviations are reported. For AB+ blood on antibody-A treated paper, the total wicking distance ( $z$ ) after 10 minutes was found to be a weak function of the antibody concentration. The wicking length of blood with RBC ( $z_1$ ) gradually decreased as increased the concentration of antibody on paper. Blood serum, with the red blood cells agglutinated/separated by specific antibody-antigen interaction, traveled longer distances ( $z_2$ ); this tendency was further accentuated by increasing the antibody concentration on paper (Figure 5a, b). There was not much difference in the blood separation and transport after 4 or 10 minutes wicking. Figure 5c quantifies the effect of

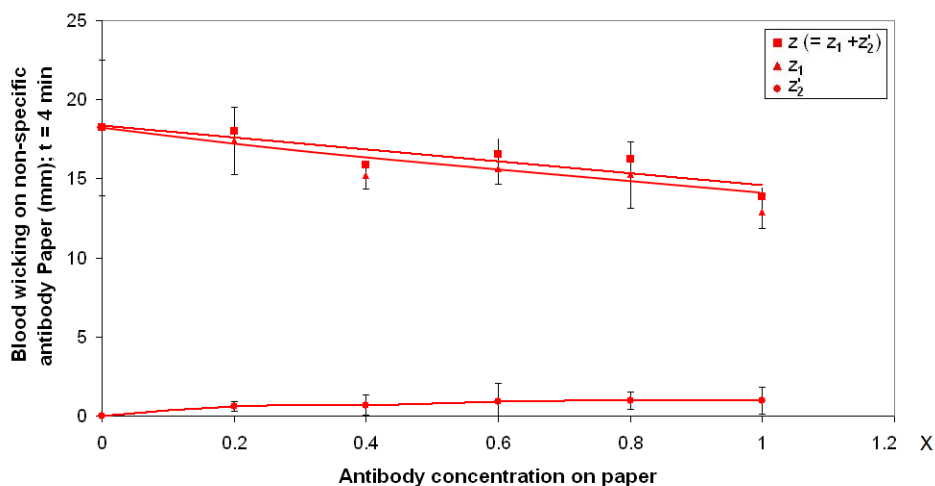
antibody (A) concentration on blood (B+) wicking after 4 minutes for a non-specific system. There was virtually no separation of the red blood cells from the serum ( $z = z_1$ ,  $z_2 \approx 0$ ). The separated layer of blood ( $z_1$ ) at the wicking threshold was much smaller than that of the specific system (AB+ blood). The total wicking distance ( $z$ ) for the non-specific system (B+ blood) was also shorter than for the specific system. Interestingly, the wicking distance decreased as increased the concentration of non-specific antibody on paper; this may be caused either by some interaction between non-specific systems, or by the antibody adsorption blocking or collapsing some of the pores of the paper structure.



(a)



(b)



(c)

**Figure 5:** Blood wicking on paper treated with different concentrations of antibody-A. AB+ blood wicking after (a) 4min, (b) 10 min, (c) B+ blood wicking after 4 min;  $n = 6$ . 'X' represents the dilution factor.

### 3.3. Wicking Kinetics of blood on Antibody treated Paper

The transport dynamics of blood droplets deposited on paper strips treated with an antibody was quantified by image analysis. Droplets of two types of blood, AB+ and B+, were deposited on paper strips treated with antibody A (Figure 6). Figure 6a illustrates the evolution of wicking for the AB+ blood, able of specific antibody-antigen interactions with the treated paper. Two phenomena are observed: wicking and separation of the blood components. The RBC and the blood serum separated as a function of time or of the extent of wicking. The RBCs rapidly wicked in the first minute to level-off after around 4 minutes. The blood serum separated from RBC wicked for longer periods. Figure 6b illustrates the evolution of B+ blood wicking on the antibody-A treated paper; this system is unable of specific antibody-antigen interactions. Basically no separation of the RBC from the serum was observed. The blood wicking was rapid in the first minute and reached saturation after 4 minutes.

The wicking dynamics of two blood types (AB+ and B+) on antibody-A treated paper was quantified (Figure 7); the average and standard deviations are presented. For the specific antibody-antigen system (blood AB+), the wicking rate of the red blood cells ( $z_1$ ) on treated paper (antibody A) drastically slowed down after about 2 min. and leveled-off thereafter. However, wicking by the serum fraction ( $z_2$ ) proceeded at a constant rate of 1.0 mm/min (Figure 7a). Blood wicking ( $z$ ) on paper for non-specific

antibody-antigen systems was slower (Figure 7b), and basically no blood phase separation occurred ( $z = z_1, z_2 \approx 0$ ).

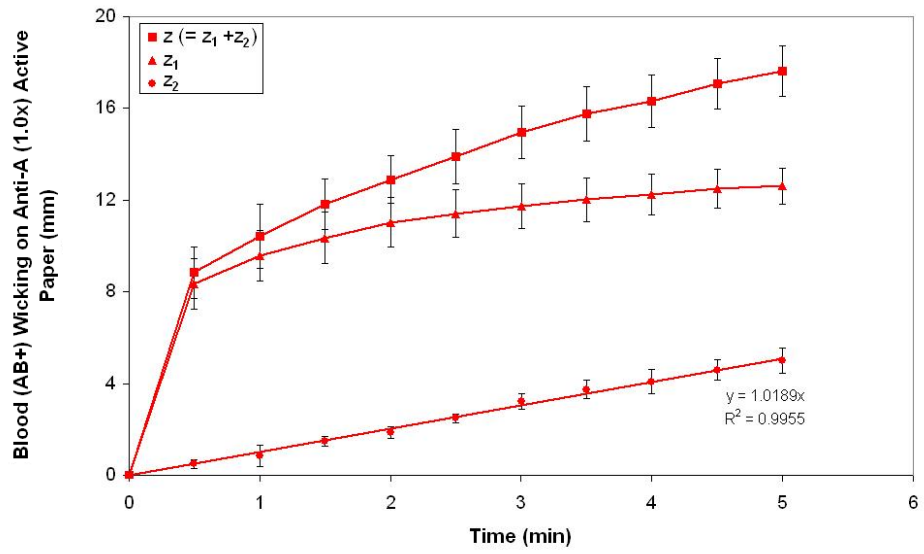
Time, t (min)	Blood wicking on Anti-A (1.0x) active paper
0.0	
1.0	
2.0	
3.0	
4.0	
5.0	

(a)

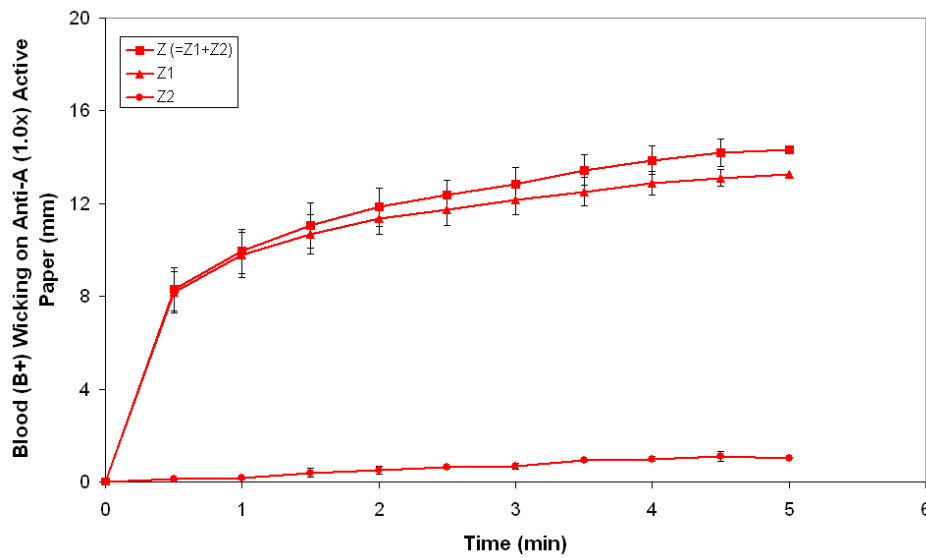
Time, t (min)	Blood wicking on Anti-A (1.0x) active paper
0.0	
1.0	
2.0	
3.0	
4.0	
5.0	

(b)

**Figure 6:** Evolution of blood wicking on antibody-A active paper; paper strips soaked in Anti-A of 1.0x. (a) AB+ blood, (b) B+ blood.



(a)



(b)

Figure 7: Blood wicking dynamics on paper treated with antibody-A. (a) AB+ blood, (b) B+ blood;  $n = 6$ .

## 4. DISCUSSION

### 4.1. Mechanism of Blood coagulation

The red blood cells were agglutinated by one of their specific antibody. From a colloidal perspective, this can proceed by two main mechanisms. The first is polymer bridging, in which a macromolecule of radius of gyration larger than the electrical double layer thickness binds the colloids particles (RBC) into aggregates. The second is charge reversal; this involves the surface electrical neutralization by adsorption of oppositely charged small molecules. It is of interest to analyze the ability of blood antibody to agglutinate the blood red cells by bridging and charge reversal mechanism.

Blood can simplistically be viewed as a concentrated colloid suspension with its negatively charged red cells electrostatically stabilized in the serum, a weak aqueous electrolyte continuous phase. The RBCs have an average diameter of 7  $\mu\text{m}$  and bear a moderate negative charge characterized by a zeta potential ( $\zeta$ ) of -15 mV<sup>20</sup>. The concentration of the main electrolytes in blood: sodium (Na), potassium (K) and calcium (Ca) - are respectively of 140, 5 and 2.5 mmole/L<sup>21</sup>. These electrolytes compress the double electrical layer of the red blood cells, therefore diminishing their stability.

The double layer thickness of the red blood cell in the electrolyte continuous phase can be approximated with the Debye length ( $1/\kappa$ ) where  $\kappa$  is calculated from the diffuse layer thickness using the classical Gouy-Chapman model<sup>22,23</sup>:

$$\kappa = \frac{\sqrt{e^2 N_A c z^2}}{\epsilon T} \quad (1)$$

where  $e$  is the electron charge ( $1.6 \times 10^{-19}\text{C}$ ),  $N_A$  the Avogadro number ( $6.02 \times 10^{23}$  1/mol),  $c$  the electrolyte concentration ( $\text{mol}/\text{m}^3$ ) of valency  $z$ ,  $\epsilon$  the media permittivity ( $\text{C}^2/\text{Jm}$ ),  $k$  the Boltzmann constant ( $1.38 \times 10^{-23}$  J/ K) and  $T$  the temperature (K). Assuming additive effect of the salts, we calculate at room temperature (25°C) a double layer thickness of 0.8 nm; for blood samples diluted by a factor of 10 and 100, the double layer thickness is of 2.5 and 8 nm, respectively. A bridging molecule needs to be

at least twice as big as the double electrical layer thickness for efficient coagulation between 2 colloids.

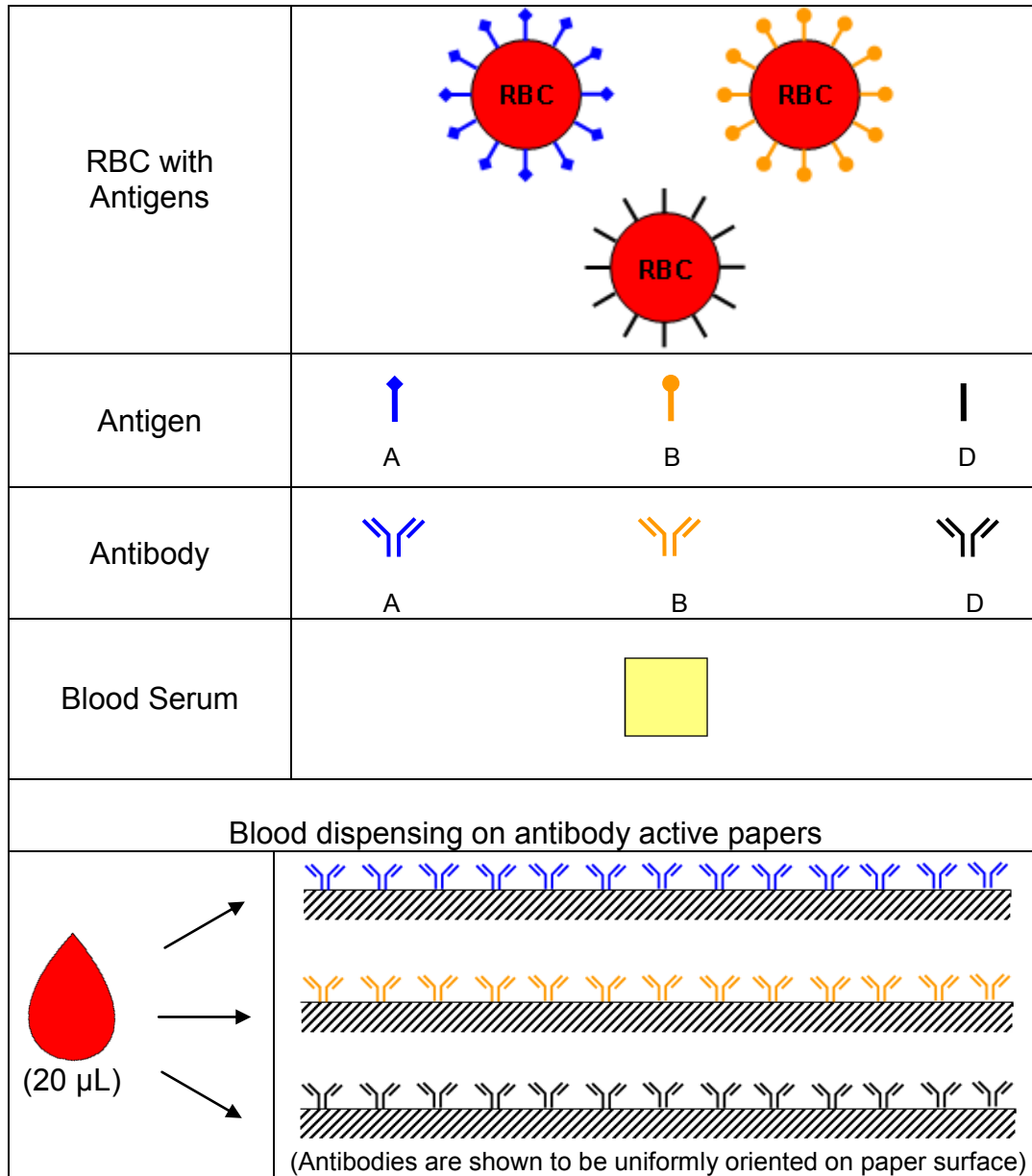
On the surface of the red blood cells, lie antigen molecules able to selectively bind only with their counter antibody. Antibodies are made of 5 different immunoglobins (Ig), denoted as IgM, IgG, IgA, IgD and IgE, varying in molecular weight and concentration in the blood as indicated in Table I<sup>21, 24, 25</sup>. Two of these immunoglobins can assemble into bigger units: IgM into a star shape pentamer carrying 10 antigen binding sites, and IgA able to dimerize into a linear structure. IgM and IgA can both self-assemble by the base of their heavy chains, leaving their antigen binding sites at the extremities. The diameters of an IgM molecule and a pentamer assembly are of 11 nm and 40 nm, respectively<sup>26-28</sup>. This means that the IgM molecules can easily agglutinate the red cell blood by bridging.

**Table I: Molecular weight and concentration of immunoglobins (Ig) in human blood<sup>21, 24, 25</sup>**

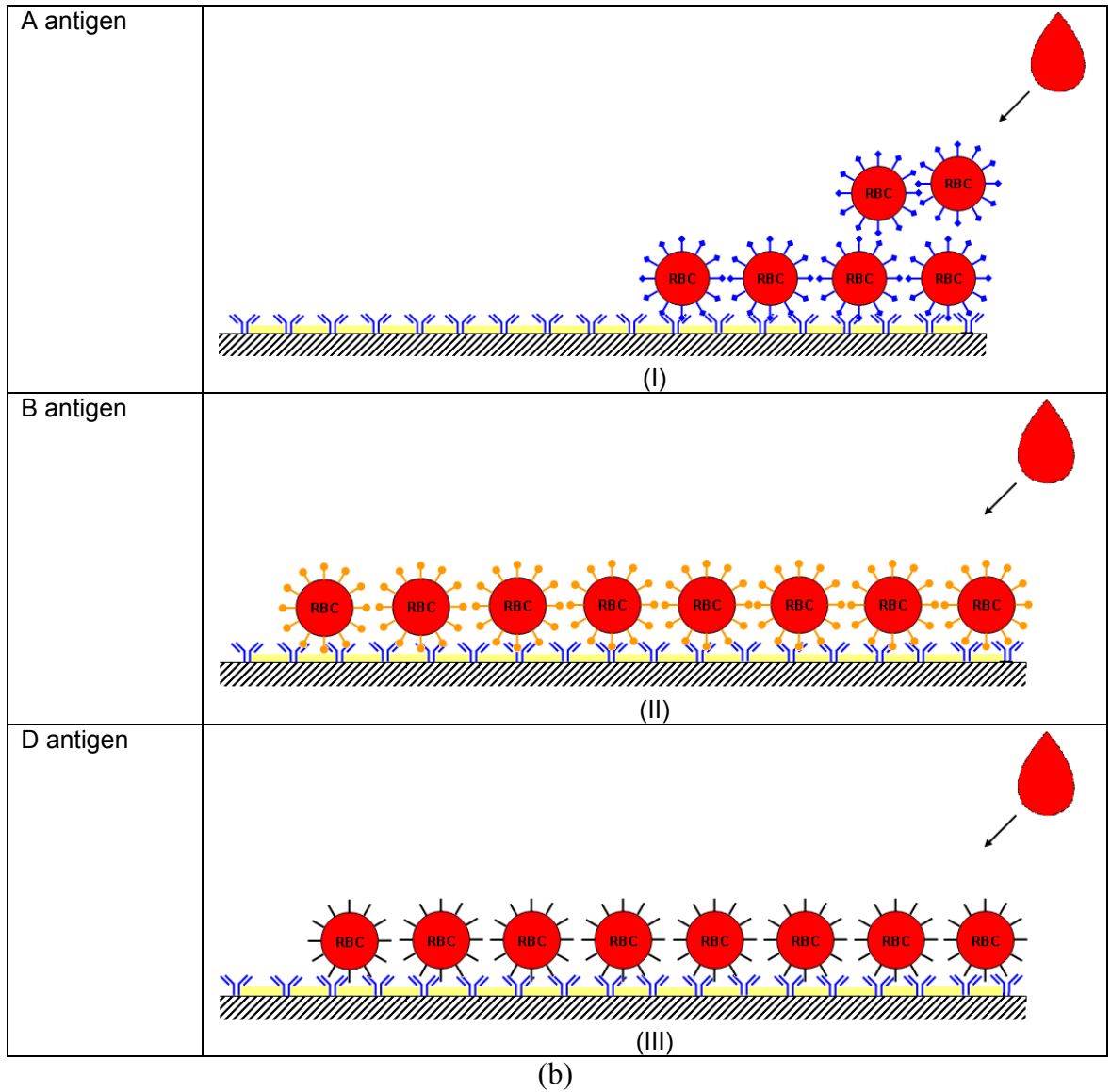
Immunoglobulin	Mw (g/mole)	Concentration (mg/mL)
IgM	970,000	1.5
IgG	146-165,000	0.5-0.9
IgA	160,000	3
IgD	184,000	0.03
IgE	188,000	$5 \times 10^{-5}$

## 4.2. Mechanism of blood transport on paper

The transport of agglutinated blood on paper was found to drastically vary from that of non-agglutinated blood (stable blood). When a droplet of stable blood is deposited onto paper, it wicks as a uniform phase with the red cells well dispersed in the serum. However, when agglutinated blood is deposited or been agglutinated on paper, separation of the red cells from the serum and chromatographic separation occur; wicking of the serum fraction proceeds at a faster rate than that of the original blood sample. The mechanism is schematically represented on Figure 8.



(a)





Blood transports in paper mostly by wicking through the inter-fiber spaces. The driving force is capillarity driven by the difference in surface energy between the fluid and the solid. The resistances are friction and viscous dissipation. In its simplest form, wicking can be described by the liquid flow in a capillary. The Lucas-Washburn equation states that a liquid of viscosity  $\eta$  and surface tension  $\gamma$  will flow in a capillary of radius  $r$  and length  $l$  at a velocity  $V$  defined by <sup>15</sup>:

$$V = \frac{\gamma \cos \theta}{\varepsilon \eta} \quad (2)$$

where  $\theta_E$  is the equilibrium contact angle formed by the fluid on the capillary.

Red blood cell agglutination has two direct effects: a drastic increase in local red cell blood viscosity ( $\eta$ ) and the reduction of paper capillary ( $r$ ); both effects decrease the wicking of the red blood cells according to equation 2. Another effect of RBC agglutination is the separation of the serum from the blood; this reduces the viscosity of the liquid phase, which contributes to an increase in wicking velocity. Agglutination can affect the surface tension of blood solutions; agglutination of tension active molecules, such as lipids, would increase the surface tension of the solution.

Mixing the antibody solutions at increasing ratios with blood has two main effects. A first effect is to decrease the solution viscosity which increases the wicking velocity ( $\eta_{\text{antibody}} < \eta_{\text{blood}}$ ). A second effect is to increase the concentration of antibody in solution and also the ratio antibody/antigen molecules. This affects the kinetics and the extent of blood agglutination. Optimal colloid coagulation by polymer bridging occurs at half surface coverage, when there are as many polymer patches as empty surface patches (homo polymers typically adsorb as monolayers: a polymer patch deposits on a bare surface patch) <sup>22, 29</sup>. The question of interest regards the concentrations of antibody and antigen. The antibody solutions were used as received and their concentrations were not measured. However our observations, by comparing the transport behavior of the same type of blood but from different subjects, suggest that antigen concentration on red blood cells and RBC concentration can both vary from subject to subject. Likewise, similar laboratory observations advocate a variation in concentration among the different types of antibody solution used (A, B and D). A strategy relying on dilutions was therefore adopted in this study to alleviate these issues.

The specific interaction between the antibody solution and the red cell antigen proved very efficient in agglutinating blood, which controls the blood wicking and separation onto paper. All systems (A, B and D) had different (uncontrolled) ratio antibody/antigen and red cell concentrations but they all behaved similarly. This suggests a remarkable resiliency for controlled wicking through red cell agglutination. We believe this concept can be generalized for the transport of any stable/coagulated colloids onto porous media.

Small reductions in paper wicking rate were also observed between blood in contact with one of their non-specific antigens, especially at high antibody concentrations. It is unclear whether the phenomena is attributed to a non-specific interaction antibody-antigen causing some agglutination, if the antibody solution might have been impure and indeed contain traces of a specific antibody, or if the antibody solution might simply have caused a reduction in the paper capillarity ( $r$ ).

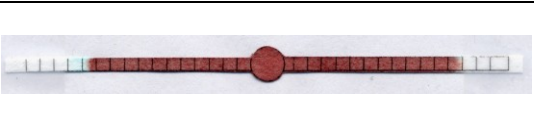
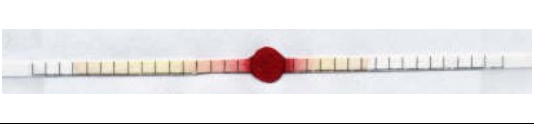
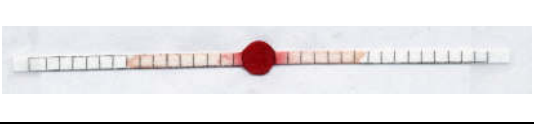
### 4.3. Paper diagnostic for blood typing

Instantaneous paper based blood diagnostics can be engineered from the difference in wicking between a stable and an agglutinated blood sample. Blood agglutination can be triggered by the specific interaction between the antigen naturally present on the surface of the red blood cells and the corresponding antibody immobilized on the paper test.

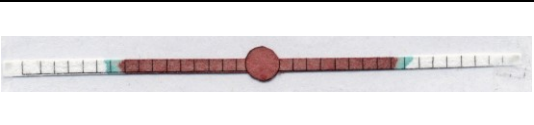
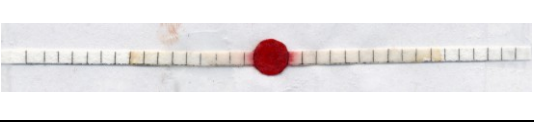
Figure 9 presents blood typing of unknown blood samples using the wicking behavior of blood/antibody mixture on paper. In the first example two blood samples were separately mixed with the 3 antibody solutions- A, B and D- in 50:50 volumetric ratios. A 20  $\mu$ L droplet of each blood/antibody mixtures was deposited on a buffer soaked filter paper strip. Clear phase separation resulted for the mixtures of blood sample 1 with antibody-B and D (Figure 9a) and no separation occurred for the blood sample 1/antibody-A mixture. For blood sample 2, phase separation only happened for the blood/antibody-D mixture (Figure 9b). These observations confirm blood samples 1 and 2 to be of type B+ and O+, respectively.

An antibody treated paper diagnostic was designed for blood typing. Figure 10 illustrates blood group detection from RBC/serum separation on the antibody treated paper. Blood wicking was guided through three fluidic channels, each treated with a different antibody solution (A, B, D). The diagnostic is used as follow. Upon depositing

a 20  $\mu\text{L}$  droplet of the blood sample on the paper strip, clear RBC/blood serum separation is observed at the wicking front on the fluidic channel(s) treated with one of the antibodies specific to the blood sample. By contrast, no distinct separation occurs on the fluidic channel(s) treated with a non-specific antibody. Figure 10b and 10c present two replicates of the same blood sample. For both trials, RBC/blood serum separation was observed on the antibody-A and D treated fluidic channels, which confirms A+ blood. To improve resolution, the original RBG (red-blue-green) images (Figure 10b(I) and 10c(I)) were converted to BRG (blue-red-green) image (Figure 10b(II) and 10c(II)).

Blood sample with antibody (v:v @50:50)	Sample – 2
Anti-A	
Anti-B	
Anti-D	

(a)

Blood sample with antibody (v:v @50:50)	Sample – 3
Anti-A	
Anti-B	
Anti-D	

(b)

**Figure 9: Blood group detection using wicking of agglutinated colloids from specific antigen/antibody interaction on dry paper strips; Blood typing: (a) B+, (b) O+.**

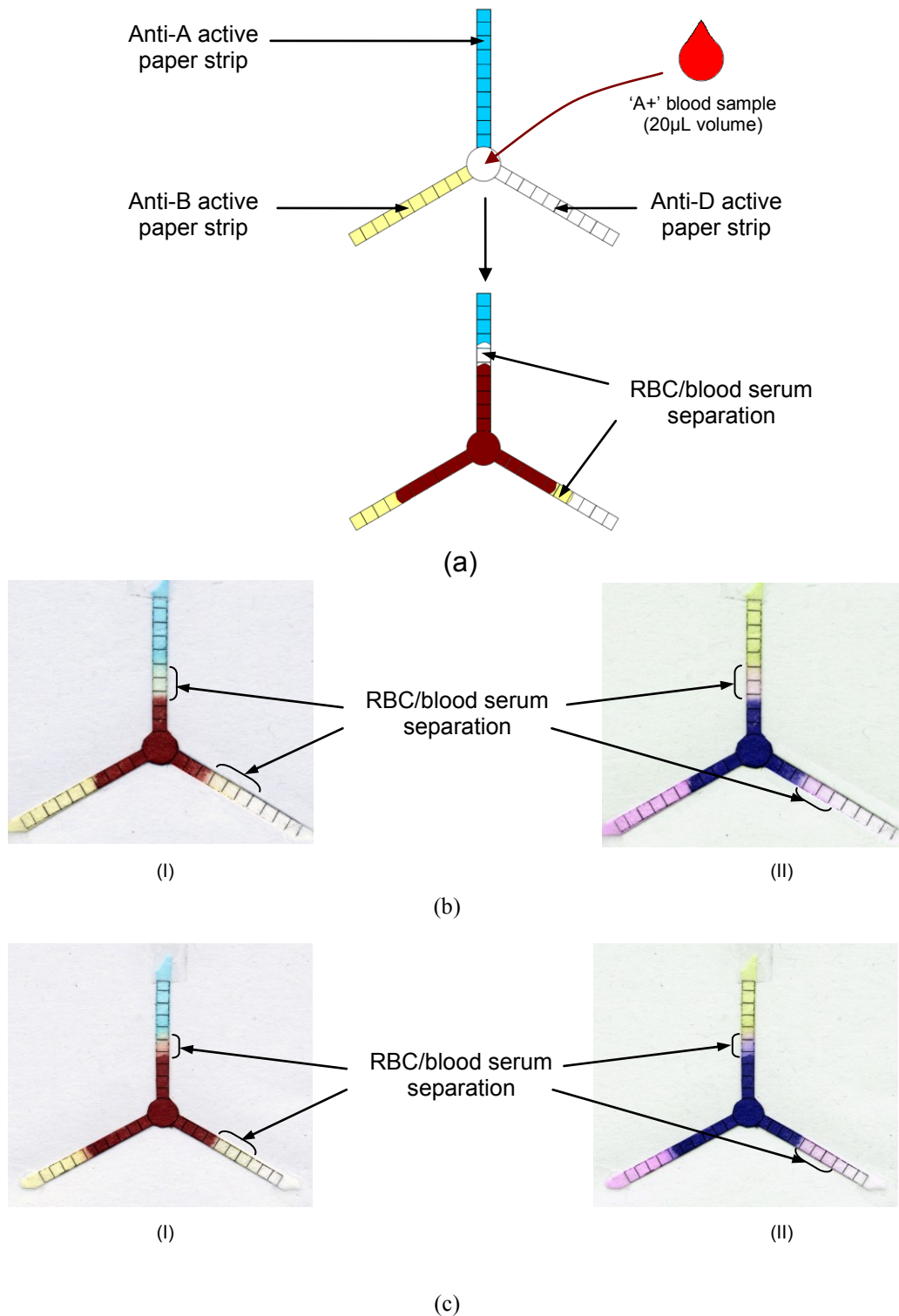


**Figure 10:** Blood group detection using RBC/blood serum separation on antibody active paper fluidic device; (a) schematic of colorimetric indication of phase separation on the paper channels; (b) and (c) are two replicates of same blood samples confirm A+ blood typing; for better resolution RGB images of b(I) and c(I) are converted into BRG images: b(II) and c(II), respectively.

## 5. CONCLUSION

Agglutinated and agglutinating blood transports very differently onto a porous media, such as paper, than stable blood with well dispersed cells. This concept was explored to engineer paper diagnostics for instantaneous blood typing.

Two series of experiments were performed. In the first, blood samples (A+, B+, AB+, O+) were mixed with different amounts of antibody solutions (A,B,D) and a droplet of each mixture was deposited onto a filter paper strip. As expected, blood mixed with its corresponding antibody agglutinated but transported differently in paper than the stable blood solutions (blood mixed with a non-specific antibody). The agglutinated blood phase separated, with the red blood cells (RBC) forming a distinct spot upon contact with paper, while the serum wicked; in contrast, the stable blood solutions wicked uniformly. In the second series of experiments, the filter paper strips were pretreated with an antibody solution (A, B or D) varying in concentration. Droplets of blood were deposited on the antibody-treated paper, and their wicking kinetics was quantified by image analysis. Drastic differences in transport were observed. Blood agglutinated by interaction with one of their specific antibodies phase separated, causing a chromatographic separation. The red blood cells wicked very little while the serum wicked at a rate of 1 mm/min, faster than the original (stable) blood sample which wicked as a uniform solution. The concept of blood typing using a paper diagnostic was demonstrated with a 3 arms prototype- each arm treated with a different solution of antibody (A, B and D).

Blood agglutination and blood wicking in paper follow the concepts of colloids and surface chemistry. The antibodies (IgM) selectively agglutinated the red blood cells (RBC) by polymer bridging upon adsorption on the corresponding RBC antigens. Transport kinetics also follows expectations and is viscosity controlled, with the red cell viscosity increasing by orders of magnitude upon RBC agglutination.

Paper diagnostics for blood typing can promote health in developing countries. The concept of diagnostics based on differences in wicking and chromatography upon colloids stability/agglutination can be generalized to other blood testing and bioassays. All is needed is the ability to control the stability of a colloid system by selective adsorption or by another mechanism.

## **ACKNOWLEDGMENT**

Many thanks to Prof. Kerry Hourigan for use of his bioengineering laboratory and to Lisa Collison from the Monash University Health Service for organizing blood collection from the volunteers. Thanks to N. Sharmin, Dr. F. Mazid, K. Phu, R. Lee, K. Contreras, for useful discussion and all the volunteers for donating blood. Many thanks to Monash University for postgraduate scholarships (MSK).

## REFERENCES

- (1) Proverbio, D.; Spada, E.; Baggiani, L.; Perego, R. *Veterinary Research Communications* **2009**, *33*, S201-S203.
- (2) Swarup, D.; Dhot, B. P. S.; Kotwal, J.; Verma, A. K. *Medical Journal Armed Forces India* **2008**, *64*, 129-130.
- (3) Bromilow, I. M. *Medical Laboratory Science* **1992**, *49*, 129-132.
- (4) Ota, M.; Fukushima, H.; Yonemura, I.; Hasekura, H. *Zeitschrift for Rechtsmedizin* **1988**, *100*, 215-221.
- (5) Ramasubramanian, M. K.; Alexander, S. P. *Biomedical Microdevices* **2009**, *11*, 217-229.
- (6) Masaki, F.; Yoshinori, A.; Toshihiro, A.; Takeshi, N.; Masataka, N.; Toshiki, M.; Kenichi, H.; Kiyohiro, H.; Koji, M. In *EP1997432 (A1)*; Application, E. P., Ed.; Panasonic Corp (JP): Japan, 2009; Vol. PCT International Patent.
- (7) Clawson, B. E.; Office, U. S. P., Ed.; Newport Beach, CA: United State, 2009, pp 11.
- (8) Bilgicer, B.; Thomas, S. W.; Shaw, B. F.; Kaufman, G. K.; Krishnamurthy, V. M.; Estroff, L. A.; Yang, J.; Whitesides, G. M. *Journal of American Chemical Society* **2009**, *131*, 9361-9367.
- (9) Maule, J.; Wainwright, N.; Steele, A. In *NASA Astrobiology Conference: Santa Clara, CA, 2008*.
- (10) LaStella, V.; Patent, U. S., Ed.; Immunostics, Inc.: United State, 2008, pp 17.
- (11) Bland, T. A.; Patent, U. S., Ed.: United States, 1995; Vol. United States Patent5383885.
- (12) Woodcock, J. P. *Reports on Progress in Physics* **1976**, *39*, 65-127.
- (13) Rodak, B. F.; Fritsma, G. A.; Doig, K. *Hematology : clinical principles and applications*, 3rd ed.; Elsevier Saunders: Philadelphia, Pa., 2007.
- (14) Webster, J. G., Ed. *Encyclopedia of Medical Devices and Instrumentation*; John Wiley & Sons, 2006.
- (15) Cecil, R. L.; Andreoli, T. E. *Cecil Essentials of Medicine*; Saunders: Philadelphia, 1993.
- (16) Ganguly, P. *Blood* **1969**, *34*, 511-520.
- (17) Reid, M. E.; Lomas-Francis, C. *The Blood Group Antigen FactsBook*, 2nd ed.; Academic Press: London ; San Diego, Calif. , 2004.
- (18) CSL In *Murine Monoclonal IgM Blood Grouping Reagents*; CSL Limited (www.csl.com.au): Melbourne, 2007.
- (19) CSL In *Murine Monoclonal IgM Blood Grouping Reagents*; CSL Limited (www.csl.com.au): Melbourne, 2007.
- (20) Jan, K.-M.; Chien, S. *The Journal of General Physiology* **1973**, *61*, 638-654.
- (21) Nelson, D. L.; Cox, M. M. *Lehninger Principles of Biochemistry*, 4th ed.; W.H. Freeman & Co.: New York, 2005.
- (22) Hiemenz, P. C.; Rajagopalan, R. *Principles of Colloid and Surface Chemistry, Third Edition, Revised and Expanded*; Marcel Dekker: New York, 1997.
- (23) Shaw, D. J. *Introduction to Colloid and Surface Chemistry*, 4th ed.; Butterworth-Heinemann,: Oxford; Boston, 1992.
- (24) Hoffbrand, V.; Moss, P.; Pettit, J. *Essential Haematology*, 5th ed.; Wiley-Blackwell, 2006.

- (25) Janeway, C. A.; Travers, P.; Walport, M.; Shlomchik, M. *Immunobiology :The Immune System in Health and Disease*, 6th ed.; Garland Science and Churchill Livingstone: New York, 2005.
- (26) Czajkowsky, D. M.; Shao, Z. *PNAS* **2009**, *106*, 14960-14965.
- (27) Munn, E. A.; Bachmann, L.; Feinstein, A. *Biochimica et Biophysica Acta, Protein Structure* **1980**, *625*, 1-9.
- (28) Feinstein, A.; Munn, E. A. *Nature* **1969**, *224*, 1307-1309.
- (29) Fleer, G. J.; Stuart, M. A. C.; Scheutjens, J. M. H. M.; Cosgrove, T.; Vincent, B. *Polymers at Interfaces*, 1st ed.; Chapman & Hall: London, 1998 (Reprint).

---

# Chapter 6

---

Isothermal Non-  
Coalescence of Liquid  
Droplets at the Air-Liquid  
Interface

---

This page is intentionally blank

**Monash University**

**Declaration for Thesis Chapter 6**

**Declaration by candidate**

In the case of Chapter 6, the nature and extent of my contribution to the work was the following:

Nature of contribution	Extent of contribution (%)
Initiation, key ideas, experimental and analysis works, development and writing up of the paper	65

The following co-authors contributed to the work. Co-authors who are students at Monash University must also indicate the extent of their contribution in percentage terms:

Name	Nature of contribution	Extent of contribution (%) for student co-authors only
<b>Gil Garnier</b>	Initiation, key ideas, reviewing and editing of the paper	Co-supervisor
<b>Wei Shen</b>	Initiation, key ideas, reviewing and editing of the paper	Co-supervisor
<b>Dushmantha Kannangara</b>	Initiation and experimental work	25

Candidate's Signature

[Redacted Signature]

Date

18/12/09 ✓

**Declaration by co-authors**

The undersigned hereby certify that:

- (1) the above declaration correctly reflects the nature and extent of the candidate's contribution to this work, and the nature of the contribution of each of the co-authors.
- (2) they meet the criteria for authorship in that they have participated in the conception, execution, or interpretation, of at least that part of the publication in their field of expertise;
- (3) they take public responsibility for their part of the publication, except for the responsible author who accepts overall responsibility for the publication;
- (4) there are no other authors of the publication according to these criteria;
- (5) potential conflicts of interest have been disclosed to (a) granting bodies, (b) the editor or publisher of journals or other publications, and (c) the head of the responsible academic unit; and
- (6) the original data are stored at the following location(s) and will be held for at least five years from the date indicated below:

**Location(s)**

Australian Pulp and Paper Institute (APPI), Department of Chemical Engineering, Monash University, Clayton, VIC 3800, Australia.

**Signature 1**

[Redacted Signature]

Date

17/12/09

**Signature 2**

[Redacted Signature]

Date

17/12/09

**Signature 3**

[Redacted Signature] (for Dushmantha Kannangara)

Date

17/12/09

# Isothermal Non-Coalescence of Liquid Droplets at the Air-Liquid Interface

Mohidus Samad Khan, Dushmantha Kannangara, Wei Shen and Gil Garnier\*

Australian Pulp and Paper Institute,  
Department of Chemical Engineering,  
Monash University, Clayton, VIC 3800, Australia.

\*Corresponding author: Gil.Garnier@eng.monash.edu.au

Chapter 6	153
Isothermal Non-Coalescence of Liquid Droplets at the Air-Liquid Interface	153
Abstract	156
1. Introduction	157
2. Experimentals	160
2.1. Materials	160
2.2. Methods	161
3. Results	163
3.1. Mechanism of Drop Coalescence	163
3.2. The Physical Origin of the Non-Coalescence Droplets	165
3.3. Predicting the Occurrence of Secondary Non-Coalescent Droplets	166
4. Discussion	168
5. Conclusion	170
Acknowledgment	170
References	171

## ABSTRACT

The mechanism of generation and sustainability of non-coalescent droplets (N-C-D) was investigated on the liquid-air interface of the same liquids in the context of inkjet printing. The Weber Number ( $We$ ) was used to correlate and predict the generation of N-C-D in a falling drop experiment. This study found that N-C-D can be generated for  $We$  higher than 130.  $We$  of this magnitude are relevant to inkjet printing. The formation of N-C-D can reduce the print quality, as the N-C-D droplets roll away uncontrollably from the print target, thus reducing print resolution. This study also used a simple experiment to demonstrate the physical origin of the N-C-D, which is the existence of a gaseous cushion between the

liquid drop and the liquid-air interface that supports the drop. The gaseous cushion has a thickness greater than the van der Waals attraction range (around 10 nm).

## **1. INTRODUCTION**

The fluid mechanics of liquid drops impacting on liquid surfaces is of importance in a variety of applications, such as droplet combustions, separation of emulsion, pesticide delivery, fire fighting and inkjet printing<sup>1-4</sup>. Inkjet printing is a digital printing method which can be easily adapted to print biomolecules, such as peptides, DNA, antigens, or antibody, onto desirable substrates. Inkjet printing offers potential in bio-printing since it is a non-contact technique which can provide high printing resolution if the ink-substrate interaction is understood and controlled. Of special interest is the use of inkjet printing to manufacture bioassays and low cost paper diagnostics. These products can require a printing resolution better than 100  $\mu\text{m}$  for optical (fluorescence, luminescence) and conductive/potential detections. Inkjet printing typically delivers a series of droplets, 20  $\mu\text{m}$  in diameter, onto a surface. The substrates are often hydrophilic, porous and have a roughness length scale ranging from 0.5  $\mu\text{m}$  to 20  $\mu\text{m}$ ; paper and non-woven are good examples. Two phenomena are of concern to the engineer when an inkjet drop comes into contact with a surface. The first is the formation of satellite drops from the inkjet nozzle, which may form N-C-D that rolls from their target (Figure 1, Figure 2). The second is the wicking of the delivered droplet into long surface grooves, fibres or surface imperfections driven by capillary forces. Both phenomena reduce the print definition and consume non-functional biomolecules<sup>5-7</sup>. This study aims at preventing wastage of biomolecules due to print defect caused by the formation of non coalescent droplets.

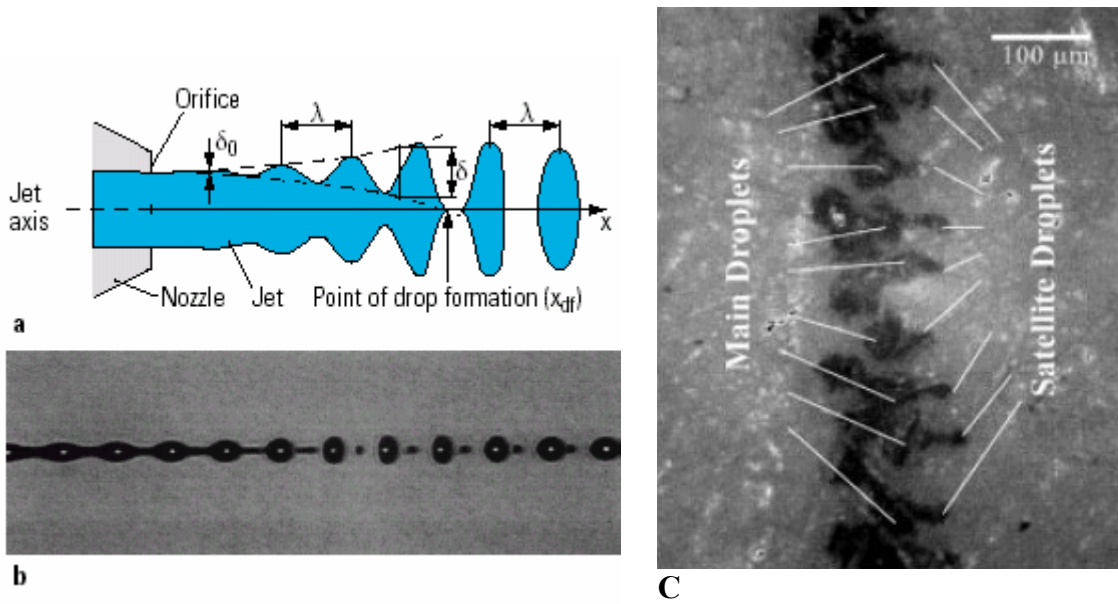


**Figure 1:** Drop formation with continuous inkjet and effect on printing: (a) Constriction of the inkjet to form a drop, (b) A stream of inkjet drops with satellite droplets behind the main drops in flight, (c) A magnified image of printed vertical line; (a) and (b) are taken from<sup>8</sup> and c from<sup>6</sup> (with permission).

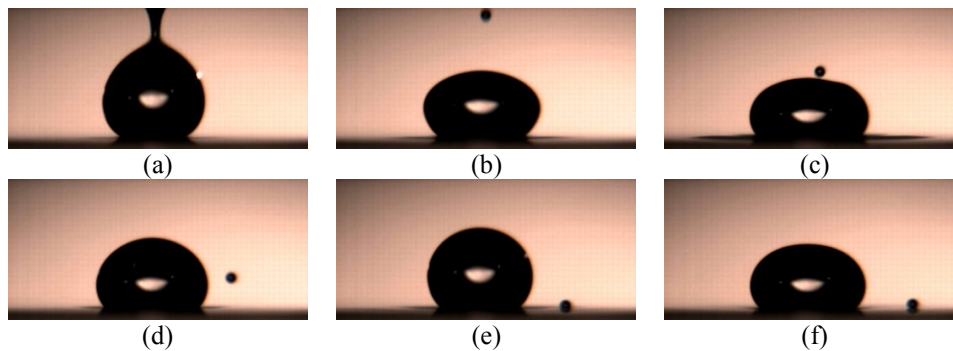


**Figure 2:** Non-coalescence behaviour of a satellite droplet.

A non-coalescent droplet is defined as a liquid droplet that retains its identity over a flat air-liquid interface<sup>9, 10</sup>. Droplet and flat liquid interface typically have the same bulk composition. We observe many manifestations of non-coalescent droplets in our daily life. An example is a drop of coffee falling from the percolator to roll and disappear into the coffee pot; another is the rain splashing and rolling over a puddle before disappearing. There are three broad categories of non-coalescence mechanisms: (a) the Leidenfrost effect, (b) the thermo-capillary induction, and (c) the isothermal non-

coalescence<sup>2, 11</sup>. The Leidenfrost effect describes a non-coalescent phenomenon of a liquid drop when it produces an insulating vapour layer which prevents the liquid drop from vapourizing rapidly. This occurs when the drop is in near contact with a mass whose temperature is significantly higher than the boiling point of the liquid<sup>12</sup>. The thermo-capillary induction is a bulk-fluid motion driven by temperature-induced variations of surface tension. Such temperature variation is also transferred to the surrounding ambient air, creating a stable air film between the drop and the surface, which prevents wetting and coalescence<sup>2, 13</sup>. In our daily life, we mostly observe the isothermal non-coalescence phenomenon. Moreover, N-C-Ds can be primary or secondary<sup>14</sup>. Primary N-C-Ds form when the droplet is delivered from a height of one or two centimetres, whereas secondary N-C-Ds form when the droplets fall from a height sufficient to splash and send satellite droplets rolling in different directions.

The isothermal non-coalescence of droplets was first reported by Lord Rayleigh as early as 1879 and by Osborne Reynolds in 1881<sup>11-13</sup>. Despite the number of investigations recorded since the 19<sup>th</sup> century, scientists were yet to explain different facets of the isothermal non-coalescence phenomenon. Study by Neitzel and Dell'Aversana showed that the generation of N-C-Ds requires the droplets to have a tangential velocity relative to the flat liquid surface<sup>11</sup>. It has been recognized that the droplet floats on a “gaseous cushion” (air in most cases) that must be drained to permit coalescence<sup>15</sup>. Charles and Mason<sup>16</sup> suggested that the coalescence of liquid drops was due to the contact of the liquid drop with the liquid surface supporting the drop. There is a need to better understand the isothermal non-coalescence behaviour of liquids.

Non-coalescent droplets form when a liquid drop impinges on a planar air-liquid interface. The drop impingement can also result in the complete engulfment of the drop in the pool of liquid (splashing), or in bouncing off the free surface<sup>9, 10</sup>. The collision of a drop with a surface is governed by many parameters. An analysis using dimensionless numbers, such as the Capillary Number, Bond Number and Weber Number, can shed light on the governing process<sup>3, 9-11, 17</sup>. The Capillary Number (Eq.1) represents the relative effect of viscous force versus the interfacial tension force acting across a liquid-gas interface. The Bond Number (Eq.2) is the ratio of gravity force to the surface tension of a liquid. The Weber Number (Eq.3) is perhaps better suited to explain the non-coalescence behaviour of liquid droplets. The Weber Number ( $We$ ) links the fluid inertia to the fluid surface tension and is useful to analyse the formation of droplets and bubbles.  $We > 1$  indicates that a high inertia force is required to overcome the surface

tension of a liquid and to provide sufficient axial velocity to the floating droplets. The dimensionless numbers are defined as:

$$\text{Capillary Number, } Ca = \frac{\mu v}{\gamma} = \frac{\text{Viscous Force}}{\text{Interfacial Tension Force}} \quad (1)$$

$$\text{Bond Number, } Bo = \frac{\rho R^2}{\gamma} = \frac{\text{Gravity Force}}{\text{Interfacial Tension Force}} \quad (2)$$

$$\text{Weber Number, } We = \frac{\rho v^2 R}{\gamma} = \frac{\text{Inertial Energy}}{\text{Interfacial Energy}} \quad (3)$$

where  $\rho$  is the liquid density,  $R$  is the radius of liquid drop,  $\mu$  is the viscosity of liquid,  $\gamma$  is the liquid surface tension,  $g$  is the acceleration associated with the body force, and  $v$  is the impact velocity of liquid the drop.

The objectives of this study are twofold. The first is to experimentally elucidate the mechanism of non-coalescent droplets and to control the coalescence process. The second is to quantify the non-coalescence/coalescence transition in a configuration relevant to inkjet printing. This study aims at increasing the print resolution through understanding and controlling the N-C-D ink droplets, which could lead to print defects and decreasing consumption of biomolecules to efficiently manufacture bio-medical devices.

## 2. EXPERIMENTALS

### 2.1. Materials

Analytical grade n-undecane (Aldrich), ethyl alcohol (99.7%, Aldrich), water (Millipore, 18M $\Omega$ ), surfactant solutions (Triton X-100, C<sub>34</sub>H<sub>62</sub>O<sub>11</sub>, from AJAX Chemicals, Australia. CMC  $\approx$  0.2 mM (25°C)), Alkenyl Ketene Dimer (liquid AKD, melting point  $<$  0°C, from Hercules Chemicals Australia Pty Ltd.), 0.095M sulphuric acid solution and 0.22M sodium hydroxide solution were used. All experiments were performed at 23°C, and 50% relative humidity. The surface tension of the surfactant solution was measured using an *OCAH-230* apparatus (Dataphysics, Germany). Density was measured with a *METTLER TOLEDO Densito 30Px* (Switzerland).

Burettes were used to generate the sessile droplets. Glass slides were obtained from Bio Lab, Australia. Large glass petri-dishes (15cm Diameter) and beakers were used to enclose the liquid surfaces.

## 2.2. Methods

### 2.2.1. Drop Coalescence Mechanism

To observe the coalescence mechanism of liquid drops, an *OCAH-230* apparatus (Dataphysics, Germany) and a *Photron Fastcam Super 10KC* (San Diego, USA) were used. The *OCAH-230* consists of a computer controlled liquid drop dispensing syringe pump. For capturing the droplet coalescence, the high speed camera *Photron Fastcam Super 10KC* was set at 500 frames per second (fps), with a shutter speed of 1/500 sec. To generate drops of surfactant solution, a syringe with a flat-tip stainless steel needle (O.D. 0.31 mm) was fitted to the syringe pump, controlled with the *Dataphysics Instruments GmbH* program. The needle was placed above the liquid surface such that the drop generated could just touch the surface. *Image-pro Plus* software was used to analyse the droplet images.

### 2.2.2. Interphase between Non-Coalescent Droplet and Liquid Interface

Two liquid solutions of different pH were used. A weak sulphuric acid solution [0.095M] was placed into a large beaker. A concentrated phenolphthalein solution was added to the acidic solution. Phenolphthalein is a colour indicator that sharply changes the colour of the solution into an intense red when pH exceeds 8.3<sup>18</sup>; below its critical pH, phenolphthalein remains colourless. The beaker was manually rotated to create an angular surface velocity in the acidic solution. Drops of an alkaline solution (sodium hydroxide, 0.22M) were delivered on the rotating liquid surface (Figure 6). The drops were formed from the tip of a dropper (I.D. 0.5 mm) maintained between one and two centimetres above the surface to generate primary N-C-Ds. A white ceramic-tile was used as background to increase contrast and detect the colour change caused by any diffusion across the acid-alkaline solution interface. A standard SONY DCR-HC36 video camera equipped with *Windows Movie Maker* software was used to capture the images of the primary non-coalescence phenomena.

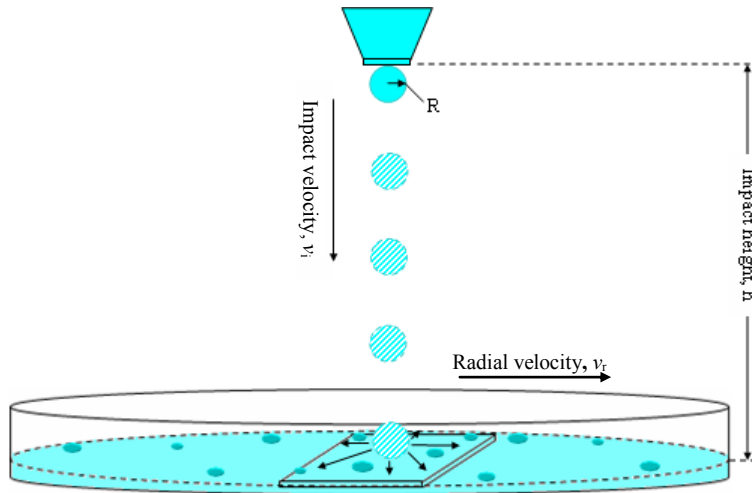


**Figure 3: Schematic diagram of formation of secondary Non-Coalescent Droplets.**

### 2.2.3. Formation of Secondary Non-Coalescent Droplet

A simple setup was used to generate liquid drops from different heights ( $h$ ) on the stationary surface of the same liquid and to crack the drops on the surface and generate secondary N-C-D of different sizes (Figure 3). The configuration of the experimental setup can help to predict the occurrence of secondary N-C-Ds in inkjet printing by impinging the liquid drop on the liquid surface at a certain velocity. To quantify the formation of secondary N-C-Ds, five model liquids were studied: n-undecane, water, aqueous surfactant solutions, ethanol and mercury. Liquids of different surface tensions but similar viscosities were selected (Table I). Drops of identical size were generated at a constant rate with burettes (standard deviation  $< 0.1$  for  $n=20 \times 5$  drops, Table I). Drop samples were taken at different time intervals of the experiment and were weighed in a four digit digital balance (20 droplets each time, 5 samples for each liquid). The burette was placed on a mechanical jack to vary the droplet heights. The drops were dispensed onto the middle of a glass slide ( $2.54\text{cm} \times 2.54\text{cm}$ ) placed horizontally into the petri-dish and just submerged into the same liquid to a depth of around 0.5 mm (Figure 3). The submerged glass slide provides a hard surface to break the falling drops into smaller droplets as they hit the liquid surface with a sufficient kinetic energy. The frequency of drop dispensing rate was chosen to allow adequate time for impact disturbances or ripples in the Petri dish to settle. The drop radius used in the calculation is the equivalent spherical radius of the

drop,  $R$  (Eq.4), determined by weighing 100 drops. Impact height of the dispensed drop along with its impact velocity,  $v$  (Eq.5) were calculated with:

$$R = \sqrt{\frac{3m}{4\pi n \rho}} \quad (4)$$

$$v = \sqrt{2gh} \quad (5)$$

where,  $m$  is the total mass of  $n$  drops,  $\rho$  is the density of liquid at 23°C and  $h$  is the impact height. The probability of generating secondary N-C-Ds from this impact study was calculated by determining the number of drops that generate N-C-Ds in every ten drops tested.

**Table I: Physical properties of liquid droplets at 23°C<sup>19</sup>**

Name of Liquid	Surface Tension, $\gamma$ (N/m)	Density, $\rho$ (kg/m <sup>3</sup> )	Viscosity, $\mu$ (mPa-s)	Equivalent Radius of Droplet, $R$ (mm)	St. Dev. Radius (n=20×5)
Ethanol	$2.21 \times 10^{-2}$	789.0	1.131	2.67	0.0977
n-Undecane	$2.44 \times 10^{-2}$	740.0	1.147	2.87	0.0067
Surfactant Solution	$3.01 \times 10^{-2}$	998.4	0.962*	2.56	0.0323
Water	$7.20 \times 10^{-2}$	997.5	0.962	3.84	0.0092

\* assuming same as water

### 3. RESULTS

#### 3.1. Mechanism of Drop Coalescence

Pendant drops of aqueous surfactant were first studied to quantify the coalescing behaviour. Photographs of a typical sequence are shown in Figure 4. When the drop was brought into contact with a flat surface of the same solution, drop coalescence occurred within 20 ms. The drop and the flat liquid surface first established a very small area of contact (Figure 4b). This contact point forms a liquid hyperbolic pillar of very small radius of curvature (ring). This ring extends out radially due to the Laplace pressure associated with the curvature. The Laplace pressure quickly reduces as the radius of curvature of the ring increases (Figure 4b, c). At the same time, the contact area between the drop and the flat liquid surface increases and the drop forms a neck

and eventually coalesces. Once the Laplace pressure instigates the coalescing mechanism (Figure 4b, c), the collapse is rapid (Figure 4 d – h) due to the combined effects of gravitational force and Laplace pressure.

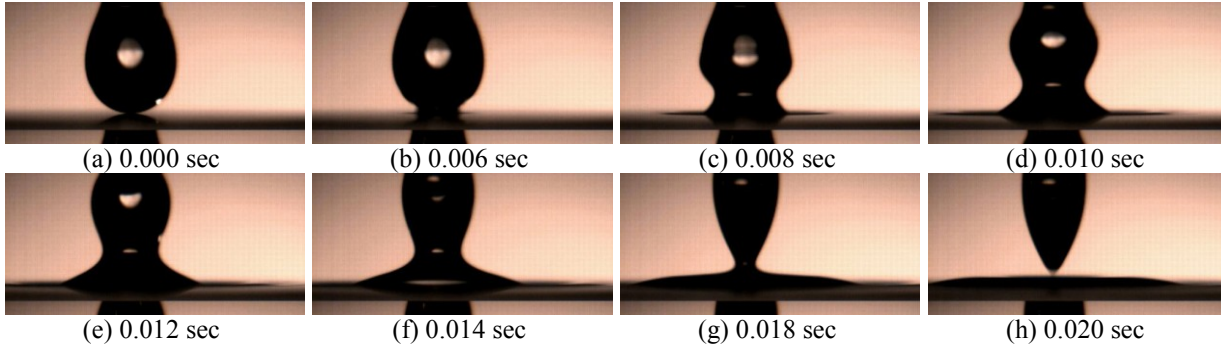


**Figure 4: Pendant droplet: coalescing mechanism at the air-liquid interface of a surfactant solution. (Video 1 on the web)**

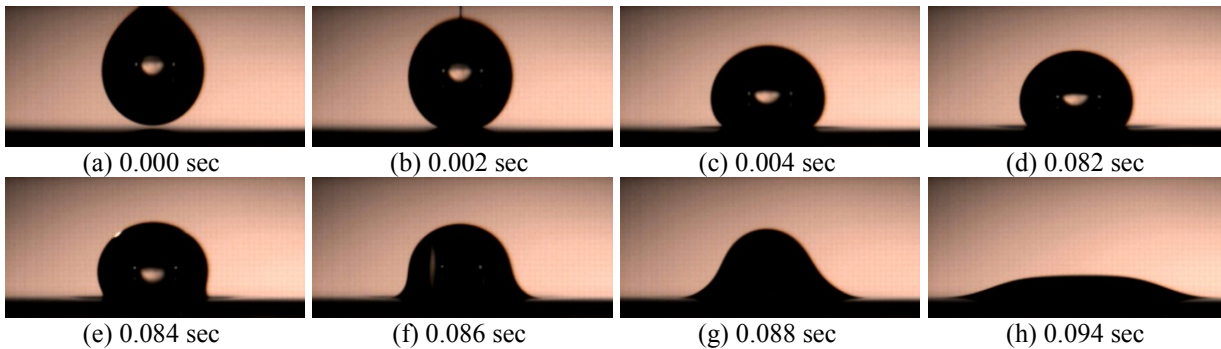


**Figure 5: Sessile droplet: coalescing mechanism at the air-liquid interface of AKD. (Video 2 on the web)**

Figure 5 shows sequential pictures of the typical coalescence behaviour of a liquid AKD sessile drop on a flat surface of liquid AKD. The drop was gently placed onto the liquid surface. The small momentum of the drop did not cause splashing or engulfment of the drop by the liquid; the drop retained its size and shape for about 78 ms. The flat liquid surface was slightly depressed by the drop's weight. However, no sign of a liquid pillar connecting the drop to the liquid surface was visible. The coalescing of the immobile drop commenced after 80 ms of drop-liquid surface contact. A pillar of small radius of curvature developed between the drop and the flat liquid surface (Figure 5e). The growth of the ring and the final coalescence of the AKD

sessile drop occurred in a similar fashion to that of the surfactant pendant drop. We have recorded this behaviour of drop coalescence for several other liquids: water, ethanol and n-undecane; it is likely universal. The only liquid studied which did not show N-C-D behaviour was mercury. This agrees with the observations of Rayleigh and Hsiao<sup>1, 11</sup>.

### 3.2. The Physical Origin of the Non-Coalescence Droplets

Liquid drops can be sustained on the flat surface of the same liquids for periods ranging from milliseconds to minutes<sup>11, 12</sup>. The life of a droplet gently rotated over the surface of the same liquid is shown on Figure 6.

It has been proposed that isothermal non-coalescent droplets could be supported by a gaseous interphase between the drop and the flat liquid surface<sup>15, 16</sup>. Here we present direct experimental evidence supporting the existence of a gaseous interface.

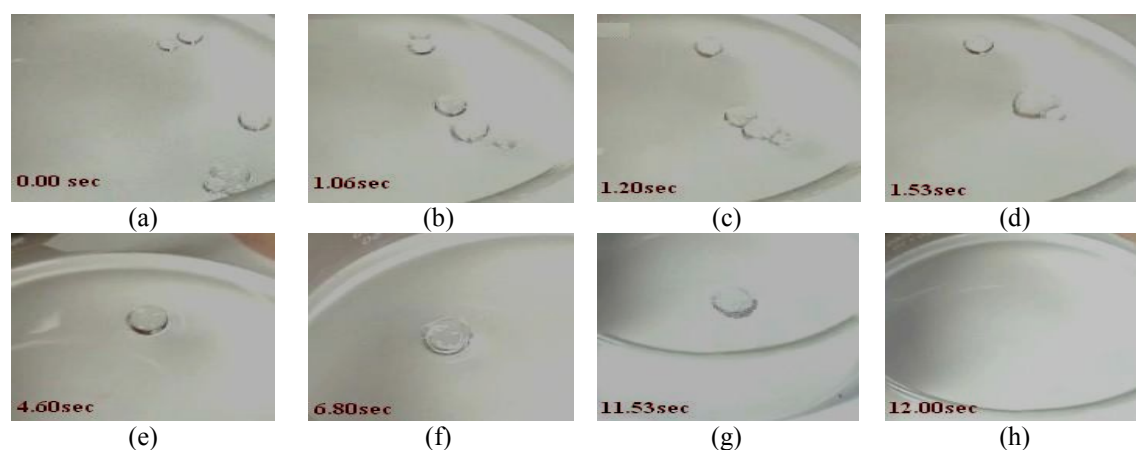


**Figure 6:** Formation of non-coalescent droplets of NaOH [0.22M] in a TritonX-100 solution (0.8 mM) on air-liquid interfaces ( $\text{H}_2\text{SO}_4$ , 0.095M in the same surfactant solution with phenolphthalein dye). The non-coalescent droplets and the interface showed no colour change. (Video 3 on the web)

Our investigation is focused on determining whether or not any material transfer occurs between the liquid phase and the non-coalescent drop. Non-coalescent droplets of sodium hydroxide [0.22M] in a TritonX-100 solution (0.8 mM) were formed over the air-liquid interface of a weak sulphuric acid [0.095M] in a TritonX-100 solution (0.8 mM) containing phenolphthalein. A relative movement between the droplet and the

interface over some critical velocity is required<sup>20</sup> for the N-C-D to survive. An angular motion was provided to the beaker, which held the acidic solution, and primary N-C-Ds were generated on the acidic liquid surface by depositing droplets of alkaline solution on the acidic solution. The longest life-time of N-C-D observed was 11.53 seconds (Figure 6g). Under non-coalescence conditions the colour of N-C-Ds remained unchanged, indicating that no transfer of phenolphthalein occurs from the acid solution into the alkaline drop. Immediately upon coalescence of the droplet, a transient red cloud formed in the acid solution, driven by the high local pH causing the colour change of the phenolphthalein.

### 3.3. Predicting the Occurrence of Secondary Non-Coalescent Droplets

Understanding secondary N-C-D is important in inkjet printing. The amount of (kinetic) energy a liquid drop carries before impinging onto a flat liquid surface affects N-C-D generation. In our experiment, we converted the potential energy of the drops into kinetic energy by breaking them into smaller secondary N-C-Ds supplied with horizontal momentum (Figure 3). A series of drops were dispensed onto the interfaces of the same liquid from different heights, and the probability of forming non-coalescent droplets was reported. Different fluids were investigated. Results are presented in terms of probability of forming a non-coalescent droplet as a function of impingement height (Figure 7) and Weber Number (Figure 8).

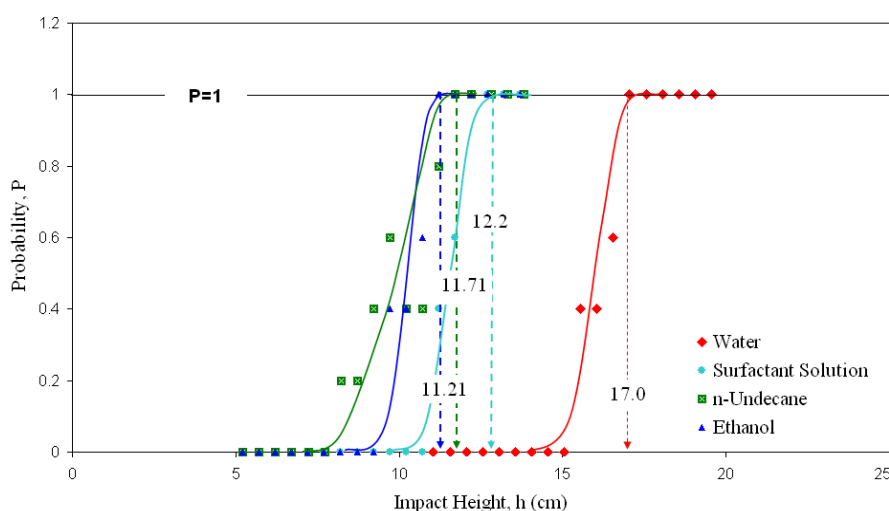


**Figure 7:** Probability of forming secondary non-coalescent droplets as a function of the impinging height.

Compared with low surface tension liquids (e.g. n-undecane), drops of high surface tension liquids (e.g. water) require a greater kinetic energy to break and generate secondary N-C-Ds. There is a critical potential energy level required for each liquid to form secondary N-C-D. Beyond this critical level, all fluids form N-C-Ds (probability = 1).

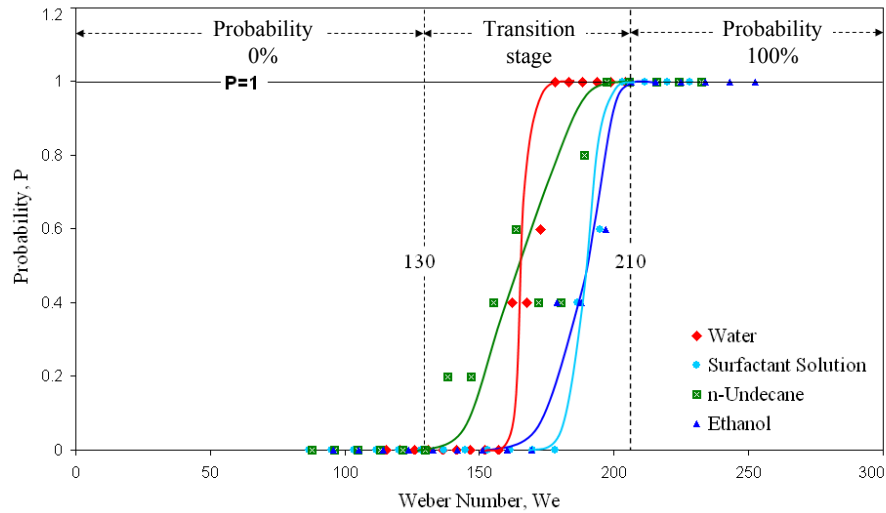


**Figure 8: Probability of forming secondary non-coalescent droplets as a function of the Weber Number.**

The correlation of the Weber Number ( $We$ ) with the N-C-Ds can be used as a predictive indicator of the occurrence of N-C-Ds. The probability of forming secondary N-C-D becomes unity when a critical value of  $We$  ( $\approx 210$ ) is reached, whereas the probability is virtually zero for  $We \leq 130$  (Figure 8). In the sharp sigmoidal transition stage ( $210 > We > 130$ ) the probability varies between zero and unity. The drop height and Weber Number for which the probability of forming non-coalescent droplets is one are defined as the critical impact height ( $h_c$ ), and critical Weber Number ( $We_c$ ), respectively. The critical values vary slightly from liquid to liquid according to their surface tension (Figure 7, Figure 8).

#### 4. DISCUSSION

The formation of a contact point between the liquid drop and the flat liquid surface triggers drop coalescence for pendant drops and sessile drops. This mechanism of drop coalescence is the same for all liquids (fluid independent). The initial triggering contact between the drop and the liquid surface does not have to be on the vertical centre line of symmetry. The non-symmetric movement of the liquid pillar supports our claim (Figures 5 e and 5 f). The initial driving force for the liquid pillar is the Laplace pressure associated with the curvature of its ring (Figure 9). The Laplace pressure may be written as:

$$\Delta P = \gamma \left( \frac{1}{R} - \frac{2}{d} \right) \quad (7)$$

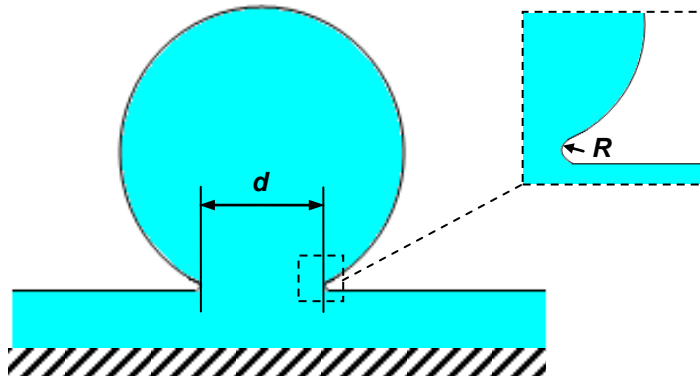


**Figure 9:** Schematic presentation of droplet coalescence as triggered by the Laplace Pressure.

where,  $d$  is the diameter of the liquid pillar (drop-liquid contact circle) and  $R$  is the radius of curvature of the liquid pillar. According to the *Laplace Pressure*, a small value of capillary radius dominates the coalescence-driving force ( $\Delta P$ ), which increases the diameter of the liquid pillar and eventually triggers the sudden collapse of the liquid drop to the horizontal liquid surface (when a critical flow rate can be reached).

The simple acid-base indicator approach was used to demonstrate the existence of a gaseous interphase separating the liquid drop from the flat liquid surface. The composition of this interphase is unknown. It has been previously suggested that the

interphase is saturated by the liquid vapour<sup>10, 11, 21</sup>. The interphase must have a thickness greater than the van der Waals attraction force range so that the macro-body van der Waals attraction forces between the drop and the liquid surface can be cut off. The van der Waals attraction range between macro-bodies is in the order of 10 nm<sup>22, 23</sup>. The small gaseous gap between the drop and the liquid surface, however, may strongly encourage the vapour to condense at a vapour pressure much lower than the saturated vapour pressure. The condensed vapour could provide the initial seed of the drop-liquid contact.

The formation of secondary N-C-Ds is controlled by the physical properties of the liquids: viscosity, interfacial tension, and surface mobility<sup>11</sup>, along with the mechanical properties of the flat interface. The solid surface properties are assumed to be constant during the experiment. The probability of occurrence of secondary N-C-Ds was quantified in terms of impact height and the Weber Number. There is a critical value of  $We$  for any liquid, below which the probability of generating secondary N-C-Ds becomes zero. However, no perfect master line was achieved for the different fluids, suggesting that some factors other than interfacial force and inertia affect the phenomena. An explanation could simply be that the thickness variability of the liquid film (around 0.5 mm) covering the solid surface.

Despite achieving no perfect master curve for all liquids, Figure 8 shows a Weber Number transition range over which secondary N-C-D formation was observed ( $We$ : 130 – 210). The probability of forming secondary N-C-D exists at  $We$  greater than 130. For inkjet printing where the ink droplet size is very small, the critical ink droplet size for N-C-D can also be calculated from the Weber Number. Assuming the density of ink to be 1000 Kg/m<sup>3</sup>, the surface tension 0.03 N/m and the ink drop speed 20 m/s<sup>24</sup>,<sup>25</sup>, the  $We$  transition regime suggests that any ink droplets bigger than 4.0 pL (= 4.0×10<sup>-15</sup> m<sup>3</sup>) can form N-C-D. Therefore, print quality defects caused by N-C-Ds can be a real problem in inkjet printing where many ink droplets impinge on other droplets.

Non-coalescent droplets can also be formed at  $We$  much lower than these critical values under inkjet printing configuration<sup>3, 10, 12</sup>. To create secondary N-C-Ds, a higher inertial force is required to break the drops on the surface and to convert the axial momentum/velocity of the dispensed drop into radial velocity of floating droplets. The Weber Number ( $We_r$ ) corresponding to the radial velocity ( $v_r$ ) of N-C-D is most likely the dimensionless number that determines the probability of forming primary N-C-D (Figure 3).

## **5. CONCLUSION**

A simple experiment was designed to demonstrate the mechanism which enables the occurrence of non-coalescence droplets. Our results show that there is no liquid transfer across the interface between a non-coalescent droplet and the liquid phase supporting it. This is because a third phase (gas or air) of a thickness greater than the van der Waals attraction force range is present between the two liquid phases, preventing the attractive van der Waals attraction force from pulling the two liquid phases together. Inertia or an impact height greater than a critical value is required to create secondary N-C-Ds. The probability of forming secondary N-C-Ds can be quantified from the Weber Number and a pseudo master curve (Figure 8). Better understanding of the mechanism of liquid droplet coalescence allows us to improve inkjet resolution, thus increasing the economy and the quality of biomolecule printing.

## **ACKNOWLEDGMENT**

M.S.K and D.K would like to gratefully acknowledge the Department of Chemical Engineering, Monash University for their Postgraduate Scholarships.

## REFERENCES

- (1) Rein, M. *Fluid Dynamic Research* **1993**, *12*, 61-93.
- (2) Savino, R.; Monti, R.; Nota, F.; Fortezza, R.; Carotenuto, L.; Piccolo, C. *Acta Astronautica* **2004**, *55*, 169-179.
- (3) Sikalo, S.; Ganic, E. N. *Experimental Thermal and Fluid Science* **2006**, *31*, 97-110.
- (4) Kannangara, D.; Zhang, H.; Shen, W. *Colloids and Surfaces A: Physicochem. Eng. Aspects* **2006**, *280*, 203-215.
- (5) Barbulovic-Nad, I.; Lucente, M.; Sun, Y.; Zhang, M.; Wheeler, A. R.; Bussmann, M. *Critical Reviews in Biotechnology* **2006**, *26*, 237-259.
- (6) Tseng, F.-G.; Kim, C.-J.; Ho, C.-M. *Journal of Microelectromechanical Systems* **2002**, *11*, 427-436.
- (7) Tseng, F.-G.; Kim, C.-J.; Ho, C.-M. *Journal of Microelectromechanical Systems* **2002**, *11*, 437-447.
- (8) Kipphan, H., Ed. *Handbook of Print Media*; Springer, 2001.
- (9) Fedorchenko, A. I.; Wang, A.-B. *Physics of Fluids* **2004**, *16*, 1349-1365.
- (10) Honey, E. M.; Kavehpour, H. P. *Physical Review E* **2006**, *73*, 027301-027301 - 027301-027303.
- (11) Neitzel, G. P.; Dell'Aversana, P. *Annual Review of Fluid Mechanics* **2002**, *34*, *ProQuest Science Journals*, 267-289.
- (12) Sreenivas, K. R.; De, P. K.; Arakeri, J. H. *Journal of Fluid Mech.* **1999**, *380*, 297-307.
- (13) Dell'Aversana, P.; Neitzel, G. P. *Physics Today* **1998**, *51*, 38-41.
- (14) Seth, J. B.; Anand, C.; Mahajan, L. D. *Philosophical Magazine (1798-1977)* **1929**, *7*, 247-253.
- (15) Jayaratne, O. W.; Mason, B. J. *Proceedings of the Royal Society of London Series a-Mathematical and Physical Sciences* **1964**, *280*, 545-&.
- (16) Charles, G. E.; Mason, S. G. *Journal of Colloid and Interface Science* **1960**, *15*, 105-122.
- (17) Miura, K.; Miura, t.; Ohtani, S. *AIChE Symposium Series* **1977**, *73*, 95-102.
- (18) Jeffery, G. H.; Bassett, J.; Mendham, J.; Denney, R. C. *Vogel's Textbook of Quantitative Chemical Analysis*, 5 ed.; ELBS, 1989.
- (19) Lide, D. R., Ed. *CRC Handbook of Chemistry and Physics*, 76 ed.; CRC Press, INC., 1995-96.
- (20) Dell'Aversana, P.; Monti, R.; Gaeta, F. S. *Adv. Space Res.* **1995**, *16*, 95-98.
- (21) Xue, H.; Koshizuka, S.; Oka, Y. *International Journal for Numerical Methods in Fluids* **2004**, *45*, 1009-1023.
- (22) Adamson, A. W.; Gast, A. P. *Physical Chemistry of Surfaces*, 6 ed.; John Willey & Sons: Chapter XII, Section 8, New York, 1997 (b).
- (23) Hiemenz, P. C.; Rajagopalan, R. *Principles of Colloid and Surface Chemistry*, 3 ed.; Marcel Dekker: Chapter 6 and Chapter 10, New York, 1997.
- (24) Asai, A.; Shioya, M.; Hirasawa, S.; Okazaki, T. *Journal of Imaging Science and Technology* **1993**, *37*, 205-207.
- (25) Le, H. P. *Imaging Science and Technology* **1998**, *42*, 49 - 62.

This page is intentionally blank

---

# Chapter 7

---

Wicking of a Liquid  
Droplet in a Surface  
Groove

---

This page is intentionally blank

**Monash University**

**Declaration for Thesis Chapter 7**

**Declaration by candidate**

In the case of Chapter 7, the nature and extent of my contribution to the work was the following:

Nature of contribution	Extent of contribution (%)
Initiation, key ideas, experimental and analysis works, development and writing up of the paper	45

The following co-authors contributed to the work. Co-authors who are students at Monash University must also indicate the extent of their contribution in percentage terms:

Name	Nature of contribution	Extent of contribution (%) for student co-authors only
<b>Wei Shen</b>	Initiation, key ideas, reviewing and editing of the paper	Co-supervisor
<b>Dushmantha Kannangara</b>	Initiation, key ideas, experimental and analysis works, development and writing up of the paper	45

**Candidate's Signature**



**Date**

16/12/09

**Declaration by co-authors**

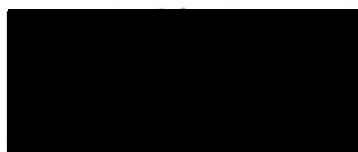
The undersigned hereby certify that:

- (1) the above declaration correctly reflects the nature and extent of the candidate's contribution to this work, and the nature of the contribution of each of the co-authors.
- (2) they meet the criteria for authorship in that they have participated in the conception, execution, or interpretation, of at least that part of the publication in their field of expertise;
- (3) they take public responsibility for their part of the publication, except for the responsible author who accepts overall responsibility for the publication;
- (4) there are no other authors of the publication according to these criteria;
- (5) potential conflicts of interest have been disclosed to (a) granting bodies, (b) the editor or publisher of journals or other publications, and (c) the head of the responsible academic unit; and
- (6) the original data are stored at the following location(s) and will be held for at least five years from the date indicated below:

**Location(s)**

Australian Pulp and Paper Institute (APPI), Department of Chemical Engineering, Monash University, Clayton, VIC 3800, Australia.

**Signature 1**



**Date** 17/12/09

**Signature 2**

Dushmantha Kannangara

**Date** 17/12/09

# Wicking of a Liquid Droplet in a Surface Groove

Dushmantha Kannangara<sup>1</sup>, Mohidus Samad Khan<sup>1</sup> and Wei Shen\*

Australian Pulp and Paper Institute,  
Department of Chemical Engineering,  
Monash University, Clayton, VIC 3800, Australia.

<sup>1</sup> First authors

\*Corresponding author: Wei.Shen@eng.monash.edu.au

Chapter 7	173
Wicking of a Liquid Droplet in a Surface Groove	173
Abstract	176
1. Introduction	177
2. Experimentals	179
2.1. Materials	179
2.2. Sample Preparation and Cleaning	182
2.3. Experimental Setup	183
3. Theory	185
3.1. Background	185
3.2. Model Considerations in this Study	187
4. Results and Discussion	188
4.1. V-Groove Geometry	188
4.2. Spreading of Liquid Droplet on Smooth Quartz Surface	188
4.3 Spreading and Wicking of Water on Quartz Surface with V-grooves	189
4.4. Model consideration and derivation	192
4.5. Water Wicking Kinetics in V-grooves	198
5. V-groove wicking – comparison of experimental data and models	205
6. Implication of using the V-groove geometry to control ink wicking rate in an inkjet printing application	208
7. Conclusions:	208
Acknowledgment	209
References	210

## ABSTRACT

**T**his paper reports a study of liquid wicking in V-shaped grooves (open capillaries) in early stage of liquid-groove contact. An experimental setup consisting of two high-speed video cameras is developed to capture images of first few milliseconds of the liquid wicking in V-shaped grooves. The

rate of wicking considered in this study is about two orders of magnitude faster than those previously reported in literature. V-groove geometry is systematically varied to understand the effect of apex angle and the groove width on liquid wicking rate. Our results show that both the groove width and the apex angle significantly influence on the rate of wicking. We presented an alternative mathematical model to calculate liquid wicking distance ( $z$ ) in V-groove. Our new model shows a square root of time dependence of wicking distance similar to the literature. Laplace pressure in the threshold region of the wicking front is used to derive the driving force, instead of surface energy change used by Rye and coworkers. Special attention was given to the liquid-solid wetting condition inside the groove; the equilibrium contact angle inside the groove was found to be different from the macroscopic contact angle ( $\alpha$ ) measured on flat solid surface. This difference in contact angle resulted in a conclusion that liquid wicking is possible when  $\theta = \alpha$ . The gravity effect was also considered as a possible driving force in this study. Our model, together with the literature model, shows reasonably good agreement with the experimental data. Differentiation between the models is mainly in proportionality term containing groove geometry parameters and liquid wetting condition. The understanding of V-groove wicking has direct implications to the surface design of uncoated papers for inkjet printing and in low-cost microfluidic devices.

**Key Words:** V-shaped grooves, capillary wicking, inkjet printing, surface topography

## 1. INTRODUCTION

Understanding the kinetics of liquid wetting and wicking on surfaces with patterned topographic features is an important requirement in many industrial applications including printing technology [1-3], textile industries [4], pharmaceutical applications [5] and microfluidic systems [6, 7]. Surface chemical and topographical properties of the substrate, as well as the physical properties of the liquid, play different but equally important roles in controlling the wetting and wicking process.

Many liquid penetration systems involving porous solid media have been studied using the Washburn model [8]. This model predicts that the liquid penetration

distance in a cylindrical capillary is linearly related to the square root of time. Such a relationship for cylindrical capillaries was later confirmed experimentally by many researchers including Fisher and Lark [9]. Attempts to adapt the original Washburn model to liquid penetration in porous media have shown that the general relationship of penetration distance and the square root of time is obeyed.

A special case of liquid penetration in a porous medium is the liquid wicking in open capillaries on solid surface. Liquid wicking in open capillary channels is relevant to many applications including the management of spacecraft propellant under low-gravity conditions [10], liquid transport in biomedical chips [11], wetting of human skin by water [5] and surface wicking of water-based inks on paper surface in printing [1], to name just a few. However, liquid wicking in open capillaries cannot be explained by the original Washburn model, which was derived and adapted for cylindrical pores [12].

The development of inkjet printing technology and the fabrication of low-cost microfluidic sensors using paper have motivated further research on the wetting and wicking of water or water-based inks on and into paper [1, 3, 13-15]. The microscopic behaviour of liquid penetration in paper has also been reported [1, 16-18]. These studies have presented a fresh understanding of liquid penetration behaviour in responding to the geometric features of the pores. Roberts et al. [16] showed that a wetting fluid on a paper surface has four flow paths. These flow paths can be within the bulk pores, along the channels formed by inter fibre gaps, along crevices formed by indentations and surface roughness of the intra-fibre pores, and within intra fibre pores. It has been observed that the capillary channels of inter fibre gaps in paper are the preferred flow path for liquids, since this flow path has fewer discontinuities that hinder the liquid flow.

Rye et al. [19] proposed one of the first models for liquid wicking in V-groove capillary channels. Their model was established on the principle of (interfacial) energy balance, and at the same time considered the balance of a capillary driving force and the Poiseuille type liquid flow resistance force in a V-groove channel. By applying the boundary conditions that the V-groove connected to a large reservoir with no external pressure, Rye et al. arrived at a model which gives the similar penetration and time relationship to that by the Washburn model for cylindrical capillaries [19]. Rye's model shows a strong dependence of liquid wicking rate upon V-groove geometry. However, it is worth noting that Rye's model did not focus on the actual liquid wetting condition

inside in the groove. This model predicts the liquid wicking in V-groove becomes zero when the liquid contact angle  $\theta$  equals to  $\alpha$ , see Figure 4.

The motivation of this study is to further pursue our understanding of the liquid wicking behaviour in an open surface groove with two specific interests: First, the wicking of water-based inks on paper surface in inkjet printing. This is because uncontrolled ink wicking in inkjet printing is a significant cause of poor print quality. Therefore, the driving force of surface wicking or feathering of ink on paper needs to be understood and minimized. Second, transport liquid sample through open microfluidic channels. In open microfluidic system which relies only on capillary action as the driving force, the groove geometry can be used to optimize liquid transport efficiency.

In this study, we report the establishment of our experimental setup which allows the acquisition of the liquid wicking data in the very early stage of liquid wicking in grooves. The collection of these data then allows a comparison of the experimental observations and the theoretical predictions. V-grooves formed on quartz surface are used in our experiment. The advantage of using V-grooves on quartz, besides simplicity, is that the groove geometry can be precisely characterized using a range of different methods [19]. An alternative capillary wicking model is also presented by taking a different consideration from that of the literature models. We focus on the geometry of the liquid wicking threshold and the Laplace driving force generated by the curved liquid surface. We found, unexpectedly, that liquid wicking can proceed even when the principle curvature of the liquid threshold becomes zero and the Laplace pressure also becomes zero. Further analysis shows that liquid equilibrium contact angle in the groove is different from the equilibrium contact angle on a flat solid surface. An analysis of the gravity effect of the liquid reservoir on V-groove wicking is also given.

## 2. EXPERIMENTALS

### 2.1. Materials

Quartz V-groove samples of different groove angle ( $\beta$ ) = 60°, 90°, 120° and groove width ( $w_0$ ) = 200 $\mu$ m, 500  $\mu$ m, were obtained from Hatakensaku Pty Ltd, Japan. The supplier also provided measurements of the dimensions of the V-groove using an undisclosed automated measurement system (Figure 1, Table I).

The V-groove cross-section profile (apex angle) and the width were checked to verify the supplier's specifications. Scanning Electron Microscopy (SEM) (FEG-SEM, JSM-6300F, JEOL, Japan), profilometry (COTEC-Altisurf© 500) and optical microscopy (Olympus BX60 with a CCD camera) were used for the V-groove dimension verification (Figure 2).

Millipore water (18M $\Omega$ ) was used as the wicking liquid. All glassware were washed in 5% HNO<sub>3</sub> solution prepared using concentrated nitric acid (Labscan Analytical Science Pty Ltd) and rinsed with ample amount of water [20]. The cleaned glassware were first dried with fast flowing high purity nitrogen gas and then in an oven at 80°C for 8 h.

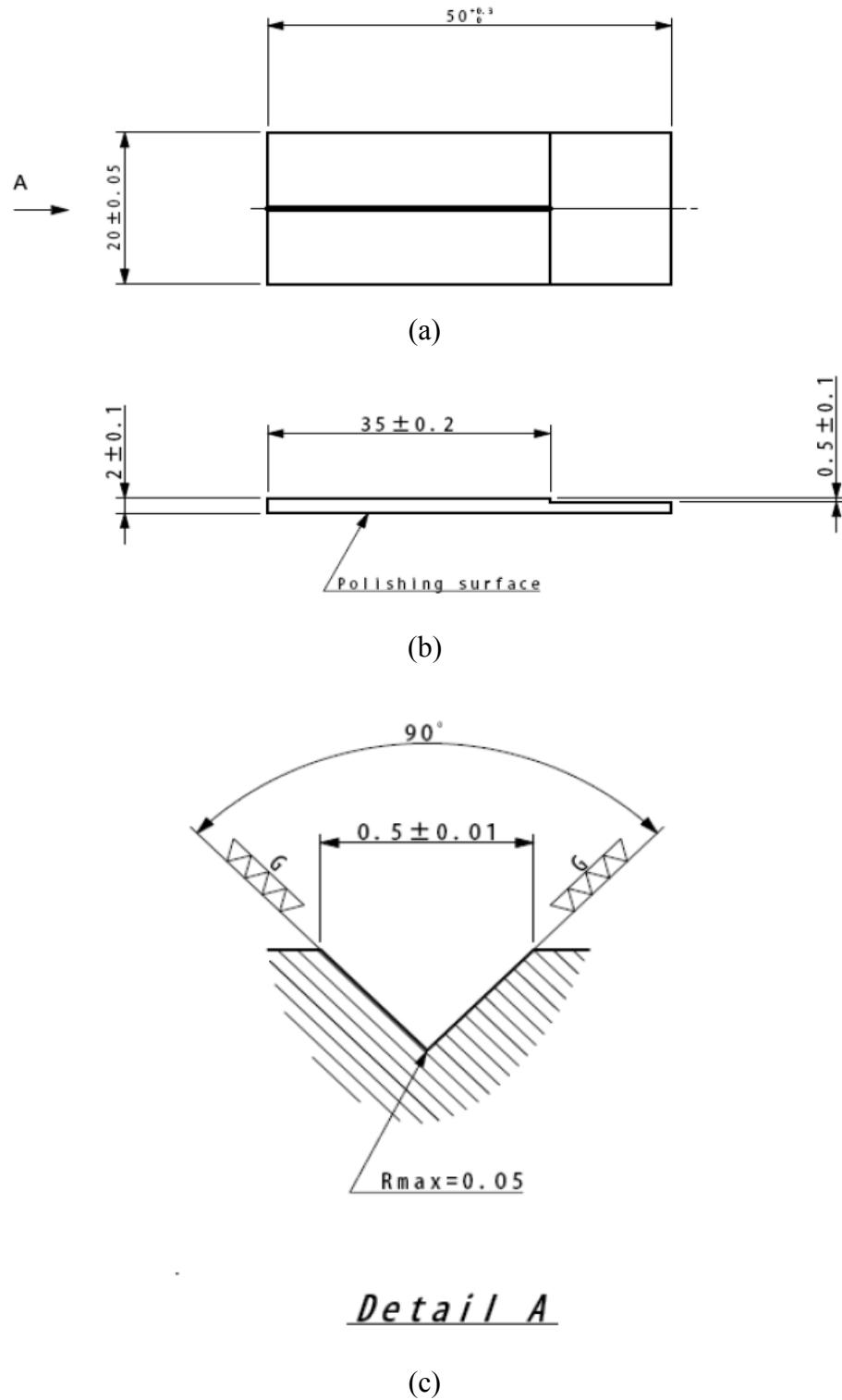


**Figure 1:** Details of a V-groove made on quartz surface (all dimensions in mm). (a) top-view, (b) front-view, (c) cross-section of V-groove.

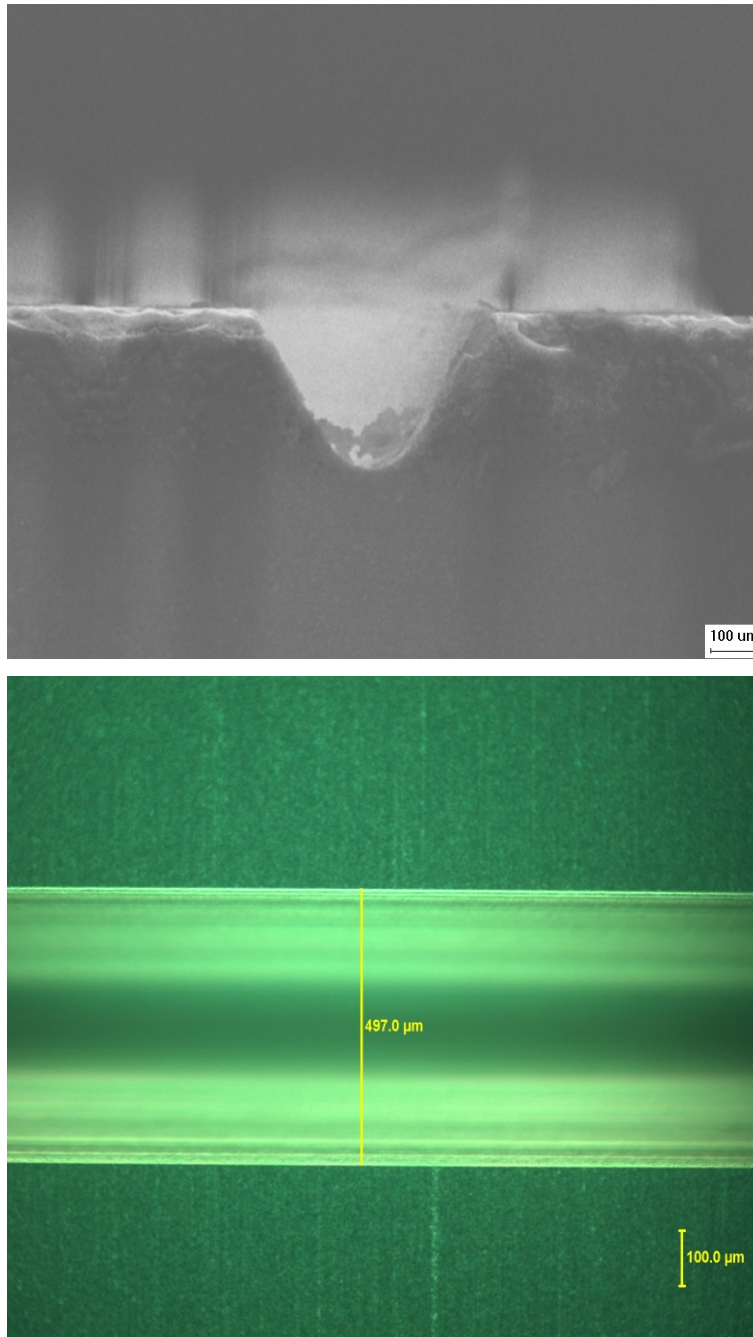


**Figure 2:** SEM micrograph and optical microscopic image of a 0.5 mm ( $\theta = 60^\circ$ ) groove.

## 2.2. Sample Preparation and Cleaning

The V-groove samples were first cleaned with laboratory detergent solution (RBS 35) followed by exhaustive rinsing with Millipore water. The samples were then soaked in a 5%  $\text{HNO}_3$  solution overnight and rinsed thoroughly with water. Finally, the

samples were dried at 80°C in an oven filled with nitrogen gas for at least 8 hours and allowed to cool down in a desiccator before use. The effectiveness of this cleaning procedure was verified by batch contact angle comparison and the uniformity of the wetting area on the sample surface. Cleaned samples were used within 24 hours after the cleaning procedure was completed.

### 2.3. Experimental Setup

The experimental setup consists of two high-speed cameras, a droplet dispensing system and two specially designed back light illumination units. Figure 3 is a schematic representation of the experimental configuration.

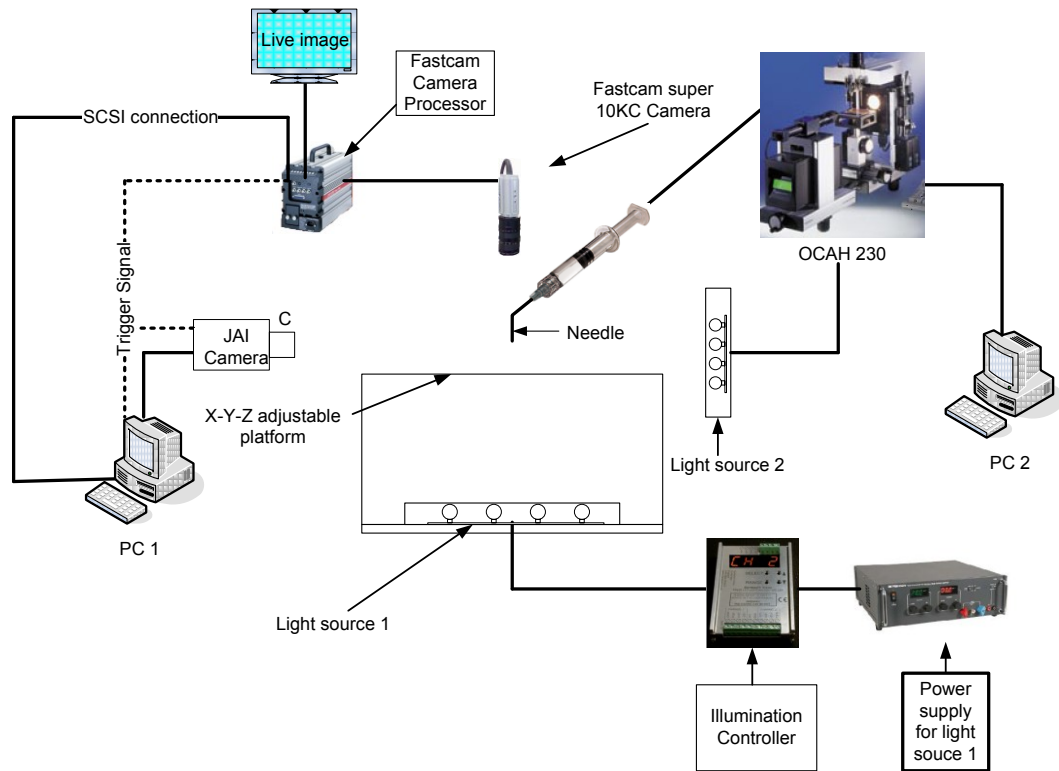


**Figure 3:** Schematic diagram of the experimental setup.

#### 2.3.1. Droplet Generation

We consider a sessile droplet of known diameter ( $d$ ) introduced gently onto the quartz surface as a reservoir feeding the V-groove wicking in both directions. The syringe pump of the OCAH-230 contact angle device (Dataphysics, Germany) was used

to generate water droplets. A stainless steel flat-tipped needle of 0.21 mm outer diameter (Hamilton) was fitted to the syringe pump, which was programmed to dispense liquid at a speed of 0.11  $\mu\text{L/s}$ . Water droplets were delivered onto the quartz surface by gravity and the droplet size was approximately 4  $\mu\text{L}$ . The needle was placed 2.4 mm vertical distance over the V-groove to dispense droplet on the surface to ensure minimum impact ( $\approx 0.00$  m/s).

### 2.3.2. Image Capturing and Analysis

Fastcam Super10KC high-speed camera (Photron USA, Inc., San Diego) was used to capture top-view images of wicking and wetting of the impacting droplet on the V-grooves at 500 frames per second (fps) and 5  $\mu\text{s}$  shutter speed. For illumination, Luxeon Flood® LED array powered by PP600F LED current controller (Gardasoft vision, Cambridge, UK) was positioned behind the impact area of interest. Distance between the sample surface and the illumination source was adjusted to obtain high contrast shadow of V-groove against a clear white background. Image-Pro Plus 5.0 software was used to analyze the top-view images. A second camera (CV- M30 from JAI-Copenhagen, Denmark), capable of recording at 360 fps, was used at a horizontal angle. The second camera was used as a support to the top-view camera to calculate the exact time,  $t_{\text{impact}}$ , at which the impacting droplet touches the surface. The wicking distance and wicking time are counted zero at  $t_{\text{impact}}$ . Both the cameras were triggered together at about 2 s prior to droplet detachment from the needle.

### 3. THEORY

#### 3.1. Background

Liquid wicking in open capillary channels on surfaces of solids has attracted research attention since early times [21]. However, the first mathematical model was not published until 1996 [19, 22]. Rye et al [19] and Romeo & Yost [22] investigated liquid wicking kinetics along V-shaped grooves on metal surface with three different groove angles ( $30^\circ$ ,  $60^\circ$ ,  $90^\circ$ ). Figure 4 shows the schematic of a wetting liquid droplet wicking along a V-groove. The key dimensional parameters, which include the groove width ( $w_0$ ), the apex angle ( $\beta$ ) (or  $\alpha (= 90-\beta/2)$ ), the threshold angle ( $\varphi$ ), which is experimentally determined from the threshold length and the theoretical groove depth, and the liquid-solid contact angle ( $\theta$ ), are also shown in Figure 4. Rye et al. [19] and Romeo & Yost [22] proposed two mathematical models assuming the Poiseuille flow and static advancing contact angle. Both the models used sessile droplet as liquid reservoir.

The model by Rye et al. [19] was based on the original Washburn/Rideal approach and total interfacial energy change as the liquid flows along the groove (Eq. 1).

The model by Romeo et al. is also of pseudo Washburn; it makes similar wicking rate prediction to the model by Rye et al., with the difference in the proportionality term which is related to the groove geometry and liquid contact angle [19].

Both the models showed that the liquid wicking rate in V-groove is related to the groove geometry, particularly the apex angle [19, 22]. The wicking rate becomes slower when the apex angle increases. The authors commented that their models qualitatively agreed with an early study by Parker and Smoluchowski [21] who investigated that the capillary rise of molten silver through V-grooves on iron surface of a given depth (0.127 mm) was faster for apex angle of  $60^\circ$ , slower for  $90^\circ$  and not wicking at all for  $120^\circ$ .

A conclusion reached by both models is that liquid wicking will stop when liquid contact angle with the groove-bearing solid surface ( $\theta$ ) equals to  $\alpha (= 90-\beta/2)$ , (i.e. when the liquid surface inside the groove becomes flat, Figure 4). This conclusion is intuitively acceptable, since when  $\theta = \alpha$  the Laplace pressure of the liquid surface in the groove becomes zero. However, it should be noted that  $\theta$  is the macroscopic liquid contact angle measured on flat (horizontal) solid surface [19]. If the liquid contact angle

in the threshold region of the wicking front is examined more closely, one can see that even when the liquid surface in the groove is flat, the liquid contact angle with the groove wall in the threshold region is still slightly greater than  $\alpha$ . This means that liquid wicking in V-grooves can still proceed even when the macroscopic liquid-solid contact angle  $\theta$  is greater than  $\alpha$ . A detailed discussion on this point will be presented in discussion section.

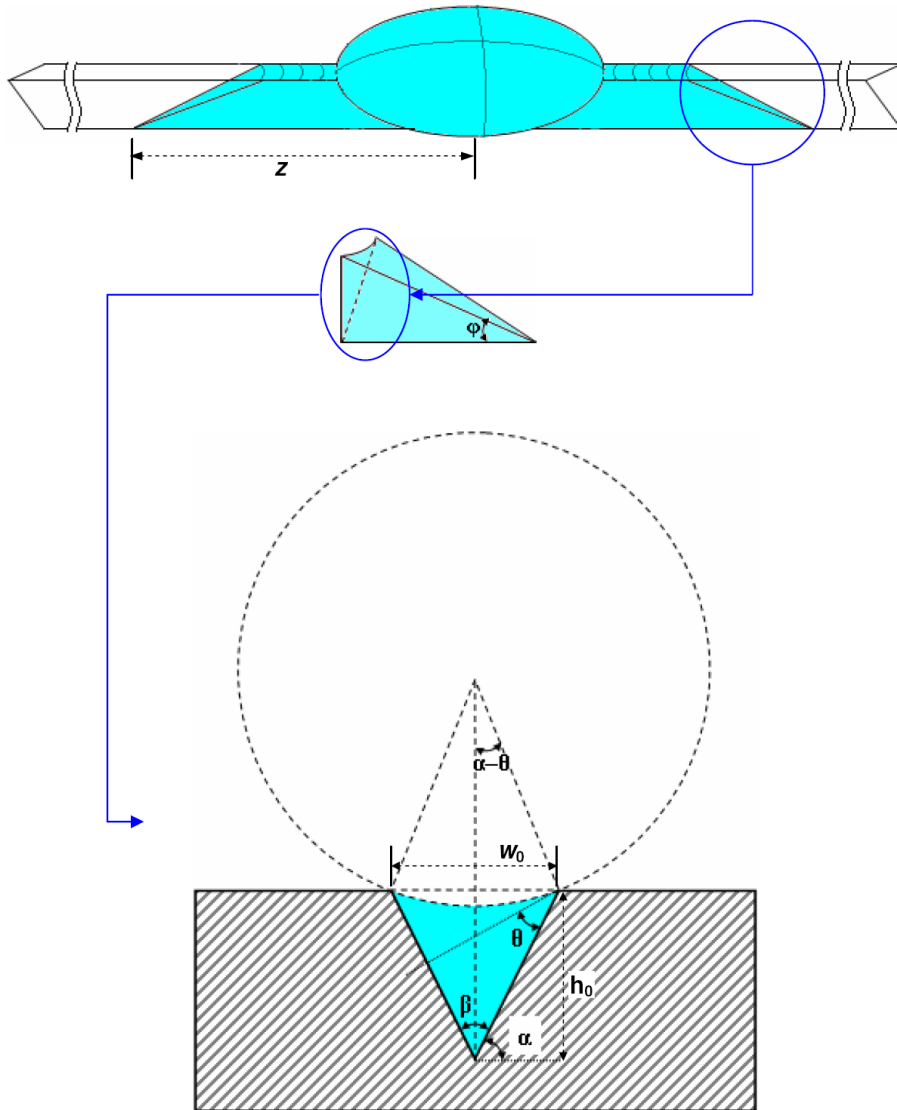


**Figure 4:** Schematic representation of the V-groove wicking. Liquid wicks through a distance  $z$  into a wettable V-groove. V-groove of apex angle  $\beta$ , width  $w_0$  and height  $h_0$  creates  $\alpha$  angle with the horizontal surface. Wicking threshold creates  $\phi$  angle along the wicking direction.

Another interesting point to be noticed is that the stated qualitative agreement between the model by Romeo et al [22] and the observation by Parker and Smoluchowski [21] highlighted by the authors. The model and the observation were made under different conditions and should not be directly comparable. Whilst Parker and Smoluchowski made their observation by immersing a groove of iron into molten silver and observed no capillary raise of molten silver (against gravity) in the groove with  $120^\circ$  apex angle, the model by Romeo et al [22] did not consider gravity at all in their original mass conservation capillary flow equation. It is also worth noting that even for horizontal V-grooves the liquid droplet that feeds the wicking could potentially exert gravity force onto wicking. Therefore the gravity effect on V-groove wicking is still unknown and require investigation.

### 3.2. Model Considerations in this Study

In this study we take a different approach to model the V-groove wicking by focusing on the geometry of the threshold region of the wicking front. Experimentally we placed a liquid droplet (with minimum impact) over the groove to feed the wicking. This model arrangement allows two symmetric wicking thresholds to be formed in opposite directions. The average speed of the two thresholds is taken as the wicking speed for a particular V-groove.

We consider (in separate steps) two driving forces, i.e. Laplace pressure due to the liquid surface curvature in the threshold region and the gravity effect due to hydraulic pressure of the droplet sitting over the V-groove. The flow resistance force is assumed, based on the same consideration by Rye (1996), to be equal to the Poiseuille resistance of a cylindrical capillary of the equal flow rate and equivalent flow cross section. The V-groove wicking equation was then established by considering the balance of the driving and the resistant forces. In the first step we consider the Laplace pressure as the only driving force. In the second step we included the gravity effect.

## 4. RESULTS AND DISCUSSION

### 4.1. V-Groove Geometry

Since V-groove geometry strongly affects the liquid wicking rate, all V-grooves used in this study were carefully measured of their key geometrical parameters (i.e.  $\beta$  and  $w_0$ ). Table I shows results measured by three different methods. All measured values agree with the manufacturer's specification within 2%.

**Table I. V-groove geometrical parameters.**

Groove Specification ( $\beta$ , $w_0$ )	SEM		Profilometry		Microscopy
	$w_0$ ( $\mu\text{m}$ )	$\beta$ ( $^\circ$ )	$w_0$ ( $\mu\text{m}$ )	$\beta$ ( $^\circ$ )	$w_0$ ( $\mu\text{m}$ )
60°, 0.5 mm	496	61.0	499	60.3	497
60°, 0.2 mm	201	60.5	202	59.9	204
90°, 0.5 mm	497	90.1	499	90.2	501
90°, 0.2 mm	204	89.8	203	90.1	202
120°, 0.5 mm	-	-	504	119.5	502
120°, 0.2 mm	-	-	201	118.9	198

The only deviation of the V-groove geometry from our model was that the apex angle was not sharp (Figure 4), instead, it was a symmetrically curved apex. Interestingly, the curved apex geometry was also reported by Rye et al. [19]. This curved apex geometry was limited by the manufacturing approach taken by the manufacturer [23]. Information about the manufacturing technique was limited. However, our measurement confirmed that the depth of curved apex geometry is consistent among samples. For all modelling calculations, apex angles of 60°, 90° and 120° were used.

### 4.2. Spreading of Liquid Droplet on Smooth Quartz Surface

The spreading of water droplet on flat and smooth quartz surfaces was studied using the high speed camera. Figure 5 shows the top view of the droplet spreading. At near zero impact the droplet shows weak recoiling due to process of contacting and

reaching the equilibrium contact angle with the surface. Water contact angle with quartz surface was measured to be  $29.6^{\circ} \pm 0.4^{\circ}$  (for all modeling calculations,  $\theta=30$  was used). On smooth quartz surface, two critical observations are made: First, water droplet does not de-wet the quartz surface during weak recoil phase. The wetting behaviour on quartz is similar to water spreading over glass surface [1]. Second, water droplet and quartz contact line during droplet placement and recoil is circular. Kannangara et al. [1] analyzed the liquid droplet recoil behaviour from both hydrophobic and hydrophilic surfaces. They observed that the cross section profiles of recoiling droplets were always symmetrical on topographically and chemically homogeneous surfaces. When the surface was not clean, water spreading pattern was found to be non-circular [1]. Therefore the circular spreading pattern of water on quartz surface can be taken as a confirmation that the quartz surface was homogeneous and clean.

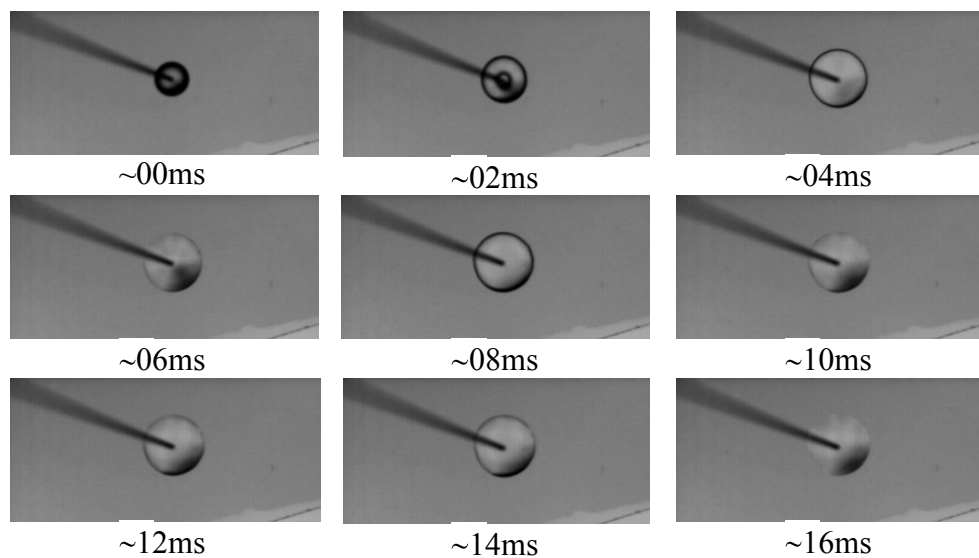


**Figure 5: Dynamics of a sessile water droplet when introduced on a flat, smooth quartz surface.**

### 4.3 Spreading and Wicking of Water on Quartz Surface with V-grooves

Figure 6 shows the spreading of a water droplet on quartz surface with a V-groove and the wicking of a water along the grooves of the same width ( $w_0 = 0.5$  mm) but different apex angles ( $\beta = 60^{\circ}, 90^{\circ}, 120^{\circ}$ ). A few observations can be made. First, immediately after the water droplet was placed on the surface, water wicking fronts in

grooves of 60°, 90° apex angles were found to be ahead of the water spreading contact line on smooth quartz surface. The wicking front developed slightly slowly in the groove of 120° apex angle. A slight V-groove wicking asymmetry can be observed in the very beginning of the wicking. By the time of 7 ms both wicking fronts in all grooves are ahead of the spreading fronts.

The initial asymmetry in the V-groove wicking is likely to be caused by the slight surface chemical asymmetry along the groove.

Second, the shape of the water-quartz surface contact area in the presence of the V-groove (of 60° and 90°) was not circularly symmetric (Figure 6) compared to the water-quartz contact line on the smooth areas of the quartz (Figure 5). The contact line was distorted by the V-groove, elongating in the V-groove direction. This distortion is more profound for the deeper V-grooves (results not shown). For the 120° groove, however, the distortion of the contact line was less obvious and it was still quite circular.

The spreading of the water droplet on quartz surface is sensitive to surface homogeneity; V-groove presents topographic heterogeneity on the quartz surface and water-quartz contact line responses to such heterogeneity, leading to the non-circular contact lines. Whereas the capillary force and the gravity effect of the droplet reservoir can both contribute to liquid wicking in V-groove, the qualitative observation in Figure 6 clearly shows that the capillary force is the dominating driving force when the apex angle is small. This is not only because the wicking rate in 60° and 90° apex angle grooves are faster than the 120° groove, but also because that the former more strongly distort the water-quartz surface contact line. This latter observation therefore suggests that water experience stronger driving force along the V-groove in smaller apex angle grooves than in the large apex groove while the gravity effect due to the droplet reservoir is quite similar in all grooves.

V-groove wicking can be linked to a practical problem in inkjet print quality: Fast ink wicking through inter fibre gaps of uncoated papers is responsible for poor print quality. When an ink droplet lands on an inter fibre gap, the dot shape is elongated along the direction of the gap and wicks along the interfibre gap, leading to the deterioration of the dot fidelity [24].

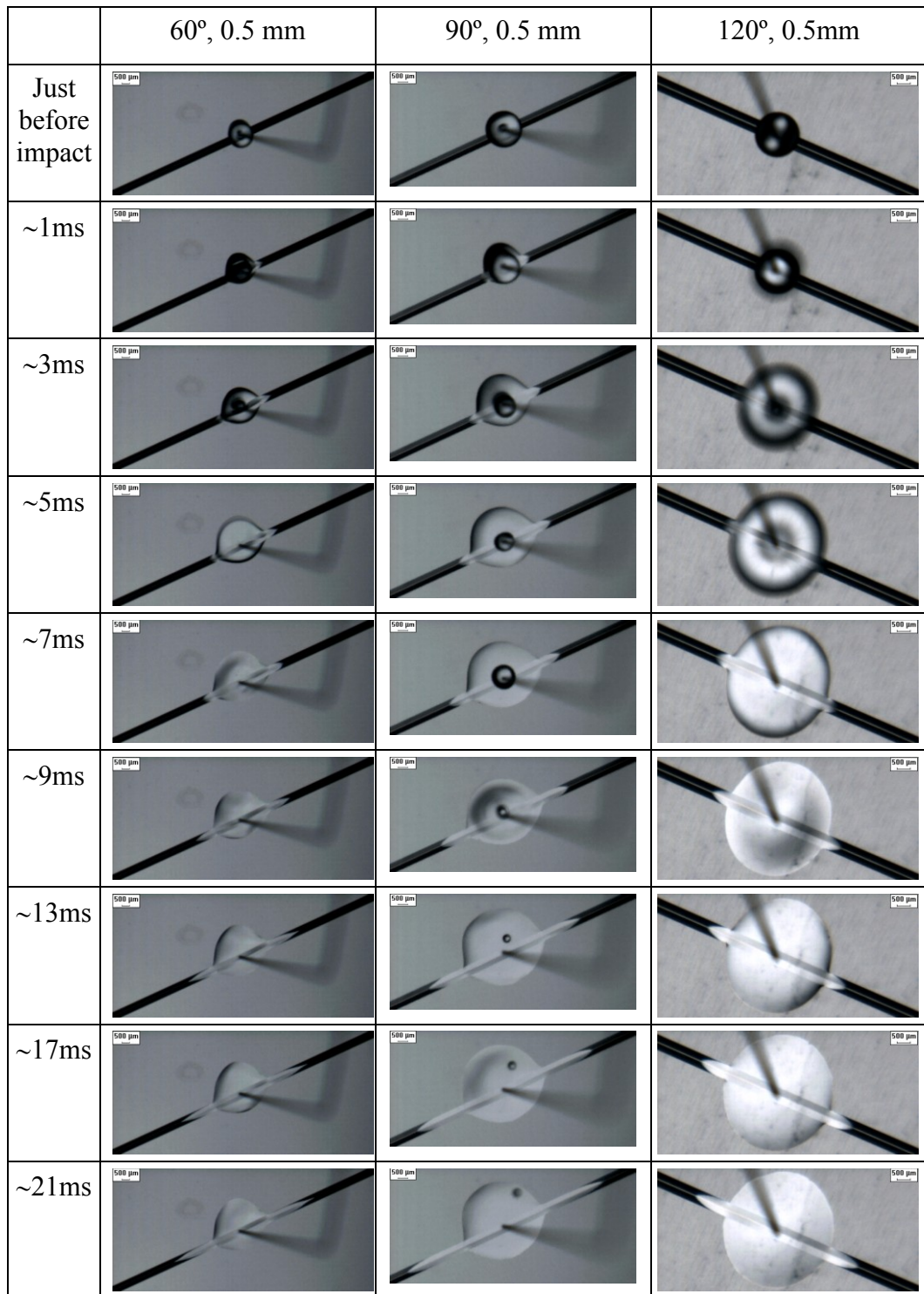
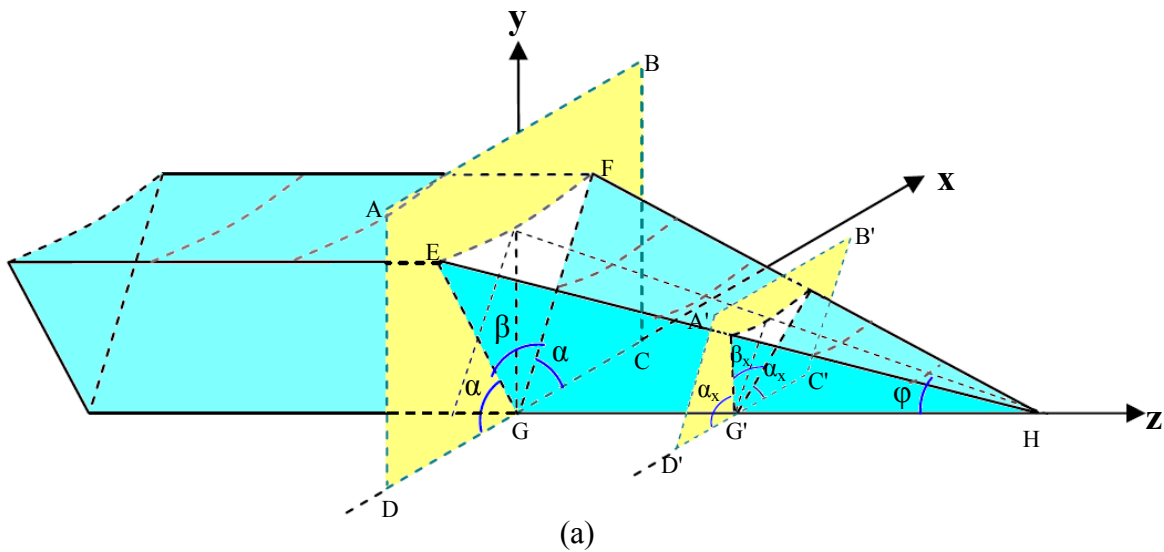


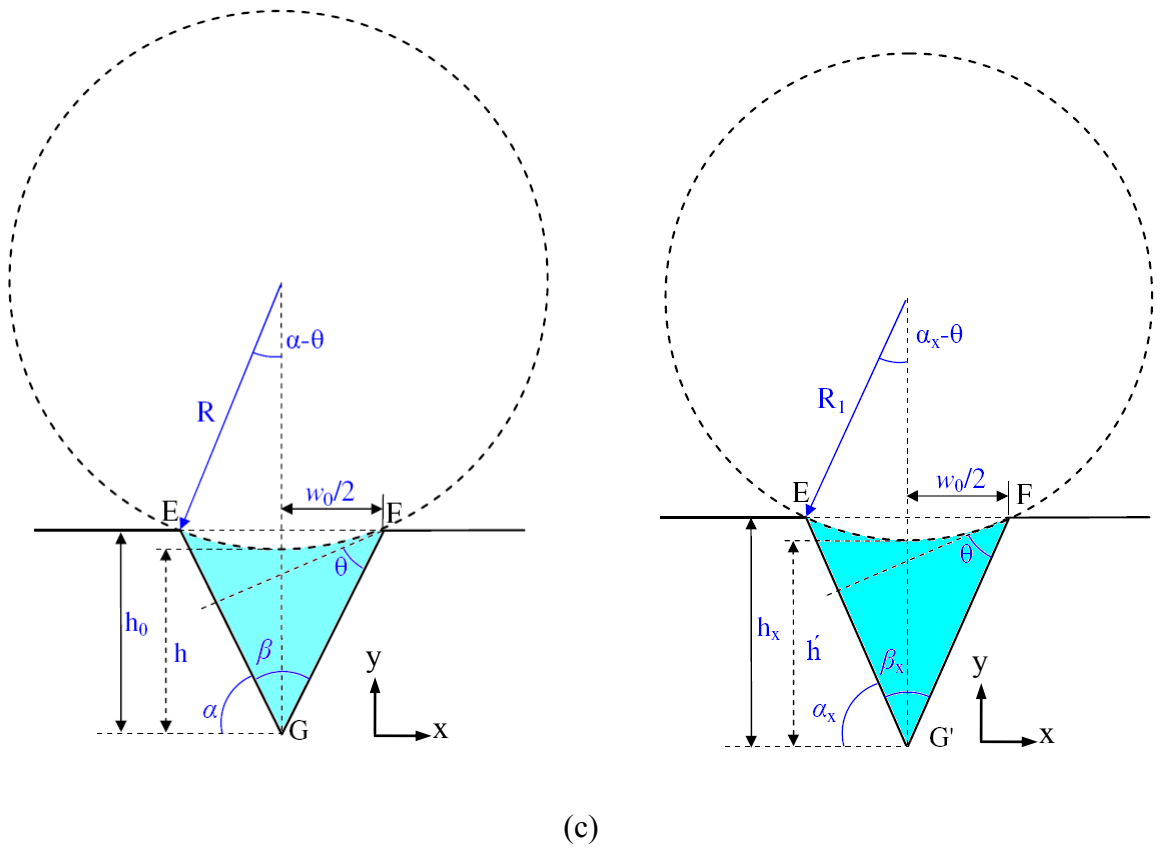
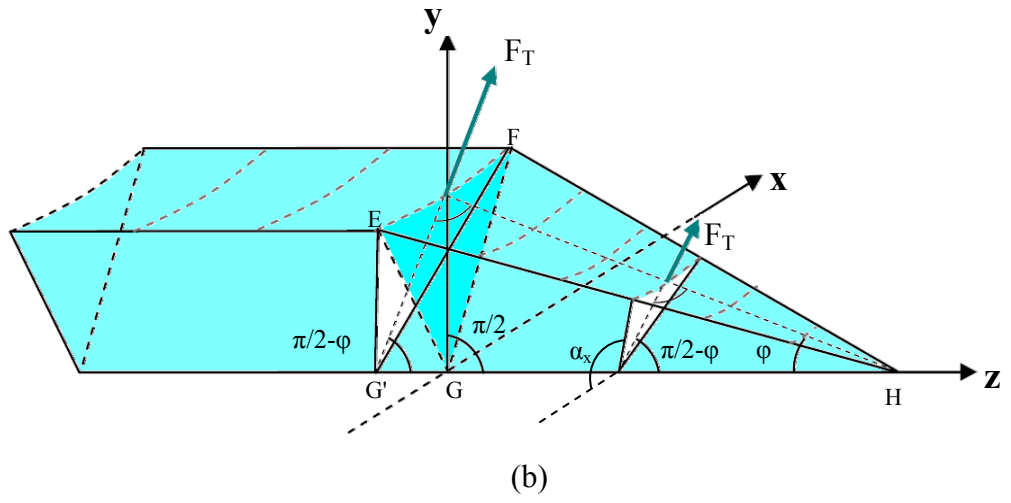
**Figure 6:** Dynamics of a sessile water droplet when introduced on a quartz surface with a V-groove ( $\beta = 60^\circ, 90^\circ, 120^\circ$ ;  $w_0 = 0.5$  mm). Images were taken at different magnifications.

#### 4.4. Model consideration and derivation

As wicking starts in the V-groove, the threshold region of the wicking front develops and its length changes with time. However, the threshold region reaches to a steady length shortly after the wicking starts. It can be assumed that by then the shape of the length and the shape of the threshold region is no longer dependent on time and the driving force of the liquid wicking can be described by the Laplace pressure of the threshold region.

In modeling the Laplace driving force, we consider the following assumptions: First, the threshold region provides the driving force to liquid wicking in V-groove. Second, the Laplace pressure component parallel to the groove provides the driving force; the Laplace pressure component perpendicular to the wicking direction does not contribute to the driving force for liquid wicking. Third, liquid fills up the V-groove in the way that the groove length behind the threshold region is completely filled by the wicking liquid, as illustrated in Figure 4. Figure 7 and 8 represent the schematics of Laplace driving force on the wicking threshold.





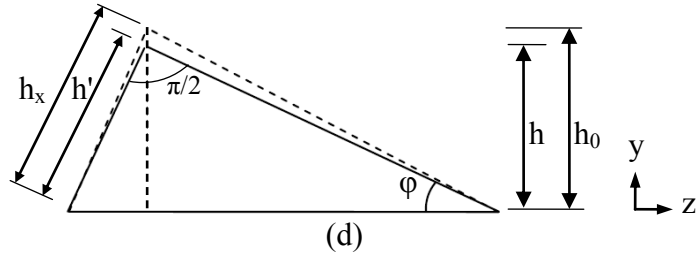


**Figure 7:** Laplace driving force on wicking threshold. (a) Laplace driving force working perpendicular to the threshold, (b) planes (EFG and EFG') perpendicular or inclined ( $\pi/2-\phi$ ) with respect to z-axis, (c) threshold geometry: for plane EFG and EFG', (d) threshold geometry: y-z plane.

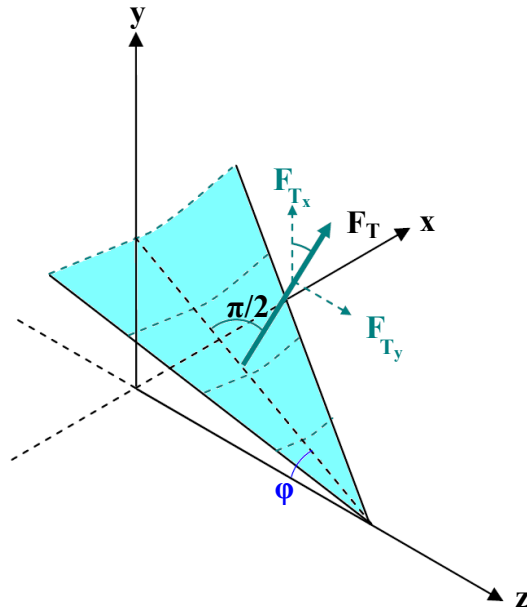


**Figure 8:** Laplace driving force of the threshold.

Under these assumptions the threshold driving force can be calculated starting from the Laplace equation:

$$\Delta P = \left( \frac{1}{R_1} + \frac{1}{R_2} \right) \quad (3)$$

where  $R_1$  is the radius of curvature perpendicular to the threshold region (Figure 7 c) and  $R_2 (= \infty)$  is the radius of curvature along the threshold region.

In Figure 7, the liquid contact angle for threshold cross-sections EFG and EFG' is considered as  $\theta$ .

From Figure 4 and 7c,

$$h_0 = \frac{W_0}{2} \tan \alpha \quad (4.1)$$

$$h_x = \frac{W_0}{2} \tan \alpha_x \quad (4.2)$$

$$\therefore \frac{\tan \alpha_x}{\tan \alpha} = \frac{h_x}{h_0} \quad (4.3)$$

From Figure 7d,

$$\sec \varphi = \frac{h'}{h} \quad (5.1)$$

For simplicity, assuming,

$$\sec \varphi = \frac{h'}{h} \approx \frac{h_x}{h_0} \quad (5.2)$$

And therefore, Eq. (4.3) can be derived as,

$$\therefore \frac{\tan \alpha_x}{\tan \alpha} = \frac{h'}{h} = \sec \varphi \quad (6)$$

$$\therefore \alpha_x = \tan^{-1} \left( \frac{\tan \alpha}{\cos \varphi} \right) \quad (7)$$

And,

$$R_1 = \frac{h_0 \cot \alpha}{\sin (\alpha_x - \alpha)} = \frac{h_0}{\tan \alpha \sin (\alpha_x - \alpha)} \quad (8)$$

Therefore, the liquid cross sectional area in the V-groove is,

$$A(\alpha, \theta) = h_0^2 \left[ \frac{\tan \alpha \sin^2(\alpha - \theta) + \sin(\alpha - \theta) \cos(\alpha - \theta) - \alpha - \theta}{\tan^2 \alpha \sin^2(\alpha - \theta)} \right] \quad (9)$$

$$A(\alpha, \theta) = h_0^2 A^*(\alpha, \theta) \quad (10.1)$$

where

$$A^*(\alpha, \theta) = \frac{\tan \alpha \sin^2(\alpha - \theta) + \sin(\alpha - \theta) \cos(\alpha - \theta) - \alpha - \theta}{\tan^2 \alpha \sin^2(\alpha - \theta)} \quad (10.2)$$

The function  $A(\alpha, \theta)$  and  $A^*(\alpha, \theta)$  in Eq. (10.1) and (10.2) appear to be singular at limiting condition,  $\alpha \rightarrow \theta$ , but it is not. At the limit of  $\alpha \rightarrow \theta$ ,  $A(\alpha, \theta)$  can be derived as Eq. (11); detailed shown in the Appendix.

$$\lim_{\alpha \rightarrow \theta} A(\alpha, \theta) = h_0^2 \lim_{\alpha \rightarrow \theta} A^*(\alpha, \theta) = \frac{h_0^2}{\tan \theta} \quad (11)$$

Since  $R_1 = \frac{h_0}{\tan \alpha \sin(\alpha - \theta)}$  and  $R_2 = \infty$ , the Laplace pressure in the Eq.

3 can be rewritten as,

$$\Delta P = \frac{\gamma}{h_0} \tan \alpha \sin(\alpha_x - \theta) \quad (12)$$

Assuming that the threshold region is triangular as shown in Figure 7 and Figure 8, driving force perpendicular to the surface of the threshold region,

$$F_T = \int dF = \int \Delta \, dA = \int \Delta \, w_0 \cdot ds \quad (13)$$

Substitution of  $\Delta P$ ,  $w_0$  and  $s$  in Eq. (13) and integration yield,

$$F_T = \gamma h_0 \frac{\sin(\alpha_x - \theta)}{\sin \varphi} \quad (14)$$

Effective force in the direction of flow can be estimated by taking the horizontal projection of  $F_T$ .

$$F_\gamma = F_T \sin \varphi = 2\gamma h_0 \sin(\alpha_x - \theta) \quad (15)$$

The Newtonian equation of motion can be written as follows:

$$\frac{d(mv)}{dt} = \frac{d}{dt} \left[ \rho z_L A(\alpha, \theta) \left( \frac{dz_L}{dt} \right) \right] = \rho A(\alpha, \theta) \left[ \left( \frac{dz_L}{dt} \right)^2 + z_L \frac{d^2 z_L}{dt^2} \right] = F_\gamma - F_\mu \quad (16)$$

where,  $z_L$  is the wicking length along the V-groove channel due to Laplace pressure force.

Substituting  $F_\gamma$  and  $F_\mu$  in Eq. (16) we can obtain,

$$2 \left[ \left( \frac{dz_L}{dt} \right)^2 + z_L \frac{d^2 z_L}{dt^2} \right] + a z_L \frac{dz_L}{dt} = b \quad (17)$$

where,

$$a = \frac{8\pi\mu}{\rho A(\alpha, \theta)} \text{ and } b = \frac{4\gamma h_0 \sin(\alpha_x - \theta)}{\rho A(\alpha, \theta)} \quad (18)$$

Solving the differential equation (Eq. 17) we find,

$$z_L^2 = \frac{b}{a} \left[ t + \frac{1}{a} \left( e^{-at} - 1 \right) \right] \quad (19)$$

For small cross sectional area, exponential term approaches to 1 and therefore, Eq. 19 can be simplified to

$$z_L^2 = \left( \frac{b}{a} \right) = \left[ \frac{\gamma_0 \sin(\alpha_x - \theta)}{2\pi\mu} \right] \quad (20)$$

In our model, since we consider the total Laplace driving force perpendicular to the curved liquid surface in the threshold region, our derivation requires the projection of angle  $\alpha$  (Figure 7) on to plane y-z. The angle in this projection,  $\alpha_x$  is related to  $\alpha$  and  $\varphi$  by Eq. (7). Therefore in our model, the liquid wetting condition is defined as  $(\alpha_x - \theta)$ . The liquid wicking rate is zero when  $\theta$  approaches to  $\alpha_x$ .

#### 4.5. Water Wicking Kinetics in V-grooves

Experimental results of wicking kinetics of sessile droplet placed over the V-groove of different geometries are shown in Figure 9. The apex angle and groove width are used as parameters to identify the results (apex angle (D)\_groove width (mm)). For any specific apex angle, liquid wicking was found faster in wider V-groove than in narrow one. For a given groove width, the effect of apex angle on liquid wick rate can also be seen. For 500  $\mu\text{m}$  grooves, the liquid wicking rate reduces as the apex angle increase, i.e. (60D\_0.5mm) > (90D\_0.5mm) > (120D\_0.5mm). For 200  $\mu\text{m}$  grooves, the data shows a different trend with the increase in the apex angle, i.e. (60D\_0.2mm) > (120D\_0.2mm) > (90D\_0.2mm) (Figure 9). The Laplace driving force calculated using Eq. (15) for the 60D\_0.5mm groove, for example, was  $3.3 \times 10^{-5}$  N.

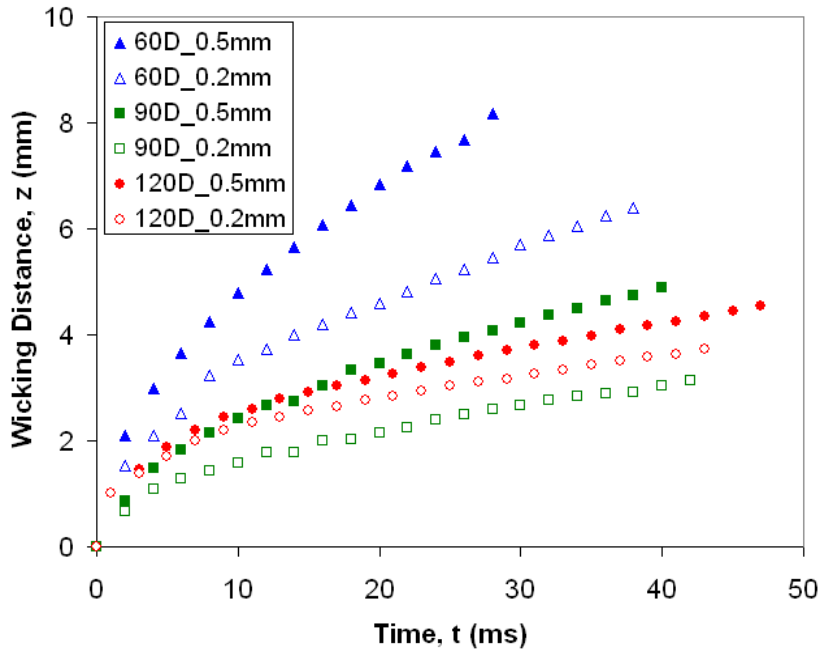


**Figure 9:** Water wicking distance ( $z$ ) as a function of time in V-grooves on quartz surface of difference geometry ( $\beta = 60^\circ, 90^\circ, 120^\circ$ ;  $w_\theta = 0.2, 0.5$  mm).

The wicking distance and time relationship predicted by our model is also of pseudo Washburn. Plotting  $z^2$  vs.  $t$  yields linear relationship, which can be extrapolated to the origin (Figure 10). It is therefore expected that, for a particular apex angle, wider grooves allow faster wicking. This is mainly because of the flow resistant force is lower for wider grooves. Since the flow resistant force is modelled using the Poiseuille principle, the flow rate is proportional to the fourth power of the capillary radius [12]. Smaller capillary size will therefore encounter low flow rate.

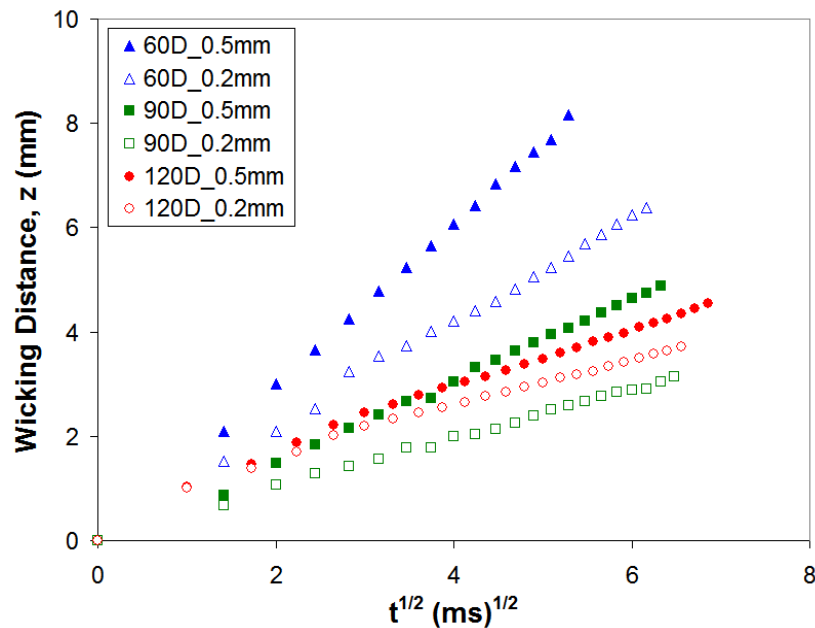


**Figure 10:** Water wicking distance as a function of square root of  $t$  ( $\text{ms}^{1/2}$ ) in V-groove on a quartz surface of different geometry ( $\beta = 60^\circ, 90^\circ, 120^\circ$ ;  $w_\theta = 0.2, 0.5$  mm).

Previous models have used macroscopic liquid contact angle on smooth and flat solid as the modelling contact angle ( $\theta$ ). A close analysis of the liquid contact angle inside the groove with the groove wall reveals that it is slightly greater than the liquid contact angle on a flat and smooth surface. The analysis can be seen from Figure 7 (a). In the threshold region the plane ABCD is perpendicular to with the two groove walls, EGH and FGH. Liquid contact angle in the groove with the groove walls can only be measured perpendicular to the liquid-solid contact lines (EH and FH). Therefore, liquid contact angle with the groove wall must equal to  $\alpha_x$  in order for the liquid surface of the

threshold to become flat (i.e. for the Laplace pressure to become zero). Figure 11 shows vectors of different plans in the threshold. Since plane ABCD is not parallel to plane A'B'C'D' when  $\varphi > 0$ ,  $\alpha_x$  will always be greater than  $\alpha$  (Figure 7 b, c). Therefore, the equilibrium wetting condition in the groove is  $\theta = \alpha_x$  ( $> \alpha$ , see Table II). A mathematical solution for the non-wicking liquid contact angle with the groove wall can be obtained by calculation the angle ( $\theta$ ) between the vector normal to the groove wall ( $\mathbf{F}_W$ ) and the vector normal to the flat liquid surface in the threshold region ( $\mathbf{F}_T$ ), which is,  $\theta = \cos^{-1}[(\mathbf{F}_T \cdot \mathbf{F}_W) / (F_T F_W)]$  (Figure 11). To reflect the Laplace driving force and the equilibrium wetting condition in the groove, we defined the angle  $\alpha_x$ . The working equation of the model (Eq. 20) shows that liquid wicking will stop when  $(\alpha_x - \theta)$  becomes zero.

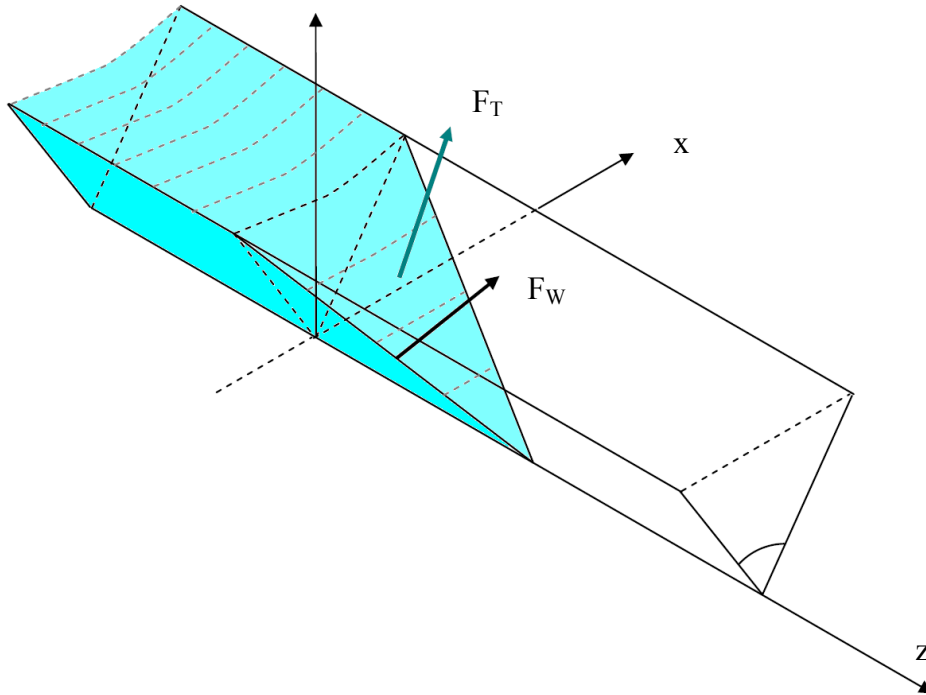


**Figure 11:** Vectors representations of the threshold region; vector normal to the groove wall ( $\mathbf{F}_W$ ) and the vector normal to the flat liquid surface in the threshold region ( $\mathbf{F}_T$ ).

Figure 11 shows the limiting liquid-groove wall contact angle when the liquid surface in the groove is flat. The contact angle of the filled section,  $\theta = \cos^{-1}[(\mathbf{F}_W \cdot$

$\hat{y})/(F_T)] = \alpha$ . The contact angle of the threshold region,  $\theta = \cos^{-1}[(\mathbf{F}_T \cdot \mathbf{F}_W)/(F_T F_W)] = \alpha_x$ . Since  $\alpha_x > \alpha$ , liquid wicking is possible when liquid surface in the groove becomes flat.

**Table II. Critical Parameters of Liquid Wicking along V-groove.**

Groove Specification ( $\beta, w_0$ )	$\varphi$ (°)	$\alpha$ (°)	$\theta$ (°)	$\alpha_x$ (°)	$h_0$ (m)	A( $\alpha, \theta$ ) (normalized against 60°, 0.5mm)	$F_\gamma$ (normalized against 60°, 0.5mm)
60°, 0.5 mm	20.3	60	30	61.6	$4.33 \times 10^{-4}$	1	1
60°, 0.2 mm	22.54	60		61.9	$1.73 \times 10^{-4}$	0.16	0.403
90°, 0.5 mm	25.09	45		47.8	$2.50 \times 10^{-4}$	0.38	0.336
90°, 0.2 mm	10.7	45		45.5	$1.00 \times 10^{-4}$	0.06	0.118
120°, 0.5 mm	11.61	30		30.5	$1.44 \times 10^{-4}$	-	0.006
120°, 0.2 mm	9.17	30		30.3	$5.77 \times 10^{-5}$	-	0.0014

The model also reasonably well predicted the effect of the apex angle of grooves of a particular width. The only unexpected exception is the reversed trend of (120D\_0.2mm) > (90D\_0.2mm), which will be discussed below. Sharper apex angle provides higher Laplace driving force, as the liquid surface in the groove assumes more curved surface. This is reflected by our model through the  $[\sin(\alpha_x - \theta)/\tan \alpha]$  term.

#### 4.5.1. Liquid Wicking in Grooves of 120° Apex Angle by Capillary Driving Force

The most surprising observation from the experimental results is the liquid wicking in the 120° grooves. Since  $\alpha = \beta = 30^\circ$ , models by Rye et al. (1996) and Romeo (1996) would both predict no wicking. From the analysis given above, gravity effect and the actual wetting condition of liquid with the groove wall may be the two factors responsible for the disagreement.

Since our model considered the actual wetting condition of inside the groove, where the non-wicking condition is  $\theta = \alpha_x$ , our model predicts that a liquid with a macroscopic contact angle equal to the angle  $\alpha$  (i.e.  $\theta = \alpha = 30^\circ$ ) should still be able to wick along the groove since  $\alpha < \alpha_x$ . Although Rye et al. (1996) and Romeo (1996) commented that their models showed qualitative agreements with the observation

reported by Parker & Smoluchowski [21], these authors' modelling condition (horizontal grooves) were different from the experimental condition used by Parker & Smoluchowski (vertical grooves) [21]. The experimental data in our study (horizontal V-groove wicking) present a real test of the V-groove models. When the Laplace pressure is considered to be the only driving force, our model predicted a small capillary driving force (Table II). However, even the actual wetting condition of liquid inside the groove is considered, we still unable to reconcile the substantial discrepancy between the experimental results and our model (Figure 14). Such a discrepancy suggests that gravity effect may be another factor responsible for the wicking behaviour in 120° grooves.

Another unexpected result is the change in the trend of V-groove wicking rate for the 0.2 mm grooves. For these grooves the measured wicking rates were (120D\_0.2mm) > (90D\_0.2mm) (Figure 10). This result was unexpected not only because the trend is different from that of the 0.5 mm grooves, but also because it disagrees with the model prediction, which indicates that (120D\_0.2mm) groove should have the lowest wicking rate. Most likely, this change in wicking rate trend is due to the uncertainty in the experiments.

#### **4.5.2. Liquid Wicking in Grooves of 120° Apex Angle by Gravity Effect**

Since the liquid droplet reservoir over the groove exerts a small but finite hydraulic pressure to liquid in the groove, the effect of gravity on the liquid wicking cannot be ruled out without a close examination. Such hydraulic pressure was not discussed by Rye et al. [19] and Romeo et al. [22]. In a more recent study, however, Holdrich et al. [25] reported that both capillary and gravitational forces play a role in wicking of a liquid droplet in a surface groove. Although the hydraulic pressure by the liquid droplet over the groove is small (only a few Pa), it may become important when the capillary driving force diminishes as the apex angle increases. Since a simple calculation shows that the liquid droplet reservoir retains 70 – 90% of its original volume in the duration of our experiment (Figure 12), such a condition allows the assumption of constant gravity-related hydraulic pressure in V-grooves. For horizontal V-grooves, this assumption implies that the effect of gravity can be considered independently from the capillary driving force.

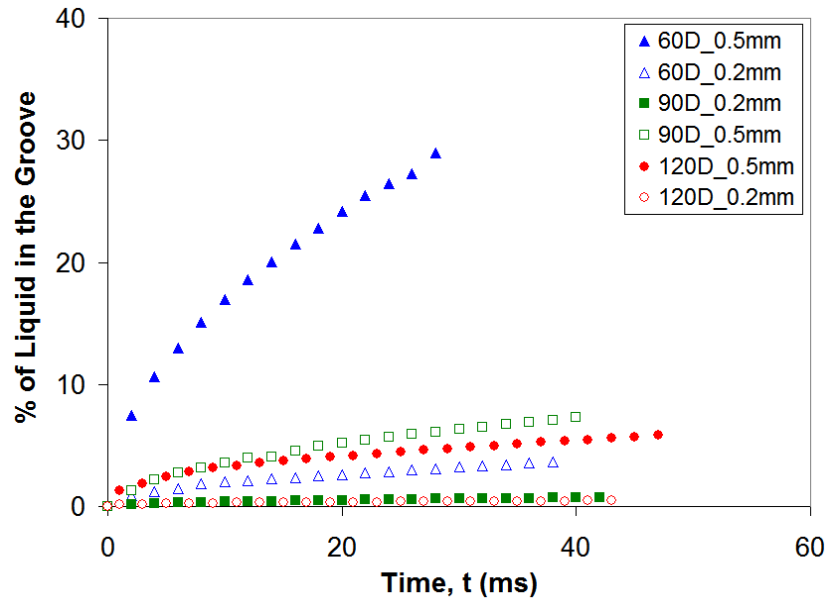


**Figure 12:** Percentage of droplet volume into the V-groove.

In estimating the hydraulic pressure of the liquid droplet reservoir, a cylindrical shaped liquid column of equal volume and equal base area to that of the liquid droplet over the V-groove is used to define the hydraulic head (Eq. 21). The height of an equal volume cylinder of same radius was considered (Figure 13). The force due to the hydraulic head was added to the driving force term (Eq. 22) to give a new working equation (Eq. 23):

$$F_g = \rho g A_e \alpha, \theta \quad (21)$$

$$\frac{d(mv)}{dt} = \rho A_e \alpha, \theta \left[ \left( \frac{dz}{dt} \right)^2 + z \frac{d^2z}{dt^2} \right] = \tau_\gamma + \tau_g - \tau_\mu \quad (22)$$

where,

$F_g$  = Hydraulic driving force,

$$h_e = \text{equivalent height} = \frac{\text{Droplet Volume, } V}{\pi R_\theta^2}$$

$$R_\theta = \text{equivalent radius} = \sqrt{\frac{3V}{\pi (-\cos\theta + \cos^3\theta)}}$$

$V$  = Volume of liquid droplet and

$z_h$  = wicking length due to gravitational force

Therefore, total liquid wicking along V-groove can be expressed:

$$z^2 = \left( \frac{2\gamma \cos(\alpha - \theta) + \rho g R_0^2 \sin^2 \alpha}{4\pi\mu} \right) \quad (23)$$

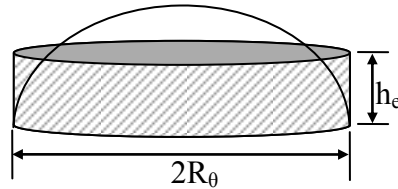


**Figure 13: Schematic of liquid droplet hydraulic head estimation using equal volume cylinder.**

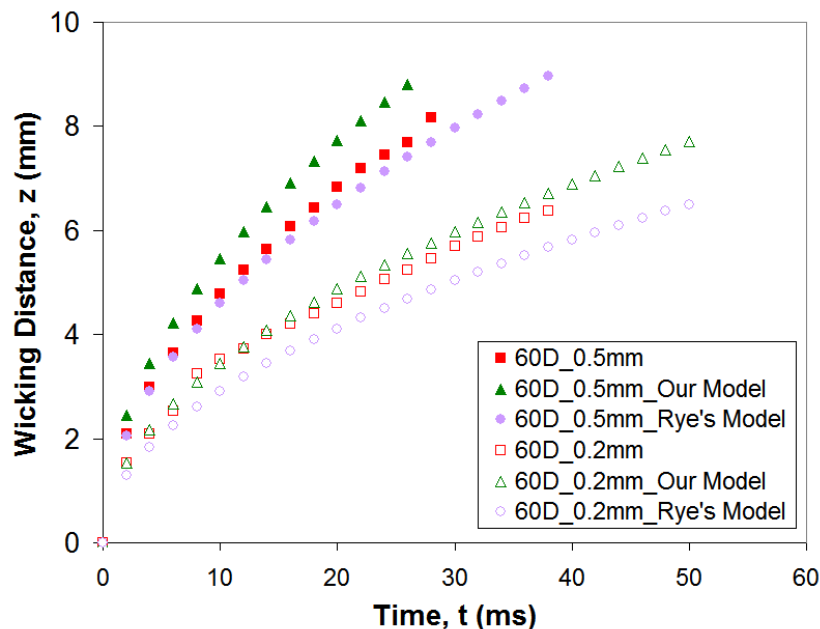
Calculation using Eq. (23) shows that for the 60° and 90° grooves, capillary force is the dominating driving force and that the gravity effect has a negligible contribution to the liquid wicking rate ( $F_g/F_\gamma = 0.0006 - 0.001$ ). For 120° grooves, however, our model suggests that capillary force calculated from the contact angle data, taking into account of the wetting condition inside the groove, is weak ( $F_g/F_\gamma = 0.08 - 0.12$ ). Wicking observed in 120° grooves is therefore dominated by the gravity effect. This modelling conclusion is also supported by the observation of the subtle difference in the shape of the liquid-groove wall contact line. While the liquid-groove wall contact line in the 60° and 90° grooves are straight, the contact line in the 120° groove was noticeably curved. Since our model predicts that the Laplace pressure force at the point of the threshold is the highest, the liquid-groove wall contact line should therefore be straight due to the tension force between the point of the threshold and subsequent section of the threshold. If the point of the threshold no longer provides such driving force, liquid movement at the point of the threshold will be driven by the liquid movement of the subsequent section of the threshold.

The shape change of the wicking threshold can also be appreciated through analysing the flow resistance. Since the flow resistance is modelled using the Poiseuille principle where laminar flow is assumed, the velocity of the flow lamina at the surface of the groove wall should therefore be lower than lamina away from the groove wall. When gravity force becomes dominant, the flow velocity distribution in the groove will also change. Flow velocity close to the point of the threshold will reduce (due to the loss

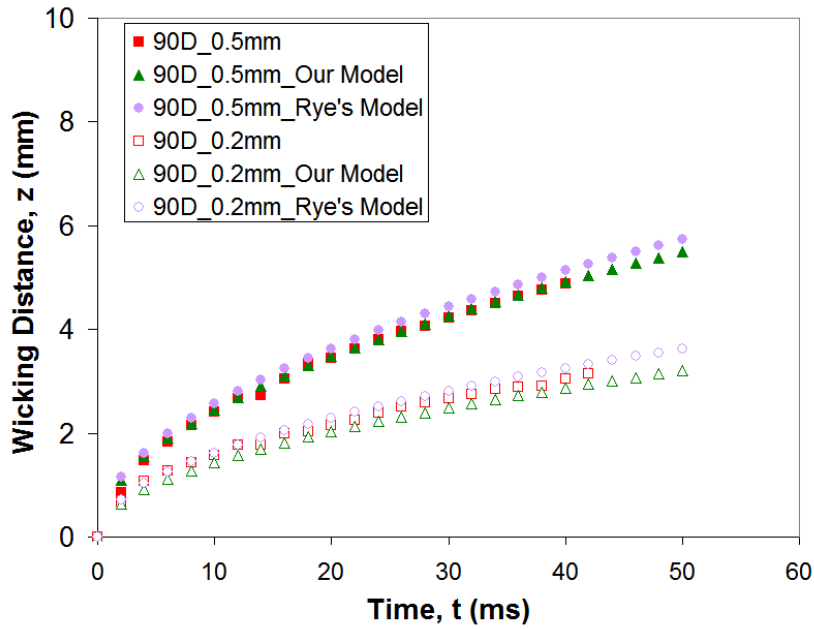
of capillary driving force) relative to the flow velocities of the flow laminae away from the wall. Such a change in flow velocity distribution not only shortens the length of the threshold, but also makes the flow velocity profile in the 120° groove to change from a “v” shaped profile towards a more rounded “u” shaped profile.

## 5. V-GROOVE WICKING – COMPARISON OF EXPERIMENTAL DATA AND MODELS

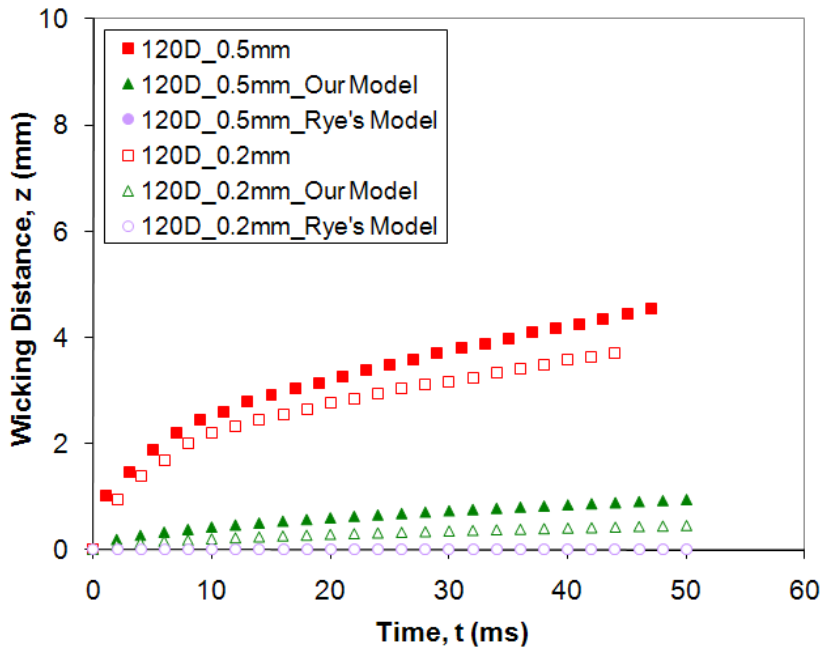
The experimental results of water droplet wicking distances ( $z$ ) in V-grooves are presented as functions of time; comparisons of the mathematical models are made with the experimental data. Figures 14 (a), (b) and (c) show comparison of 60°, 90° and 120° grooves. For the 60D\_0.5mm groove, our model predicted a higher wicking velocity than the experimental data, whereas the model by Rye et al. predicted a slightly lower wicking velocity than the experimental data. Interestingly, however, our model shows a better fit to the experimental data of 60D\_0.2mm groove than the model by Rye et al. (Figure 14a). For the 90D\_0.5mm and 90D\_0.2mm grooves, our model shows better fitting with the experimental data than the model by Rye et al. (Figure 14b).



(a)



(b)



(c)

**Figure 14:** Theoretical prediction of wicking dynamics on V-groove surfaces in contrast with the experimental results. (a)  $\beta = 60^\circ$ ;  $w_0 = 0.2, 0.5$  mm, (b)  $\beta = 90^\circ$ ;  $w_0 = 0.2, 0.5$  mm, (c)  $\beta = 120^\circ$ ;  $w_0 = 0.2, 0.5$  mm.

The reasonably good (although not perfect) agreement between the models and the experimental results for the  $60^\circ$  and  $90^\circ$  grooves shows that the wicking of liquids of high  $\gamma/\mu$  ratio, such as water, in open capillary channels can also be described by the Washburn type relationship (i.e.  $z^2$  is proportional to  $t$ ; Eq. (23)). Although Rye et al.

[19] found that the Washburn type relationship was obeyed by the liquids of low  $\gamma/\mu$  ratio (60 – 1000 cm/s) wicking in open capillaries in a much longer time scale, our work shows the Washburn type relationship was also obeyed by liquids of high  $\gamma/\mu$  ratio (7300 cm/s) at the wicking rates of 2 orders of magnitude higher than those reported by Rye et al. [19]. Our experimental and modeling results show that the sensitivity of liquid wicking rate to the groove geometry applies to liquids with wide range of different  $\gamma/\mu$  ratios. In an open capillary, in spite of the general Washburn relationship is still obeyed, both the capillary size ( $w_0$ ) and the capillary “shape” (or the apex angle- $\beta$ ) affects the wicking rate.

For the 120° groove, the model by Rye et al. predicts no wicking, whereas our model predicts wicking. However, large disagreement between our model and the experimental results are still present even when the gravity effect and the actual wetting condition inside the groove were considered (Figure 14). The cause of such disagreement is not clear. One possible reason is that the flow resistance was over estimated for the 120° groove by the Poiseuille principle. The Poiseuille flow resistance was derived based on the laminar flow assumption in a cylindrical capillary; liquid has full contact with the wall of the cylindrical capillary. Liquid wicking in V-groove, however, does not have full contact with the capillary wall. Figure 4 shows the cross section of the groove wicking. When the liquid wetting condition reaches  $\theta = \alpha$ , the liquid contact with the groove wall decreases from 67% for the 60° groove, to 59% for the 90° groove and only 54% for the 120° groove. Liquid wicking in the 120° groove is therefore closer to planer flow which cannot be accurately modeled by the Poiseuille principle.

## 6. IMPLICATION OF USING THE V-GROOVE GEOMETRY TO CONTROL INK WICKING RATE IN AN INKJET PRINTING APPLICATION

An interesting implication of V-groove wicking to ink wicking on uncoated paper surface is that the size and the shape of the inter fibre gap can strongly influence ink wicking and therefore the print quality. When small inkjet ink droplets are delivered on paper surface, their small size makes the hydraulic pressure exerted by the droplets negligibly small. Capillary driving force will therefore be the only force to consider. Whereas internal paper sizing can reduce the ink wicking driving force (Eq. 12) by reducing  $(\alpha_x - \theta)$ , the result of internal sizing is not uniform [1]. There are always some inter fibre gaps that acquire low levels of sizing relative to the other areas and that can facilitate ink wicking [24, 26]. However, by applying surface sizing to uncoated paper surface, one may fill the inter fibre gaps to some extent with surface sizing starch. This can reduce the inter fibre gap width ( $w_0$ ). But, more likely, it may increase the apex angle (which corresponds to a reduction of  $\alpha_x$ ). Our results predict that a decrease in  $w_0$  and particularly, an increase in apex angle can reduce ink wicking very effectively.

## 7. CONCLUSIONS

The liquid wicking dynamics during short contact time in V-shaped grooves (open capillaries) has been studied. An experimental setup consisting of two cameras was established to investigate liquid wicking in V-grooves. A simple model, which considers the driving force at the threshold region of the wicking front, was developed.

Through considering the actual liquid wetting condition inside the groove, we proposed that the liquid wetting condition corresponding to non-wicking for V-grooves should be  $\theta = \alpha_x$ , where  $\alpha_x$  is always greater than  $\alpha$ . This finding leads to an unexpected but significant prediction that wicking is possible even when the liquid surface inside the groove becomes flat.

This study also considered gravity effect on liquid wicking in V-grooves. Gravity driving force is negligibly small for grooves with  $60^\circ$  and  $90^\circ$  apex angles, but becomes important for grooves with  $120^\circ$  apex angle. Our results show that gravity driving force

is the dominant driving force for liquid wicking in  $120^\circ$  grooves. Our results also suggest that the use of Poiseuille principle to model flow resistance in V-grooves may lead to greater error for the  $120^\circ$  grooves than for  $60^\circ$  and  $90^\circ$  grooves. Error in flow resistance modelling may be responsible for the discrepancy observed between the experimental and modelling results.

The understanding achieved from this study will be helpful to solve practical problems such as the surface treatment strategy of uncoated inkjet papers for high print quality.

## **ACKNOWLEDGMENT**

Many thanks to D.Chakraborty for useful discussion, and to Monash University for postgraduate scholarships (MSK, DK).

## REFERENCES

- [1] Kannangara D, Zhang H, Shen W, *Colloids and Surfaces A: Physicochem Eng Aspects*, 2006; 280: 203-215.
- [2] Asai A, Shioya M, Hirasawa S, Okazaki T, *J. Imaging Sci. Technol.*, 1993; 37: 205-207.
- [3] Khan MS, Fon D, Li X, Tian J, Forsythe J, Garnier G, Shen W, *Colloids and Surfaces B: Biointerfaces*, 2010; 75 (2): 441-447.
- [4] Kissa E, *Textile Research Journal*, 1996; 66: 660-668.
- [5] Dussaud AD, Adler PM, Lips A, *Langmuir*, 2003; 19: 7341-7345.
- [6] Baret J-C, Decre MMJ, Herminghaus S, Seemann R, *Langmuir*, 2007; 23: 5200-5204.
- [7] Seemann R, Brinkmann M, Kramer EJ, Lange FF, Lipowsky R, *Proc. National Academy of Sciences of the United States of America*, 2005; 102:1848-1852.
- [8] Washburn EW, *Phys Rev*, 1921; 17: 374-375.
- [9] Fisher LR, Lark PD, *Colloid and Interface Sc*, 1979; 69: 486-492.
- [10] Rosendahl U, Ohlhoff A, Dreyer ME, Rath HJ, *Microgravity Sci Technol*, 2002; 13: 53-59.
- [11] Kim WS, Kim MG, Ahn JH, Bae BS, Park CB, *Langmuir*, 2007; 23: 4732-4736.
- [12] Hiemenz PC, Rajagopalan R, *Principles of Colloid and Surface Chemistry*, Third Edition, Revised and Expanded, Marcel Dekker, New York, 1997.
- [13] X. Li, J. Tian, W. Shen, *Anal and Bioanal Chem*, 2010; 396: 495-501.
- [14] Khan MS, Xu L, Shen W, Garnier G, *Colloids and Surfaces B: Biointerfaces*, 2010; 75 (1): 239-246.
- [15] Khan MS, Kannangara D, Shen W, Garnier G, *Langmuir*, 2008; 24: 3199-3204.
- [16] Roberts RJ, Senden TJ, Knackstedt MA, Lyne MB, *Pulp Paper Sci*, 2003; 29: 123-131.
- [17] Kent HJ, Lyne MB, *Nord Pulp Paper Res*, 1989; 4: 141-145.
- [18] Senden TJ, Knackstedt MA, Lyne MB, *Nord Pulp Paper Res*, 2000; 15: 554-563.
- [19] Rye RR, Mann JA, Yost FG, *Langmuir*, 1996; 12: 555-565.
- [20] Garnier G, Wright J, Godbout L, Yu L, *Colloids and Surfaces A: Physicochem Eng Aspects*, 1998; 145: 153-165.
- [21] Parker ER, Smoluchowski R, *Trans ASME*, 1944; 35: 362.
- [22] Romero LA, Yost FG, *Fluid Mech*, 1996; 322: 109-129.
- [23] Kumagai T, Abe Y, Muramatsu K, Kaneko J, Suzuki O, 20060233510. Hatakensaku Co., Ltd.Namics Co. 2006.
- [24] Shen W, Urquhart R, *Inkjet ink and paper Interaction*, Australian Printer, 2004.
- [25] Holdich R, Starov VM, Prokopovich P, Njobuenwu DO, Rubio RG, Zhdanov S, Velarde MG, *Colloids and Surfaces A: Physicochem Eng Aspects*, 2006; 282-83: 247-255.
- [26] Shen W, Filonanko Y, Truong Y, Parker I, Brack N, Pigram P, Liesegang J, *Colloids and Surfaces. A: Physicochem Eng Aspects*, 2000; 173: 117-126.

---

# Chapter 8

---

Effect of Liquid Droplet  
Impact Velocity on Its  
Wicking Kinetics in a  
Surface V-Groove

---

This page is intentionally blank

## Monash University

### Declaration for Thesis Chapter 8

**Declaration by candidate**

In the case of Chapter 8, the nature and extent of my contribution to the work was the following:

Nature of contribution	Extent of contribution (%)
Initiation, key ideas, experimental and analysis works, development and writing up of the paper	65

The following co-authors contributed to the work. Co-authors who are students at Monash University must also indicate the extent of their contribution in percentage terms:

Name	Nature of contribution	Extent of contribution (%) for student co-authors only
Gil Garnier	Initiation, key ideas, reviewing and editing of the paper	Co-supervisor
Wei Shen	Initiation, key ideas, reviewing and editing of the paper	Co-supervisor
Dushmantha Kannangara	Initiation and experimental work	25

Candidate's  
Signature

[Redacted Signature]

Date

17/12/09

**Declaration by co-authors**

The undersigned hereby certify that:

- (1) the above declaration correctly reflects the nature and extent of the candidate's contribution to this work, and the nature of the contribution of each of the co-authors.
- (2) they meet the criteria for authorship in that they have participated in the conception, execution, or interpretation, of at least that part of the publication in their field of expertise;
- (3) they take public responsibility for their part of the publication, except for the responsible author who accepts overall responsibility for the publication;
- (4) there are no other authors of the publication according to these criteria;
- (5) potential conflicts of interest have been disclosed to (a) granting bodies, (b) the editor or publisher of journals or other publications, and (c) the head of the responsible academic unit; and
- (6) the original data are stored at the following location(s) and will be held for at least five years from the date indicated below:

Location(s)

Australian Pulp and Paper Institute (APPI), Department of Chemical Engineering, Monash University, Clayton, VIC 3800, Australia.

Signature 1

[Redacted Signature]

Date

22/12/09

Signature 2

[Redacted Signature]

Date

17/02/10

Signature 3

[Redacted Signature] D. Kannangara

Date

17/02/10

# Effect of Liquid Droplets Impact Velocity on Its Wicking Kinetics in a Surface V-Groove

Mohidus Samad Khan, Dushmantha Kannangara, Gil Garnier and Wei Shen\*

Australian Pulp and Paper Institute,  
Department of Chemical Engineering,  
Monash University, Clayton, VIC 3800, Australia.

\*Corresponding author: Gil.Garnier@eng.monash.edu.au

Chapter 8	211
Effect of Liquid Droplet Impact Velocity on Its Wicking Kinetics in a Surface V-Groove	211
Abstract	214
1. Introduction	215
2. Experimental	217
2.1. Materials	217
2.2. Sample Preparation and Cleaning	217
2.3. Experimental Setup	218
3. Background	219
4. Results	221
4.1. V- Groove Geometry	221
4.2. Forced Spreading of the Impacting Droplets on Smooth Quartz Surface	221
4.3. Forced Liquid Drop Spreading and Recoiling on V-Groove Quartz Surface	223
4.4. V-groove Wicking	225
5. Discussion	227
5.2. Liquid Droplet Inertia Effects	227
5.3. Implication to Control Liquid Wicking Rate in an Inkjet Printing Application	229
6. Conclusion	230
Acknowledgment	230
References	231

## ABSTRACT

In this work the effect of droplet inertia on the liquid wicking in V-shaped open capillary on solid surface is investigated experimentally. The aim of this work is to understand the liquid droplet inertia effect on the forced liquid wicking in V-grooves. V-grooves are important topographic features for modeling uncoated paper surface for ink jet printing. Inter fibre gaps on uncoated paper surface have strong capillary guidance effect on ink penetration; ink wicking along paper surface inter fibre gaps is a significant cause for poor ink jet printing quality. In this study, the liquid droplet inertia and the V-groove geometry

The fewer the facts, the stronger the opinion.

– Arnold H. Glasow

are systematically varied to understand the effect of V-groove apex angle and groove width on the liquid wicking rate in the groove. Our results show that both the apex angle and the groove width influence the rate of liquid wicking in V-grooves forced by the liquid droplet inertia. The outcome of this work shows that liquid wicking forced by the liquid droplet inertia can be controlled by changing the V-groove geometric parameters. This work shows that applying surface sizing to uncoated ink jet papers is likely to be an effective way to change the geometry of the inter fibre gaps and therefore can reduce the feathering effect encountered in ink jet printing.

**Key Words:** Liquid drop impact, V-shaped grooves, capillary flow, ink jet printing.

## **1. INTRODUCTION**

Understanding the kinetics of wetting and penetration of liquid on a rough and porous solid surface is an important requirement in many industrial applications including printing technologies [1, 2], textile industries and microfluidic systems [3, 4]. The surface chemical and topographical properties of the substrate, as well as the physical properties of the liquid, play different but equally important roles in controlling the wetting and penetration process.

Recently, liquid penetration in open capillaries on a solid surface has been investigated by several research groups [5-7]. Liquid wicking in open capillary channels is highly relevant to many applications including the management of spacecraft propellant under low-gravity conditions [8], liquid penetration in biomedical chips [9], wetting and penetration of water on human skin [10] and wicking and penetration of water-based ink on paper surface in printing applications [2], to name just a few. Research work on liquid wicking in V-shaped grooves has resulted in the proposal of three mathematical models, all give good predictions to the liquid wicking kinetics in the V-groove [5-7].

The development of ink jet printing technology has motivated further research on the wetting and wicking of water-based inks into paper [11]. Several more recent studies have focused on the microscopic behaviour of liquid penetration in paper [2, 6, 11, 12]. These studies have presented a fresh understanding of the liquid penetration behaviour in responding to the geometric features of the pores. Paper is a porous material; its liquid absorption ability makes it an important material for printing. The

surface of uncoated papers is dominated by topographic features of cellulose fibres and fibre gaps. These unique topographic features strongly affect the liquid-paper interaction, since they provide capillary guidance to liquid wicking along the fibre gaps. Kannangara et al [2] have shown that ink jet ink penetration along the fibre gaps can be modelled by V-grooves. In this work we further consider the liquid droplet impact on liquid wicking kinetics in a V-groove. The rationale of this research is to closely examine the influence of liquid wicking kinetics in a V-groove through experiments and to understand the effect of droplet inertia on the liquid-paper interaction where fibre gaps are present on the paper surface as the dominant topographic features.

Rye et al. [6] proposed one of the first models for liquid wicking in V-groove capillary channels. Their model was established on the principle of (interfacial) energy balance, and at the same time considered the balance of a capillary driving force and the Poiseuille type liquid flow resistance force in a V-groove channel. By applying the boundary conditions that the V-groove connected to a large reservoir with no external pressure, Rye et al. arrived at a model which gives the similar penetration and time relationship to that by the Washburn model for cylindrical capillaries. Rye's model shows a strong dependence of liquid wicking rate upon V-groove geometry. However, the Rye's model does not predict liquid wicking rate when liquid droplet impacts on the V-groove with inertia.

Kannangara et al. [2] showed that the liquid droplet inertia significantly influences the ink droplet spreading on paper forced by the impact. Asai et al. [1] also reported the effect of inkjet ink droplet inertia on ink droplet impact on paper surface. Their work took the paper surface as a flat and uniform surface and did not focus on the topographic features. Although it is widely suspected that liquid droplet inertia influences the "subsequent" penetration of ink into the paper, there is no published report in the literature which addresses this issue in depth.

The motivation of this study is to further pursue our understanding of the liquid wicking behaviour in an open capillary groove on a solid surface with specific interest in the forced wicking situation where a liquid droplet impacts on such surfaces with inertia. This is because the impact of a liquid droplet onto a solid surface with surface capillary features sets a condition which may affect the subsequent liquid wicking in the surface grooves that have different geometric parameters. Previous V-groove wicking studies have shown that liquid wicking in V-grooves are sensitively related to the groove geometry. In this work, we will focus on the effect of forced liquid wicking in

V-groove of different geometric parameters due to droplet inertia. An improved understanding of liquid droplet inertia effect on liquid wicking will provide information for the surface design optimization of uncoated ink jet papers to improve ink jet print quality.

## **2. EXPERIMENTAL**

### **2.1. Materials**

Quartz V-groove samples of different groove angle ( $\beta$ ) = 60°, 90°, 120° and groove width ( $w_0$ ) = 0.2mm, 0.5 mm, were obtained from Hatakensaku Pty Ltd, Japan. The supplier also provided measurements of the dimensions of the V-groove using an undisclosed automated measurement system [7]. The V-groove cross-section profile (apex angle) and the width were checked to verify the supplier's specifications. Scanning Electron Microscopy (SEM) (FEG-SEM, JSM-6300F, JEOL, Japan), profilometry (COTEC-Altisurf© 500) and optical microscopy (Olympus BX60 with a CCD camera) were used for the V-groove dimension verification. Table 1 summarises our own measurements of the groove parameters, which are in good agreement with the supplier's specification.

Millipore water (18M $\Omega$ ) was used as the wicking liquid. All glassware were washed in 5% HNO<sub>3</sub> solution prepared using concentrated nitric acid (Labscan Analytical Science Pty Ltd) and rinsed with ample amount of water [13]. The cleaned glassware were first dried with fast flowing high purity nitrogen gas and then in an oven at 80°C for 8 hrs.

### **2.2. Sample Preparation and Cleaning**

The V-groove samples were first cleaned with laboratory detergent solution (RBS 35) followed by exhaustive rinsing with Millipore water. The samples were then soaked in a 5% HNO<sub>3</sub> solution overnight and rinsed thoroughly with water. Finally, the samples were dried at 80°C in an oven filled with nitrogen gas for at least 8 hrs and allowed to cool down in a desiccator before use. The effectiveness of this cleaning procedure was verified by the batch contact angle comparison and the uniformity of the

wetting area on the sample surface. Cleaned samples were used within 24 hrs after the cleaning procedure was completed.

## 2.3. Experimental Setup

The experimental setup consists of two high-speed cameras, a droplet dispensing system and two specially designed back light illumination units. Figure 1 is a schematic representation of the experimental configuration.

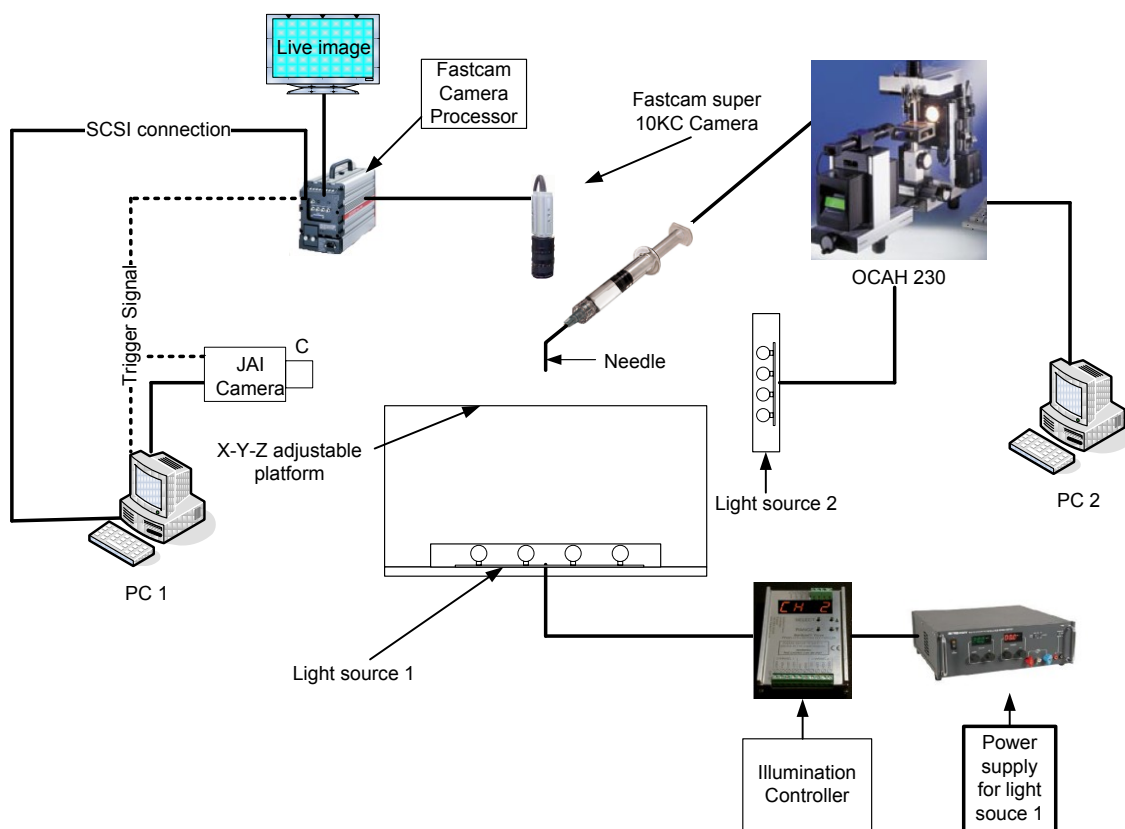


**Figure 1:** Schematic diagram of the experimental setup.

### 2.3.1. Droplet Generation

Millipore water (18M $\Omega$ ) was used as wicking liquid. The syringe pump of the OCAH-230 contact angle device (Dataphysics, Germany) was used to generate water droplets. A stainless steel flat-tipped needle of 0.21 mm outer diameter ( $d$ ) was fitted to the syringe pump, and programmed to dispense liquid at 0.11  $\mu\text{L/s}$ . To avoid water wetting the external wall, the needle was coated with a hydrophobization agent provided

by Dataphysics. Water droplets were delivered to the V-grooves by gravity. The droplet volume was around 4-5  $\mu\text{L}$  and the droplet diameter was around 2.0 mm. The droplet impact velocity was varied by controlling the height of free fall. The impact velocity was calculated using the free fall equation,  $v = (2gh)^{1/2}$ , where 'h' is the height of free fall and 'g' is the gravitational acceleration. The impact heights and corresponding impact velocities used in the experiment are respectively: (0 mm, 5 mm, 10 mm, 15 mm) and (0.00 m/s, 0.31 m/s, 0.44 m/s, 0.54 m/s). The experiments were performed at 23°C and 50% relative humidity (RH).

### **2.3.2. Image Capturing and Analysis**

Fastcam Super10KC high-speed camera (Photron USA, Inc., San Diego) was used to capture top-view images of wicking and wetting of the impacting droplet on the V-grooves at 500 frames per second (fps) and 5  $\mu\text{s}$  shutter speed. For illumination, Luxeon Flood® LED array powered by PP600F LED current controller (Gardasoft vision, Cambridge, UK) was positioned behind the impact area of interest. Distance between the sample surface and the illumination source was adjusted to obtain high contrast shadow of V-groove against a clear white background. Image-Pro Plus 5.0 software was used to analyze the top-view images. A second camera (CV- M30 from JAI-Copenhagen, Denmark), capable of recording at 360 fps, was used at a horizontal angle. The second camera was used as a support to the top-view camera to calculate the exact time,  $t_{\text{impact}}$ , at which the impacting droplet touches the surface. The wicking distance and wicking time are counted zero at  $t_{\text{impact}}$ . Both the cameras were triggered together at about 2 s prior to the droplet detachment from the needle.

## **3. BACKGROUND**

Liquid wicking kinetics in V-grooves modelled by several research groups have all resulted in pseudo Washburn relationships which can be written in the form below [5-7]. Those models are only different in the proportional term ( $K(\alpha, \theta)$ ), which is related to the detailed considerations of the liquid wicking driving forces.

$$z_0^2 = K(\alpha, \theta) \frac{\gamma h_0}{\mu} t \quad (\text{Eq.1})$$

where  $z_0$  is the liquid wicking along the V-groove,  $h_0$  is the groove depth,  $\theta$  is the liquid-solid contact angle and the angle  $\alpha = 90 - \beta/2$ , the apex angle ( $\beta$ ),  $\mu$  and  $\gamma$  are liquid's viscosity and surface tension. Kannangara et al. [7] summarized the driving force considerations of those models and revealed common conclusions of the wicking kinetics in relation to the groove geometric parameters. In the absence of liquid droplet inertia and impact, wicking kinetics data fit reasonably well in Eq. (1); liquid wicking in V-grooves of different geometric parameters can be extrapolated back to the origin. All models predicted that liquid wicking in V-grooves of larger groove width ( $w_0 = h_0/\tan\alpha$ ) and smaller apex angle ( $\beta$ ) is faster than that in V-grooves of smaller  $w_0$  and larger  $\beta$ . The previous models assumed that the droplet inertia and impact has negligible or no effect on capillary wicking. However, there was no attempt to justify this assumption.

In the Washburn model, external driving forces other than the Laplace pressure can be easily introduced to a closed cylindrical model. However, it is not easy for external forces to be considered in the modelling of liquid wicking in a V-groove, since the capillary channel is open to the atmosphere. The importance of the liquid droplet inertia effect in inkjet printing is that the surface capillary channels are exposed to ink droplets, which are not infinite liquid reservoirs. The partition of the limited liquid reservoir in several capillary channels will set a precondition of the subsequent wicking. A critical question is whether or not the V-groove geometric parameters also affect the wicking partition of a liquid droplet that impact on the grooves with inertia.

We take an experimental approach to investigate the inertia effect on liquid wicking in V-grooves. Through controlling the V-groove geometric parameters and the liquid droplet inertia, the forced liquid wicking data can be collected. By analysing liquid wicking acceleration inside the groove, the effect of liquid droplet inertia on liquid wicking in V-groove can be revealed.

## 4. RESULTS

### 4.1. V- Groove Geometry

Since the V-groove geometry strongly affects the liquid wicking rate, all V-grooves used in this study were carefully measured of their key geometrical parameters (i.e. apex angle,  $\beta$  and width,  $w_0$ ). Table 1 shows results measured by three different methods. All measured values agree with the manufacturer's specification within 2%.

**Table 1.** V-groove geometry from different techniques.

Groove Specification	SEM		Profilometry		Microscopy
	$w_0$ ( $\mu\text{m}$ )	$\beta$ ( $^\circ$ )	$w_0$ ( $\mu\text{m}$ )	$\beta$ ( $^\circ$ )	$w_0$ ( $\mu\text{m}$ )
60°, 0.5 mm	496	61.0	499	60.3	497
60°, 0.2 mm	201	60.5	202	59.9	204
90°, 0.5 mm	497	90.1	499	90.2	501
90°, 0.2 mm	204	89.8	203	90.1	202
120°, 0.5 mm	-	-	504	119.5	502
120°, 0.2 mm	-	-	201	118.9	198

The only deviation of the V-groove geometry from our model was that the apex angle was not sharp [7], instead, it was a symmetrically curved apex. Interestingly, the curved apex geometry was also reported by Rye et al. [6]. This curved apex geometry was limited by the manufacturing approach taken by the manufacturer [14]. Information about the manufacturing technique was limited. However, our measurement confirmed that the depth of curved apex geometry is consistent among samples.

### 4.2. Forced Spreading of the Impacting Droplets on Smooth Quartz Surface

The spreading and recoiling of water droplet on flat and smooth quartz surfaces over a range of impacting velocities were studied using the high speed CCD camera. Figure 2 shows the top views of droplet impacts at these velocities. At zero impact velocity, the droplet shows weak recoiling. At non-zero impacting velocities, a general

behaviour of droplet impaction is that the droplet spreads on the quartz surface under the inertia to the maximum wetting diameter and then starts to recoil without dewetting the quartz surface.

Several previous studies [2, 6, 12] have shown that the maximum droplet wetting area at the impact and the final equilibrium area on the solid surface depend on the droplet kinetic energy (impact velocity) and the degree of hydrophobicity/hydrophilicity of the solid surface. Kannangara et al. [2] showed that the spreading front of an impact droplet has a small contact angle with clean glass as the droplet was forced to spread out on the glass at the impact. As the water droplet recoils from the glass surface, water does not de-wet from the glass surface.

On quartz surface, three critical observations are made: first, water droplet recoils towards the droplet centre, leaving a ring of thin water film around the recoiled droplet. This confirms that water droplet does not de-wet the quartz surface when it recoils. Such behaviour is the same compared with the water droplet recoil from glass surface [2]. Second, water droplet recoil occurs around  $8 \text{ ms} \pm 1 \text{ ms}$  after the impact. This suggests that, irrespective to the droplet kinetic energy, droplet recoiling occurs at almost the same time after the impact. Third, the water droplet and quartz contact line during droplet impact and recoil is circular. Kannangara et al. [2] analyzed the liquid droplet recoil behaviour on both hydrophobic and hydrophilic surfaces. They observed that the cross section profiles of recoiling droplets were always symmetrical.

Figure 2 shows that the top view of droplet spreading and the recoil are circularly symmetrical on flat and smooth quartz surface. It was noticed, however, that the droplet spreading was not symmetric when quartz surface was not clean. This is because that the surface chemical heterogeneity influences the forced spreading and recoiling of an impacting droplet on solid surface.

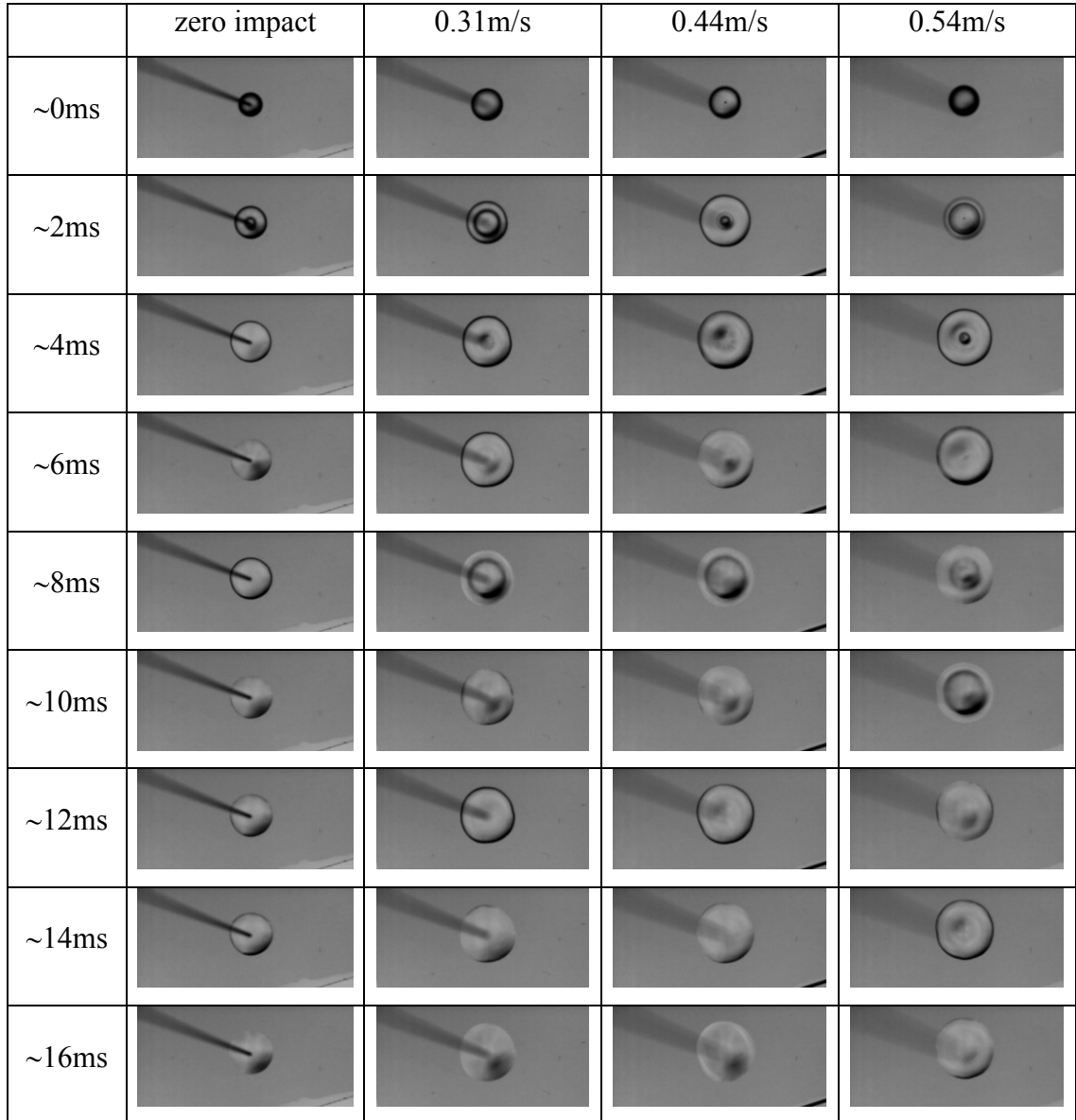


**Figure 2:** Dynamics of a sessile water droplet impinging, with different impact velocities, a flat quartz surface; images were taken at different magnifications.

### 4.3. Forced Liquid Drop Spreading and Recoiling on V-Groove Quartz Surface

The results of a water droplet impact on a quartz V-groove are shown in Figure 3. A syntax of apex angle, groove width and impact height are used as parameters to identify the results (apex angle (D)\_groove width (mm)\_impact height(mm)). Based on water droplet impact results, a few observations can be made. First, as the droplet

impacts on the surface, the water wicking front in the V-groove is ahead of the water droplet/quartz surface contact line on the smooth surface. A slight V-groove wicking asymmetry is observed in the very beginning of the impact (e.g. at 1 ms and 3 ms). By the time it reaches 5 ms, both wicking fronts are ahead of the spreading fronts (Figure 3). Since the droplet impact data on the smooth areas of the quartz surface (Figure 2) indicates that the forced spreading of the droplet after impact lasts for 8 ms, the droplet is still in the process of inertia-forced spreading after ~5 ms of droplet impact on the V-groove (Figure 3). This suggests liquid wicking in the V-groove is ahead of the forced droplet spreading after the impact. The initial asymmetry in the V-groove wicking could be caused by a slight surface chemical asymmetry along the groove.

Second, the shape of the water-quartz surface contact area in the presence of the V-groove is not circularly symmetric compared to the water-quartz contact line on the smooth areas of the quartz. When a V-groove is present, the water-quartz contact line has two curved sections. The curvature of the contact line diminishes as the contact line converges to the V-groove. Such an asymmetric spreading behaviour on V-groove surfaces starts from the beginning of the impact and maintains throughout the entire impact process. It indicates that surface topographic features such as V-grooves influence both free spreading (zero impact) and the forced spreading (non-zero impact) of droplet on solid surface. The clear observation of this behaviour from the beginning of the droplet – V-groove contact suggests that the effect of V-groove wicking shows no time delay.

Third, the droplet recoiling also occurs on surface with a V-groove. However, the presence of the V-groove reduces the intensity of the droplet recoil (see Figure 2 and Figure 3). Possible reasons for this phenomenon will be discussed later.

From the ink jet printing application point of view, the fast capillary wicking of ink on an uncoated paper surface is responsible for the poor print quality. When an ink drop impacts on an inter fibre gap, the dot shape is elongated along the direction of the gap due to wicking, leading to the deterioration of the dot fidelity [15].

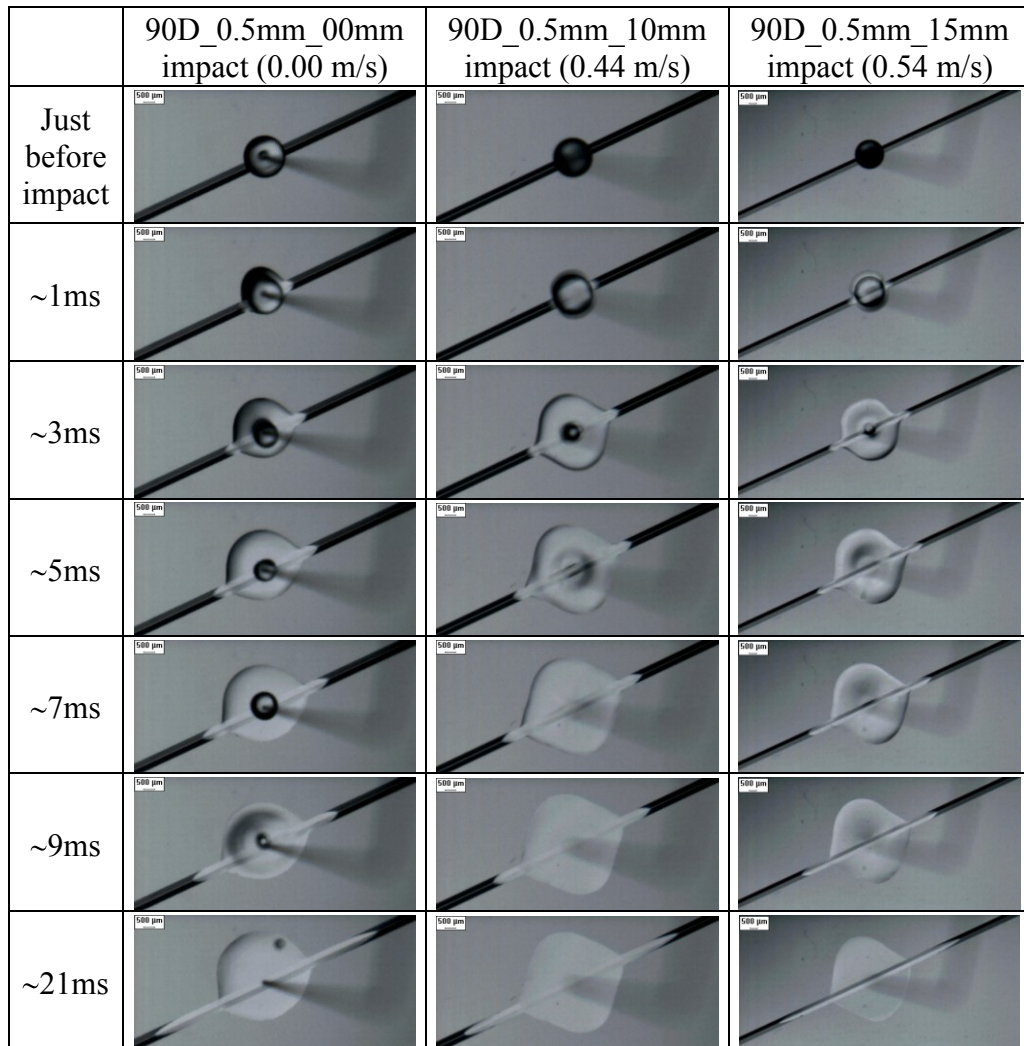
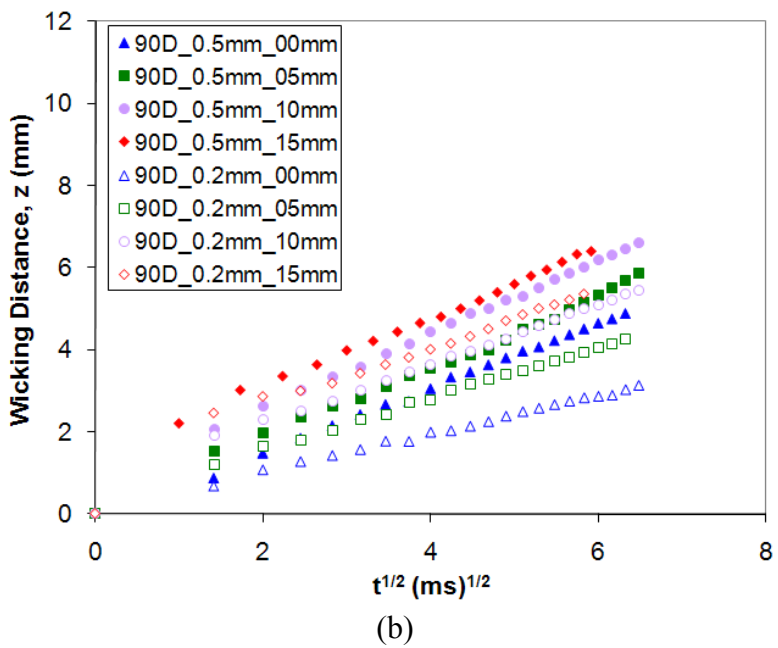
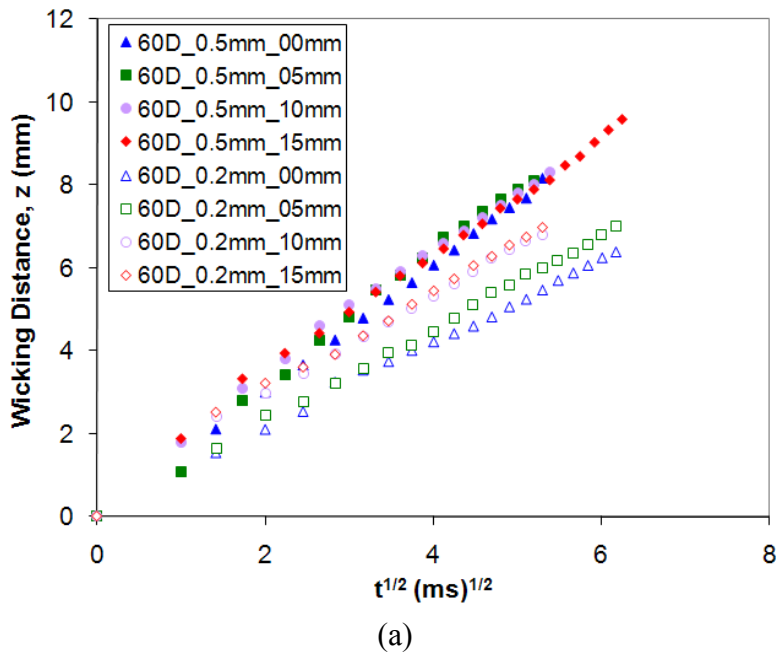


**Figure 3:** Dynamics of a sessile water droplet impinging, with different impact velocities, a V-groove ( $\beta = 90^\circ$ ,  $w_0 = 0.5\text{mm}$ ) quartz surface; images were taken at different magnifications.

#### 4.4. V-groove Wicking

The experimental results of water droplet wicking distances ( $z$ ) in V-grooves are presented as a function of square root of time. Figure 4 presents experimental results of water droplets impacting on all given V-groove geometry at different impact velocities. For a given groove geometry ( $\beta = 60^\circ, 90^\circ, 120^\circ$ ;  $w_0 = 0.2, 0.5\text{ mm}$ ) the highest wicking rate is observed for drop impact velocity of 0.54 m/s, followed by 0.41, 0.31 and 0 m/s (although for the 60D\_0.5mm groove the wicking speed does not show strong change

with the impact speed). For any droplet impact velocity, the wider groove shows the higher liquid wicking rate than the narrower groove of same groove angle (Figure 4 a - c).



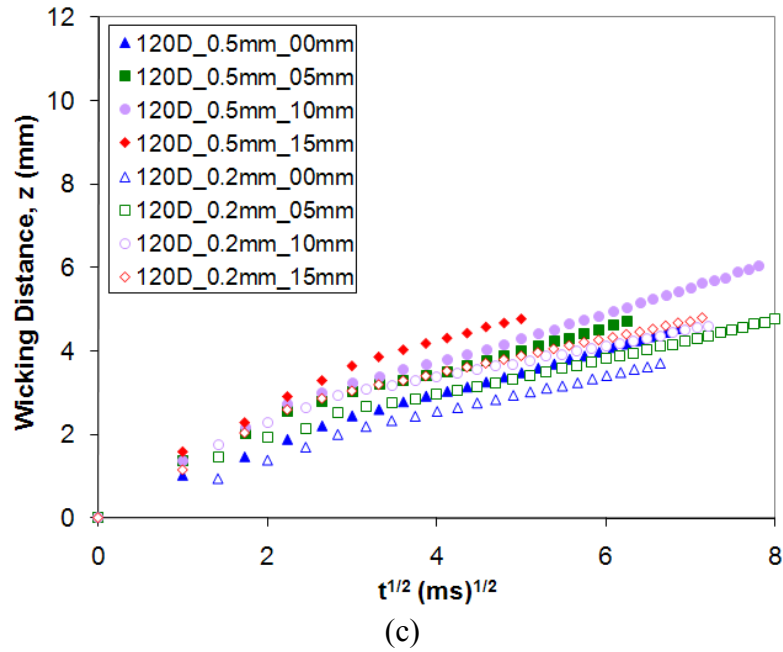


**Figure 4:** Effect of the impact velocity on the wicking dynamic; water wicking distance as a function of square root of  $t$  ( $\text{ms}^{1/2}$ ), V-groove on a quartz surface ( $v = 0.00\text{m/s}, 0.31\text{m/s}, 0.44\text{m/s}, 0.54\text{m/s}$ ). (a)  $\beta = 60^\circ$ ;  $w_0 = 0.2, 0.5\text{ mm}$ , (b)  $\beta = 90^\circ$ ;  $w_0 = 0.2, 0.5\text{ mm}$ , (c)  $\beta = 120^\circ$ ;  $w_0 = 0.2, 0.5\text{ mm}$ .

## 5. DISCUSSION

### 5.2. Liquid Droplet Inertia Effects

Our experimental results show that at 0 mm impact the water wicking distances with respect to the square root of time are linearly correlated; the linear data plots can be extrapolated to the origin (Figure 4). At non-zero impact velocities, Figure 4 shows that water wicking distances with respect to the square root of time are still linearly correlated. However, these linear data plots do not go through the origin (Figure 4). The higher the droplet inertia, the further the extrapolations deviate from the origin. This behaviour can only be explained as the effect of droplet inertia. The liquid wicking driving force of a droplet with inertia is greater than just the capillary driving force alone.

The instantaneous groove wicking velocity ( $\Delta z/\Delta t = dz/dt$ ) of sessile droplet impinging onto groove surfaces ( $\beta = 60^\circ, 90^\circ, 120^\circ$ ;  $w_0 = 0.2, 0.5\text{ mm}$ ) with different inertia was calculated and presented in Figure 5. As expected the wicking velocity reaches the maximum immediately after the droplet impinges upon the V-groove; the wicking velocity then sharply decays with time and reaches a state where further

deceleration is zero. At this state, for any given V-groove geometry, the wicking velocity is constant regardless the initial droplet impact velocity. For grooves of any given apex angle but different width, the maximum initial wicking velocity is greater for wider groove (Figure 5).

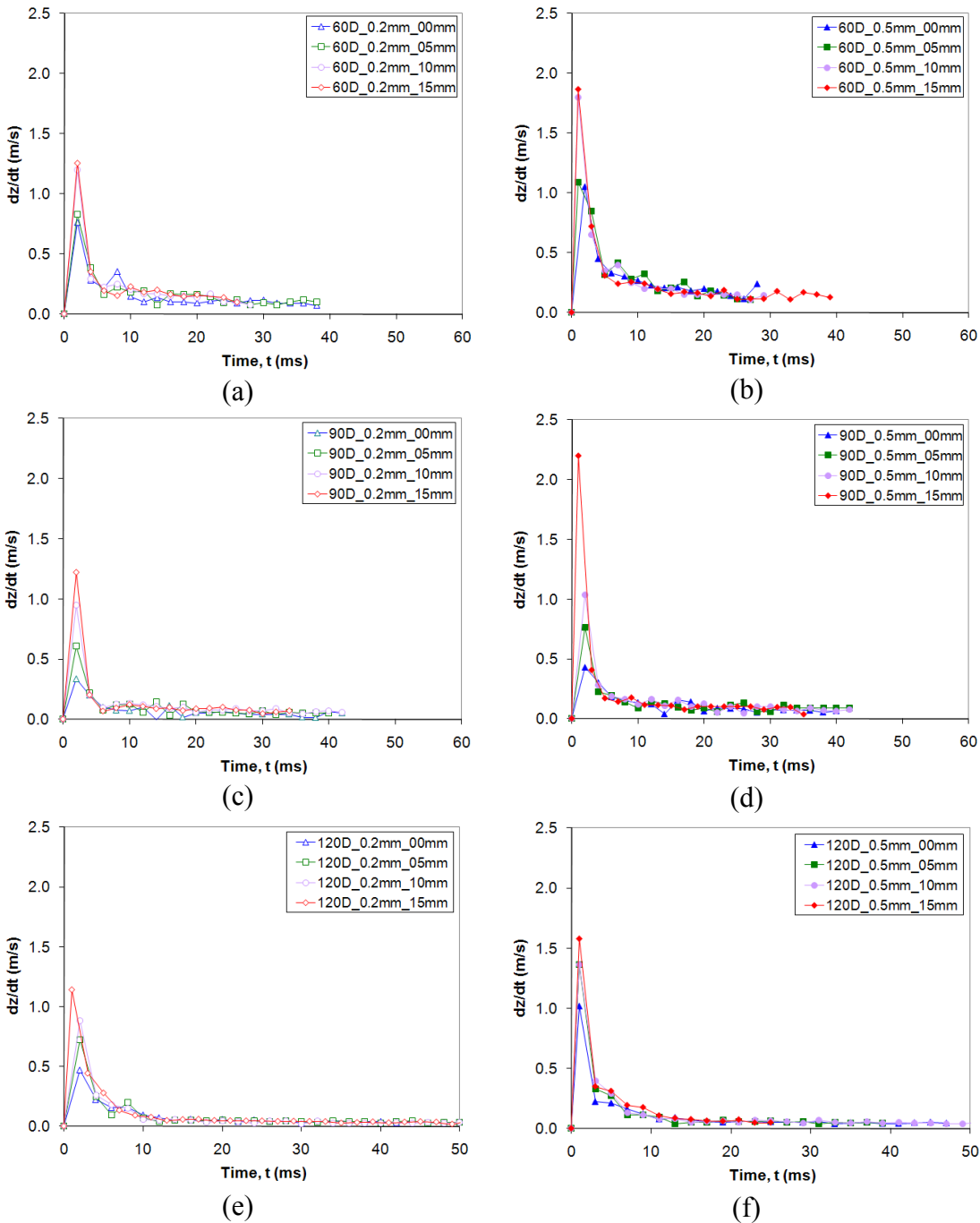


**Figure 5:** Effect of the groove geometry and inertia on the instantaneous wicking velocity ( $dz/dt$ ). (a)  $\beta = 60^\circ$ ,  $w_0 = 0.2$  mm, (b)  $\beta = 60^\circ$ ,  $w_0 = 0.5$  mm, (c)  $\beta = 90^\circ$ ,  $w_0 = 0.2$  mm, (d)  $\beta = 90^\circ$ ,  $w_0 = 0.5$  mm, (e)  $\beta = 120^\circ$ ,  $w_0 = 0.2$  mm, (f)  $\beta = 120^\circ$ ,  $w_0 = 0.5$  mm.

The instantaneous velocity data (Figure 5) suggests that, while a part of the inertia effect is consumed by overcoming the liquid flow resistance in the groove at a higher velocity, the rest is dissipated as the droplet recoils and to finally settle down [2, 6]. Our results show that time required for an impacting water droplet to reach its maximum diameter on a flat quartz surface is typically in the range of  $8\pm 1$  ms. It is reasonable to assume that the liquid droplet inertia effect on the forced V-groove wicking will also disappear within this time frame; since when the liquid droplet recoils, the non-dissipated kinetic energy is converted back to liquid surface energy and hydraulic potential energy. Data in Figure 5 suggest, however, that forced liquid wicking acceleration in V-grooves lasts for a period less than 8 ms. This is most likely because that the recoiling of liquid droplets from a surface with V-grooves is weaker than that from a flat surface, due to the loss of kinetic energy to forced groove wicking.

Figure 5 shows the effects of droplet inertia on V-grooves of different geometries. The data show that, for a given apex angle, the droplet inertia affects the wider V-grooves more significantly than the narrow grooves, since the forced liquid wicking in wider V-grooves causes the data plots to depart further away from that of the zero impact. However, it is noticeable that, even in the presence of inertial effect, V-grooves with higher apex angles still have slower overall wicking rates.

### **5.3. Implication to Control Liquid Wicking Rate in an Ink jet Printing Application**

The kinetic energy of the droplet pushes the liquid through the V-groove, making the liquid wicking rate in the V-groove faster than the natural capillary driven wicking rate. Our results show that the droplet inertia affects the liquid wicking rate in V-grooves, but the inertia effect quickly disappears. If an ink droplet impacts on more than one open capillary channel, the droplet inertial effect is expected to influence the ink wicking partition. Our results confirm that in the initial stage of the droplet impact, the droplet inertia effect will push more liquid into wider grooves with sharper apex angles. Therefore, the liquid droplet effect will affect liquid wicking partition into grooves of different geometries. An interesting implication of V-groove wicking to ink wicking on the uncoated paper surface is that the size and the shape of the inter fibre gap can strongly influence ink wicking and therefore the print quality. Internal paper sizing can reduce the ink wicking driving force, however, the result of internal sizing is

not uniform [2]. There are always some inter fibre gaps that acquires a low level of sizing relative to the other areas, and that can facilitate ink wicking [13, 16]. By applying surface sizing to the uncoated paper surface, one may fill the inter fibre gaps to some extent with the surface sizing starch. The filling of the inter fibre gaps is expected to reduce the gap width and to increase the gap apex angle. These groove geometrical changes are expected to effectively reduce the forced ink wicking by ink droplet impact. These changes are also expected to reduce the capillary driven ink wicking in inter fibre gaps after the droplet impact.

## **6. CONCLUSION**

The liquid wicking kinetics of an impacting droplet onto the V-shaped surface capillaries has been studied experimentally. We have developed an experimental setup to investigate the liquid wicking forced by the droplet inertia. With our experimental setup, we have shown that the liquid droplet impact on the V-groove surface with inertia has an effect in forcing the liquid to wick through the V-grooves. This effect influences the liquid wicking kinetics in the initial stage of droplet impact onto the groove; the wicking kinetics rapidly return to the capillary driven regime as the liquid droplet rebounds from the surface. The V-groove width and the apex angle also influence the liquid wicking rate in V-grooves forced by the droplet inertia. The liquid droplet inertia effect on V-groove wicking kinetics is relevant to ink-paper interactions in ink jet printing on uncoated papers. Preferential wicking of ink along wide and deep inter fibre grooves is a significant cause of the ink feathering which lowers the ink jet print quality. We proposed, based on the finding of this study, that surface sizing may be a very effective way to reduce the ink drop inertia effect on the preferential wicking of inks along inter fibre gaps and improve the ink jet print quality.

## **ACKNOWLEDGMENT**

M.S.K. and D.K. would like to gratefully acknowledge Monash University, Departments of Chemical Engineering and CRC SmartPrint for funding this work.

## REFERENCES

- [1] A. Asai, M. Shioya, S. Hirasawa, T. Okazaki, Impact of an Ink Drop on Paper, *J. Imaging Sci. Technol.* 37 (1993) 205-207.
- [2] D. Kannangara, H. Zhang, W. Shen, Liquid-paper interactions During Liquid Drop Impact and Recoil on Paper Surfaces, *Colloids and Surfaces, A: Physicochemical and Engineering Aspects* 280 (2006) 203-215.
- [3] J.-C. Baret, M.M.J. Decre, S. Herminghaus, R. Seemann, Transport Dynamics in Open Microfluidic Grooves, *Langmuir* 23 (2007) 5200-5204.
- [4] R. Seemann, M. Brinkmann, E.J. Kramer, F.F. Lange, R. Lipowsky, Wetting morphologies at microstructured surfaces, *Proceedings of the National Academy of Sciences of the United States of America* 102 (2005) 1848-1852.
- [5] L.A. Romero, F.G. Yost, Flow in an Open Channel Capillary, *Journal of Fluid Mechanics* 322 (1996) 109-129.
- [6] R.R. Rye, J.A. Mann, F.G. Yost, The flow of liquids in surface grooves, *Langmuir* 12 (1996) 555-565.
- [7] D. Kannangara, M.S. Khan, W. Shen, Wicking of a Liquid Droplet in a Surface Groove, *Advances in Colloid and Interfaces Science* (Submitted).
- [8] U. Rosendahl, A. Ohlhoff, M.E. Dreyer, H.J. Rath, Investigation of forced liquid flows in open capillary channels, *Microgravity Sci. Technol.* 13 (2002) 53-59.
- [9] W.S. Kim, M.G. Kim, J.H. Ahn, B.S. Bae, C.B. Park, Protein Micropatterning on Bifunctional Organic-Inorganic Sol-Gel Hybrid Materials, *Langmuir* 23 (2007) 4732-4736.
- [10] A.D. Dussaud, P.M. Adler, A. Lips, Liquid transport in the networked microchannels of the skin surface, *Langmuir* 19 (2003) 7341-7345.
- [11] R.J. Roberts, T.J. Senden, M.A. Knackstedt, M.B. Lyne, Spreading of Aqueous Liquids in Unsized Papers is by Film Flow, *Journal of Pulp and Paper Science* 29 (2003) 123-131.
- [12] T.J. Senden, M.A. Knackstedt, M.B. Lyne, Droplet penetration into porous networks: role of pore morphology, *Nordic Pulp & Paper Research Journal* 15 (2000) 554-563.
- [13] G. Garnier, J. Wright, L. Godbout, L. Yu, Wetting Mechanism of Alkyl Ketene Dimers on Cellulose Films, *Colloids and Surfaces A: Physicochem. Eng. Aspects* 145 (1998) 153-165.
- [14] T. Kumagai, Y. Abe, K. Muramatsu, J. Kaneko, O. Suzuki, Optical fibre array, Hatakensaku Co., Ltd. Namics Co., US, 2006.
- [15] L.R. Fisher, P.D. Lark, Experimental-Study of the Washburn Equation for Liquid Flow in Very Fine Capillaries, *Journal of Colloid and Interface Science* 69 (1979) 486-492.
- [16] E.R. Parker, R. Smoluchowski, Capillarity of Metallic Surfaces, *Trans. ASME* 35 (1944) 362.

This page is intentionally blank

---

# Chapter 9

---

Wetting and Wicking  
Kinetics of a Sessile  
Droplet Impinging a  
Narrow Groove

---

This page is intentionally blank

## Monash University

### Declaration for Thesis Chapter 9

**Declaration by candidate**

In the case of Chapter 9, the nature and extent of my contribution to the work was the following:

Nature of contribution	Extent of contribution (%)
Initiation, key ideas, experimental and analysis works, development and writing up of the paper	60

The following co-authors contributed to the work. Co-authors who are students at Monash University must also indicate the extent of their contribution in percentage terms:

Name	Nature of contribution	Extent of contribution (%) for student co-authors only
Gil Garnier	Initiation, key ideas, reviewing and editing of the paper	Co-supervisor
Wei Shen	Initiation, key ideas, reviewing and editing of the paper	Co-supervisor
Dushmantha Kannangara	Initiation and experimental work	30

Candidate's Signature

[Redacted Signature]

Date

16/12/09

**Declaration by co-authors**

The undersigned hereby certify that:

- (1) the above declaration correctly reflects the nature and extent of the candidate's contribution to this work, and the nature of the contribution of each of the co-authors.
- (2) they meet the criteria for authorship in that they have participated in the conception, execution, or interpretation, of at least that part of the publication in their field of expertise;
- (3) they take public responsibility for their part of the publication, except for the responsible author who accepts overall responsibility for the publication;
- (4) there are no other authors of the publication according to these criteria;
- (5) potential conflicts of interest have been disclosed to (a) granting bodies, (b) the editor or publisher of journals or other publications, and (c) the head of the responsible academic unit; and
- (6) the original data are stored at the following location(s) and will be held for at least five years from the date indicated below:

Location(s)

Australian Pulp and Paper Institute (APPI), Department of Chemical Engineering, Monash University, Clayton, VIC 3800, Australia.

Signature 1

[Redacted Signature]

Date

17/12/09

Signature 2

[Redacted Signature]

Date

17/12/09

Signature 3

Dushmantha Kannangara

Date

17/12/09

# Wetting and Wicking Kinetics of a Sessile Droplet Impinging a Narrow Groove

Mohidus Samad Khan, Dushmantha Kannangara, Wei Shen and Gil Garnier\*

Australian Pulp and Paper Institute,  
Department of Chemical Engineering,  
Monash University, Clayton, VIC 3800, Australia.

\*Corresponding author: Gil.Garnier@eng.monash.edu.au

Chapter 9	233
Wetting and Wicking Kinetics of a Sessile Droplet Impinging a Narrow Groove	233
Abstract	236
1. Introduction	237
2. Theory	239
2.1. Wetting	239
2.2. Wicking	239
3. Experimental	242
3.1. Sample Preparation and Cleaning	242
3.2. Experimental Setup	243
3.3. Droplet Generation	243
3.4. Image Capturing System and Image Analysis	244
4. Results	245
5. Discussion	250
6. Conclusion	257
Acknowledgment	257
References	258

## ABSTRACT

The dynamic of wicking and wetting of sessile droplets impinging a narrow groove of wide angle ( $120^\circ$ ) was investigated. This system plays a critical role in many industrial processes such as ink jet printing. The variables of interest were the impinging droplet velocity and the groove width; the surface energetic and droplet size were kept constant. Wetting and wicking velocities were measured by high speed image analysis. The maximum wetting and wicking velocities were found to be equal. The wetting velocity reaches a maximum instant after it touches the surface and decreases exponentially until the resting contact angle is reached, at which instant wetting stops. Groove wicking velocity has a similar

behaviour. However, at steady state, wicking proceeds at constant velocity (0.05 m/s), which goes against the prediction of theoretical models for a non-wetting groove ( $\theta \geq 120^\circ$ ). The maximum wetting and wicking velocity both increase with the droplet impinging velocity.

**Key Words:** Wicking, wetting, V-groove, sessile droplet, impact, kinetics.

## 1. INTRODUCTION

The distribution of a liquid over a solid surface plays a critical role in nature and in many industrial processes. For molecularly smooth solid surfaces, wetting is the dominant mechanism. The physics and dynamics of free wetting are now well understood [1-8]; much less understood is the dynamic of forced wetting. Most surfaces are imperfect with chemical and physical heterogeneities of different length scales typically ranging from the nanometer to the micron. These surface defects can either be random or structured, discrete or continuous. The physics of imperfect solid surfaces with discrete periodic defects has generated wide interest to understand and control phenomena such as superhydrophobicity and superhydrophilicity with the rose petal and the lotus leaf as models, and applications such as self-cleaning and fogless surfaces [9-11]. Grooves and open channel capillaries are two important examples of continuous surface defects. Wicking plays a crucial role in nature and many industrial processes by controlling the fluid distribution and the dynamics of a liquid contacting a groove.

Model systems developed to quantify wicking typically consist of a well-defined groove fed by an infinite reservoir of liquid [12-16]. Groove angle, geometry and dimensions were found to be the key variables [12, 14, 15]. While the groove wicking mechanism for liquid in infinite reservoir is fairly well understood, that of finite droplets contacting a capillary of similar dimension to the droplet radius remains obscure. This configuration is especially important for ink jet printing technology, now widely investigated for functional printing in novel applications such as bio-assays [17-19], tissue engineering, solar panel manufacturing and the engineering of superhydrophobic or superhydrophilic surfaces.

Recent work in our laboratory has shown, groove angle and dimension to be the two important variables for the wicking of a sessile droplet touching a triangular section

channel [20]. However, droplets are very seldom gently deposited onto a surface. Most often the droplets are impinged with significant potential or kinetic energy onto a grooved surface. This is the case of the rain hitting a leaf or a brick wall, the inkjet droplet colliding with paper, or the paint sprayed onto wood. Surprisingly little information is available on the motion of small sessile droplets impinging an imperfect surface with grooves.

For many industrial applications the specific case of grooves having a contact angle higher than  $90^\circ$  and being narrower than the liquid droplet are of special interest. This is the case of ink jet printing and spraying over coated surfaces. Also critical and inadequately understood are the dynamics of droplets in the short contact time during which a droplet has full mobility to wick and wet, prior to any subsequent adsorption, evaporation or reaction. This experimental investigation aims at providing a better understanding of the dynamics of sessile droplets impinging a grooved surface.

A well controlled system consisting of a water droplet impinging at various velocities a triangular groove (groove angle,  $\beta = 120^\circ$ ) on a smooth quartz surface was engineered. The dynamics of wicking and wetting was recorded by high speed image analysis. The surface energy of the system was kept constant. It is the objective of this study to quantify the effect of droplet impinging velocity on the liquid wicking and wetting kinetics for droplets impinging a narrow groove (groove angle,  $\beta = 120^\circ$ ).

In this study wetting and wicking are defined as the movement of fluid over a flat surface and within a groove, respectively. Wetting can either be ‘free’, when the liquid advances on a solid surface towards equilibrium without any external force or ‘forced’ when some external hydrodynamic or mechanical forces are imposed on the system [21, 22].

## 2. THEORY

### 2.1. Wetting

Liquid wetting on a solid surface can be broadly classified as free or forced wetting. The contact angle of a sessile droplet freely wetting a surface can be described by the Hoffman-Tanner equation [23, 24]:

$$\theta^3 - \theta_E^3 \propto Ca \quad (\text{Eqn.1})$$

Where  $Ca$  is the capillary number defined as:

$$Ca = \frac{\mu u}{\gamma} \quad (\text{Eqn.2})$$

and  $\theta_{(t)}$  is the instantaneous contact angle formed by a fluid of viscosity  $\mu$  and surface tension  $\gamma$ , moving at a velocity  $u$ , and  $\theta_E$  is the equilibrium contact angle. Eqn. (1) states that the surface forces expressed by a function of the difference of the droplet equilibrium contact angle minus its instantaneous angle are balanced by viscous forces. In forced wetting, an externally imposed hydrodynamic or mechanical force increases the solid-liquid interface beyond the static equilibrium [21, 22].

### 2.2. Wicking

The kinetics of capillary flow in closed capillaries is well known [27]. The Washburn equation expresses liquid wicking in a cylindrical capillary [14, 25, 26].

$$z^2 = \cos^2 \theta \frac{\gamma r}{\mu} t \quad (\text{Eqn.3})$$

where  $z$  is the length of liquid column entering the cylindrical capillary of radius  $r$ ,  $\theta$  is the contact angle, forced by a liquid of viscosity  $\mu$  and surface tension  $\gamma$  (Figure 1 and 2).

By performing a force/mass balance and by relying on the Poiseuille flow and the Laplace equations, the wicking kinetics through an open triangular groove was analytically derived as [13]:

$$z_0^2 = \frac{\gamma \cos \alpha}{\mu} \left( \frac{\gamma h_0}{\mu} t \right) \equiv \zeta(\alpha) \left( \frac{\gamma h_0}{\mu} t \right) \quad (\text{Eqn.4})$$

where  $z_0$  is the liquid wicking along the V-groove,  $h_0$  is the groove depth,  $\theta$  is the liquid-solid contact angle and the angle  $\alpha = 90 - \beta/2$ , the apex angle ( $\beta$ ).

Rideal performed a simple force balance with an inertia and surface tension contributor [25] :

$$m \frac{d^2 z}{dt^2} = F_\gamma - F_\mu \quad (\text{Eqn.5})$$

where,  $F_\gamma$  is the surface tension driving force and  $F_\mu$  is the retarding force due to viscosity of the liquid. From the force balance Rye et al. derived the liquid kinetics of liquid wicking along a V-groove as [14]:

$$z^2 = \zeta(\alpha, \theta) \frac{\gamma h_0 t}{\mu} \quad (\text{Eqn.6})$$

$$K(\theta, \alpha) = \frac{1}{2\pi \sin \alpha} \left[ \cos \theta - \frac{\alpha - \theta}{\sin(\alpha - \theta)} \cos \alpha \right] \quad (\text{Eqn.7})$$

where,  $\theta$  = contact angle,  $h_0$  = groove height,  $\alpha = 90^\circ - \beta/2$ ,  $\beta$  = groove angle,  $\gamma$  = liquid surface tension,  $\mu$  = viscosity,  $t$  = time and  $z$  = liquid wicking distance along the groove.

When  $\alpha = \theta$ , the V-groove becomes fully filled with liquid and form a flat liquid surface (Figure 2); at the limit of  $\alpha \rightarrow \theta$ , Eqn. (6) and (7) reduce to the Washburn solution expressed by Eqn. (8) [13, 14].

$$z^2 = \zeta(\alpha, \theta) \frac{\gamma h_0 t}{\mu} = \frac{\cos \theta - \cos \alpha}{2\pi \sin \alpha} \frac{\gamma h_0 t}{\mu} \quad (\text{Eqn.8})$$

The Washburn approach is limited to angle  $\alpha > \theta$  predicts a rate which approaches zero as  $\alpha \rightarrow$  [14] and does not consider droplet impact.

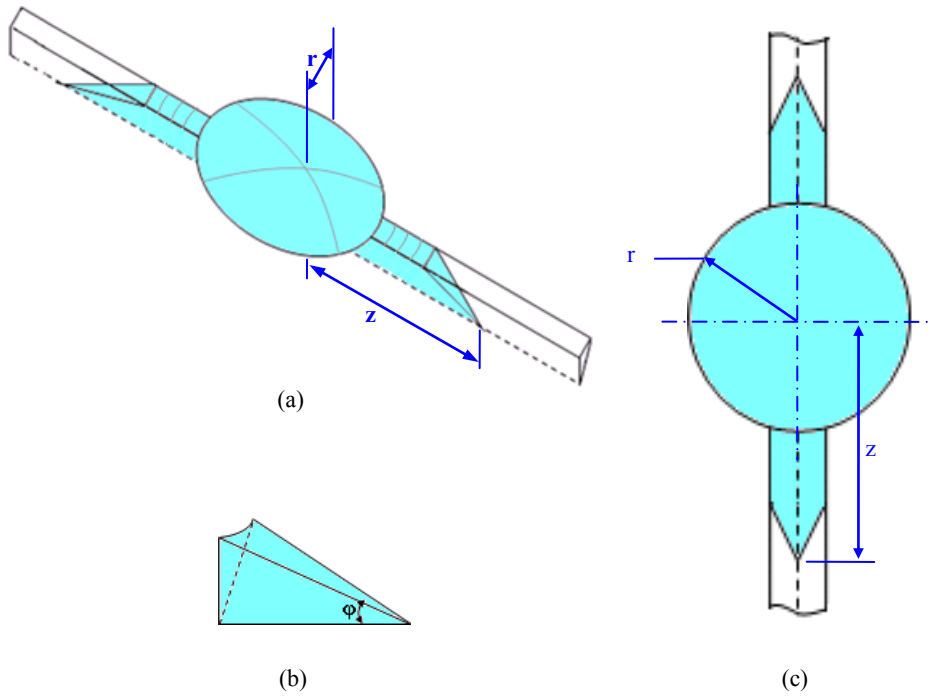


**Figure 1** Schematic representation of wetting  $[r(t)]$  and wicking  $[z(t)]$  of a sessile droplet impinging the middle of a V-groove. (a) Isometric view, (b) threshold region, (c) top view.

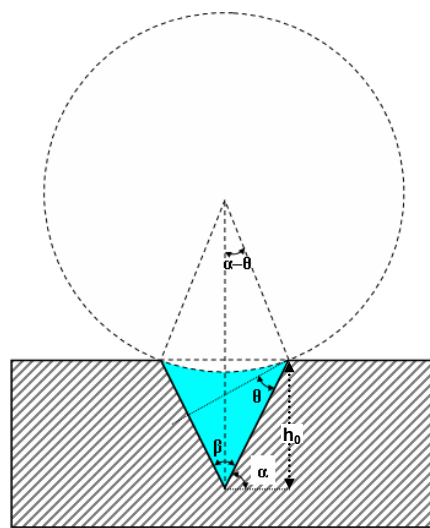


**Figure 2** Schematic representation of the V-groove.

### 3. EXPERIMENTAL

#### 3.1. Sample Preparation and Cleaning

Quartz surfaces with  $120^\circ$  V-groove were purchased from Hatakensaku Pty Ltd, Japan. The V-groove profile as observed by Talysurf Series, supplied by the supplier, is shown in Figure 3.

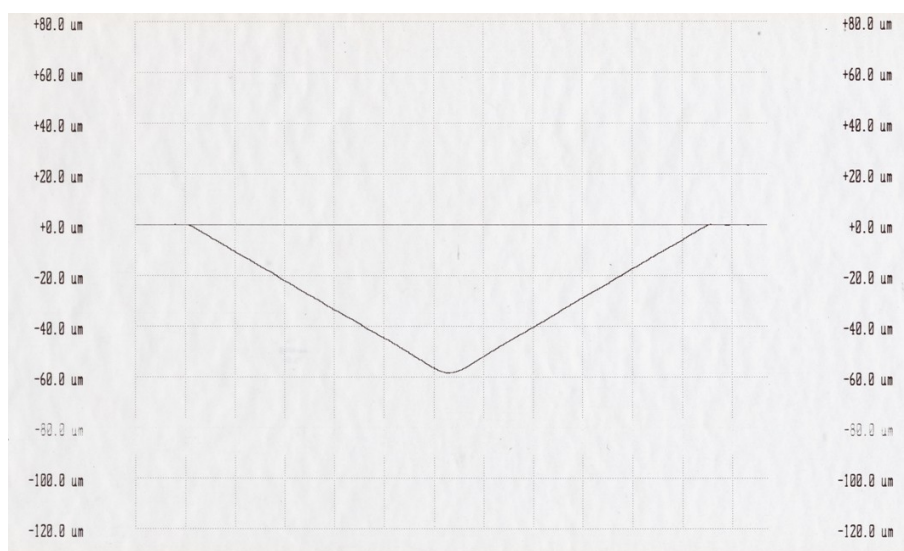


**Figure 3** Schematic of surface profile of V-groove ( $\beta=120^\circ$ ,  $w_0 = 0.2$  mm) measured using Talysurf Series; measurement: Slope =  $\alpha = 90^\circ - \beta/2 = 30^\circ$ .

The V-groove surfaces were first cleaned with a detergent solution (RBS 35), exhaustively rinsing with Millipore water, then soaked in a 5%  $\text{HNO}_3$  solution overnight and rinsed thoroughly with water [4]. Finally, the cleaned surfaces were dried for 8 hours at  $80^\circ\text{C}$  in an oven (Mettler Universal Oven, Schwabach, Germany) filled with nitrogen cooled and stored in a desiccator until use. The effectiveness of this cleaning procedure was verified by batch contact angle comparison and the uniformity of the wetting area on the sample surface. The surfaces were used for the impact experiment within 24 hours after the cleaning procedure.

### 3.2. Experimental Setup

The experimental setup consists of a high-speed camera, a droplet dispensing system and a back light illumination system (Figure 4).

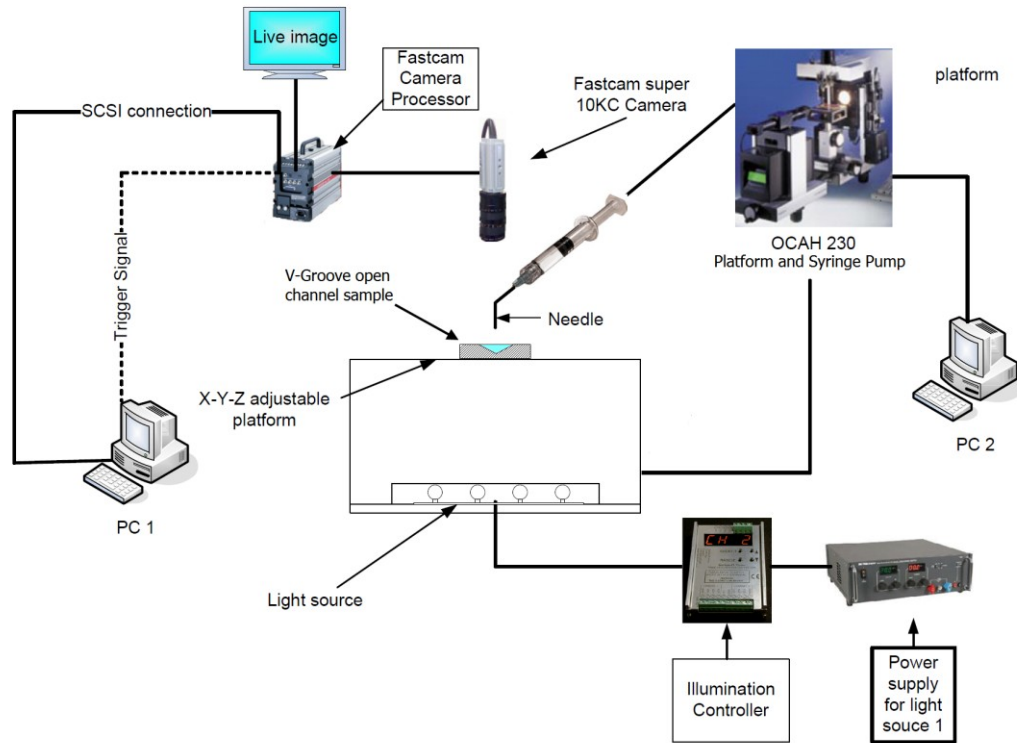


**Figure 4** Experimental system to measure wicking and wetting.

### 3.3. Droplet Generation

Millipore water (18M $\Omega$ ) was used as wicking liquid. The syringe pump of the OCAH-230 contact angle device (Dataphysics, Germany) was used to generate water droplets. A stainless steel flat-tipped needle of 0.21 mm outer diameter ( $d$ ) was fitted to the syringe pump, programmed to dispense liquid at 0.11  $\mu\text{L/s}$ . To avoid water wetting the external wall, the needle was coated with a hydrophobization agent provided by Dataphysics. Water droplets were delivered to the V-grooves by gravity and the droplet volume was around 4-5  $\mu\text{L}$  and the droplet diameter was around 2.0 mm. The velocity of impact of the droplet was varied by controlling the height of free fall. The impact velocity was calculated using the free fall equation,  $v = (2gh)^{1/2}$ , where  $h$  is the height of

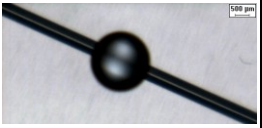
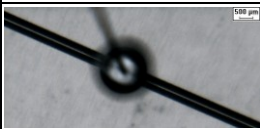
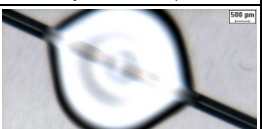
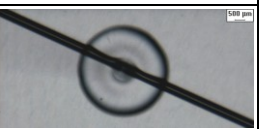
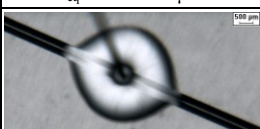
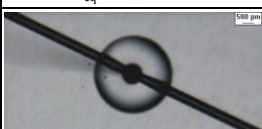
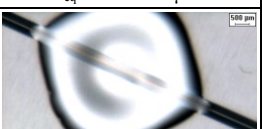
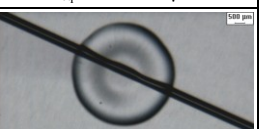
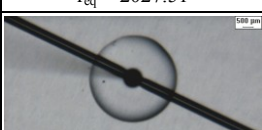
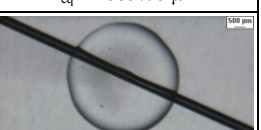
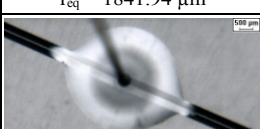
free fall and  $g$  is the gravitational acceleration. The impact heights and corresponding impact velocities used in the experiment are respectively: (0 mm, 5 mm, 10 mm, 15 mm) and (0.00 m/s, 0.313 m/s, 0.443 m/s, 0.542 m/s). The experiments were performed at 23°C and 50% relative humidity (RH).

### **3.4. Image Capturing System and Image Analysis**

A fastcam Super10KC high-speed camera (Photron USA, Inc., San Diego) captured top-view images of wicking and wetting of the impacting droplet on the V-grooves at 500 frames per second (fps) and 5  $\mu$ s shutter speed. For illumination, Luxeon Flood® LED array powered by a PP600F LED current controller (Gardasoft vision, Cambridge, UK) was positioned behind the impact area. Distance between the sample surface and the illumination source was adjusted to obtain high contrast shadow of V-groove against a clear white background. Image-Pro Plus 5.0 software was used to analyze the images. The wicking and wetting distances were counted zero at  $t_{\text{impact}}$ , the time at which the impacting droplet touches the surface.

## 4. RESULTS

The Dynamics of wetting and wicking of sessile droplets impinging onto a V-groove were captured by high speed image analysis (Figure 5, Figure 6). The surface energetic of the system was kept constant. The equilibrium contact angle of water over quartz was measured to be  $30^\circ (\pm 2^\circ)$  [20]. The V-groove angle was fixed at  $120^\circ$ , and two groove widths were investigated: 0.2 and 0.5 mm ( $\beta = 120^\circ$ ,  $w_0 = 0.2, 0.5$  mm). The radius of dispensed droplet, around 2 mm, was significantly larger than the groove width.

	No Inertia (0.00m/sec)		With Inertia (0.542m/sec)	
	V-groove surface	flat surface	V-groove surface	flat surface
Just before impact	 $r_{eq} = 872.77 \mu\text{m}$	 $r_{eq} = 1065.74$	 $r_{eq} = 1013.44 \mu\text{m}$	 $r_{eq} = 993.80 \mu\text{m}$
~2ms	 $r_{eq} = 1244.16 \mu\text{m}$	 $r_{eq} = 1403.66$	 $r_{eq} = 1977.48 \mu\text{m}$	 $r_{eq} = 1739.16 \mu\text{m}$
~4ms	 $r_{eq} = 1634.12 \mu\text{m}$	 $r_{eq} = 1715.59$	 $r_{eq} = 2463.18 \mu\text{m}$	 $r_{eq} = 2285.76 \mu\text{m}$
~6ms	 $r_{eq} = 1788.80 \mu\text{m}$	 $r_{eq} = 2027.51$	 $r_{eq} = 2740.72 \mu\text{m}$	 $r_{eq} = 2559.06 \mu\text{m}$
~8ms	 $r_{eq} = 1841.94 \mu\text{m}$	 $r_{eq} = 2235.46 \mu\text{m}$	 $r_{eq} = 2879.50 \mu\text{m}$	 $r_{eq} = 2782.66 \mu\text{m}$
~10ms	 $r_{eq} = 1930.49 \mu\text{m}$	 $r_{eq} = 2261.46 \mu\text{m}$	 $r_{eq} = 2931.53 \mu\text{m}$	 $r_{eq} = 2857.20 \mu\text{m}$

**Figure 5** Dynamics of a sessile water droplet impinging, with and without initial velocity, a flat quartz surface or a V-groove ( $\beta = 120^\circ$ ,  $w_0 = 0.5$  mm; quartz surface) on a quartz surface; images were taken at different magnifications.

The impact velocity of the droplet was varied from 0 to 0.54 m/s by controlling the height of free fall (Figure 5). The combined wetting and wicking dynamics of sessile droplets impinging, with and without inertia, onto a flat or a grooved quartz surface are illustrated on Figure 5 for short intervals of time (1 to 10 ms). Few observations are of interest. First, the three phase contact line of the droplet wetting the flat quartz surface remains circular independently of the initial velocity of impact. Second, the profile of the droplet wicking/wetting a groove surface loses its circular symmetry to become elongated toward the axis of the groove. Third, the droplet elongation behaviour on the groove and the dynamics of wetting and wicking both increased with the impact velocity of the impinging droplet.

The effect of the groove width on the wetting and wicking dynamics of a water droplet impinging at 0.54 m/s the centre of a 120° groove on a quartz surface is illustrated in Figure 6. The images were taken at different magnifications. Increasing groove width increases the elongation of the droplet along the groove axes and the wicking dynamics.

The wicking kinetics of a water droplet impinging the centre of the V-groove is quantified for different impinging velocities for the wider groove (0.5 mm) and for the narrow groove (0.2 mm) on Figure 7a and 7b, respectively. Figure 8 represents the wetting kinetics for the same system. The groove width and impact heights are used to identify the experiments (i.e. groove width (mm) \_ impact height (mm)). There are a few commonalities. A two-phase behaviour with a steep transient phase (up to 10 ms) decelerating to constant steady state kinetics (10 to 60 ms) is observed both for wetting and groove-wicking. The initial wicking and wetting velocities, represented by the initial slopes of Figure 7 and 8, are both increasing with the initial impingement velocity of the droplet. In the transition phase the wicking and wetting distances were basically proportional to the droplet impact velocities. The exception was the droplet wetting with no impact on the 0.2 mm wide groove, probably due to experimental error. After the transition phase, wicking velocity of the droplet proceeds at a constant velocity in the groove which is independent of the initial droplet impact velocity. The initial wetting velocity of the droplet three-phase line outside the groove also increases with the droplet initial impinging velocity. Once the water droplet reaches its resting contact angle, after around 10 ms, wetting stops and the droplet remains on the quartz surface while wicking proceeds.

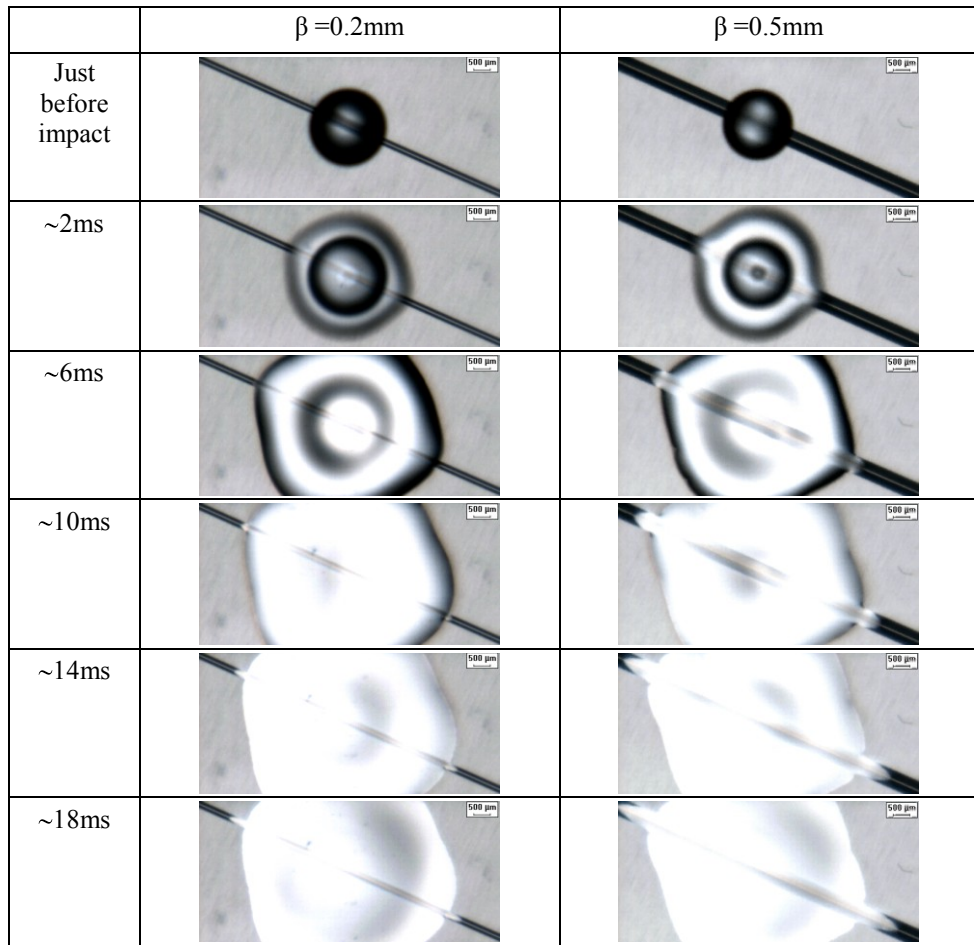
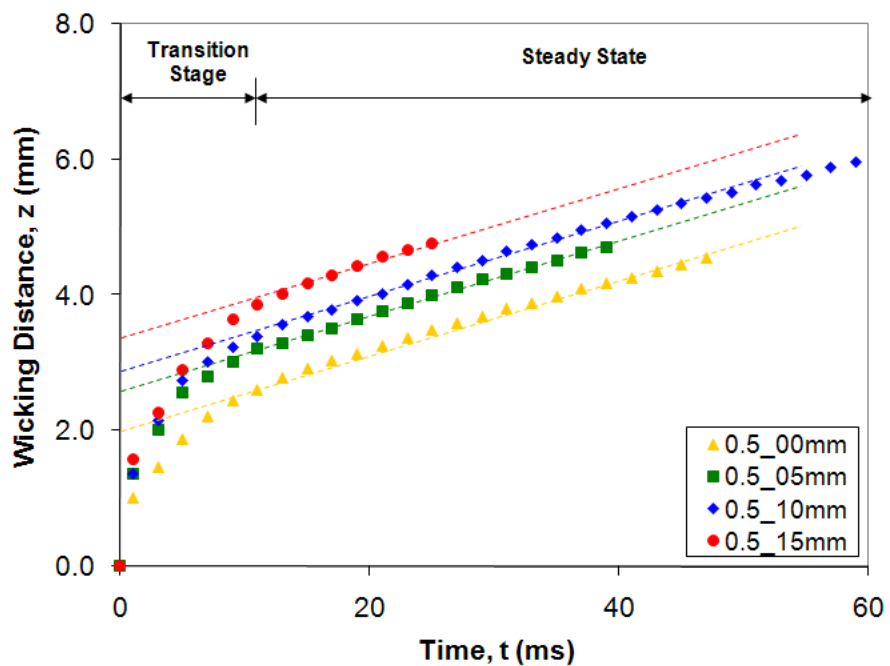
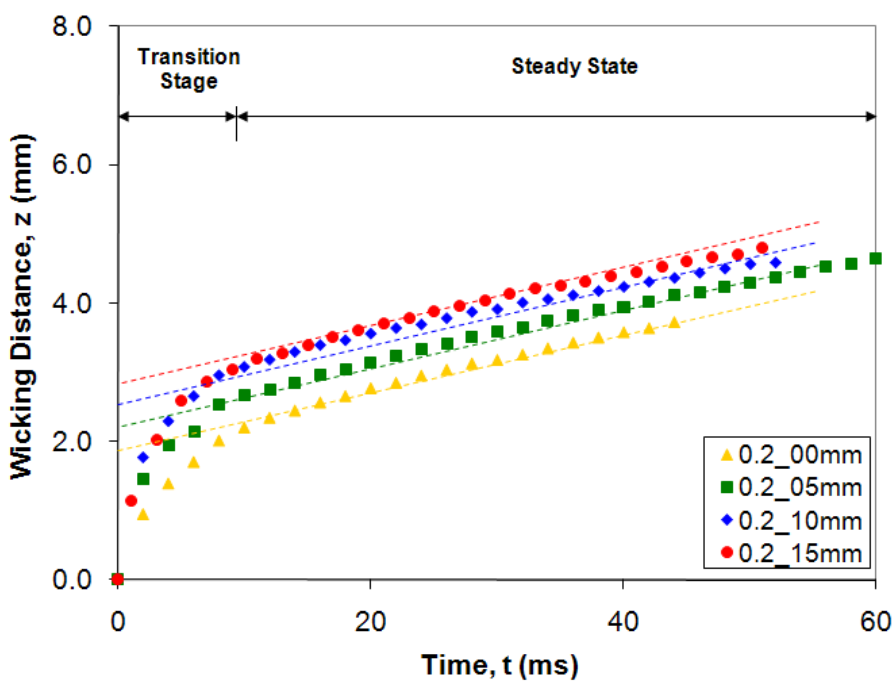


**Figure 6** Dynamics of a sessile water droplet impinging, with initial velocity 0.54 m/s, a V-groove ( $\beta = 120^\circ$ ,  $w_0 = 0.2, 0.5$  mm) on a quartz surface; images were taken at different magnifications.

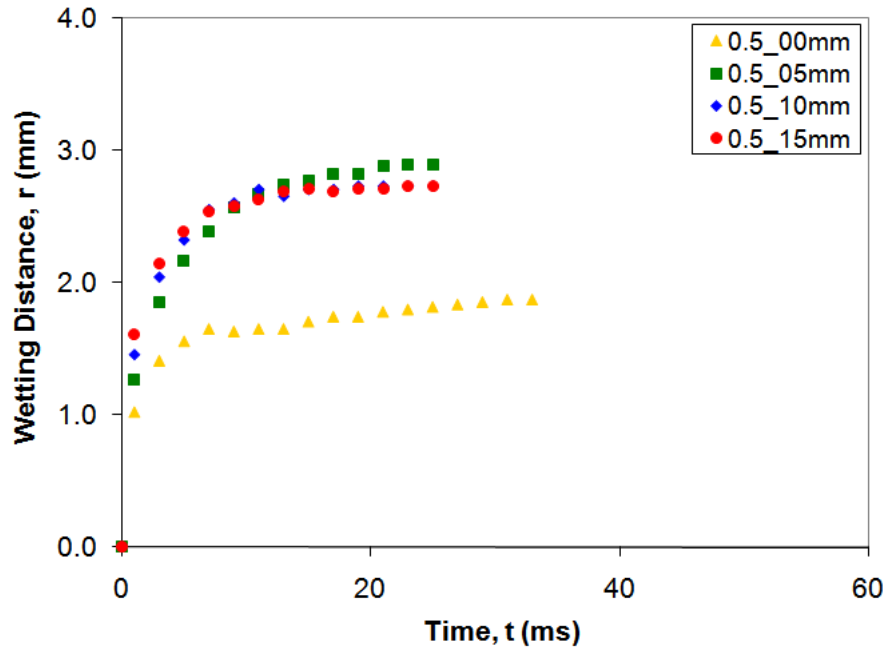


(a)

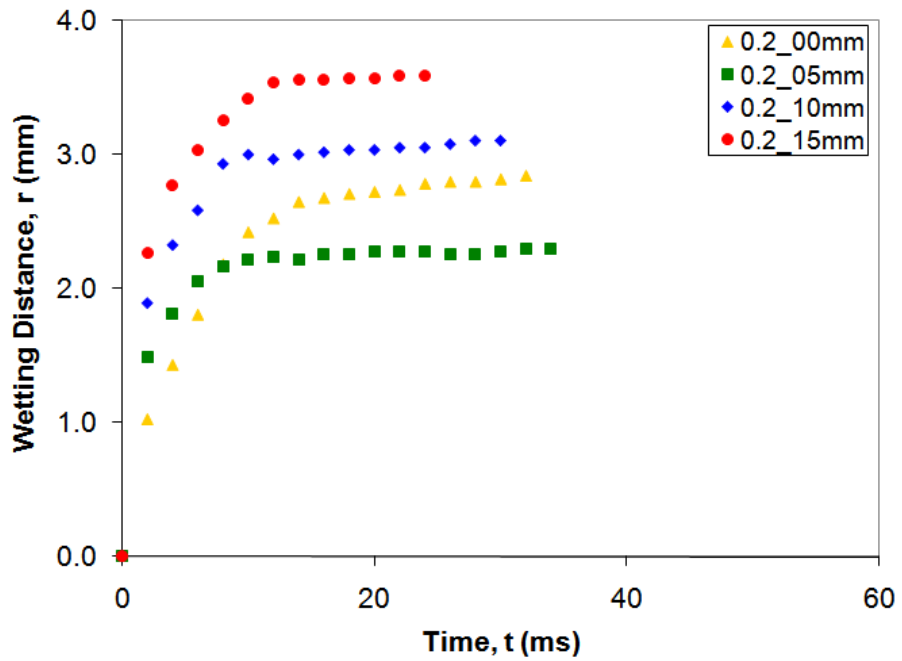


(b)

Figure 7 Effect of groove width and droplet inertia on the wicking dynamic. (a)  $\beta = 120^\circ$ ,  $w_0 = 0.5$  mm, (b)  $\beta = 120^\circ$ ,  $w_0 = 0.2$  mm.



(a)



(b)

**Figure 8** Effect of groove width and droplet inertia on the wetting dynamic. (a)  $\beta = 120^\circ$ ,  $w_0 = 0.5$  mm, (b)  $\beta = 120^\circ$ ,  $w_0 = 0.2$  mm.

## 5. DISCUSSION

The evolution of wicking and wetting of a droplet impinging a V-groove was measured in the first instances of contact. Shadows are observed over the droplets dispensed on the groove surface with inertia due to some energy dissipation. The shadows of the pictures (Figure 5) illustrate inflection in the curvature. This was previously observed in our lab for a time span of 5 to 10 ms [20].

The motion of the three phase line of sessile droplets was measured to identify possible interactions between groove wicking and surface wetting. Figure 9 represents the percentage of the droplet volume located into the groove as a function of time for the two grooves. For simplicity the volume was calculated as liquid wicking distance ( $z$ ) along V-groove times the groove cross-sectional area ( $A$ ). The volume of liquid droplets were about 4-5  $\mu\text{L}$ . Only a negligible fraction of the droplet (1%) is located into the narrow groove (0.2 mm), while up to 6% of the droplet is moving into the wider groove (0.5 mm). This suggests that for the short interval studied, the system is analogue to the bi-direction flow of an infinite reservoir droplet of different initial energy flowing into the groove. The phenomena can be represented by the forced wetting of a sessile droplet with some interaction on the 2 apexes of the droplet.

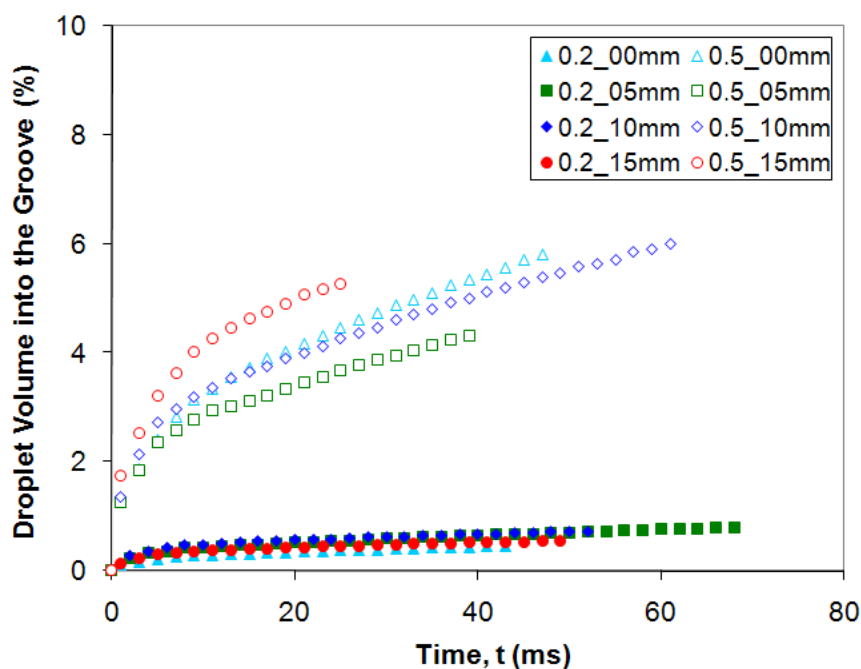


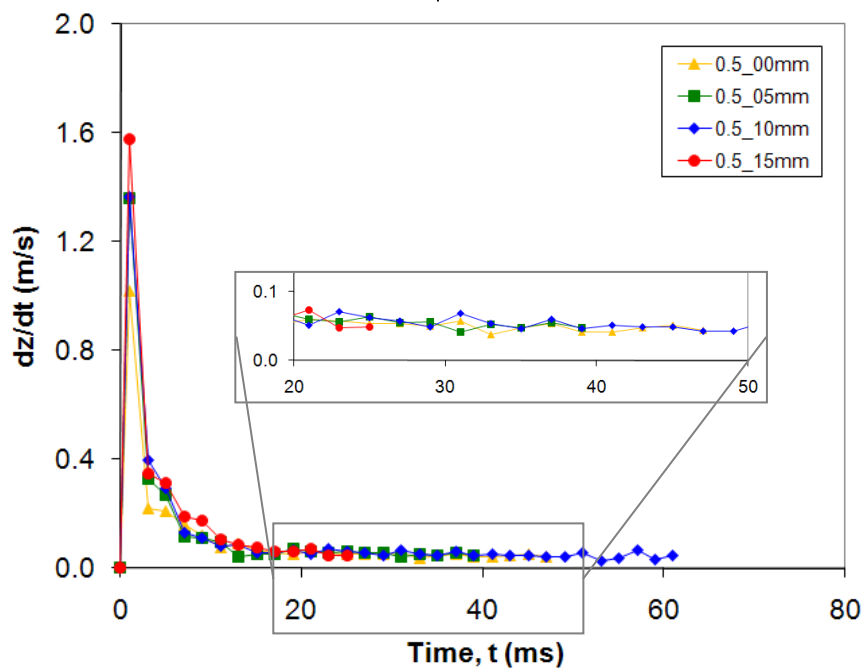
**Figure 9** Percentage of droplet volume into the V-groove.

The instantaneous groove wicking velocity ( $\Delta z/\Delta t = dz/dt$ ) of sessile droplet impinging onto groove surfaces with different inertia (impact velocity) was calculated for the wide and narrow grooves on Figure 10a and 10b respectively. The instantaneous wetting velocity ( $\Delta r/\Delta t = dr/dt$ ) for the same system is shown on Figure 11. As expected, the maximum wetting and wicking velocities occur immediately upon contact of the droplet with the surface. The droplet velocity profiles, for wetting and wicking, then exponentially decay with time due to viscous and friction dissipation. The maximum initial wicking and wetting velocities are increasing proportionally with the droplet impact velocity.

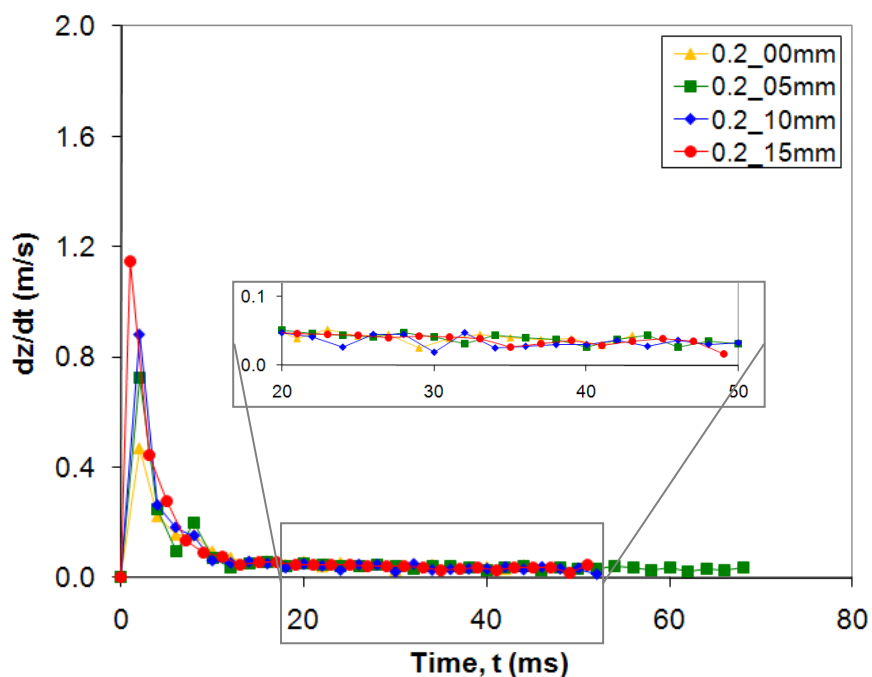
For the large groove (0.5 mm) the maximum wicking velocity ranges from 1.0 to 1.6 m/s for droplet having impact velocities of 0 and 0.54 m/s, respectively. Lower maximum wicking velocities ranging from 0.50 to 1.1 m/s were achieved in the narrow groove (0.2 mm) for initial droplet impact velocities of 0 and 0.50m/s, respectively. Similar results are observed for the maximum droplet wetting velocities (Figure 11). That is, the initial wetting velocity increases with the droplet impact velocity, and higher maximal droplet wetting velocities are reached for droplets impacting the wider groove. The later observation exhibits coupling between wetting and wicking.

It is of interest to consider the established droplet velocity for time ranging from 10 to 60 ms. This time frame is critical in industry as it also represents the period of droplet mobility, before significant absorption, evaporation or reaction proceeds. The established wicking velocity for the water droplet in the 120° quartz groove is constant at 0.05 m/s and is independent of the initial droplet impact velocity or groove width.

For wetting, the instantaneous wetting velocity exponentially decays to zero in about 20 ms. Groove width and initial droplet impact velocity play no significant role in the time required for wetting to stop. Wetting proceeds until the instantaneous contact angle reaches the resting contact angle, at which time any driving force vanishes and advance of the contact line stops.

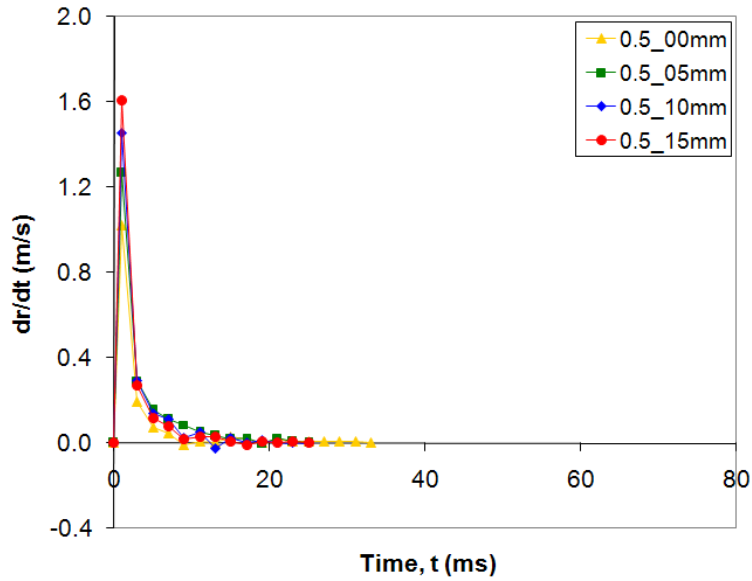


(a)

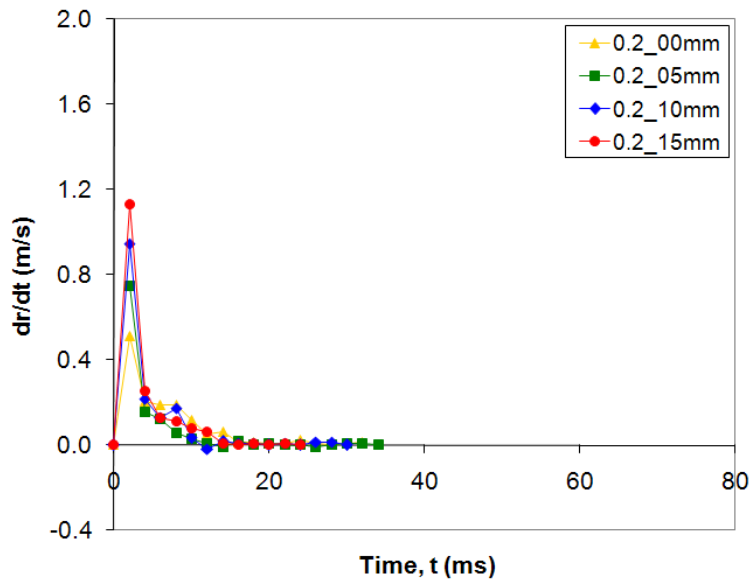


(b)

**Figure 10** Effect of groove width and droplet inertia on the instantaneous wicking velocity ( $dz/dt$ ). (a)  $\beta = 120^\circ$ ,  $w_0 = 0.5$  mm, (b)  $\beta = 120^\circ$ ,  $w_0 = 0.2$  mm.



(a)



(b)

**Figure 11** Effect of the groove width and droplet inertia on the instantaneous wetting velocity ( $dr/dt$ ). (a)  $\beta = 120^\circ$ ,  $w_0 = 0.5$  mm, (b)  $\beta = 120^\circ$ ,  $w_0 = 0.2$  mm.

The maximum droplet wicking and wetting velocities were found to be identical, irrelevant of the initial impact velocity or groove width (Figure 12). This might suggest that wetting triggers wicking in the initial instant. This is for  $120^\circ$  grooves; experimental evidences in our laboratory suggest that wicking is faster than wetting for narrower

grooves ( $60^\circ$  and  $90^\circ$ ) [20]. Higher maximum velocities (wicking and wetting) were also reached for droplet impinging the wider grooves.

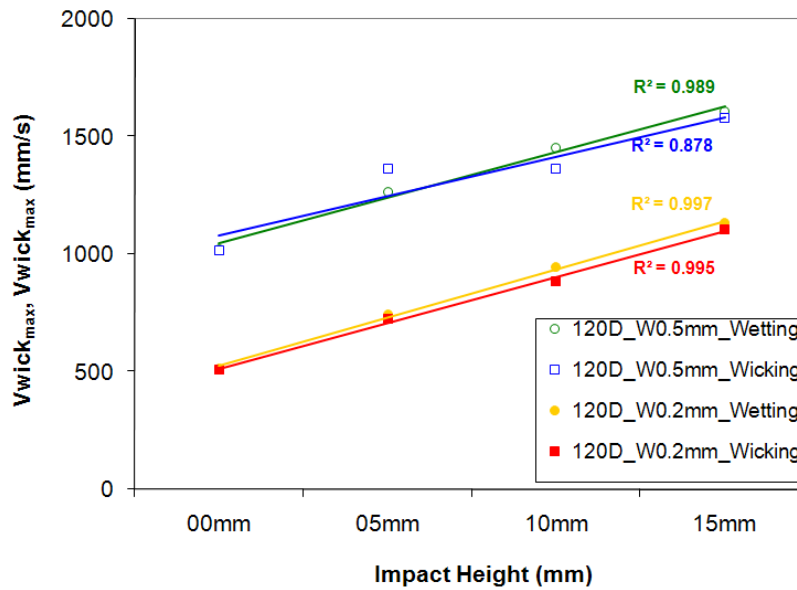
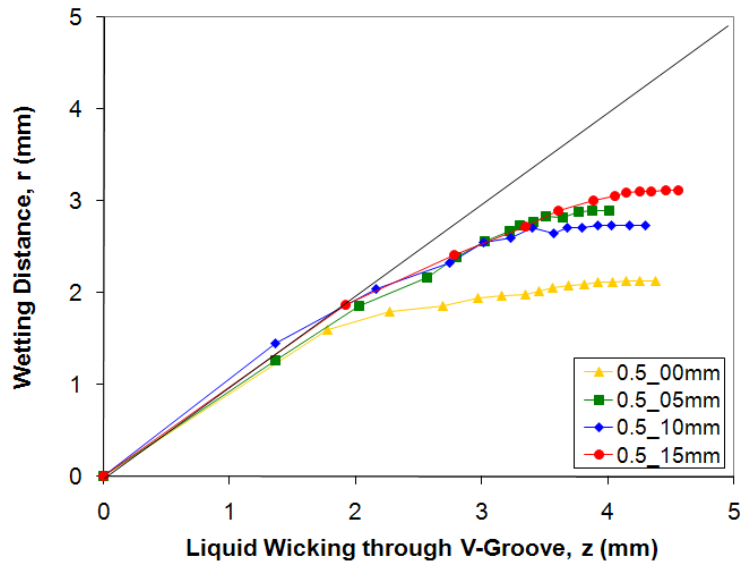
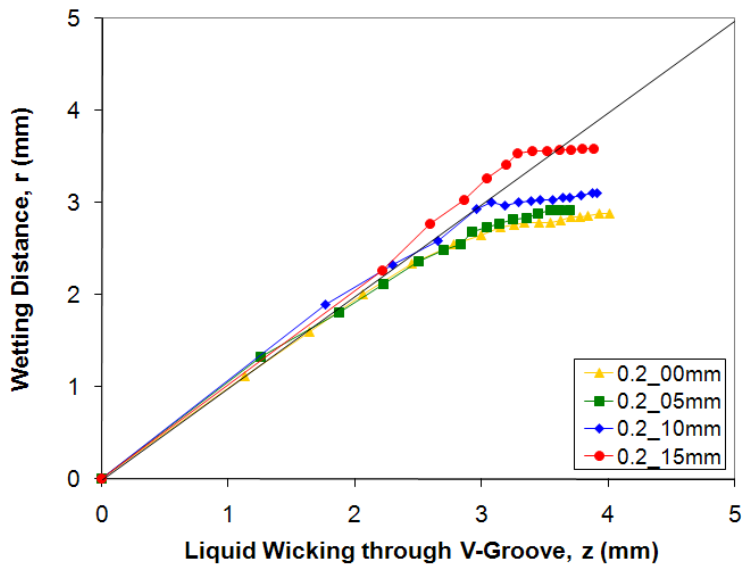


**Figure 12** Maximum Wicking ( $V_{wick_{max}}$ ) and Wetting ( $V_{wet_{max}}$ ) velocities for different droplet impact velocities.

For many industrial applications, such as printing and spraying, the path travelled by the liquid droplet is critical. Figure 13 compares the distance travelled by droplets by wicking and wetting. It highlights that the maximum wetting and wicking velocities are identical; wetting proceeds only for about 10 ms while groove wicking proceeds as long as the liquid reservoir is not depleted. No asymptotic maximum wicking or wetting velocity was recorded in our experiments.



(a)



(b)

**Figure 13** Comparison of average liquid wetting and wicking distance on V-groove geometry: (a)  $\beta = 120^\circ$ ,  $w_0 = 0.5$  mm, (b)  $\beta = 120^\circ$ ,  $w_0 = 0.2$  mm.

Figure 14 compares the predicted wicking kinetics using Eqn. (7) (for  $\alpha > \theta$ ) and Eqn.(8) ( $\alpha = \theta$ ) as a function of groove angle ( $\beta$ ) and width ( $w$ ) with our experimental results. At zero impact velocity, no groove wicking should occur for water in a  $120^\circ$  groove in a quartz surface, as  $\alpha = 90^\circ - \beta/2 = \theta = 90^\circ$  (Eqn. (7)). Our experimental results go against the theoretical prediction (Figure 7). A few explanations are possible: first, by continuity, wetting of the droplet on the surface causes wicking to proceed.

This wicking triggered is improbable as wicking stopped long after the wetting was terminated. A second explanation shows the shortcoming of the purely hydrodynamic model; surface interactions need to be considered. The third explanation can be the gravitational effect on wicking. Holdrich et al.[1] reported that both capillary and gravitational forces affect wicking of a liquid droplet in a surface groove. The dimensionless Bond number (Eqn. (9)) can be used to estimate the relative effect of gravity.

$$\text{Bond number, } Bo = \frac{\text{gravity force}}{\text{interfacial force}} = \frac{\rho g L^2}{\gamma} \quad (\text{Eqn. 9})$$

where,  $\rho$  is the liquid density,  $g$  is the gravity,  $\gamma$  is the liquid surface tension and  $L$  is the characteristic length, typically the droplet radius ( $R$ ). At 23°C, considering  $\rho = 997.5 \text{ kg/m}^3$ ,  $g = 9.81 \text{ m/s}^2$ ,  $\gamma = 7.2 \times 10^{-2} \text{ N/m}$  and  $L = R = 2 \times 10^{-3} \text{ m}$ , we calculate  $Bo = 0.54$ . While interfacial forces are twice stronger than gravity force, the effect of the later cannot be neglected.

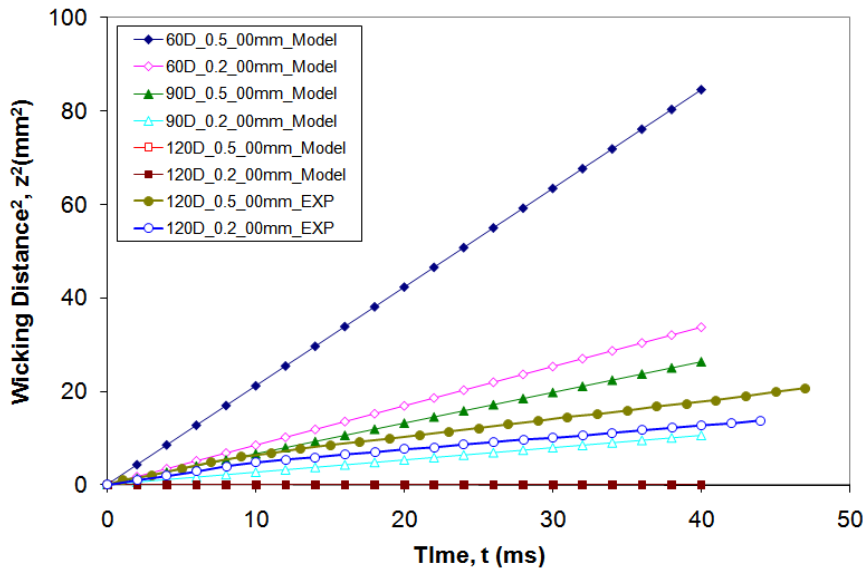


Figure 14 Theoretical prediction of wicking dynamics on V-groove surfaces compared with experimental results; Washburn model:  $z^2 \propto ct$ , for  $\alpha > \theta$  and  $\alpha = \theta$ .

## **6. CONCLUSION**

The dynamics of wetting and wicking of sessile liquid droplets impinging, with different impact velocities, a groove surface was investigated experimentally. The specific case of a 120° V-groove for water on quartz surface was studied. The classical models predict no groove wicking because of the equilibrium contact angle of water is smaller than  $90^\circ - (\text{groove angle})/2$ . This predicted behaviour was contradicted by our experimental results.

The maximum wetting and wicking velocities were measured to be equal. Wetting and wicking kinetics both increase with the initial droplet impact velocity. Wicking velocity decreases at a much slower rate than wetting and proceeds as long as there is a liquid reservoir. As a result, the trajectory and area covered by a droplet in a V-groove surface capillary are higher than those covered by classical wicking models. This explains the effect of surface grooves on inkjet printing resolution causing feathering defect. It also highlights the interaction of physical and chemical heterogeneity on the wetting and wicking kinetics and the need to further understand the dynamics of liquids on non-ideal surfaces.

## **ACKNOWLEDGMENT**

M.S.K. and D.K. would like to gratefully acknowledge Monash University, Departments of Chemical Engineering and CRC SmartPrint for funding this work.

## REFERENCES

- [1] Holdich, R.; Starov, V. M.; Prokopovich, P.; Njobuenwu, D. O.; Rubio, R. G.; Zhdanov, S.; Velarde, M. G., Spreading of Liquid Drops from a Liquid Source. *Colloids and Surfaces A: Physicochemical and Engineering Aspects*. 282-83 (2006) 247-255.
- [2] De Gennes, P. G., Wetting: Statics and Dynamics. *Reviews of Modern Physics*. 57 (1985) 827-863.
- [3] De Gennes, P. G., Dynamics of Wetting. In *Liquids at Interfaces*, Charvolin, J.; Joanny, J. F.; Zinn-Justin, Eds. North-Holland: Amsterdam, 1990; pp 273-291.
- [4] Garnier, G.; Wright, J.; Godbout, L.; Yu, L., Wetting Mechanism of Alkyl Ketene Dimers on Cellulose Films. *Colloids and Surfaces A: Physicochem. Eng. Aspects*. 145 (1998) 153-165.
- [5] Garnier, G.; Bertin, M.; Smrkova, M., Wetting Dynamics of Alkyl Ketene Dimer on Cellulosic Model Surfaces. *Langmuir*. 15 (1999) 7863-7869.
- [6] Gentner, F.; Ogonowski, G.; Coninck, J. D., Forced Wetting Dynamics: A Molecular Dynamics Study. *Langmuir*. 19 (2003) 3996-4003.
- [7] Hayes, R. A.; Ralston, J., The Dynamics of Wetting Processes. *Colloids and Surfaces A: Physicochemical and Engineering Aspects*. 93 (1994) 15-23.
- [8] Urban, D.; Topolski, K.; Coninck, J. D., Wall Tension and Heterogeneous Substrate. *Physical Review Letters*. 76 (1996) 4388-4391.
- [9] Feng, L.; Zhang, Y.; Xi, J.; Zhu, Y.; Wang, N.; Wang, F.; Xia, F.; Jiang, L., petal effect: A Superhydrophobic State with High Adhesive Force. *Langmuir*. 24 (2008) 4114-4119.
- [10] Yu, Y.; Zhao, Z.-H.; Z, Q.-S., Mechanical and Superhydrophobic Stabilities of Two-Scale Surface Structure of Lotus Leaves. *Langmuir*. 23 (2007) 8212-8216.
- [11] Campo, A. n. d.; Greiner, C.; Arzt, E., Contact Shape Controls Adhesion of Bioinspired Fibrillar Surfaces. *Langmuir*. 23 (2007) 10235-10243.
- [12] Mann, J. A.; Romero, L. A.; Rye, R. R.; Yost, F. G., Flow of Simple Liquids Down Narrow V Grooves. *Physical Review E*. 52 (1995) 3967-3972.
- [13] Romero, L. A.; Yost, F. G., Flow in an Open Channel Capillary. *Journal of Fluid Mechanics*. 322 (1996) 109-129.
- [14] Rye, R. R.; Mann, J. A.; Yost, F. G., The flow of liquids in surface grooves. *Langmuir*. 12 (1996) 555-565.
- [15] Rye, R. R.; Yost, F. G.; Mann, J. J. A., Wetting Kinetics in Surface Capillary Grooves. *Langmuir*. 12 (1996) 4625-4627.
- [16] Yost, F. G.; Rye, R. R.; Mann, J. A., Solder Wetting Kinetics in Narrow V-Grooves. *Acta Materialia*. 45 (1997) 5337-5345.
- [17] Abe, K.; Suzuki, K.; Citterio, D., Inkjet-Printed Microfluidic Multianalyte Chemical Sensing Paper. *Analytical Chemistry*. 80 (2008) 6928-6934.
- [18] Barbulovic-Nad, I.; Lucente, M.; Sun, Y.; Zhang, M.; Wheeler, A. R.; Bussmann, M., Bio-Microarray Fabrication Techniques - A Review. *Critical Reviews in Biotechnology*. 26 (2006) 237-259.
- [19] Calvert, P., Inkjet Printing for Materials and Devices. *Chemistry of Materials*. 13 (2001) 3299-3305.
- [20] Kannangara, D. Phenomena of Liquid Drop Impact on Solid Surfaces in Very Early Stages. PhD Thesis. Monash University, Melbourne, 2007.

- [21] Butt, H.-J.; Graf, K.; Kappl, M., *Physics and Chemistry of Interface*. WILEY-VCH GmbH & Co. KGaA: 2003.
- [22] Kissa, E., *Wetting and Wicking*. *Textile Research Journal*. 66 (1996) 660-668.
- [23] Basu, S.; Nandakumar, K.; Masliyah, J. H., *A Study of Oil Displacement on Model Surfaces*. *Journal of Colloid and Interface Science*. 182 (1995) 82-94.
- [24] Seaver, A. E.; Berg, J., *Spreading of a Droplet on a Solid Surface*. *Journal of Applied Polymer Science*. 52 (1994) 431-435.
- [25] Washburn, E. W., *Dynamics of capillary flow*. *Phys. Rev.* 17 (1921) 374-5.
- [26] Fisher, L. R.; Lark, P. D., *Experimental-Study of the Washburn Equation for Liquid Flow in Very Fine Capillaries*. *Journal of Colloid and Interface Science*. 69 (1979) 486-492.
- [27] Kannangara, D.; Zhang, H.; Shen, W., *Liquid-paper interactions During Liquid Drop Impact and Recoil on Paper Surfaces*. *Colloids and Surfaces, A: Physicochemical and Engineering Aspects*. 280 (2006) 203-215.

This page is intentionally blank

---

# Chapter 10

---

Biosurface Engineering  
through Ink Jet Printing

---

This page is intentionally blank

## Monash University Declaration for Thesis Chapter 10

### Declaration by candidate

In the case of Chapter 10, the nature and extent of my contribution to the work was the following:

Nature of contribution	Extent of contribution (%)
Initiation, key ideas, experimental and analysis works, development and writing up of the paper	50

The following co-authors contributed to the work. Co-authors who are students at Monash University must also indicate the extent of their contribution in percentage terms:

Name	Nature of contribution	Extent of contribution (%) for student co-authors only
<b>Wei Shen</b>	Initiation, key ideas, reviewing and editing of the paper	Co-supervisor
<b>Gil Garnier</b>	Initiation, key ideas, reviewing and editing of the paper	Co-supervisor
<b>John Forsythe</b>	Initiation and key ideas	Co-supervisor
<b>Deniece Fon</b>	Initiation, key ideas, experimental and analysis works and writing up of the paper	25
<b>Xu Li</b>	Initiation and experimental Work	10
<b>Junfei Tian</b>	Initiation and experimental Work	10

Candidate's  
Signature

[Redacted Signature]

Date

16/12/09

### Declaration by co-authors

The undersigned hereby certify that:

- (1) the above declaration correctly reflects the nature and extent of the candidate's contribution to this work, and the nature of the contribution of each of the co-authors.
- (2) they meet the criteria for authorship in that they have participated in the conception, execution, or interpretation, of at least that part of the publication in their field of expertise;
- (3) they take public responsibility for their part of the publication, except for the responsible author who accepts overall responsibility for the publication;
- (4) there are no other authors of the publication according to these criteria;
- (5) potential conflicts of interest have been disclosed to (a) granting bodies, (b) the editor or publisher of journals or other publications, and (c) the head of the responsible academic unit; and
- (6) the original data are stored at the following location(s) and will be held for at least five years from the date indicated below:

Location(s)

Australian Pulp and Paper Institute (APPI), Department of Chemical Engineering, Monash University, Clayton, VIC 3800, Australia.

Signature 1

[Redacted Signature]

Date

17/12/09

Signature 2

[Redacted Signature]

Date

17/12/09

Signature 3

[Redacted Signature] (for John Forsythe)

Date

17/12/09

Signature 4

[Redacted Signature]

Date

17/12/2009

Signature 5

[Redacted Signature]

Date

16/12/2009

Signature 6

[Redacted Signature]

Date

18/12/2009

# Biosurface Engineering through Ink Jet Printing

Mohidus Samad Khan<sup>1</sup>, Deniece Fon<sup>2</sup>, Xu Li<sup>1</sup>, Junfei Tian<sup>1</sup>, John Forsythe<sup>2</sup>, Gil Garnier<sup>1\*</sup> and Wei Shen<sup>1\*</sup>

<sup>1</sup> Australian Pulp and Paper Institute,  
Department of Chemical Engineering,  
Monash University, Clayton, VIC 3800, Australia.

<sup>2</sup> Department of Materials Engineering,  
Monash University, Clayton, VIC 3800, Australia

\*Corresponding authors:

Wei.Shen@eng.monash.edu.au, Gil.Garnier@eng.monash.edu.au

Chapter 10	261
Biosurface Engineering through Ink Jet Printing	261
Abstract	264
1. Introduction	265
2. Experimentals	267
2.1. Materials	267
2.2. Methods	268
3. Results and Discussion	270
3.1. Control of Ink Supply and Colour Management	270
3.2. Bio-Inks	270
3.3. Printing Bio-Ink on Porous Substrate	272
3.4. Activity of Printed Biomolecules	274
3.5. Printing Concentration Gradients	276
3.6. Printing Micro-Fluidic Paper Diagnostics	278
4. Conclusion	280
Acknowledgment	281
References	282

## ABSTRACT

The feasibility of thermal ink jet printing as a robust process for biosurface engineering was demonstrated. The strategy investigated was to reconstruct a commercial printer and take advantage of its colour management interface. High printing resolution was achieved by formulating bio-inks of viscosity and surface tension similar to those of commercial inks. Protein and enzyme denaturation during thermal ink jet printing was shown to be insignificant.

Every great advance in science has issued from a new audacity of imagination.

– Jay Lene

This is because the time spent by the biomolecules in the heating zone of the printer is negligible; in addition, the air and substrate of high heat capacity absorb any residual heat from the droplet.

Gradients of trophic/tropic factors can serve as driving force for cell growth or migration for tissue regeneration. Concentration gradients of proteins were printed on scaffolds to show the capability of ink jet printing. The printed proteins did not desorb upon prolonged immersion in aqueous solutions, thus allowing printed scaffold to be used under in vitro and in-vivo conditions. Our group portrait was ink jet printed with a protein on paper, illustrating that complex biopatterns can be printed on large area. Finally, patterns of enzymes were ink jet printed within the detection and reaction zones of a paper diagnostic.

**Key Words:** Inkjet printing, microfluidic, manufacturing, bioassays, tissue scaffold, protein, enzyme.

## 1. INTRODUCTION

The ability to generate accurate patterns of biomolecules on surfaces and to maintain the functionality of the immobilized biomolecules are two critical requirements to engineer biosurfaces. Recent developments in bio-interface engineering have shown printing as a promising method to create biomolecular patterns onto surfaces [1-4]. Among the multitude of applications, two are of special interest. The first is in scaffolds for tissue engineering. Polymeric scaffolds can be functionalized with proteins for controlling cell growth such as directed neuron outgrowth for neural regeneration applications. The second main application is paper-based diagnostics. These two applications require biomolecules to be very precisely printed in fine patterns, concentration gradients or within fluidic channels. Digital ink jet printing is attractive as manufacturing process for the precision, speed and flexibility it offers. The suitability of ink jet printing to large scale of biosurface manufacturing and the effective engineering of bio inks are two critical issues to address.

Nerve regeneration is a complex biological process with many biochemical and biomechanical variables affecting the outgrowth of neuronal axons [3, 5, 6]. Advances in tissue engineering for nerve regeneration promises solutions to degenerative illnesses like Parkinson and Alzheimer diseases. The effective control of neuron outgrowth and direction

can potentially be achieved with signalling molecules, such as nerve growth factor (NGF) immobilized onto scaffolds to produce a local concentration gradient [7-9]. Bio-printing has the capability to become a rapid and accurate process of generating NGF concentration gradient patterns for controlling neuron growth. The challenge is to produce continuous concentration gradient patterns that are smooth enough to be prescribed as an effective guidance cue by growing axons. Ink jet printing can become invaluable in tissue engineering to create such controlled concentration gradients.

Recent work by Martinez et al. (2007; 2008) [10, 11] has highlighted paper as a low-cost substrate for microfluidic diagnostics. These devices have tremendous potential for telemedicine when used in conjunction with communication hardware such as camera phones and internet. These devices also show potential in general health and environmental monitoring applications [10-12]. The major challenges are to ensure precision and integrity of biomolecular patterns within the device and to preserve the activity of the immobilized biomolecules.

Among the many printing processes, digital ink jet printing is becoming a technique of choice for biosurface functionalization thanks to its non-contact operation and reduced cross contamination between samples [13-18]. This technique has been used to print arrays or patterns of proteins and nucleic acids [1, 17, 19-23]. The current drop-on-demand (DOD) ink jet printing technology is capable of delivering ink droplets of a few picolitres [24, 25], therefore, satisfying many requirements for biosurface modification. The two main types of ink jet printers used in biomolecular printing are thermal and piezoelectric [26]. In piezoelectric ink jet printing, a voltage signal is applied to a piezoelectric element fixed to the printing head; the deformation of the piezoelectric element caused by the voltage signal pressurizes the ink in the nozzle and ejects ink droplets from the nozzle [25]. In the thermal ink jet printing, an electric current pulse heats a micro resistor, causing rapid formation of ink vapour bubbles, which creates a pressure pulse ejecting an ink droplet from a nozzle. The electric current pulse lasts microseconds ( $\sim 10\mu\text{s}^{-1}$ ) and it was estimated that the resistor surface temperature can increase to 200-300°C [1, 22]. It is not certain if biomolecules can sustain such high temperatures [27].

The availability of robust and affordable bio-ink jet printer is currently restricting the development of biosurface engineering. An alternative and cost effective strategy is to reconstruct commercial ink jet printers; a further advantage is to benefit

from the built-in highly developed ink management systems and computer-based user interfaces currently available. Compared to piezoelectric printers, thermal ink jet printers offer a simpler printer head design, more robust and easier to reconstruct for bio-printing applications. Several research groups have pursued this approach [16, 19, 22, 28]. Xu et al. (2005) and Prado et al. (2003) redesigned their bio-ink compatible printers using HP printers [21, 23]. Allain et al. (2001) reported a partial modification of a HP printer to print very small quantities of inks (60 $\mu$ L) for each refilling [19]. However, frequent refilling of bio-inks increases the probability of contamination of the ink supply system, thus compromising the bio-fabrication quality. Another critical issue for printing biomolecules using thermal ink jet printing is to understand the effect of the printing action on the activity of biomolecules. Allain et al. (2001) reported that DNA can be spotted with thermal ink jet printers and remained intact. However, proteins are more fragile molecules, the activity of printed protein patterns by a thermal printer needs to be assessed [19].

This study investigates the flexibility of modifying a standard commercial thermal ink jet printer to engineer biosurfaces. The strategy investigated is to ensure good printability by identifying the critical parameters of commercial inks and to formulate bio-inks of similar properties. Two critical requirements must be satisfied. First, the printing resolution with bio-inks must be good and preferably similar to that achieved with regular inks. Second, the printed molecules must be able to sustain the heat and shear generated by ink jet printing. The versatility of thermal ink jet printing for biosurface engineering is analyzed.

## **2. EXPERIMENTALS**

### **2.1. Materials**

Fluorescein isothiocyanate-conjugated bovine albumin (albumin-FITC) and horseradish peroxidase (HRP) (Sigma Aldrich) solutions were used to formulate bio-inks. The tagged fluorescent dye (FITC) allows the protein (albumin) to be tracked by UV-light or by confocal microscope. Albumin-FITC solutions of a wide range of concentrations (0.2mg/mL to 1.0mg/mL) were prepared; a protein buffer, 10mM Tris(hydroxymethyl) amiomethane (Aldrich), was used to maintain the pH of the albumin solution at  $\geq 7.0$ . HRP was dissolved in 100mM sodium-phosphate buffer

solution to maintain the pH at 6.0 to a concentration of 1.0mg/mL. A liquid substrate system, 3,3'-Diaminobenzidine (DAB) (Aldrich), was used to identify the enzymatic activity of the printed HRP. Water (Millipore, 18M $\Omega$ ) was used for making all solutions in the study. The bio-inks were stored at a temperature below 4°C. Polymer solutions for electrospinning were prepared from poly( $\epsilon$ -caprolactone) (PCL) (Lactel Absorbable Polymers), which was dissolved in a solvent mixture consisting of chloroform and methanol (Merck Chemicals Ltd.), and a cationic surfactant, dodecyltrimethylammonium bromide (DTAB) (Sigma Aldrich). Whatman filter paper #4 was selected as the paper base for sensor fabrication.

## 2.2. Methods

### 2.2.1. Characterization of Ink Properties

To assist the formulation of bio-inks, ink jet inks of three major brands were surveyed. First two inks were thermal ink jet ink and the third one was piezo ink jet ink. Density ( $\rho$ ), surface tension ( $\gamma$ ) and viscosity ( $\mu$ ) of the commercial inks were measured (section 3.2). Surface tensions of commercial ink jet inks were measured with a Wilhelmy balance (Cahn Instrument, DCA 322); shear viscosities of the inks were measured using a Rheometrics Fluids Spectrometer (RFSII, USA). Surface tensions of the bio-ink solutions were measured using OCAH-230 (Contact Angle Measuring Device; Dataphysics, Germany) with the pendant drop method. The densities of the inks were measured with a Mettler Toledo Densito 30Px (Switzerland). All the physico-chemical properties of bio-ink were measured at 23°C. Glass capillary viscometer (BS/U Tube; Standard: ASTM D 445, D446/ISO3104) was used to measure the kinematic viscosity of bio-ink solutions.

### 2.2.2. Printing Bio-ink on Porous Substrate

A Canon ink jet printer (Pixma ip4500) and ink cartridges (CLI, Y-M-C-BK, PGBK model) were reconstructed for bio-printing. The sponges inside the ink cartridges were removed and cleaned. The ink tanks were cleaned and the sponges were restored. This printer is of the bubble jet design which offers a resolution of 9600 $\times$ 2400 dot per inches (dpi). The printer was controlled by a personal computer which supplies page-data to the printer using MS Office 2003 and IrfanView v4.24 software. Filter paper was

the printing substrate. A paper-based microfluidic pattern was created using the method described elsewhere [29]. HRP was printed inside the fluidic channels of the pattern. Albumin-FITC was also ink jet printed onto porous biodegradable electrospun PCL scaffold. The scaffold was electrospun from a solution consisting of 12% (w/v) PCL dissolved in a 3:1 chloroform:methanol with 1mM DTAB. Electrospun PCL scaffolds were sputter coated with gold (25 mA for 90s; Balzers SCD005 Sputter coater), and analyzed via scanning electron microscopy (acceleration voltage = 15 kV; Hitachi S570 SEM). Electrospun PCL had average fibre diameter of  $240 \pm 60$  nm (Figure 1).

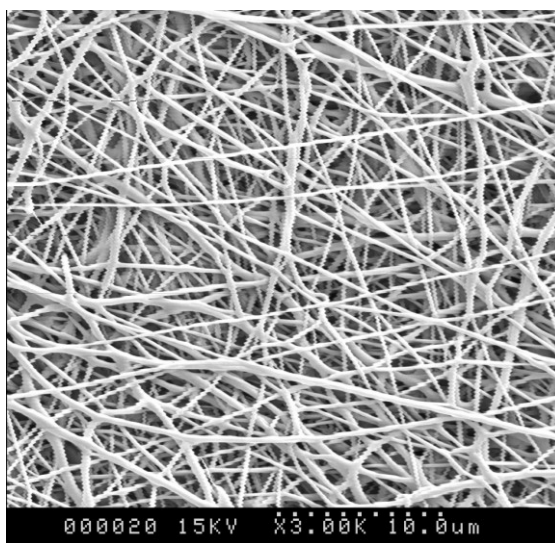


**Figure 1:** Scanning electron microscopic (SEM) image of the electrospun PCL nanofibres scaffold.

### 2.2.3. Printing Analysis

The albumin-FITC printed images were analyzed by laser-scanning krypton confocal microscope and UV-light (Spectroline, ENF-240C/F). The biochemical reaction of HRP and DAB substrate generates the characteristic brown colour on paper [30]. A digital SLR camera (SONY-DSLR-A100) with additional close-up lenses was used to capture images of printed and reacted patterns.

### 3. RESULTS AND DISCUSSION

#### 3.1. Control of Ink Supply and Colour Management

The reconstruction of the Canon ink jet printer was detailed elsewhere [31, 32]. Controlling the colour management of the printer and the Windows software interface is necessary to prevent cross-contamination of the printed bio-inks. The colour management system of a desk top ink jet printer reproduces a colour defined using a combination of different proportions of primary CMYK standards: cyan (C), magenta (M), yellow (Y) and black (K). To reproduce a colour from the computer screen onto a substrate using the control software, the printer may need to dispense two or more inks from different ink cartridges to print a colour on the substrate that matches that on the screen. Such colour management system is not ideal for bio-printing, as it prevents the printer from dispensing a single protein from a single cartridge. However, simple modifications of the colour settings of MS Office 2003 can prevent the printing of the second bio-ink when unwanted [31, 32].

#### 3.2. Bio-Inks

Surface tension and viscosity are the two critical parameters of inks, which affect the ink droplet formation in ink jet printing [24]. In the first step, the surface tension, density and viscosity of a series of commercial ink jet were measured. In a second step, bio-inks having characteristics ( $\gamma, \rho, \mu$ ) similar to that of these commercial inks were formulated. Finally, bio-inks were thermal ink jet printed and the pattern resolution was compared to that achieved with the commercial inks.

Table I shows the viscosity, surface tension and density of commercial inks of different colours (C,M,Y,K) and three different manufacturers (1,2,3). The properties of two bio-inks, albumin-FITC and HRP, are also shown.

**Table I: Physical Properties of Commercial Ink Jet Inks and Bio-Inks at 23°C**

Description		SurfaceTension (mN/m)	Viscosity (cP)	Density (Kg/m <sup>3</sup> )
Commercial Inkjet ink-1 (Canon)	C	28.5	2-5	1007-1089
	M	29.1		
	Y	30.5		
	K	28.6		
Commercial Inkjet Ink-2 (HP)	C	30.3	2-9	
	M	29.7		
	Y	31.2		
	K	46.2		
Commercial Inkjet Ink-3 (Epson)	C	30.7	2-3	
	M	30.5		
	Y	32		
	K	38.8		
Bio-ink-1 (albumin-FITC)		54.4-56.4	0.935-0.97	996-999
Bio-ink-2 (HRP)		49.1	0.935 <sup>a</sup>	997-1000

<sup>a</sup> Assumed to be the same as for water

The surface tension of C, M, Y inks were found to be consistently in the range of 28.5 – 32.0 mN/m, whereas the range of black inks (K) is much wider: 28.6-46.2mN/m. The densities of inks were similar to that of water (Table I). The range of viscosity of the inks was found to be 2-9 cP.

The average surface tension of albumin-FITC and HRP were of 56.6 mN/m and 49.1 mN/m respectively. The densities of the bio-inks were similar to that of water: 997-1000kg/m<sup>3</sup>. The viscosity of the bio-inks was also adjusted to that of water. The dynamic viscosity of water at 23°C is 0.935 cP [33] and the dynamic viscosity of the bio-inks varies from 0.935-0.970cP, which was similar to the lower limit of the commercial ink viscosity.

To evaluate the effects of the physical properties of inks on their printing performance, commercial inks and the bio ink (albumin-FITC) were printed using the

same printer onto a polymer scaffolds and the definition of printed ink dots was analyzed by optical and confocal microscopy.

The diameter  $d$  (in  $\mu\text{m}$ ) of a dispensed droplet through inkjet nozzle can be expressed as:

$$d = \sqrt{\left(\frac{6}{\pi} V\right)} = 2.4V^{1/3} \quad (1)$$

where,  $V$  is the volume (in pL) of the dispensed droplet. According to the manufacturer, the bubble jet printer used in our study generates droplet of 1 pL. The minimum dispensed droplet diameter is then 12.4  $\mu\text{m}$  (Eq.1). Asai et al. (1993) reported that the diameter of impacted (but non-splashing) droplet delivered by ink jet printing on paper is 1.42 times larger than that of the dispensed droplet [34]. Therefore, the corresponding impacted droplet diameter is 17.6  $\mu\text{m}$ . This calculated value is in good agreement with our experimental results: the impacted droplet diameter corresponding to the smallest single droplet dispensed by our printer nozzle was  $18.3 \pm 1.4 \mu\text{m}$  ( $n=8$ ) for commercial ink jet ink (Canon, Cyan ink) and  $18.8 \pm 1.8 \mu\text{m}$  ( $n=8$ ) for bio-ink, albumin-FITC. These measured data corresponds to a 1% increase in the dispensed ink drop diameter of the bio-ink compared with the commercial ink, and a 3% increase in the ink spot diameter on the substrate. This shows that the changes in ink physical properties within the ranges specified in our study have no impact on the ink droplet size dispensed.

### 3.3. Printing Bio-Ink on Porous Substrate

Figure 2a is the photograph of text printed with albumin-FITC using two different cartridges (black and magenta cartridges). The fluorescent protein was visible under UV light. The top two lines were printed using Times New Roman, Font 5pt and the bottom two lines were in Font 10pt. The left hand-side text was printed using the black ink cartridge and the right hand-side with the magenta cartridge. The bottom of the photo is blurred because the photo was taken at an angle to accommodate the UV lamp. As a result, the bottom of the image was slightly out of focus. The printing resolution is shown by the confocal image of the Font 5pt text on Figure 2b.

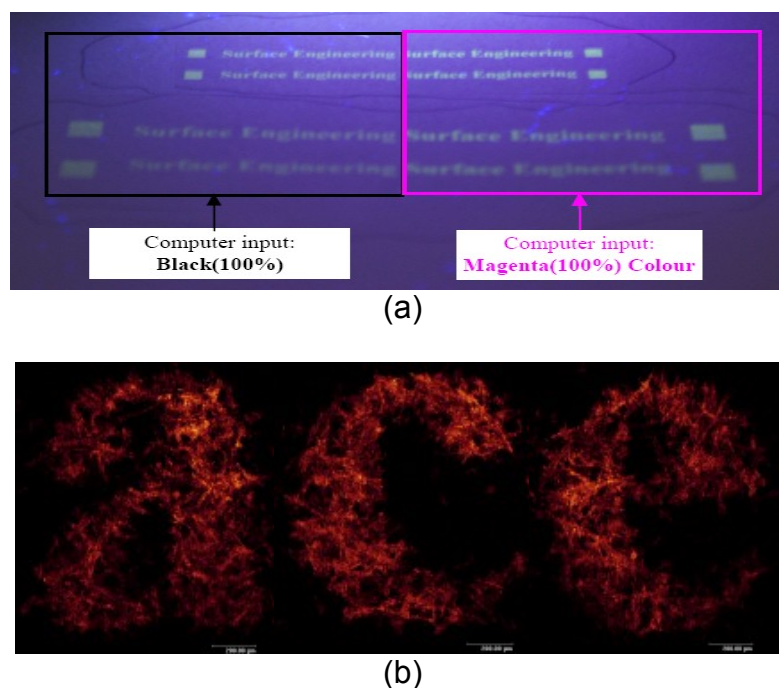


**Figure 2** Text printed using albumin-FITC on paper (Times New Roman, 5pt and 10pt); (a) printing from two different cartridges (UV-light), (b) a confocal microscopy (Krypton, 5x)

Good printing resolution was achieved with different proteins using either one or more ink cartridges. Reconstructed ink jet printer can print very sophisticated patterns involving many bio-inks.

The digital picture of our research group was printed on paper (modified size) with albumin-FITC as bio-ink (Figure 3). Since only albumin-FITC was used, the monochromatic printing mode was selected. The original photo was first converted into grey-scale; albumin-FITC was printed from the black ink cartridge. Since albumin-FITC fluoresces under UV light, the printed image (Figure 3a) was actually the negative image of the original photo when viewed under UV light. To visually appreciate the printing result, a positive image is required. Figure 3a was converted into its negative using a graphics software (IrfanView); this operation brought the printed negative (Figure 3a) into a positive form (Figure 3b). Good tone variation was reproduced.



(a)



(b)

**Figure 3 (a) Printed digital photo using albumin-FITC on paper surface. (b) Negative image of the photo.**

### 3.4. Activity of Printed Biomolecules

To test the activity of the printed biomolecules, a text pattern was printed on paper using the bio-ink formulated with an enzyme, horseradish peroxidase (HRP). The enzymatic activity of the peroxidase was determined by spraying the DAB liquid substrate onto the printed patterns. The oxidation of 3,3'-Diaminobenzidine by  $H_2O_2$  in the liquid substrate catalyzed by the printed horseradish peroxidase produces the characteristic brown colour observed in Figure 4. This indicates that the enzyme was active after being printed.



**Figure 4:** Text printed with of HRP enzyme on paper (Times New Roman, 14Bpt). The application of DAB liquid substrate reveals the characteristic brown-coloured precipitates of the oxidized DAB, indicating HRP enzyme activity.

Risio and Yan (2007) have shown that horseradish peroxidase printed using a piezoelectric ink jet printer retained its enzymatic activity [17]. Piezoelectric printer ejects ink droplets by pulses generated by deformation of the crystal from the piezoelectric element. This printing action does not increase temperature. Therefore, piezoelectric printer has had a perceived advantage for bio-printing.

Figure 4 clearly shows that thermal ink jet printer can also retain the activity of the printed protein molecules. Although it was estimated that the electric pulses could increase the surface temperature of the micro resistor to 200 – 300°C [1, 26], the duration of the pulse is less than 10  $\mu$ s. As soon as the ink droplet is ejected from the nozzle, it is again exposed to room temperature. Since the usual distance between the printer head and the substrate surface is 2 mm, the ink droplet reaches the surface of the substrate in 200  $\mu$ s, assuming of flight speed of ink droplet of 10 m/s [25]. Due to inertia, the ink droplet rapidly forms a thin circular pancake upon impacting on the substrate [34, 35], which resides at ambient temperature. The printed ink droplet rapidly equilibrates its temperature with the substrate having high heat capacity, in an exaggerated estimation, the ink droplet experiences the boiling temperature for a maximum 250  $\mu$ s.

Chang et al. (1988) studied the thermal stability of HRP heated in aqueous solutions and found that the enzymatic activity of HRP decreased by 50% in 20 seconds under near-boiling condition (93°C) [36]. Assuming similar trend, the expected loss of activity for the HRP enzyme induced by printing is of 0.001%. This estimation shows that thermal deactivation of HRP during thermal ink jet printing is negligible. This confirms thermal ink jet printer for biomolecular printing application as protein

denaturing by thermal printing is insignificant. The quantification of the thermal stability of enzyme printed patterns on paper can be found elsewhere [37].

### 3.5. Printing Concentration Gradients

Confocal microscopy was used to characterize the resolution of protein patterns printed on scaffolds. The first question to answer is whether printed protein pattern can be fixed on the scaffold surface simply by physisorption of the proteins. If physisorbed protein patterns are unstable and change with time when immersed in a liquid, a printed protein concentration gradient will gradually lose its ability to guide neurons. To address this issue albumin-FITC was printed on electrospun PCL scaffold; the printed pattern was immersed in an aqueous buffer solution for 2 days. The confocal images taken before and after this treatment are shown in Figures 5a and 5b, respectively. The adhesion of protein molecules to the substrate surface was sufficiently strong to maintain the printed protein pattern.

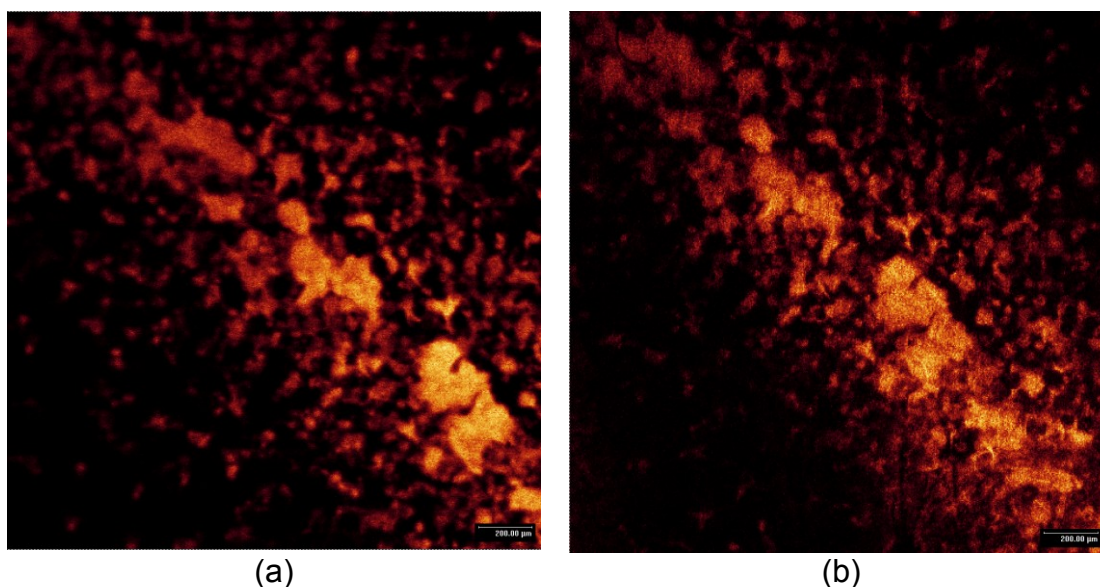


**Figure 5:** Confocal Images (Krypton, 5x) of inkjet printed patterns on electrospun PCL Scaffold using albumin-FITC; biomolecules physically adsorbed on the surface (a) before, (b) after immersing into aqueous buffer (2 days in Phosphate Buffer Solution, PBS); (bar length = 200  $\mu\text{m}$ ).

An albumin-FITC concentration gradient was also printed using a single ink cartridge; an electronically generated grey scale pattern was used as image file. Figure 6a shows the confocal microscopic image of the concentration gradient achieved (bar length = 200  $\mu\text{m}$ ). The grey scale is obtained with the printing algorithm by varying the surface density of the printed dots. Figure 6a illustrates that the printed protein dots form discrete islands of diameter smaller than 100  $\mu\text{m}$  in the low concentration end of the gradient.

In an attempt to improve the smoothness of the concentration gradient, a novel printing strategy was engineered. Two ink cartridges were used to print two bio-inks. An ascending grey-scale was printed from the albumin-FITC cartridge. Simultaneously, a descending grey-scale was printed from another nozzle using the blank tris buffer stored in a different cartridge. The overlapping of protein dots with the buffer solution dots provided beneficial mixing of the two bio-inks before drying and fixation on the surface. Printing the two combined and opposite grey-scales of the two bio-inks resulted in a more continuous concentration gradient of the protein (Figure 6b). Smoother concentration gradients can be generated with multiple cartridges and controlling the elution of inks prior to adsorption and drying onto the substrate.

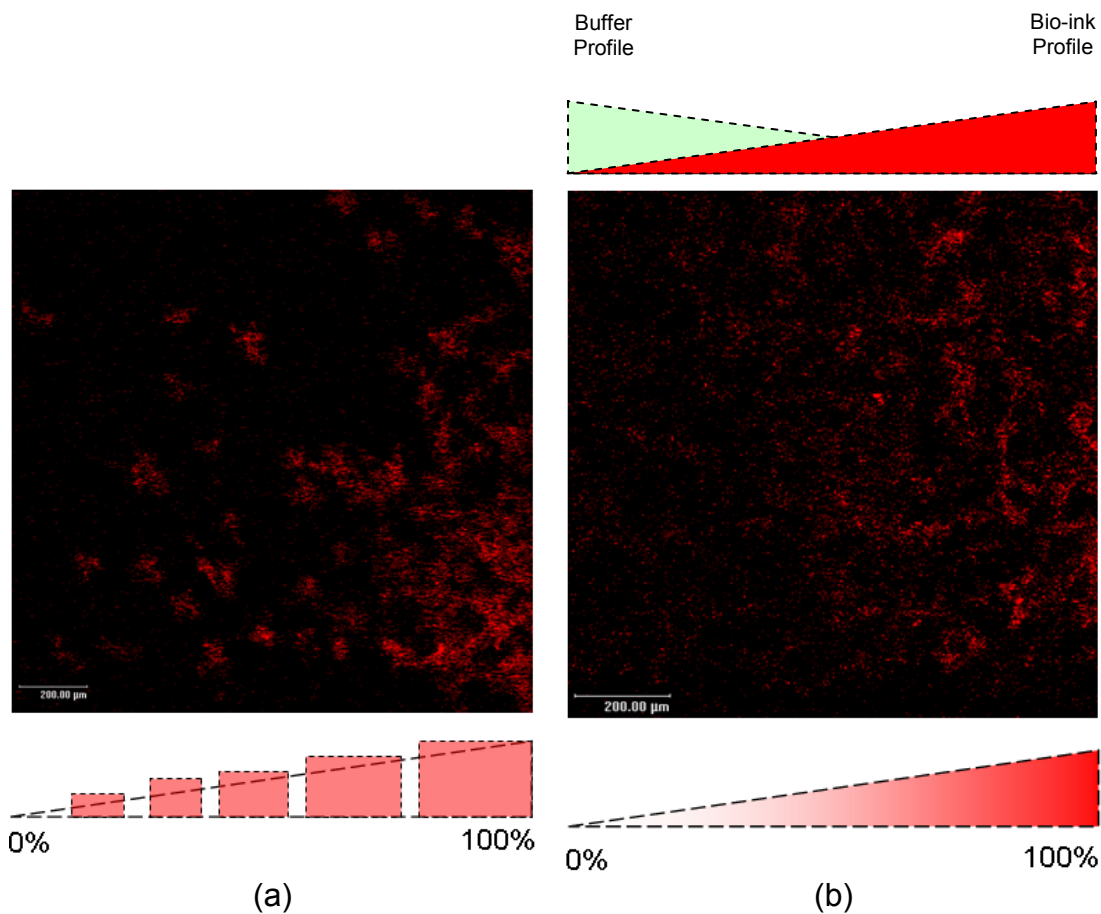


**Figure 6:** Confocal Images (Krypton, 5x) of albumin-FITC concentration gradient; (a) concentration gradient printed using mono-bio-ink (protein solution), (b) concentration gradient printed using two bio-inks printed from two cartridges (protein solution and buffer solution)

### 3.6. Printing Micro-Fluidic Paper Diagnostics

Ink jet printing was also used to fabricate a complete paper-based bioassays and diagnostic devices. Paper-based microfluidic patterns have been reported as the structure for making diagnostic devices for health care [10, 11]. Martinez et al. [10, 11] have fabricated paper-based microfluidic bioassays by photolithography. Li et al. [12] have recently reported different approach to fabricate paper-based microfluidic patterns by plasma treatment. Plasma treatment generates a hydrophilic pattern on hydrophobic paper, providing capillary penetration pathways for liquid samples. Shen et al. [29] and Li et al. [38] later showed that hydrophilic-hydrophobic contrast can be created by ink

jet printing. In the present study, we demonstrate that ink jet printing can deliver chemical and biochemical reagents inside channel patterns to form functional devices.

Ink jet printing was first used to print hydrophobic patterns on paper, forming a series of six-channel hydrophilic systems [38] (Figure 7). The three different digital patterns used for printing the biomolecules and the channels are represented in Figure 7a; colour represents the biomolecules. HRP enzyme was printed inside the hydrophilic channels (Figure 7). A few drops of DAB, the liquid enzyme substrate, were deposited in the collector at the centre of the hydrophilic pattern into the device using a micropipette. As the DAB solution penetrates along all channels, the brown colour was formed, revealing the exact position and the activity of the printed HRP. Figure 7b represents the photo of the bio-diagnostics achieved.

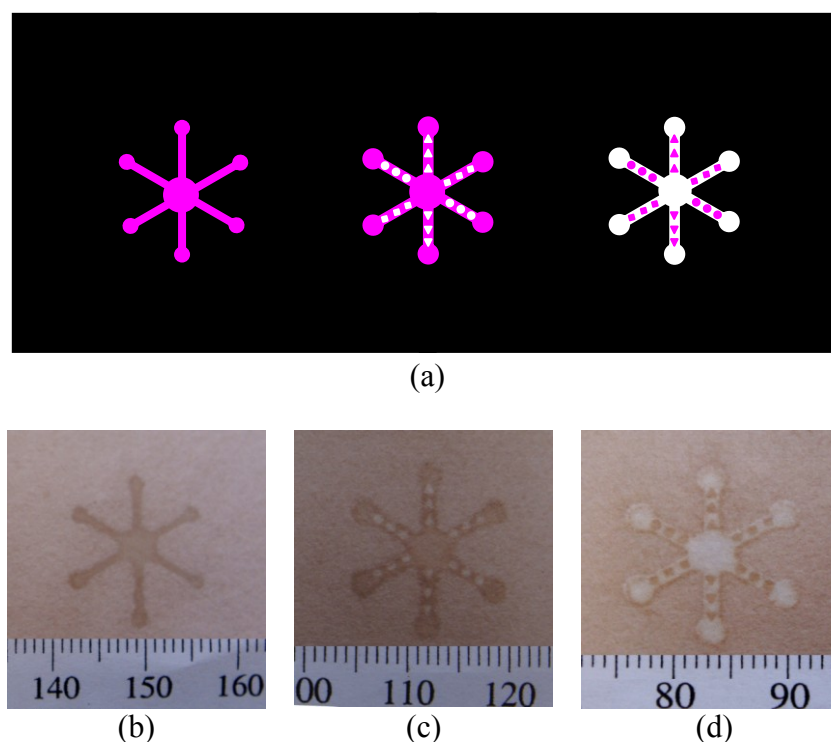


**Figure 7:** Paper-based microfluidic devices. (a) Microfluidic paper with three different designs of biomolecular patterns (magenta shades represent intended printing patterns); (b)-(d) the three different printed patterns. The scales are in mm.

Ink jet printing can be a competitive technique to fabricate paper-based microfluidic bioassays and diagnostic devices. The ability to simultaneously print multiple bio-inks enables the fabrication of more advanced paper-based bioassays and

diagnostic devices. Ink jet printing offers the resolution and the on-demand pattern variations required for micro-manufacturing. Moreover, the ability to simultaneously print multiple bio-inks opens the possibility to fabricate advanced paper-based bioassays and diagnostic devices using ink jet printing technique.

#### 4. CONCLUSION

The feasibility of thermal ink jet printing as a convenient and up scalable process for biosurface engineering was demonstrated. The strategy investigated was to reconstruct a commercial printer to take full advantage of the modern colour management interfaces already available; these printers are also low-cost. High printing resolution was achieved by formulating bio-inks. Protein and enzyme denaturation during thermal inkjet printing was experimentally and theoretically proven to be insignificant. The printed enzymes remained active. This is because the retention time spent by the biomolecules in the heating zone of the printer is very short (less than 250  $\mu$ s), and thanks to the important heat capacity of air and the printing substrate absorbing any potential residual heat from the bio-ink droplet .

Discreet and continuous concentration gradients of proteins on polymeric scaffolds were achieved by inkjet printing; these protein concentration gradients serve as potential guidance cues for cell growth generation for tissue engineering application. A novel strategy was developed to engineer very smooth, continuous concentration gradients of biomolecules by inkjet printing. It consists of simultaneously printing an increasing concentration gradient of the biomolecule on a porous surface combined with a decreasing concentration gradient of a buffer/eluent/solvent. Gradient uniformity is promoted by controlling the bio-ink dilution and elution with its solvent/buffer prior to absorption into the surface. The printed proteins thus retained by physisorption were shown not to desorb upon prolong immersion in aqueous solutions, allowing printed scaffold to be used for *in vitro* and *in vivo* conditions. Our group portrait was inkjet printed with a protein on paper, illustrating that complex biopatterns can be printed on large area. Finally, patterns of enzymes were specifically ink-jet printed within the detection and reaction zones integrated in the fluidic system of a paper diagnostic.

Inkjet printing offers precision and speed for the commercial production of sensors. Reconstructing a commercial ink-jet printer can be an economical option that

further benefits from highly developed control software which offer flexibility for biosurface engineering.

## **ACKNOWLEDGMENT**

Monash University is acknowledged for the postgraduate scholarships (MSK, DF, XL). Many thanks to Drs G. Thouas, N. Cowieson, D. Kannangara for discussion.

## REFERENCES

- [1] P. Calvert, Inkjet Printing for Materials and Devices, *Chemistry of Materials* 13 (2001) 3299-3305.
- [2] P. Molnar, M. Hirsch-Kuchma, J.W. Rumsey, K. Wilson, J.J. Hickman, Biosurface Engineering, in: J.G. Webster (Ed.), *Encyclopedia of Medical Devices and Instrumentation*, John Wiley & Sons, 2006.
- [3] D.R. Nisbet, S. Pattanawong, N.E. Ritchie, W. Shen, D.I. Finkelstein, M.K. Horne, J.S. Forsythe, Interaction of Embryonic Cortical Neurons on Nanofibrous Scaffolds for Neural Tissue Engineering, *Journal of Neural Engineering* 4 (2007) 35-41.
- [4] A. Offenhausser, S. Bocker-Meffert, T. Decker, R. Helpenstein, P. Gasteier, J. Groll, M. Moller, A. Reska, S. Schafer, P. Schultea, A. Vogt-Eisele, Microcontact Printing of Proteins for Neuronal Cell Guidance, *Soft Matter* 3 (2007) 290-298.
- [5] C.J. Flaim, S. Chien, S.N. Bhatia, An Extracellular Matrix Microarray for Probing Cellular Differentiation, *Nature Methods* 2 (2005) 119-125.
- [6] L. Lauer, S. Ingebrandt, M. Scholl, A. Offenhausser, Aligned Microcontact Printing of Biomolecules on Microelectronic Device Surfaces, *IEEE TRANSACTIONS ON BIOMEDICAL ENGINEERING* 48 (2001) 838-842.
- [7] S. Ilkhanizadeh, A.I. Teixeira, O. Hermanson, Inkjet Printing of Macromolecules on Hydrogels to Steer Neural Stem Cell Differentiation, *Biomaterials* 28 (2007) 3936-3943.
- [8] T.M. Keenan, A. Folch, Biomolecular Gradients in Cell Culture Systems, *Lab on a Chip* 8 (2008) 34-57.
- [9] E.D. Miller, G.W. Fisher, L.E. Weiss, L.M. Walker, P.G. Campbell, Dose-Dependent Cell Growth in Response to Concentration Modulated Patterns of FGF-2 Printed on Fibrin, *Biomaterials* 27 (2006) 2213-2221.
- [10] A.W. Martinez, S.T. Phillips, M.J. Butte, G.M. Whitesides, Patterned paper as a platform for inexpensive, low-volume, portable bioassays, *Angewandte Chemie International Edition* 46 (2007) 1318-1320.
- [11] A.W. Martinez, S.T. Phillips, E. Carrithe, S.W. Thomas III, H. Sindi, G.M. Whitesides, Simple Telemedicine for Developing Regions: Camera Phones and Paper-Based Microfluidic Devices for Real-Time, Off-Site Diagnosis, *Analytical Chemistry* 80 (2008) 3699-3707.
- [12] X. Li, J. Tian, T. Nguyen, W. Shen, Paper-Based Microfluidic Devices by Plasma Treatment, *Analytical Chemistry* 80 (2008) 9131-9134.
- [13] A.V. Lemmo, D.J. Rose, T.C. Tisone, Inkjet Dispensing Technology: Applications in Drug Discovery, *Current Opinion in Biotechnology* 9 (1998) 615-617.
- [14] M. Nakamura, A. Kobayashi, F. Takagi, A. Watanabe, Y. Hiruma, K. Ohuchi, Y. Iwasaki, M. Horie, I. Morita, S. Takatani, Biocompatible Inkjet Printing Technique for Designed Seeding of Individual Living Cells, *Tissue Engineering* 11 (2005) 1658-1666.
- [15] J.D. Newman, A.P.F. Turner, Ink-jet Printing For The Fabrication of Amperometric Glucose Biosensors, *Biosensors and Bioelectronics* 20 (2005) 2019-2026.
- [16] B.R. Ringeisen, C.M. Othon, J.A. Barron, D. Young, B.J. Spargo, Jet-based Methods to Print Living Cells, *Biotechnology Journal* 1 (2006) 930-948.

- [17] S.D. Risio, N. Yan, Piezoelectric Ink-Jet Printing of Horseradish Peroxidase: Effect of Ink Viscosity Modifiers on Activity, *Molecular Rapid Communications* 28 (2007) 1934-1940.
- [18] E.A. Roth, T. Xu, M. Das, C. Gregory, J.J. Hickman, T. Boland, Inkjet Printing for High-Throughput Cell Patterning, *Biomaterials* 25 (2004) 3707-3715.
- [19] L.R. Allain, M. Askari, D.L. Stokes, T. Vo-Dinh, Microarray Sampling-Platform Fabrication Using Bubble-Jet Technology for a Biochip System, *Fresenius Journal of Analytical Chemistry* 371 (2001) 146-150.
- [20] T. Goldmann, J.S. Gonzalez, DNA-printing: Utilization of a Standard Inkjet Printer for the Transfer of Nucleic Acids to Solid Supports *Journal of Biochemical and Biophysical Methods* 42 (2000) 105-110.
- [21] L. Pardo, J. W. Cris Wilson, T. Boland, Characterization of Patterned Self-Assembled Monolayers and Protein Arrays Generated by the Ink-Jet Method, *Langmuir* 19 (2003) 1462-1466.
- [22] L. Setti, C. Piana, S. Bonazzi, B. Ballarin, D. Frascaro, A. Fraleoni-Morgera, S. Giuliani, Thermal Inkjet Technology for the Microdeposition of Biological Molecules as a Viable Route for the Realization of Biosensors, *Analytical Letters* 37 (2004) 1559-1570.
- [23] T. Xu, J. Jin, C. Gregory, J.J. Hickman, T. Boland, Inkjet Printing of Viable Mammalian Cells, *Biomaterials* 26 (2005) 93-99.
- [24] H. Kipphan, *Handbook of Print Media*, Springer, 2001.
- [25] H.P. Le, Progress and trends in ink-jet printing technology, *The Journal of imaging science and technology* 42 (1998) 49-62.
- [26] I. Barbulovic-Nad, M. Lucente, Y. Sun, M. Zhang, A.R. Wheeler, M. Bussmann, Bio-Microarray Fabrication Techniques - A Review, *Critical Reviews in Biotechnology* 26 (2006) 237-259.
- [27] K. Chattopadhyay, S. Mazumdar, Structural and Conformational Stability of Horseradish Peroxidase: Effect of Temperature and pH, *Biochemistry* 39 (2000) 263-270.
- [28] H. Cho, M.A. Parameswaran, H.-Z. Yu, Fabrication of Microsensors Using Unmodified Office Inkjet Printers, *Sensors and Actuators B: Chemical* 123 (2007) 749-756.
- [29] W. Shen, T. Junfei, X. Li, M. Khan, G. Garnier, Method of Fabricating Paper-Based Microfluidic Systems by Printing, Australian Provisional Patent, 2008905776, November 7 (2008), Australia, 2008.
- [30] N.C. Veitch, Horseradish Peroxidase: A Modern View Of A Classic Enzyme, *Phytochemistry* 65 (2004) 249-259.
- [31] M.S. Khan, D. Fon, X. Li, J. Forsythe, G. Thouas, G. Garnier, W. Shen, Printing Biomolecules Part-1: Achieving Total Control of Biomolecule Delivery Using Ink Jet Printing, in: D. Chen (Ed.), *Chemeca 2008*, Engineers Australia, IChemE in Australia, City Hall, Newcastle, NSW, 2008, pp. 744-753.
- [32] M.S. Khan, D. Fon, X. Li, J.S. Forsythe, G. Garnier, W. Shen, Ink Jet Printing of Biomolecules on Porous Surfaces, in: N. Ahmed (Ed.), *International Conference on Chemical Engineering (ICChE) 2008*, Bangladesh University of Engineering and Technology (BUET), Dhaka, Bangladesh, 2008, pp. 171-176.
- [33] D.R. Lide, *CRC Handbook of Chemistry and Physics*, 84 ed., CRC Press, INC., 2003-2004.
- [34] A. Asai, M. Shioya, S. Hirasawa, T. Okazaki, Impact of an Ink Drop on Paper, *J. Imaging Sci. Technol.* 37 (1993) 205-207.

- [35] M.S. Khan, D. Kannangara, W. Shen, G. Garnier, Isothermal Noncoalescence of Liquid Droplets at the Air-Liquid Interface, *Langmuir* 24 (2008) 3199-3204.
- [36] B.S. Chang, K.H. Park, D.B. Lund, Thermal Inactivation Kinetics of Horseradish Peroxidase, *Journal of Food Science* 53 (1988) 920-923.
- [37] M.S. Khan, W. Shen, G. Garnier, Thermal Stability of Horseradish Peroxidase Enzymatic Papers, in: R. Coghill (Ed.), 63rd Appita Annual Conference and Exhibition, APPITA, Melbourne, Australia, 2009, pp. 273-280.
- [38] X. Li, J. Tian, W. Shen, Paper as Low-Cost Base Material for Diagnostic and Environmental Sensing Applications, in: R. Coghill (Ed.), 63rd Appita Annual Conference and Exhibition, APPITA, Melbourne, Australia, 2009, pp. 267-271.

---

# Chapter 11

---

Conclusion

---

This work investigated the reactivity, stability, retention, aging and the deposition of biomolecules immobilized on paper. It aims at engineering stable bioactive papers for diagnostics and industrial purposes. Bioactive papers are designed to be wetted by a biofluid or any solution of interest. It is therefore critical to maximize the retention and behaviour of the biomolecules on paper. An enzyme, alkaline phosphatase (ALP) was either directly physisorbed on paper or adsorbed on a paper treated with a polymer. Three model polymers were investigated: a high molecular weight cationic polyacrylamide (CPAM), an anionic polyacrylic acid (PAA) or a high molecular weight polyethylene oxide (PEO). Another enzyme, horseradish peroxidase (HRP), simply physisorbed and ink jet printed on paper. The reactivity and the thermal stability of enzyme bioactive paper were quantified using a colorimetric technique by measuring the colour intensity formed by the product complex. The enzymes adsorbed on paper retained their functionality and selectivity. Adsorption on paper increased the enzyme thermal stability by 2 to 3 orders of magnitude compared to the same enzyme in solution. The thermal degradation of the adsorbed enzyme was found to follow two sequential first order reactions, indication of a reaction system. Two explanations are favoured: either the enzyme thermal reaction follows two sequential reactions, or the active sites of the enzymes have two different thermal degradation kinetics.

All the model polymers used as retention aids were efficient at increasing the enzyme concentration on paper (by around 50%) and to prevent enzyme desorption/leaching upon the rewetting of the paper. Interestingly, all polymers performed similarly in spite of their different mechanism for adhering the enzyme on paper. However, the type of polymer affects the thermal stability and the aging of ALP enzyme on paper. When polymers are used as enzyme retention aid, the rapid initial deactivation becomes predominant, while it was negligible for the enzyme simply physisorbed on paper. As a result, the thermal stability significantly decreases. PAA affects enzyme stability the least; CPAM and PEO strongly decreased immobilized enzyme stability, especially at high temperatures. This suggests some interaction between the polymer and ALP probably affecting the tertiary structure of the enzyme. A mathematical model predicting the enzymatic paper's half-life time was developed. From the enzymatic deactivation model, we calculated that the half-life of ALP enzymatic paper is 22 days if stored at room temperature (23°C) and 4 months if

refrigerated. At room temperature (23°C) the half-life of HRP enzymatic paper was calculated to be 13 days.

The reaction rate of ALP enzymatic paper reacting with its substrate was measured and shown to follow a first order reaction with respect to the enzyme concentration. ALP immobilized on paper has a reaction rate 2 to 3 orders of magnitude lower than the free ALP in buffer solution, which might be due to a critical loss of enzyme flexibility upon adsorption. No increase in reaction rate was achieved by immobilizing ALP on paper treated with a polymer retention aid, such as CPAM or PAA; this suggests that enzyme orientation was not significantly affected through preferentially linking with its anionic or cationic groups. The reaction rate of ALP on PEO treated paper was lower than that on CPAM or PAA treated enzymatic papers, which is probably due to some PEO-ALP interaction affecting the tertiary structure of the enzyme molecules. PEO is a well known polymer preventing protein fouling on surfaces.

Paper bioassays to identify antigens and antibodies in a biofluid, such as blood, were investigated. Two series of experiments were performed. In the first, blood samples were mixed with different amounts of antibodies and a droplet of the mixture was deposited onto a paper strip. Agglutinated blood phase separated, with the red blood cells forming a distinct spot upon contact with paper while the serum wicked; in contrast, stable blood wicked uniformly as a single solution. In the second series of experiments, blood droplets were deposited onto the paper strips pretreated with solutions of antibodies. The wicking of blood droplets on paper strips was characterized. Blood agglutinated by interaction with a specific antibody phase separates, causing a chromatographic separation. The concept of blood typing using a paper diagnostic was demonstrated with a 3 arms prototype.

The feasibility of thermal ink jet printing technique was demonstrated for the precise deposition of biomolecules on paper and biodegradable polymer, poly( $\epsilon$ -caprolactone) (PCL). The strategy investigated was to reconstruct a commercial ink jet printer to take full advantage of the built-in modern colour management. A protein (albumin-FITC) and an enzyme (HRP) were used as biomolecules. Complex patterns of HRP and albumin-FITC were ink jet printed on paper. Microfluidic channels were also printed on paper to demonstrate the concept of paper based bioassays as diagnostic devices. Discrete and continuous concentration gradients of proteins on polymeric scaffolds were achieved by ink jet printing; these protein concentration gradients can

serve as potential guidance cues for cell growth generation for tissue engineering application. A novel strategy was developed to engineer very smooth, continuous concentration gradients of biomolecules by inkjet printing.

The ink jet delivery of biomolecules onto a porous surface involves the liquid-liquid interaction, while the acceptance of biomolecules on the porous surface is affected by the solid-liquid interaction. The liquid-liquid and solid-liquid interaction were quantified and modelled for droplets ink jet on paper. Satellite drops from the ink jet nozzle can form non-coalescence droplets (NCD), due to liquid-liquid interaction, and may roll from their target. The mechanism of generation and sustainability of NCDs was investigated on the liquid-air interface of the same liquid. The Weber number ( $We$ ) of falling liquid drops was used to correlate and to quantify the NCD generation. The  $We$  correlation suggests that any ink droplets larger than 4.0 pL can form NCDs which could disturb print resolution.

The initial liquid wicking behaviour of a droplet impacting an open V-groove at different velocities (groove angle,  $\beta = 60^\circ, 90^\circ, 120^\circ$ ) was studied. An experimental setup was developed to measure liquid wicking in narrow V-grooves. New mathematical model was developed to calculate liquid wicking distance in V-groove. The model considers the Laplace pressure in the threshold region of the wicking front to derive the driving force. The dynamics of wetting of sessile liquid droplets impinging, with different impact velocities, a specific groove surface ( $120^\circ$ ) was investigated experimentally. The understanding the dynamics of V-groove wicking and wetting is important to design uncoated papers for optimal ink jet printing and low-cost microfluidic devices.

The accomplishments in this study validates paper as a bioactive support exceptional for its flexibility and performance, and ink jet printing as a convenient and up-scalable process for the diagnostic and industrial process applications.

---

# Appendix

---

This page is intentionally blank

---

# Appendix A

---

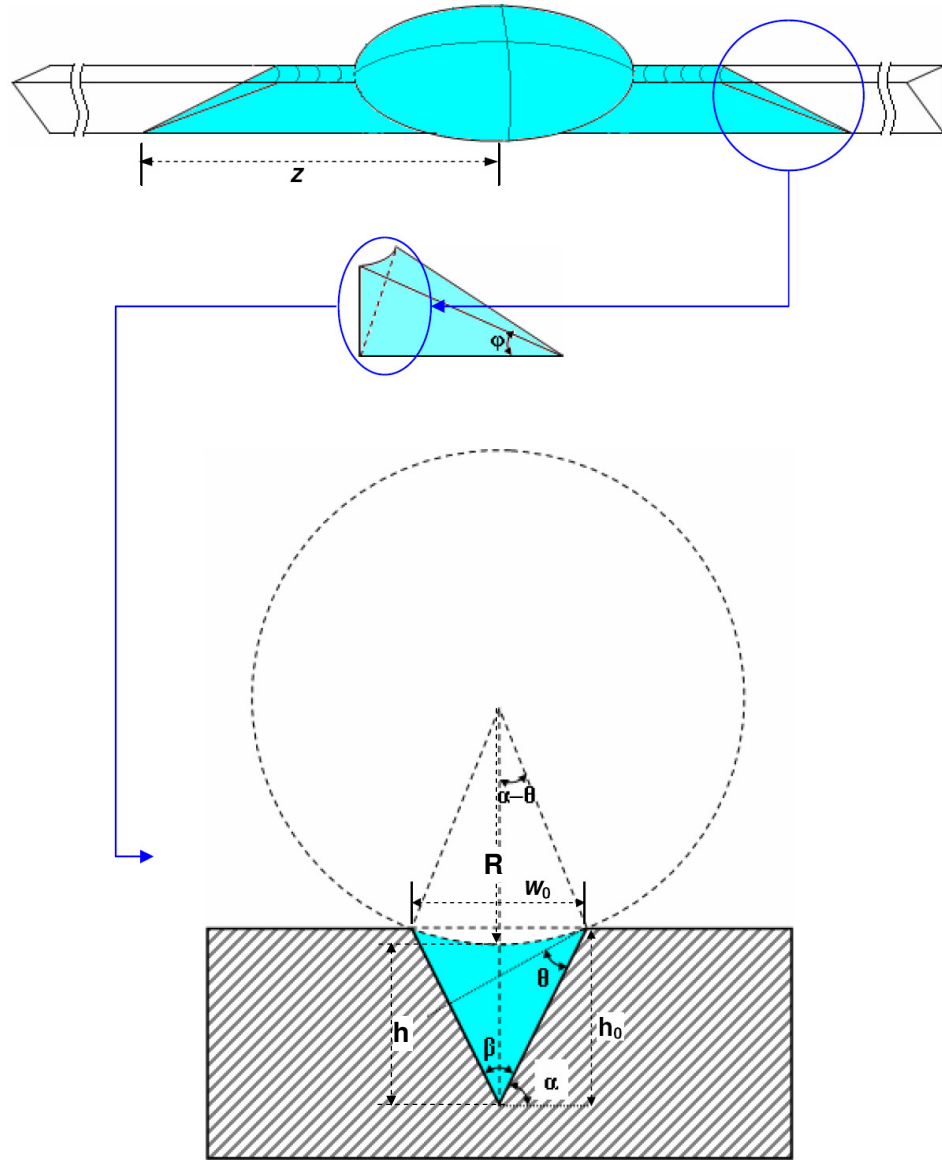
Modelling of a Liquid  
Droplet Wicking in a  
Surface Groove

---

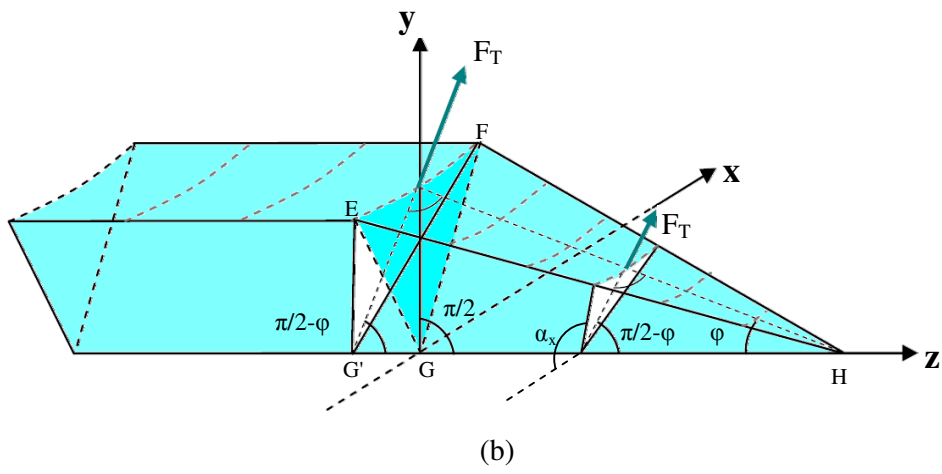
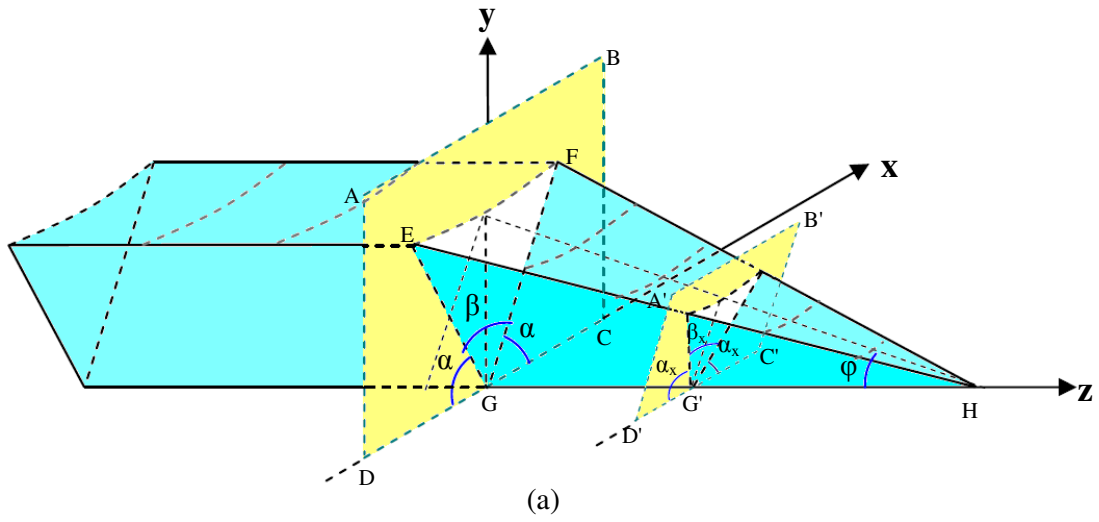
## **THEORETICAL TREATMENT**

As wicking starts in the V-groove, the threshold region of the wicking front develops and its length changes with time. However, the threshold region reaches to a steady length shortly after the wicking starts. It can be assumed that by then the length and the shape of the threshold region is no longer dependent on time and the driving force of the liquid wicking can be described by the Laplace pressure of the threshold region.

In modeling the Laplace driving force, we consider the following assumptions: First, the threshold region provides the driving force to liquid wicking in V-groove. Second, the Laplace pressure component parallel to the groove provides the driving force; the Laplace pressure component perpendicular to the wicking direction does not contribute to the driving force for liquid wicking. Third, liquid fills up the V-groove in the way that the groove length behind the threshold region is completely filled by the wicking liquid, as illustrated in Figure A1. Figure A2 and A3 represent the schematics of Laplace driving force on the wicking threshold.



**Figure A1:** Schematic representation of the V-groove wicking. Liquid wicks through a distance  $z$  into a wettable V-groove. V-groove of apex angle  $\beta$ , width  $w_0$  and height  $h_0$  creates  $\alpha$  angle with the horizontal surface. Wicking threshold creates  $\varphi$  angle along the wicking direction.



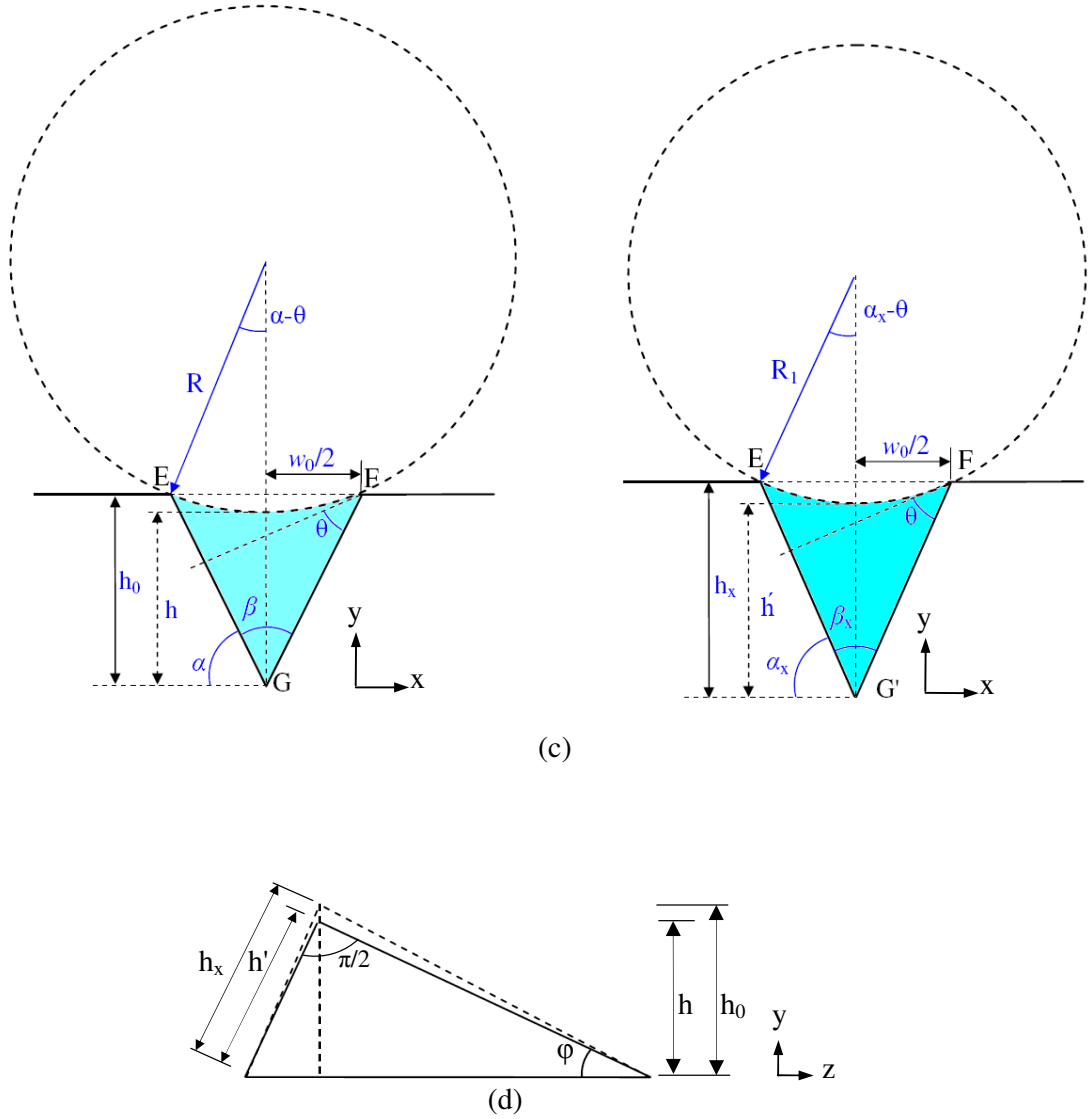


**Figure A2:** Laplace driving force on wicking threshold. (a) Laplace driving force working perpendicular to the threshold, (b) planes (EFG and EFG') perpendicular or inclined ( $\pi/2 - \phi$ ) with respect to  $z$ -axis, (c) threshold geometry: for plane EFG and EFG', (d) threshold geometry:  $y$ - $z$  plane.

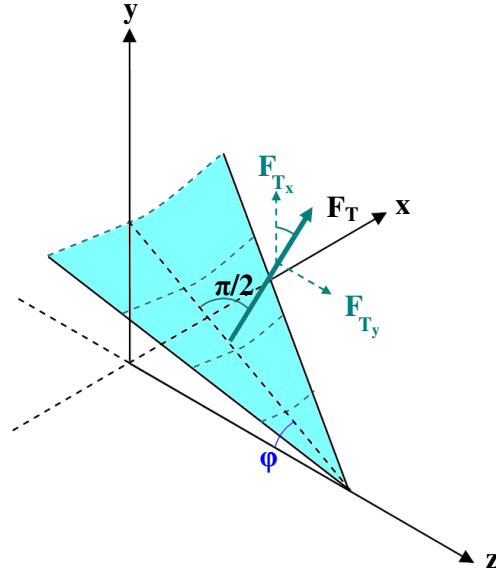


**Figure A3:** Laplace driving force of the threshold.

Under the above mentioned assumptions the threshold driving force can be calculated starting from the Laplace equation as follow.

$$\Delta P = \gamma \left( \frac{1}{R_1} + \frac{1}{R_2} \right)$$

where  $R_1$  is the radius of curvature perpendicular to the threshold region (Figure A2 c) and  $R_2 (= \infty)$  is the radius of curvature along the threshold region.

### A( $\alpha, \theta$ ) calculation

$$\begin{aligned} \text{From Figure A4, } A(\alpha, \theta) &= \text{Area(ADA'C)} \\ &= 2[\Delta ABC + \Delta OAB - \text{Area(OADB)}] \end{aligned}$$

$$\begin{aligned} \Delta ABC &= \frac{1}{2} \times (AB) \times (BC) \\ &= \frac{1}{2} \times \left(\frac{w_0}{2}\right) \times (h_0) \\ &= \frac{1}{2} \times (h_0 \cot \alpha) \times (h_0) \\ &= \frac{1}{2} \frac{h_0^2}{\tan \alpha} \end{aligned}$$

$$\begin{aligned} \Delta OAB &= \frac{1}{2} \times (AB) \times (OB) \\ &= \frac{1}{2} \times \left(\frac{w_0}{2}\right) \times \left(\frac{w_0}{2} \cot(\alpha - \theta)\right) \\ &= \frac{1}{2} \times \left(\frac{w_0}{2}\right)^2 \times \cot(\alpha - \theta) \\ &= \frac{1}{2} (h_0 \cot \alpha)^2 \cot(\alpha - \theta) \\ &= \frac{1}{2} (h_0^2) \left(\frac{1}{\tan^2 \alpha}\right) \frac{\cos(\alpha - \theta)}{\sin(\alpha - \theta)} \end{aligned}$$

$$\text{And, } \sin(\alpha - \theta) = \frac{\left(\frac{w_0}{2}\right)}{R} = \frac{h_0 \cot \alpha}{R}$$

$$\therefore R = \frac{h_0 \cot \alpha}{\sin(\alpha - \theta)}$$

As, area of a circle ( $2\pi$  rad) is  $(\pi R)^2$ . Therefore, Area(OADB) of angle  $(\alpha - \theta)$  is  $[(R)^2 (\alpha - \theta)/2]$ .

$$\begin{aligned} \therefore \text{Area(OADB)} &= \frac{(R)^2}{2} (\alpha - \theta) \\ &= \frac{1}{2} \left(\frac{h_0 \cot \alpha}{\sin(\alpha - \theta)}\right)^2 (\alpha - \theta) \\ &= \left(\frac{1}{2}\right) (h_0^2) \left(\frac{1}{\tan^2 \alpha}\right) \left(\frac{1}{\sin^2(\alpha - \theta)}\right) (\alpha - \theta) \end{aligned}$$

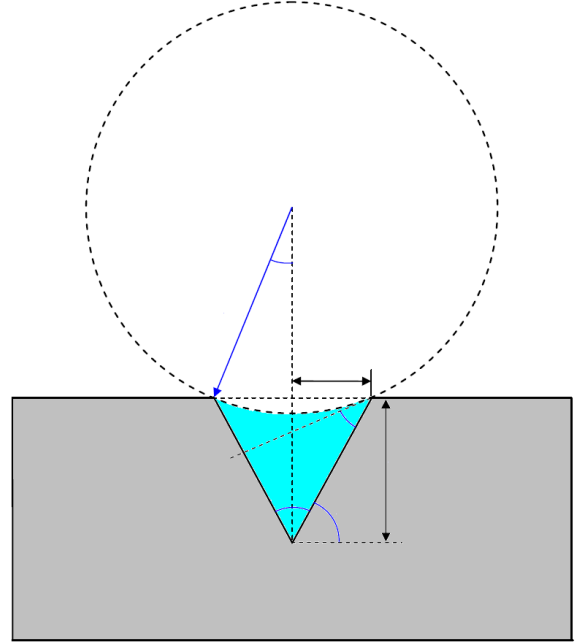


Figure A4: Cross section of the plane on which Laplace driving force works perpendicular on the filled groove.

$$\begin{aligned}
 A(\alpha, \theta) &= \text{Area}(ADA'C) \\
 &= 2[\Delta ABC + \Delta OAB - \text{Area}(OADB)] \\
 &= (h_0^2) \left[ \frac{(\tan \alpha)(\sin^2(\alpha - \theta)) + (\sin(\alpha - \theta))(\cos(\alpha - \theta)) - (\alpha - \theta)}{(\tan^2 \alpha)(\sin^2(\alpha - \theta))} \right] \\
 &= (h_0^2) A^*(\alpha, \theta)
 \end{aligned}$$

where

$$A^*(\alpha, \theta) = \frac{(\tan \alpha)(\sin^2(\alpha - \theta)) + (\sin(\alpha - \theta))(\cos(\alpha - \theta)) - (\alpha - \theta)}{(\tan^2 \alpha)(\sin^2(\alpha - \theta))}$$

Let's consider  $(\alpha - \theta) = x$ . Therefore, at the limit of  $\alpha \rightarrow \theta$ , we can write  $x \rightarrow 0$ . And  $A^*(\alpha, \theta)$  can be derived as follows:

$$\begin{aligned}
 \lim_{x \rightarrow 0} A^*(\alpha, \theta) &= \lim_{x \rightarrow 0} \frac{(\tan \alpha)(\sin^2 x) + (\sin x)(\cos x) - x}{(\tan^2 \alpha)(\sin^2 x)} \\
 &= \lim_{x \rightarrow 0} \frac{(\tan \alpha) \left( x - \frac{x^3}{3!} + o(x^3) \right)^2 + \left( x - \frac{x^3}{3!} + o(x^3) \right) \left( 1 - \frac{x^2}{2!} + o(x^2) \right) - x}{(\tan^2 \alpha) \left( x - \frac{x^3}{3!} + o(x^3) \right)^2} \\
 &= \lim_{x \rightarrow 0} \frac{(\tan \alpha) \left( x - \frac{x^3}{3!} + o(x^3) \right)^2 + \left( x - \left( \frac{1}{2!} + \frac{1}{3!} \right) x^3 + o(x^3) \right) - x}{(\tan^2 \alpha) \left( x - \frac{x^3}{3!} + \frac{x^5}{5!} - \dots \right)^2} \\
 &= \lim_{x \rightarrow 0} \frac{x^2(\tan \alpha) + x - x}{x^2(\tan^2 \alpha)}; \text{ at } x \rightarrow 0, \text{ neglecting the higher orders of } x \\
 &= \lim_{x \rightarrow 0} \frac{x^2(\tan \alpha)}{x^2(\tan^2 \alpha)} \\
 &= \lim_{(\alpha - \theta) \rightarrow 0} \frac{1}{\tan \alpha} \\
 &= \lim_{\alpha \rightarrow \theta} \frac{1}{\tan \alpha} \\
 \therefore \lim_{x \rightarrow 0} A^*(\alpha, \theta) &= \frac{1}{\tan \theta}
 \end{aligned}$$

Therefore, at limiting condition  $(\alpha \rightarrow \theta)$ , the cross sectional area can be derived as:

$$\lim_{\alpha \rightarrow \theta} A(\alpha, \theta) = h_0^2 \lim_{\alpha \rightarrow \theta} A^*(\alpha, \theta) = \frac{h_0^2}{\tan \theta}$$

### $R_1$ calculation

From Figure A2 and A5,

$$\sin(\alpha_x - \theta) = \frac{\left(\frac{w_0}{2}\right)}{R_1} = \frac{h_0 \cot \alpha}{R_1}$$

$$\therefore R_1 = \frac{h_0 \cot \alpha}{\sin(\alpha_x - \theta)} = \frac{h_0}{(\tan \alpha)(\sin(\alpha_x - \theta))}$$

### $h'$ and $h$ calculation

From Figure A2c and A5,

$$h' = CD = OC - OD$$

$$\Rightarrow h' = OB + BC - OD$$

$$\Rightarrow h' = OA \cos(\alpha_x - \theta) + h_x - R_1$$

$$\Rightarrow h' = R_1 \cos(\alpha_x - \theta) + h_x - R_1$$

$$\therefore h' = h_x - R_1 [\cos(\alpha_x - \theta) - 1]$$

Similarly, from Figure A2c,

$$h = h_0 - R [\cos(\alpha - \theta) - 1]$$

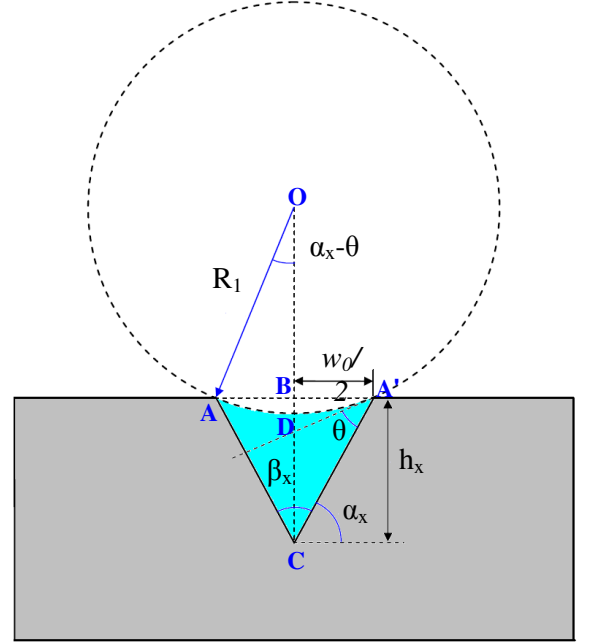


Figure A2: Cross section of the plane on which Laplace driving force works perpendicular on the threshold region.

### $\alpha_x$ calculation

In Figure A2, the liquid contact angle for threshold cross-sections EFG and EFG' is considered as  $\theta$ .

For threshold cross section EFG (Figure A2c),

$$\tan \alpha_x = \frac{h_0}{\frac{w_0}{2}} \therefore h_0 = \frac{w_0}{2} \tan \alpha_x$$

For threshold cross section EFG' (Figure A2c),

$$\tan \alpha_x = \frac{h_x}{\frac{w_0}{2}} \therefore h_x = \frac{w_0}{2} \tan \alpha_x$$

$$\therefore \frac{\tan \alpha_x}{\tan \alpha} = \frac{h_x}{h_0}$$

For simplicity let's consider the cosine functions are very close to 1 and therefore,

$$\therefore \frac{\tan \alpha_x}{\tan \alpha} = \frac{h'}{h}$$

From Figure A2(d),

$$\sec \varphi = \frac{h'}{h}$$

$$\text{Assuming, } \sec \varphi = \frac{h'}{h} \approx \frac{h_x}{h_0}$$

$$\therefore \frac{\tan \alpha_x}{\tan \alpha} = \frac{h_x}{h_0} = \sec \varphi$$

$$\Rightarrow \tan \alpha_x = \frac{\tan \alpha}{\cos \varphi}$$

$$\therefore \alpha_x = \tan^{-1} \left( \frac{\tan \alpha}{\cos \varphi} \right)$$

### $\Delta P$ calculation

$$\text{as, } R_1 = \frac{h_0}{(\tan \alpha)(\sin(\alpha_x - \theta))} \text{ and } R_2 = \infty$$

$$\begin{aligned} \therefore \Delta P &= \gamma \left( \frac{1}{R_1} + \frac{1}{R_2} \right) \\ &= \left( \frac{\gamma}{h_0} \right) (\tan \alpha)(\sin(\alpha_x - \theta)) \end{aligned}$$

### Driving force calculation

Assuming that the threshold region is triangular as shown in Figure A2 and A3, driving force perpendicular to the surface of the threshold region,

$$\begin{aligned} F_T &= \int dF = \int \Delta P dA = \int \Delta P w_0 . ds \\ &= \int_0^{s_0} \left( \frac{\gamma}{h_0} \right) (\tan \alpha)(\sin(\alpha_x - \theta)) w_0 . ds \\ &= \int_0^{s_0} \left( \frac{\gamma}{h_0} \right) (\tan \alpha)(\sin(\alpha_x - \theta)) (2h_0 \cot \alpha) . ds \\ &= 2\gamma(\sin(\alpha_x - \theta)) \int_0^{s_0} . ds \\ &= 2\gamma(\sin(\alpha_x - \theta))(s_0) \\ &= 2\gamma(\sin(\alpha_x - \theta)) \left( \frac{h_0}{\sin \varphi} \right), \text{ as } s_0 = \left( \frac{h_0}{\sin \varphi} \right) \text{ from Figure 9c} \\ &= (2\gamma h_0) \frac{\sin(\alpha_x - \theta)}{\sin \varphi} \end{aligned}$$

Effective force in the direction of flow can be estimated by taking the horizontal projection of  $F_T$ .

$$F_\gamma = F_T \sin \varphi = 2\gamma h_0 \sin(\alpha_x - \theta)$$

## Force Balance

The Newtonian equation of motion can be written as follows

$$\begin{aligned} \frac{d(mv)}{dt} &= \frac{d}{dt} \left[ (\rho \times A(\alpha, \theta) \times z_L) \left( \frac{dz_L}{dt} \right) \right] = \rho A(\alpha, \theta) \left[ \left( \frac{dz_L}{dt} \right)^2 + z_L \frac{d^2 z_L}{dt^2} \right] \\ &= F_\gamma - F_\mu = (2\gamma h_0)(\sin(\alpha_x - \theta)) - 8\pi\mu z_L \frac{dz_L}{dt} \end{aligned}$$

where,  $z_L$  is the wicking length along the V-groove channel due to Laplace pressure force and  $A(\alpha, \theta)$  is the cross sectional area of V-groove channel.

$$\begin{aligned} \therefore \rho A(\alpha, \theta) \left[ \left( \frac{dz_L}{dt} \right)^2 + z_L \frac{d^2 z_L}{dt^2} \right] &= (2\gamma h_0)(\sin(\alpha_x - \theta)) - 8\pi\mu z_L \frac{dz_L}{dt} \\ \Rightarrow \left[ \left( \frac{dz_L}{dt} \right)^2 + z_L \frac{d^2 z_L}{dt^2} \right] + \frac{8\pi\mu z_L}{\rho A(\alpha, \theta)} \frac{dz_L}{dt} &= \frac{(2\gamma h_0)(\sin(\alpha_x - \theta))}{\rho A(\alpha, \theta)} \\ \Rightarrow 2 \left[ \left( \frac{dz_L}{dt} \right)^2 + z_L \frac{d^2 z_L}{dt^2} \right] + 2a z_L \frac{dz_L}{dt} &= b \end{aligned}$$

where,

$$a = \frac{8\pi\mu}{\rho A(\alpha, \theta)} \text{ and } b = \frac{(4\gamma h_0)(\sin(\alpha_x - \theta))}{\rho A(\alpha, \theta)}$$

$$\text{Let, } y = \frac{d}{dt} (z_L^2)$$

$$\therefore y = 2z_L \frac{dz_L}{dt}$$

$$\text{and } \frac{dy}{dt} = 2 \left[ \left( \frac{dz_L}{dt} \right)^2 + z_L \frac{d^2 z_L}{dt^2} \right]$$

By substituting,

$$\begin{aligned} \frac{dy}{dt} + ay &= b \\ \Rightarrow \int_0^y \frac{1}{b-ay} dy &= \int_0^t dt \\ \Rightarrow \left(-\frac{1}{a}\right) [\ln(b-ay)]_0^y &= [t]_0^t \\ \Rightarrow \ln\left(\frac{b-ay}{b}\right) &= -at = \ln\left(\frac{b-2az_L \frac{dz_L}{dt}}{b}\right) \\ \Rightarrow b-2az_L \frac{dz_L}{dt} &= be^{-at} \\ \Rightarrow 2a \int_0^z z_L dz_L &= \int_0^t (b-be^{-at}) dt \\ \Rightarrow 2a \left(\frac{z_L^2}{2}\right) &= \left[bt + \frac{be^{-at}}{a}\right]_0^t \\ \therefore z_L^2 &= \frac{b}{a} \left[t + \frac{1}{a}(e^{-at} - 1)\right] \end{aligned}$$

For small cross sectional area, exponential term approaches to 1 and therefore, the above equation can be simplify to

$$\begin{aligned} z_L^2 &= \left(\frac{b}{a}\right)t \\ \text{as, } \frac{b}{a} &= \frac{(\gamma h_0)(\sin(\alpha_x - \theta))}{2\pi\mu} \\ \therefore z_L^2 &= \left[\frac{\gamma h_0}{2\pi\mu} \sin(\alpha_x - \theta)\right]t \end{aligned}$$

This equation offers a simple correlation of capillary liquid wicking with the driving force, resistance force, and groove parameters as a function of time:

$$\begin{aligned} &(\text{Capillary Wicking Dis tan ce})^2 \\ &= \frac{h}{2\pi} \frac{\gamma \sin(\alpha_x - \theta)}{\mu} t \\ &= \text{Parameter} \times \frac{\text{Driving Force} \times \text{Groove Parameter}}{\text{Re sis tan ce Force}} \times \text{Time} \end{aligned}$$

## Liquid Wicking in Grooves by Gravity Effect

In recent study, Holdrich et al. (2006) reported that both capillary and gravitational forces play role in wicking of a liquid droplet in a surface groove. Liquid wicking along a surface groove can be calculated considering the gravitational force along with Laplace pressure force and Poiseuille resistance force.

In estimating the hydraulic pressure of the liquid drop reservoir, a cylindrical shaped liquid column of equal volume and equal base area to that of the liquid drop over the V-groove is used to define the hydraulic head. To calculate the hydraulic head of a droplet on a surface, the height of an equal volume cylinder of same radius was considered (Figure A6). The force due to the hydraulic head was added to the driving force term:

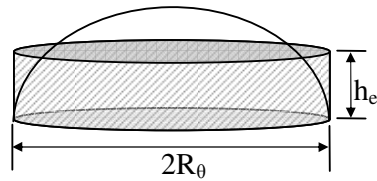


**Figure A6:** Schematic of liquid drop hydraulic head estimation using equal volume cylinder.

$$F_g = h_e \rho g A(\alpha, \theta)$$

$$\begin{aligned} \frac{d(mv)}{dt} &= \frac{d}{dt} \left[ (\rho \times A(\alpha, \theta) \times z) \left( \frac{dz}{dt} \right) \right] = \rho A(\alpha, \theta) \left[ \left( \frac{dz}{dt} \right)^2 + z \frac{d^2z}{dt^2} \right] \\ &= F_\gamma + F_g - F_\mu = (2\gamma h_0)(\sin(\alpha_x - \theta)) + h_e \rho g A(\alpha, \theta) - 8\pi\mu z \frac{dz}{dt} \end{aligned}$$

where,

$F_g$  = Hydraulic driving force,

$$h_e = \text{Equivalent height} = \frac{\text{Droplet Volume, } V}{\pi R_\theta^2},$$

$$R_\theta = \text{Equivalent radius} = \sqrt[3]{\frac{3V}{\pi(2 - 3\cos\theta + \cos^3\theta)}},$$

$V$  = Volume of liquid droplet and

$z_h$  = wicking length due to gravitational force

where,  $z$  is the wicking length along the V-groove channel due to Laplace pressure force and gravitational force.

$$\begin{aligned} \therefore \rho A(\alpha, \theta) \left[ \left( \frac{dz}{dt} \right)^2 + z \frac{d^2 z}{dt^2} \right] &= (2\gamma h_0)(\sin(\alpha_x - \theta)) + h_e \rho g A(\alpha, \theta) - 8\pi\mu z_L \frac{dz_L}{dt} \\ \Rightarrow \left[ \left( \frac{dz}{dt} \right)^2 + z \frac{d^2 z}{dt^2} \right] + \frac{8\pi\mu z}{\rho A(\alpha, \theta)} \frac{dz}{dt} &= \frac{(2\gamma h_0)(\sin(\alpha_x - \theta)) + h_e \rho g A(\alpha, \theta)}{\rho A(\alpha, \theta)} \\ \Rightarrow 2 \left[ \left( \frac{dz_L}{dt} \right)^2 + z_L \frac{d^2 z_L}{dt^2} \right] + 2az_L \frac{dz_L}{dt} &= b \end{aligned}$$

where,

$$a = \frac{8\pi\mu}{\rho A(\alpha, \theta)}, b = \frac{(4\gamma h_0)(\sin(\alpha_x - \theta)) + 2h_e \rho g A(\alpha, \theta)}{\rho A(\alpha, \theta)},$$

$$\text{Let, } y = \frac{d}{dt} (z^2)$$

$$\therefore y = 2z \frac{dz}{dt}$$

$$\text{and } \frac{dy}{dt} = 2 \left[ \left( \frac{dz}{dt} \right)^2 + z \frac{d^2 z}{dt^2} \right]$$

By substituting,

$$\frac{dy}{dt} + ay = b$$

$$\Rightarrow \int_0^y \frac{1}{b - ay} dy = \int_0^t dt$$

$$\Rightarrow \left( -\frac{1}{a} \right) [\ln(b - ay)]_0^y = [t]_0^t$$

$$\Rightarrow \ln\left(\frac{b - ay}{b}\right) = -at = \ln\left(\frac{b - 2az \frac{dz}{dt}}{b}\right)$$

$$\Rightarrow b - 2az \frac{dz}{dt} = be^{-at}$$

$$\Rightarrow 2a \int_0^z z dz = \int_0^t (b - be^{-at}) dt$$

$$\Rightarrow 2a \left( \frac{z^2}{2} \right) = \left[ bt + \frac{be^{-at}}{a} \right]_0^t$$

$$\therefore z^2 = \frac{b}{a} \left[ t + \frac{1}{a} (e^{-at} - 1) \right]$$

For small cross sectional area, exponential term approaches to 1 and therefore, the above equation can be simplified to

$$z^2 = \left( \frac{b}{a} \right) t$$

$$\text{as, } \frac{b}{a} = \frac{2\gamma h_0 \sin(\alpha_x - \theta) + h_e \rho g A(\alpha, \theta)}{4\pi\mu}$$

Therefore, total liquid wicking along V-groove can be expressed:

$$z^2 = \left( \frac{2\gamma h_0 \sin(\alpha_x - \theta) + h_e \rho g A(\alpha, \theta)}{4\pi\mu} \right) t$$

---

# Appendix B

---

Patent: Testing Device for  
Identifying Antigens and  
Antibodies in Biofluids

---

**TESTING DEVICE FOR IDENTIFYING ANTIGENS AND ANTIBODIES IN  
BIOFLUIDS**

**FIELD OF THE INVENTION**

5 The present invention is directed to the identification of antigens and antibodies within a biofluid. While the invention will be described with specific reference to its use in determining a person's blood type, it is to be appreciated that other applications of the invention are also envisaged.

**BACKGROUND TO THE INVENTION**

10 Blood is essential for sustaining living tissue, with the most important roles of supplying oxygen and other soluble nutrients, immune protection and metabolic turnover. While it is a tissue in its own right, blood in a chemical sense can be considered as a stable, highly packed colloid suspension made of red blood cells (erythrocytes, 4-6 million/mL, 6-8  $\mu\text{m}$ ), white cells (leukocytes, 4000-6000 /mL, 10-21  $\mu\text{m}$ ), platelets (150,000-400,000 /mL, 2-5  $\mu\text{m}$ ) carried within a fluid solution  
15 (serum) containing a host of biomolecules (eg albumins, fatty acids, hormones), metabolites and electrolytes. A subset of these biomolecules, such as the binding proteins responsible for tissue immunity (antigens) and blood type, are directly adsorbed onto the surface of blood cells. Common portable testing methods for blood include analysis of glucose content, cholesterol, metabolic  
20 panel (sodium, potassium, bicarbonate, blood urea nitrogen, magnesium, creatine, calcium, triglycerides), microbial and disease markers and protein molecular profile (liver, prostate). Surprisingly, and in spite of its vital importance, there are no convenient low cost disposable tests available for "on the spot" analysis of blood type. Blood samples are typically outsourced to an analytical  
25 laboratory. Reliable low cost tests which are able to instantaneously and reliably provide critical blood analysis without the requirement of sophisticated laboratory analytical instrumentation such as chromatographic and spectroscopic methods, would be invaluable for improving human health in developing countries, where economic resources are limited. Blood analysis is also important in non-human  
30 applications, such as veterinary medicine, where there is a demand for low cost and versatile devices suitable for field use.

**DESCRIPTION OF INVENTION**

With this in mind, according to one aspect of the present invention, there is provided a testing device for identifying an antigen or antibody within a biofluid sample including;

- 5 a substrate having a hydrophilic surface thereon;  
the surface including a collection zone, and at least one detection zone extending therefrom;  
wherein the biofluid sample can be mixed with a specific antigen or antibody, and deposited on the collection zone and transferred by capillary action to the detection zone;
- 10 the antigen or antibody in the biofluid sample reacting with an appropriate said antibody or antigen thereby resulting in a visual indication within the detection zone.

According to another aspect of the present invention there is provided a testing device for identifying an antigen or antibody within a biofluid sample including;

- a substrate having a hydrophilic surface thereon;  
the surface including a collection zone, and at least one detection zone extending therefrom;
- 20 the detection zone having an antibody or antigen immobilised therein;  
wherein the biofluid sample can be deposited on the collection zone and transferred by capillary action to the detection zone;
- the antigen or antibody in the biofluid sample reacting with an appropriate said antibody or antigen within the detection zone thereby resulting in a visual
- 25 indication therein.

The substrate may be formed from paper or other cellulosic materials. Alternatively, the substrate may include a chromographic layer thereon or may be a wettable porous medium.

- 30 The biofluid sample being tested may preferably be blood, and the visual indication may be due to an agglutination of the blood upon reaction with a specific antibody resulting in reduced wicking and/or separation of the blood in the detection zone.

The substrate surface may have a hydrophilic microfluidic channel pattern thereon defining the collection zone and the detection zone. Preferably, a plurality of detection zones may extend from the collection zone.

5 It has been found that red blood cell agglutination, triggered by specific antigen interaction, drastically decreases blood wicking and dispersion on paper or chromatographic media. The agglutination process also considerably enhances the chromatographic separation (elution) of the individual blood components, especially the red blood cells from the serum. The testing device according to the present invention can allow direct analysis of blood cells  
10 because of this visual indication. This can be performed instantaneously, either with a detection/reporting system built-in to the device or in conjunction with other off-line analytical equipment. The testing device may also allow for the identification and quantification of specific biomolecules (eg antigens and antibodies) based on induced coagulation, followed by the wicking and elution  
15 (separation) of the soluble protein fraction from the blood sample onto the porous substrate. The blood colloids, whose coagulation directly affects their wicking/separation, can either be present in the fluid of interest, such as the red blood cells of blood, or introduced as nanoparticles (gold, silver, micro-silica, zeolite, titanium dioxide and the like). In the latter case, the nanoparticle is typically  
20 covered with the specific counter-biomolecule or molecule of interest used as sensitive reporter component. The colloid particles may be of a size ranging from 1 nm to 100  $\mu\text{m}$  and may be introduced into the biofluid being analysed.

In the application of the present invention for determining the type of blood group, the present invention may determine the antigens present within a blood  
25 sample, the antigens determining whether the blood type is type A, B, O, AB and Rhesus +/- . Antibodies A, B and D (Rhesus) are deposited into separate detection zones. It may also be preferable to include an untreated control zone in one of the detection zones. A drop of blood is then deposited on the central collection zone, the blood sample being transferred by capillary action to each of  
30 the detection zones. When the blood sample contacts an appropriate antibody, the reaction of the red blood cells antigen with its corresponding antibody results in agglutination, or coagulation of the red cells. This agglutination results in a drop in velocity of the movement of the blood sample along the microfluidic

channel providing the detection zone and separation of the red blood cells from the serum. The velocity of the blood samples travelling along other detection zones with non-specific antibodies is unaffected. This visual contrast facilitates easy and rapid identification of the blood type of the blood sample.

5           The applicant has developed a low cost paper based microfluidic system which is described in International patent application no. PCT/AU2009/000889, details of which are incorporated herein by reference. The microfluidic systems described in this application utilise a paper based substrate, with the described fabrication methods producing hydrophilic microfluidic channels on the paper  
10 based substrates. It should be noted that the term paper is used in this application to refer to all cellulosic materials including woven fabrics and non-woven cellulosic material as well as paper. The microfluidic systems described in these applications can be readily adapted for the purpose of the present invention.

15           The testing device according to the present invention may also be used to detect illness as a result of blood cell malfunction on the blood cells being of abnormal shape as is the case with malaria. Alternatively, the testing device according to the present invention may be used to detect illness by identifying the presence of an antigen, antibody, virus (such as HIV, influenza) or protein.

20           In the International application, the microfluidic channels are fabricated by printing a hydrophobic agent on the substrate surface to define a peripheral edge of the microfluidic channels. According to the present invention, the antibody or antigen may also be printed within the microfluidic channels. The technology used, namely ink jet printing technology, may also be used to print the antigen or  
25 antibody within the microfluidic channels.

          According to a further aspect of the present invention, there is provided a method for identifying an antigen or antibody within a biofluid sample, including:  
          mixing the biofluid sample with a specific antigen or antibody,  
          depositing the mixed biofluid sample on a collection zone of a testing  
30 device including a substrate having a hydrophilic surface thereon, the surface including said collection zone and at least one detection zone extending therefrom, the biofluid sample being transferred by capillary action to the detection zone; and

identifying the antigen or antibody by a resultant visual indication within the detection zone arising where the antigen or antibody in the biofluid sample reacts with an appropriate said antibody or antigen.

According to yet another aspect of the present invention, there is provided  
5 a method for identifying an antigen or antibody within a biofluid sample, including:  
depositing the biofluid sample on a collection zone of a testing device  
including a substrate having a hydrophilic surface thereon, the surface including  
said collection zone and at least one detection zone extending therefrom, the  
detection zone having an antibody or antigen immobilised therein, the biofluid  
10 sample being transferred by capillary action to the detection zone; and  
identifying the antigen or antibody by a resultant visual indication arising  
where the antigen or antibody in the biofluid sample reacts with an appropriate  
said antibody or antigen within the detection zone.

**BRIEF DESCRIPTION OF THE DRAWINGS**

15 It will be convenient to further describe the invention with respect to the  
accompanying drawings which illustrate preferred embodiments of the testing  
device according to the present invention. Other embodiments of the invention  
are possible, and consequently, the particularity of the accompanying drawings is  
not to be understood as superseding the preceding description of the invention.

20 In the drawings:

Figure 1 shows a testing device according to the present invention used to  
determine B+ blood;

Figure 2 shows a testing device according to the present invention used to  
determine O+ blood;

25 Figure 3 shows the testing device according to the present invention using  
AB+ and B+ blood;

Figure 4 is the testing device according to the present invention showing  
blood wicking and blood separation as a function of time;

30 Figure 5 shows a testing device according to the present invention  
incorporating a valve;

Figure 6 A-F show the operation of a testing device according to the  
present invention incorporating valves and switches;

Figure 7 are schematic representations of testing devices according to the present invention adapted for testing different blood types; and

Figure 8 shows the testing device of Figure 7 showing the separation of red blood cells from the blood serum.

5 **DETAILED DESCRIPTION OF THE INVENTION**

The applicants have discovered that blood agglutination mediated by specific antibody-antigen interactions drastically affects its separation behaviour on contact with paper or any thin layer chromatographic surface. The invention relies this biochemical phenomenon to control the rate of wicking and separation, which enables (i) identification and quantitative assessment of a specific antibody/antigen, (ii) blood typing, and potentially (iii) identification of blood-borne pathogens as a disease diagnostic. The present invention is intended predominantly for applications in human and veterinary medicine and biotechnology.

Standard techniques for detection of blood agglutination are traditionally manual, involve dispensing of antibodies on a glass slide and microscopic visualization. However, the visualisation of agglutination is often subjective, and its automation requires a bank of sophisticated analytical equipment. The present invention provides a single-step blood test that simplifies and circumvents these difficulties.

One application of the invention involves a two steps process in which the blood sample is first coagulated/agglutinated by combining it with the specific antibody/antigen of interest, followed by its deposition on the analytical substrate (eg Non-woven paper or porous mesh) on which the sample wicking and separation by elution/chromatography is measured, directly or indirectly . These two mixing steps can be enhanced and more accurately performed by mixing on paper substrates using built-in valving and channelling control features .

A second application of the invention involves a single-step process in which the biofluid/sample is deposited directly on the substrate/device which has previously been treated with the specific antigen/antibody. For this process, the analyte samples simultaneously coagulate and elude on the same substrate. The measured elution velocity and the extent of sample separation are directly related

to the extend of coagulation, enabling the concentration of the biomolecule to be detected and quantified at the same time.

Both applications of the invention can be applied to a test device made of paper or any non-woven chromatographic surface, which are relatively cost effective. These substrates are also able to be modified with the use of advanced printing techniques to create microfluidic features composed of hydrophobic materials, as previously described in the applicant's International application no. PCT/AU2009/000889. Combined with methods of direct antibody deposition using printing, manufacture and placement of antibody reagent can enable very accurate spatial control of blood flow within the paper substrate.

#### EXAMPLES

Example 1: Sequential agglutination/coagulation of blood followed by wicking on paper: B+ (2 step process)(See Figure 1)

Antibody A and B (Epiclone™ Anti-A, Anti-B, and Anti-D; CSL, Australia) solutions were used. Anti-A and Anti-B come as blue and yellow colour reagents, respectively. 'B+' blood was used in this study. The blood sample was supplied into plastic vials with anti-coagulant. 'B+' blood was separately mixed with pure Anti-A and Anti-B (as received) to prepare 100µL solution. Paper strips (70mm×2mm) were made from Whatman#4 filter paper on which 2 mm unit marks were printed. The paper strips were soaked into phosphate buffer saline (PBS). Excess PBS was removed from the paper strips using standard blotting papers (Drink Coster Blotting, 280 GSM). The paper strips were then placed on Reflex Paper (80 GSM). 20 µL of every mixed solution was dispensed at the centre of paper strip using a calibrated micro-pipette. Pictures were taken after 4 minutes wicking.

It can be seen that:

B+ blood mixed with the solution of antibody A wicked and did not separate upon mixing and paper elution/wicking.

B+ blood mixed with the solution of antibody B wicked and **STRONGLY** separated (red cells from serum) and showed wicking.

B+ blood mixed with the solution of antibody D (Rhesus +) wicked and STRONGLY separated (red cells from serum).

A blood sample agglutinated/coagulated upon contact with its specific antibodies separated/eluded upon contact with paper (here Blood B+ with Anti-B and Anti-D antibodies).

A blood sample upon contact with non- specific antibody (here Blood B+ with Anti-A) does not agglutinate and does not separate/elute upon contact with paper.

This dramatic difference in elution/separation of blood/antibody mixing can be used to communicate specific agglutination and therefore can be used to identify blood typing.

Example 2: Sequential agglutination/coagulation of blood followed by wicking on paper: O+ (two steps process)(See Figure 2)

Antibody A and B (Epiclone™ Anti-A, Anti-B and Anti-D; CSL, Australia) solutions were used. Anti-A and Anti-B come as blue and yellow colour reagents, respectively. 'O+' blood was used in this study. The blood sample was supplied into plastic vials with anti-coagulant. 'O+' blood was separately mixed with Anti-A and Anti-B to prepare 100µL solution. Paper strips (70mmx2mm) were made from Whatman#4 filter paper on which 2 mm unit marks were printed. The paper strips were soaked into phosphate buffer saline (PBS). Excess PBS was removed from the paper strips using standard blotting papers (Drink Coster Blotting, 280 GSM). The paper strips were then placed on Reflex Paper (80 GSM). 20 µL of every mixed solution was dispensed at the centre of paper strip using a calibrated micro-pipette. Pictures were taken after 4 minutes wicking.

It can be seen that:

O+ blood mixed with the solution of antibody A wicked and did not separate upon mixing and paper elution/wicking.

O+ blood mixed with the solution of antibody B wicked and did not separate (red cells from serum) and showed wicking.

O+ blood mixed with the solution of antibody D (Rhesus +) wicked and STRONGLY separated (red cells from serum).

A blood sample agglutinated/coagulated upon contact with its specific antibodies separated/eluded upon contact with paper (here Blood O+ with Anti-D antibodies).

5 A blood sample upon contact with non- specific antibody (here Blood O+ with Anti-A and Anti-B) does not agglutinate and does not separate/elute upon contact with paper.

This dramatic difference in elution/separation of blood/antibody mixing can be used to communicate specific agglutination and therefore can be used to identify blood typing.

10 Example 3: Simultaneous agglutination/coagulation of blood followed by wicking on paper: Effect of antigen concentration. (1 step process)(See Figure 3)

In another embodiment of the invention, the paper is first treated with specific antibodies, dried or conditioned before been exposed to a sample of pure blood. This example provides a single step treatment in which the only  
15 requirement is to deposit a drop of blood on the paper. This example also illustrates the effect of diluting the antibody solution on the wicking and separation performance of blood on paper. Antibody dilution affects the ratio blood (with its antigen)- antibody.

Antibody A and B (Epiclone™ Anti-A and Anti-B; CSL, Australia) solutions  
20 were used. Anti-A and Anti-B come as blue and yellow colour reagents, respectively. "AB+" and 'B+' blood were used in this study. The blood sample was supplied into plastic vials with anti-coagulant. Paper strips (70mm×2mm) were made from Whatman#4 filter paper on which 2 mm unit marks were printed. Paper strips were soaked into antibody solutions of different concentrations  
25 (Anti-A@1.0x, 0.8x, 0.6x, 0.4x, 0.2x and 0.0x); phosphate buffer saline (PBS) was used as diluent. Excess antibody was removed from the paper strips with blotting papers. The antibody (Anti-A) active paper strips were then placed on Reflex Paper. Blood drops of 20µL were dispensed at the centre of paper strip using a calibrated micro-pipette. The wicking distance was measured from centre to  
30 either direction. Pictures were taken after 10 minutes.

The results are shown in Figure 3. It can be seen that:

Blood separates upon wicking with its specific antibody treated paper.

Blood separation is a non-linear function of the antibody concentration on the treated paper. The higher the antibody concentration, the more abrupt is the cell separation from the serum.

5 There is an optimum concentration to maximize wicking/separation/visualization.

Coagulation of red cell upon contact with its specific antibody drastically reduces its wicking/diffusion speed on the chromatographic surface, which promotes separation of cells from the serum. This drastic reduction and differentiation of elution speeds can serve as direct indicator of the type of blood.

10 Example 4: Effect of time on the wicking/separation of blood on bioactive antibody paper. (See Figure 4)

In another embodiment of the invention, the paper is first treated with specific antibodies, dried or conditioned before been exposed to a sample of pure blood. This example illustrates the effect of contact time blood- antibody treated paper on the wicking and separation performance of blood on paper.

15 Antibody A and B (Epiclone™ Anti-A; CSL, Australia) solutions were used. Anti-A comes as a blue colour reagent. "AB+" blood was used in this study. The blood sample was supplied into plastic vials with anti-coagulant. Paper strips (70mm×2mm) were made from Whatman#4 filter paper on which 2 mm unit marks were printed. Paper strips were soaked into antibody solutions (Anti-A@); phosphate buffer saline (PBS) was used as diluent. Excess antibody was removed from the paper strips with blotting papers. The antibody (Anti-A) active paper strips were then placed on Reflex Paper. Blood drops of 20µL were dispensed at the centre of paper strip using a calibrated micro-pipette. The wicking distance was measured from centre to either direction. Pictures were taken after different intervals of time.

It can be seen that:

blood wicking/separation levels off after about 4 minutes.

20 There is a minimum time of contact of antibody-blood required to allow proper blood coagulation/agglutination and wicking/separation.

There is an optimum time of contact of blood-antibody-paper. Too short, the blood does not properly coagulate; too long, the separation of red cell and serum can lose some of its sharpness.

5 Example 5: Paper microfluidic system to control flow, reaction and dilution.(See Figure 5)

In the embodiment of the invention, paper-based microfluidic reactors can be used to conduct blood type tests. Specific antibodies are printed into the reactor designed on paper. Then blood cell suspension is introduced into the same reactor. The required period of time is allowed so that the antibodies and cell suspension can contact and mix. After a preset period of time, the valve of the reactor is closed to facilitate penetration of blood across the valve. If only the penetration of serum is observed, the test is positive because of agglutination of blood during the mixing time. If the penetration of blood is observed, the test is negative. Thus paper-based microfluidic reactor can provide a rapid visual test of blood type.

15 Example 6: Microfluidic system with valves (See Figure 6)

Paper microfluidic devices can be designed to increase the ratio of blood/antibody and to provide the required time delay to allow blood and antibody interactions before the test. This example shows that all these steps can be performed using a paper device. Figure 6 shows the design of the paper device. (A) A filter paper sheet is printed and cut as shown, and specific antibodies are either printed or deposited in the circled region. A paper switch is made on the right hand side of the device. (B) Blood sample is introduced onto the indicated region. (C) The cut paper is folded towards the blood sample as shown. (D) Blood sample is allowed to stay in contact with the antibody loaded paper for a set time. (E) After a short period of contact time, the switch is closed as shown. If the test is positive, blood will agglomerate and only serum will wick out along the switch. (F) After a short period of contact, the switch is closed as shown. If the test is negative, blood will not agglomerate and will wick out along the switch.

Example 7: Paper microfluidic system for blood typing (See Figure 7)

In another embodiment of the invention, a microfluidic system is printed on paper or a chromatographic medium and antibodies A, B and D (Rhesus) are printed into each of the 3 detection arms. Blood typing is analysed by placing a blood droplet in the middle reservoir and reading the results. All the different combinations of blood type and their representations are represented in Figure 7.

Example 8: Chromatographic Separation of RBC/Blood Serum on Paper (See Figure 8)

Figure 8 illustrates blood group detection using chromatographic separation of red blood cells (RBC) and blood serum on antibody active paper surface; (a) schematic of chromatographic separation on paper bioassay; (b) and (c)(I) are trial 1 and 2 using A+ blood sample, respectively; (b)(II), (c)(II) are the converted images of (b)(I), (c)(I) (RGB colour to BRG colour), respectively, for better resolution.

Modifications and variations as would be deemed obvious to the person skilled in the art are included within the ambit of the present invention as claimed in the appended claims.

CLAIMS:

1. A testing device for identifying an antigen or antibody within a biofluid sample including;  
a substrate having a hydrophilic surface thereon;  
5 the surface including a collection zone, and at least one detection zone extending therefrom;  
wherein the biofluid sample can be mixed with a specific antigen or antibody, and deposited on the collection zone and transferred by capillary action to the detection zone;  
10 the antigen or antibody in the biofluid sample reacting with an appropriate said antibody or antigen thereby resulting in a visual indication within the detection zone.
  
2. A testing device for identifying an antigen or antibody within a biofluid sample including;  
15 a substrate having a hydrophilic surface thereon;  
the surface including a collection zone, and at least one detection zone extending therefrom;  
the detection zone having an antibody or antigen immobilised therein;  
wherein the biofluid sample can be deposited on the collection zone and  
20 transferred by capillary action to the detection zone;  
the antigen or antibody in the biofluid sample reacting with an appropriate said antibody or antigen within the detection zone thereby resulting in a visual indication therein.
  
3. A testing device according to claim 1 or 2, wherein the substrate is formed  
25 from paper or other cellulosic materials.
  
4. A testing device according to claim 1 or 2, wherein the substrate includes a chromatographic layer thereon or other wettable porous media.

5. A testing device according to claim 1 or 2, wherein the substrate surface has a hydrophilic microfluidic channel pattern thereon defining the collection zone and the detection zone.
6. A testing device according to claim 5, including a plurality of detection  
5 zones extending from the collection zone.
7. A testing device according to claim 1 or 2, wherein biofluid sample being tested is blood, and the visual indication is due to an agglutination of the blood upon reaction with a specific antibody resulting in reduced wicking and/or separation of the blood in the detection zone.
- 10 8. A testing device according to claim 7, wherein the testing device includes at least one valve for controlling the wicking of biofluid to the detection zone from the collection zone.
9. A testing device according to claim 7, wherein the testing device includes a switch for controlling the contact of the biofluid with the antibody or antigen.
- 15 10. A method for identifying an antigen or antibody within a biofluid sample, including:  
mixing the biofluid sample with a specific antigen or antibody,  
depositing the mixed biofluid sample on a collection zone of a testing  
device including a substrate having a hydrophilic surface thereon, the surface  
20 including said collection zone and at least one detection zone extending therefrom, the biofluid sample being transferred by capillary action to the detection zone; and  
identifying the antigen or antibody by a resultant visual indication within the  
detection zone arising where the antigen or antibody in the biofluid sample reacts  
25 with an appropriate said antibody or antigen.
11. A method for identifying an antigen or antibody within a biofluid sample, including:

depositing the biofluid sample on a collection zone of a testing device including a substrate having a hydrophilic surface thereon, the surface including said collection zone and at least one detection zone extending therefrom, the detection zone having an antibody or antigen immobilised therein, the biofluid  
5 sample being transferred by capillary action to the detection zone; and

identifying the antigen or antibody by a resultant visual indication arising where the antibody or antigen in the biofluid sample reacts with an appropriate said antigen or antibody within the detection zone.

12. A method as claimed in claim 10 or 11, including mixing nanoparticles  
10 within the biofluids sample to facilitate said reaction in the detection zone.

13. A method according to any one of claims 10 to 12, wherein biofluid sample being tested is blood, and the visual indication is due to an agglutination of the blood upon reaction with a specific antibody resulting in reduced wicking and/or separation of the blood in the detection zone.

14. A method according to claim 13, including detecting blood type from the  
15 visual indication.

15. A method according to claim 13 including detecting illness from the visual indication.

**MONASH UNIVERSITY**

**WATERMARK PATENT & TRADE MARK ATTORNEYS**

P32010AUP1

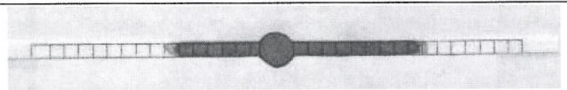
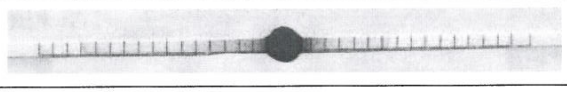
Blood sample mixed with antibody solutions	Blood Sample -B+
Anti-A	
Anti-B	
Anti-D	

Figure 1:

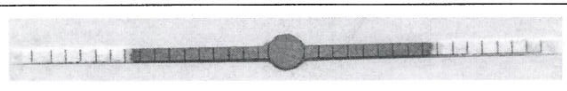
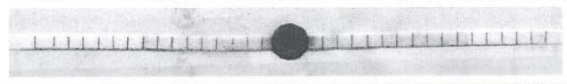
Blood sample mixed with antibody solutions	Blood Sample O+
Anti-A	
Anti-B	
Anti-D	

Figure 2:

Anti-A concentration on Paper	AB+ Blood on Anti-A active Paper	B+ Blood on Anti-A active paper
0.0 x		
0.2 x		
0.4 x		
0.6 x		
0.8 x		
1.0 x		

Figure 3: Blood wicking on Anti-A active paper: 10mins after blood drop dispensing

Time, t (min)	AB+ Blood wicking on Anti-A (1.0x) active paper
0.0	
1.0	
2.0	
3.0	
4.0	
5.0	

Figure 4:

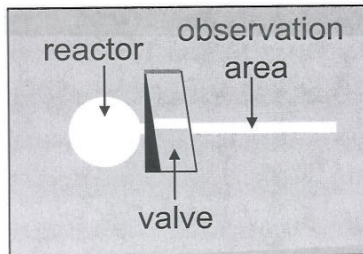


Figure 5:

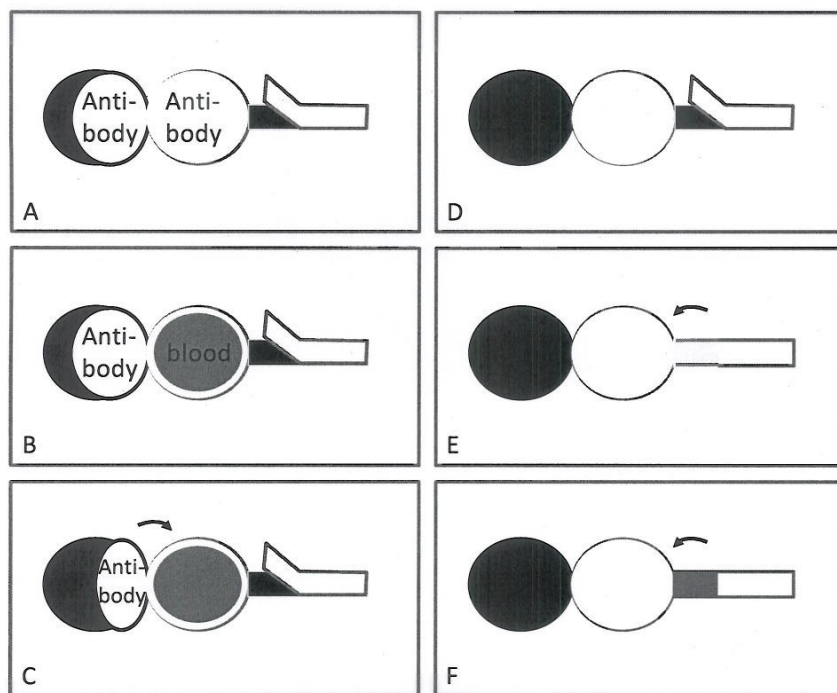


Figure 6:

Figure 7

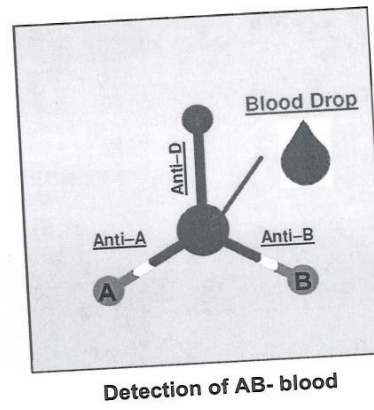
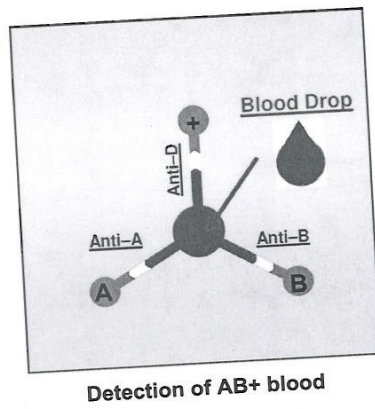
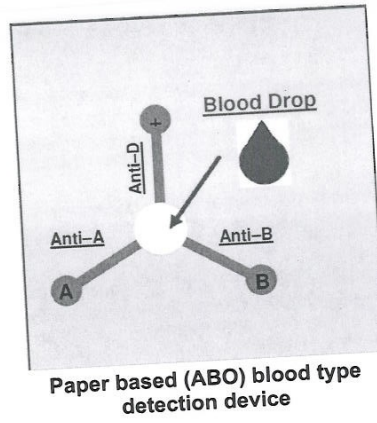
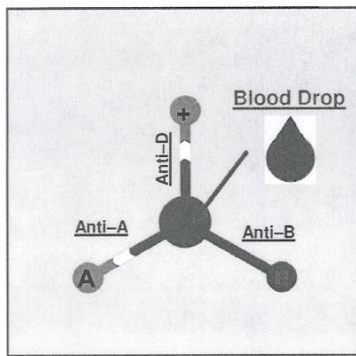
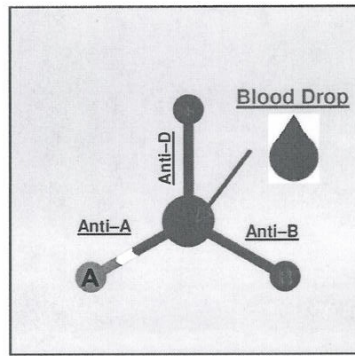


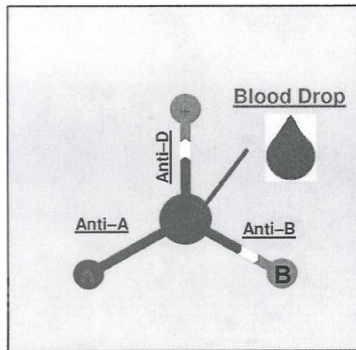
Figure 7 (cont.)



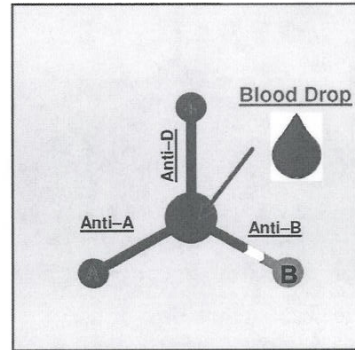
Detection of A+ blood



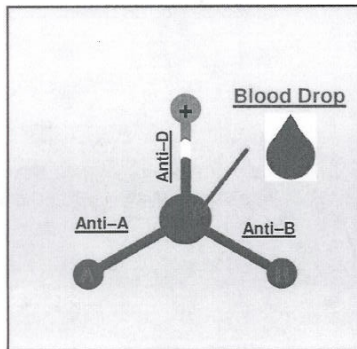
Detection of A- blood



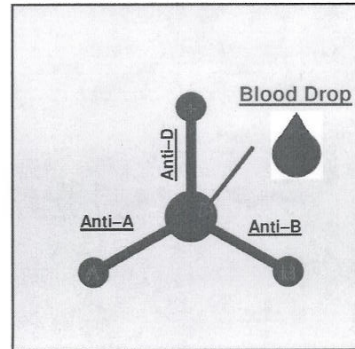
Detection of B+ blood



Detection of B- blood



Detection of O+ blood



Detection of O- blood

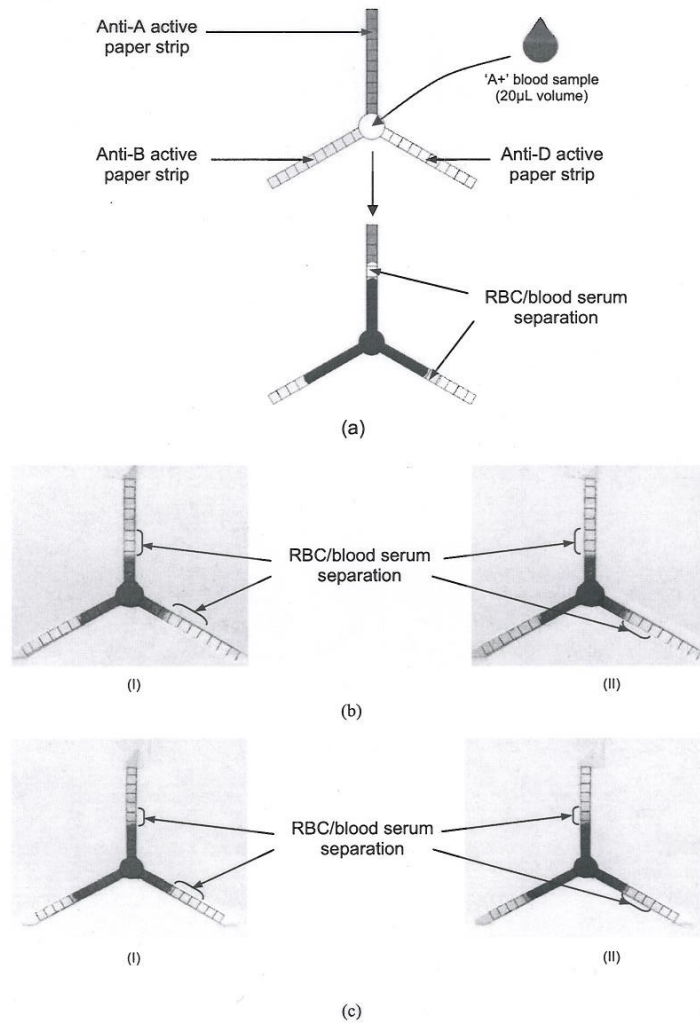


Figure 8

This page is intentionally blank

---

# Appendix C

---

Patent: Methods of  
Fabricating Microfluidic  
Systems

---

## **METHOD OF FABRICATING MICROFLUIDIC SYSTEMS**

### **TECHNICAL FIELD**

The present invention is generally directed to microfluidic systems, and  
5 fabrication of such systems on low cost substrates such as paper, fabric and non-  
woven cellulosic material.

### **BACKGROUND TO THE INVENTION**

The concept of making inexpensive microfluidic channels on paper and  
10 other woven and non-woven fibrous and porous surfaces has been successfully  
proven. The aim of building such systems has been to fabricate low-cost bio-  
analytical and indicator devices, with direct envisaged applications in detecting  
waterborne bacteria and metals ions in drinking water, the presence of some  
15 specific proteins or biomarkers in body fluid (cancer test), the level of glucose and  
other bio-chemical substances in human or animal blood and urine samples.  
Developments of low-cost paper-based bio-analytical and environmental  
analytical devices have so far allowed quick and single step reaction to detect  
analytes in a fluid sample.

Researchers in Harvard University led by Whitesides (see Martinez, A.W.,  
20 Phillips, S.T., Butte, M.J. and Whitesides G.M., and "Patterned Paper as a  
platform for Inexpensive, Low-Volume, Portable Bioassays", *Angew. Chem. Int.*  
*Ed.* 46, 1318-1320 (2007)) have recently created channels on paper by printing  
patterns of conventional photoresists polymers (PMMA). Paper provides the  
capillary channels, while the photoresist polymers form the barrier which defines  
25 the channel. More recently, the Harvard group further developed their photoresist  
technique in making fine channels in paper. They used an ink jet printer to print  
patterns on transparent polymer films, which were used as masks for photo  
lithography to generate photoresist patterns in paper following their published  
approach (Martinez, A.W., Phillips, S.T., Wiley, B.J., Gupta, M. and Whitesides,  
30 G.M. *Lab on a Chip*, (2008) DOI: 10.1039/b811135a). They showed that fine  
microfluidic channels can be generated in paper using the photoresist barrier  
approach and these channels have comparable resolution to the microfluidic  
channels made using other substrates such as silicon wafer. In another

published paper, the Harvard group used an x-y plotter to draw channels on paper surface (see Bruzewicz, D.A., Reches, M. and Whitesides, G.M., " Low-Cost Printing of Poly(dimethylsiloxane) Barriers to Define Microchannels in Paper, Anal Chem. 80, 3387-3392 (2008) and Martinez, A.W.; Phillips, S.T.; Carrilho, E.; Thomas III, S.W.; Sindi, H.; Whitesides, G.M., "Simple telemedicine for developing regions: camera phones and paper-based microfluidic devices for real-time, off-site diagnosis". Anal. Chem. 80 (2008) 3699 – 3707)). The plotter's pens were filled with a hydrophobic solution of polydimethyl siloxane (PDMS) in hexane, and a plethora of patterns several centimetres long with channel 1cm to 2 mm wide were created. Their second micro-channels system created on paper surface overcame a major drawback of the first one, *ie* the rigid and brittle barrier material of conventional photoresist polymers. Their second system, however, has a poor channel resolution and definition, since the penetration of PDMS solution in paper sheet cannot be controlled. The use of silicones to define the walls of the microchannels would also require FDA approval in view of the potential health related issues.

Abe *et al.* (Abe, K; Suzuki, K; Citterio, D. "Inkjet-printed microfluidic multianalyte chemical sensing paper", Anal. Chem. (2008) 6928-6934) presented a method of using a solution of hydrophobic polymer (PS) to impregnate paper. After the polymer physically covered the fibre surface and dried, they used a Microdrop dispensing device to deliver solvent droplets to dissolve the polymer from the fibre surface, thus forming microfluidic channels by restoring the hydrophilicity of the paper. These authors also used the Microdrop dispensing device to deliver chemical sensing agents into their pattern to form a functional device for biomedical detection.

In US 7125639, Molecular Transfer lithography, the inventor Charles Daniel Schaper (class 430/253, 430/258) describes a process for patterning a substrate comprising the steps of: 1) coating a carrier with a photosensitive material, 2) exposing the photosensitive material to a pattern of radiation, and 3) physically transferring the exposed material to the substrate.

In US 6518168, Self-assembled monolayers direct patterning of surfaces, by Paul G Clem et al (filing date 11/02/1998), A technique for creating patterns of material deposited on a surface involves forming a self-assembled monolayer in a

pattern on the surface and depositing, via chemical vapor deposition or via sol-gel processing, a material on the surface in a pattern complementary to the self-assembled monolayer pattern. The material can be a metal, metal oxide, or the like.

5           In WO/2008/060449 MICROFLUIDIC DETECTOR, by BUTTE, Manish, J. *et al* (Application date 9-11/2007), articles and methods for determining an analyte indicative of a disease condition are provided. In some embodiments, articles and methods described herein can be used for determining a presence, qualitatively or quantitatively, of a component, such as a particular type of cell, in  
10 a fluid sample. In one particular embodiment, a low-cost microfluidic system for rapid detection of T cells is provided. The microfluidic system may use immobilized antibodies and adhesion molecules in a channel to capture T cells from a fluid sample such as a small volume of blood. The captured T cells may be labelled with a metal colloid (eg, gold nanoparticles) using an antibody specific  
15 for the T Cell Receptor (TCR), and metallic silver can be catalytically precipitated onto the cells. The number of T cells captured can be counted and may indicate a disease condition of a patient such as severe combined immune deficiency or human immunodeficiency virus.

Those patent applications and research papers proposed methods to  
20 make microfluidic systems and devices using a variety of materials, including using paper and other non-woven or porous materials as substrates. Microfluidic channels can be fabricated using paper and other non-woven or porous materials in batch operations. However all of the above-noted systems utilise complex and time consuming processes that cannot be readily adapted to allow for low cost,  
25 high speed industrial production. Furthermore, all these earlier systems rely on a physical barrier to define the microfluidic channels.

#### **SUMMARY OF THE INVENTION**

With this in mind, according to one aspect of the present invention, there is  
30 provided a method of fabricating a microfluidic system having microfluidic channels on a surface of a hydrophilic substrate, the method including the steps of:

- a) hydrophobizing the substrate surface;

b) locating a mask defining the substrate surface, the mask having open areas defining the periphery of the microfluidic channels; and

c) applying an irradiation treatment to areas of the substrate surface exposed by the open areas of the mask, said exposed areas becoming  
5 hydrophilic to therefore form said microfluidic channels.

According to another aspect of the present invention, there is provided a microfluidic system fabricated according to the above described method.

The hydrophilic substrate may be provided by a cellulosic material including paper, woven and non-woven materials. The paper products can  
10 include filter paper, office paper, chromatography paper, tissues (towel, facial, bath wipes), newspaper, packaging paper, and so on.

The hydrophilic treatment acts to reduce the surface energy of the substrate surface. Various methods can be selected to hydrophobize the surface/substrate. An embodiment of the invention consists of absorbing or  
15 adsorbing a solution of hydrophobic substance dissolved in a volatile solvent. Hydrophobic substance include, but are not restricted to, alkyl ketene dimer (AKD), alkenyl succinic anhydride (ASA), rosin, latex, silicones, fluorchemicals, polyolefin emulsions, resin and fatty acids, natural and synthetic waxes and any hydrophobic substance known in the art. Another application is through vapour  
20 deposition of a hydrophobic substance.

The irradiation treatment acts to significantly increase the surface energy of the substrate surface rendering the treated areas with greater wettability by water and aqueous liquids. The wettability of the porous material by liquids then provides capillary driving force and allows the penetration of liquids within and  
25 along the channels created by the irradiation treatment.

The irradiation treatment may include plasma, corona and other irradiation treatments.

The microfluidic channels may preferably be in a pattern transporting a fluid to analyse in parallel to different detection zones. The typical channel  
30 dimensions vary in length from 1 m to 10 cm and in width from 2 cm to 100  $\mu\text{m}$ . The fluidic system has typically the same rigidity, mechanical, properties and softness as those of the original substrate.

It would also be advantageous to fabricate microfluidic systems using high volume, high speed and continuous printing methods which are able to provide on-demand microfluidic channel pattern variations.

5 With this in mind, according to a further aspect of the present invention, there is provided a method of fabricating a microfluidic system having microfluidic channels on a surface of a hydrophilic substrate, the method including the step of printing a hydrophilic agent on the substrate surface to define a peripheral edge of the microfluidic channels.

10 The printing of the hydrophilic agent provides a hydrophobic/hydrophilic contrast between the peripheral edge of the microfluidic channels and the channels themselves. This is distinguished from prior art printing methods that seek to provide a physical barrier along the peripheral edge of the microfluidic channels.

15 The advantages of the present invention are the low manufacturing cost, the high processing speed and the exceptional pattern accuracy achievable. In one form of the invention a hydrophobic chemical (wax, polymer, oligomer or molecule) is dissolved in an organic solvent and printed. In another, a stable aqueous emulsion of the hydrophobic chemical is printed. The printed substrate can further be activated to fully develop the hydrophobicity via molecular rearrangement including the creation of covalent bonds. Of special interest are 20 the hydrophobic materials used in the paper industry such as the internal sizing agents (AKD, ASA, rosin) and the surface sizing agents (polymers, latex). Our invention offers, for the first time, the possibility to manufacture at high speed, low cost and high quality micro-fluidic systems.

25 A possible manufacturing arrangement includes: 1) an unwinder, 2) a first printing station for the hydrophobic barrier, 3) an infra-red oven, (to activate) and 4) a rewinder, all arranged in series. Optional are 5) a cooling unit and 6) a second printing unit printing for the active system (biomolecule, reactive system). Should digital printers be selected (inkjet printers), on-demand pattern variations 30 can be achieved. The invention is ideally suited to manufacture paper based diagnostic devices for health or environment analysis and control. The complete fluidic can be manufactured by printing, using a single line or even a single printer.

An ink may be formed with the hydrophobizing agent. A first option is to dissolve the hydrophobizing agent in an organic solvent for printing using common technology. A second option is to emulsify the hydrophobic agent into a stable aqueous ink. The advantage of this later option is that no volatile organic compounds (VOC) are emitted. VOC are to avoid under manufacturing conditions because of their important health and fire hazards.

After printing, the hydrophobic pattern can further be activated to fully develop the hydrophobicity via molecular rearrangement including the creation of covalent bonds. This is achieved by aging, heat, reaction or radiation. This treatment will also improve the permanency of the pattern.

While all hydrophobic compounds can be used as ink, the internal and surface sizing agents common in the Paper industry are especially attractive for their effectiveness, low cost, and low toxicity. Further they fulfil many health and safety requirements. Of special interest are alkyl ketene dimmers (AKD), alkenyl succinic anhydride (ASA), rosin, and the latex and polymers used in surface sizing

The printing fluids can be printed on paper to fabricate microfluidic systems and devices using contact and non-contact printing processes and equipments, such as gravure, flexography, screen printing, ink jet printing, etc. In this application the applicants used digital ink jet printing to demonstrate the fabrication of microfluidic systems on paper.

Compared with the previous physical barrier fabrication methods, the new fabrication method according to the present invention enables the manufacturing of paper-based microfluidic devices in commercial scales and at low cost. Creation of hydrophilic-hydrophobic contrast is a simpler approach to define liquid penetration channels in paper than the physical barrier approach.

The use of digital printing technology to selectively deliver cellulose hydrophobization chemicals on paper surface to form the hydrophilic-hydrophobic contrast has some other advantages. Digital printing offers electronic pattern variation which allows fast change over for fabrication of different devices. Since the hydrophilic-hydrophobic contrast fabrication concept can retain the original flexibility of the paper, it offers natural bending and folding resistance, which

fundamentally overcomes the poor bending and folding resistance often encountered with devices fabricated with other methods.

**BRIEF DESCRIPTION OF THE DRAWINGS**

5           It will be convenient to further describe the invention with respect to the accompanying drawings which illustrate preferred embodiments of the microfluidic system according to the present invention. Other embodiments of the invention are possible, and consequently, the particularity of the accompanying drawings is not to be understood as superseding the description of the invention.

10           In the drawings:

          Figure 1 shows a single microfluidic channel fabricated according to a first embodiment of the invention;

          Figure 2 shows a capillary channel pattern on filter paper fabricated according to the first embodiment of the invention;

15           Figure 3 shows a capillary channel pattern fabricated on two ply tissue paper according to the first embodiment of the present invention;

          Figure 4 shows a capillary channel pattern fabricated on a kitchen paper towel according to the first embodiment of the present invention;

20           Figure 5 shows a capillary channel pattern fabricated on photocopy paper according to the first embodiment of the present invention;

          Figure 6 shows a capillary channel pattern fabricated on news print paper according to the first embodiment of the present invention;

          Figure 7 shows printed microfluidic patterns fabricated according to a second embodiment of the present invention;

25           Figures 8 and 9 show different microfluidic patterns printed using a desktop digital ink jet printer on filter paper according to the second embodiment of the invention.

          Figure 10 shows the benching and folding resistance of the microfluidic patterns printed according to the second embodiment of the invention; and

30           Figures 11 and 12 show the pattern of a microfluidic channel and an immunohistochemical staining enzyme printed according to the second embodiment of the invention.

**DETAILED DESCRIPTION OF THE INVENTION**

The invention will now be described with reference to the following Examples describing different possible utilisations of the present invention. It is  
5 however to be appreciated that the invention is not restricted to these examples.

Example 1

In one embodiment of the invention as shown in Figure 1, a filter paper was hydrophobized by immersion in a solution of AKD dissolved in heptane and the solvent was allowed to evaporate. A heat treatment of the treated paper in an  
10 oven at 100°C for 30 - 50 minutes was applied. In the second step, a solid mask was applied to the paper substrate and the system was exposed to a plasma reactor (K1050X plasma asher (Quorum Emitech, UK) for 10-100 seconds at the intensity of 12 - 50 W). The plasma treatment left no visible mark on the sample and the sample retained its original softness and flexibility. The treated channel  
15 becomes wettable by aqueous solutions and allows the capillary transport of the solutions. The width of the channel can be well controlled. Figure 1 shows a single channel treated with a mask of 1 mm in width on filter paper, and shows the channel before and after wetting by water.

The treated channel can have any geometrical pattern as shown in Figure  
20 2. First, a pattern includes a sample dosing zone (A) and one or multiple channels that lead to detection or reaction wells (B). Second, a pattern includes one or multiple sample dosing zones that are connected to one or multiple detection or reaction wells. In this example, a pattern of one sample dosing zone connected to multiple detection/reaction zones via capillary channels was created  
25 by plasma treatment.

A few drops of water were added to the sample dosing zone and the water was rapidly and accurately delivered to all detection/reaction wells where indicators were to be added as shown in Figure 2.

Example 2

30 In a second embodiment of the invention as shown in Figure 3, micro-channels were formed onto composites cellulosic materials. A two-ply Kleenex

mainline facial tissue was treated similarly to example 1. Figure 3 represents the liquid filled micro-channels on Kleenex two-ply tissue.

Example 3

5 In a third embodiment of the invention as shown in Figure 4, micro-channels were formed onto a layered and molded paper basesheet. A three-layer molded paper towel (Kimberly-Clark Viva) was treated similarly to example 1. Figure 4 represents the liquid filled micro-channels on three-layer Kimberly-Clark Viva towel.

Example 4

10 In the fourth embodiment of the invention as shown in Figure 5, micro-channels were created on non-woven materials containing nano- and micro-fillers. Reflex copy paper (80 gsm) contains 15% calcium carbonate fillers of the particle size typically 1 – 2  $\mu\text{m}$ . Reflex copy paper is sized and does not require hydrophobic treatment. A plasma treatment created the micro-channel pattern on  
15 to the copy paper as shown in Figure 5.

Example 5

In the fourth embodiment of the invention as shown in Figure 6, micro-channels were created on non-woven materials containing nano- and micro-fillers, lignocellulosic fibres and recycled paper fibres. Norstar newsprint paper  
20 (55 gsm) contains >50% recycle fibres, lignocellulosic fibres, calcium carbonate and clay fillers of the particle size typically 1 -2  $\mu\text{m}$ . A plasma treatment created the micro-channel pattern on the Norstar newsprinting paper.

The remaining examples illustrate a second embodiment of the present invention that utilises ink jet printing technology to define the microfluidic  
25 channels.

Example 6

Alkenyl ketene dimer (liquid AKD) was used to formulate printing fluids which were solvent-based and water-based. Any method known in the art can be selected to hydrophobize the surface/substrate. An embodiment of the invention  
30 consists of absorbing or adsorbing a solution of hydrophobic substance dissolved

in a volatile solvent or suspended in emulsion form. Hydrophobic substances include, but are not restricted to, AKD, ASA, rosin, latex, silicones, fluorochemicals, polyolefin emulsions, resin and fatty acids, natural and synthetic waxes and any hydrophobic substance known in the art. Solvent-based printing fluids were formulated using solvents in which AKD can dissolve. These typically include, but are not restricted to, chloroform, dichloromethane, toluene, hexane, heptane and their mixtures. A solvent soluble dye can also be added into the printing fluid if visibility of the printed pattern is required. Water-based printing fluid can be formulated using one or a mixture of polar solvents and water. These include, but are not restricted to, acetone, alcohols and esters. AKD can be first dissolved into polar solvent or their mixture and then mix with water. The concentration of hydrophobic agents in printing fluids was 2% - 8% v/v.

In this example digital ink jet printing method was used to print the printing fluids on paper. Microfluidic patterns were printed on Whatman #4 filter paper. Printing fluids show good penetration into the paper sheets and dry quickly. The printed patterns were subjected to a high temperature treatment to cure AKD so that it reacts with cellulose and develops strong hydrophobicity.

Figure 7 shows a printed microfluidic patterns in which liquid penetration channels are confined by the printed hydrophobic areas.

#### 20 Example 7

In this example as shown in Figures 8 and 9, the applicants show the use of printing method to fabricate microfluidic systems in a continuous manner, massive quantity, on-demand variation of patterns and very low cost.

Figure 8 shows different microfluidic patterns printed using a desktop digital ink jet printer on a large filter paper sheet. Ink jet printing can print on A4 sheets in a continuous manner.

Figure 8 and Figure 9 show different microfluidic patterns can be designed and form the page-data. Digital ink jet printing can print different patterns in any desirable sequence and in any quantity required.

#### 30 Example 8

In this example as shown in Figure 10, the applicants show that the microfluidic devices fabricated by printing of hydrophobization agents on paper

are able to retain the flexibility of the papersheet and overcome the problem associated with an early design by Martinez et al. (Angew. Chem. Int. Ed. 46 (2007) 1318 -1320).

Figure 10 shows the bending and folding resistance of the printed microfluidic patterns. A printed paper microfluidic pattern was crumbled, but it still functioned well after the paper was opened up.

#### Example 9

The applicants show in Figures 11 and 12 that printing methods can be used to fabricate devices for biomedical tests. The unique advantage of printing methods is that they can transfer several fluids onto paper or other non-woven materials to form a pattern consisting of a microfluidic system and biomedical/chemical agents for testing purposes. Modern printing methods are capable of providing accurate registration for biomedical/chemical agents to be printed inside the microfluidic systems for the designed purposes. Therefore modern printing processes can fabricate devices consisting of microfluidic channels and biomedical/chemical detection mechanisms in a single process.

Figure 11 shows the pattern of a microfluidic channel in which an immunohistochemical staining enzyme (horseradish peroxidase) was then printed. After a colour substrate (3,3'-diaminobenzidine tetrahydrochloride) was introduced into the microfluidic system via the central sample dosing site, it penetrated into channels. A colour change was obtained which confirmed that printed immunohistochemical staining enzyme was active after printing. Figure 12 shows the colour change after the microfluidic system was allowed to dry.

25

CLAIMS:

1. A method of fabricating a microfluidic system having microfluidic channels on a surface of a hydrophilic substrate, the method including the steps of:  
hydrophobizing the substrate surface;
- 5 locating a mask defining the substrate surface, the mask having open areas defining the periphery of the microfluidic channels; and  
applying an irradiation treatment to areas of the substrate surface exposed by the open areas of the mask, said exposed areas becoming hydrophilic to therefore form said microfluidic channels.
- 10 2. A method according to claim 1, wherein the hydrophilic substrate is formed of cellulosic material including paper, woven and non-woven materials.
3. A method according to claim 1 or 2, wherein the surface is hydrophobized using a solution including a hydrophobic substance dissolved in a volatile solvent, the hydrophobic substance being selected from an alkyl ketene dimer (AKD),
- 15 alkenyl succinic anhydride (ASA), rosin, latex, silicones, fluorchemicals, polyolefin emulsions, resin and fatty acids, natural and synthetic waxes.
4. A method according to any one of the preceding claims wherein the irradiation treatment includes plasma and corona treatments.
5. A microfluidic system fabricated by the method as claimed in any one of
- 20 the preceding claims.
6. A method of fabricating a microfluidic system having microfluidic channels on a surface of a hydrophilic substrate, the method including the step of printing a hydrophilic agent on the substrate surface to define a peripheral edge of the microfluidic channels.
- 25 7. A method according to claim 6 wherein the hydrophobic agent is a hydrophobic molecule, oligomer or polymer dissolved in a solvent.

8. A method according to claim 6 wherein the hydrophobic agent is a hydrophobic molecule, oligomer or polymer emulsified or in suspension in water, forming a water based ink.

9. A method according to claim 6 wherein the hydrophobic agent is an internal size (liquid AKD, ASA, rosin, silicone, fluorochemicals, polyolefin emulsions, resin and fatty acid, natural and synthetic waxes and the like) or a surface sizing material (Styrene maleic anhydride (SMA), latex).

10. A method according to claim 6 further including an activation step following printing to activate the hydrophobic agent, including the development of covalent bond with the substrate.

11. A method according to claim 10 wherein the activation step includes aging, heat treatment or radiation.

12. A method according to any one of claims 6 to 11, wherein the hydrophilic substrate is formed of cellulosic material including paper, woven and non-woven materials.

13. A microfluidic system fabricated by the method as claimed in any one of claims 6 to 12.

ABSTRACT

A method of fabricating a microfluidic system having microfluidic channels on a surface of a hydrophilic substrate, the method including the steps of:

- hydrophobizing the substrate surface;
- locating a mask defining the substrate surface, the mask having open areas defining the periphery of the microfluidic channels; and
- applying an irradiation treatment to areas of the substrate surface exposed by the open areas of the mask, said exposed areas becoming hydrophilic to therefore form said microfluidic channels.

1/6

Figure 1

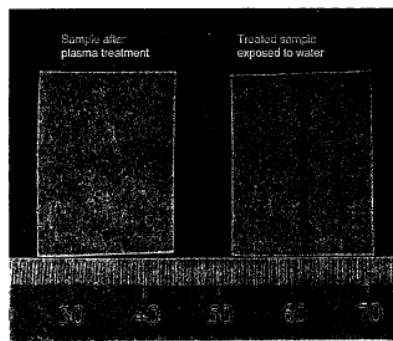


Figure 2

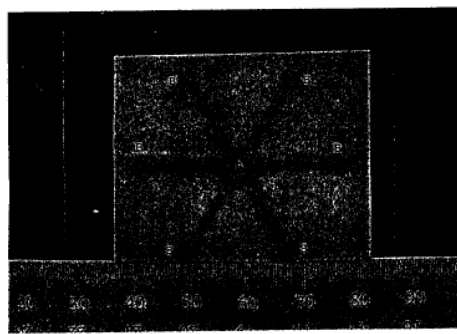


Figure 3

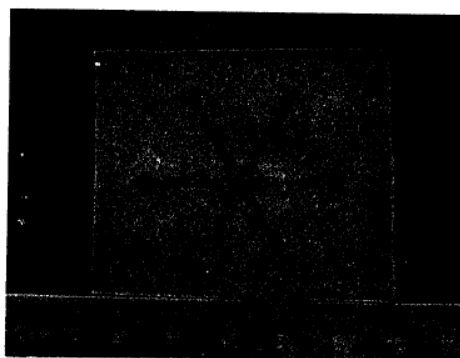
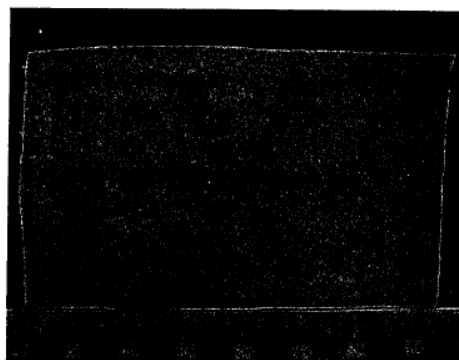


Figure 4



3/6

Figure 5

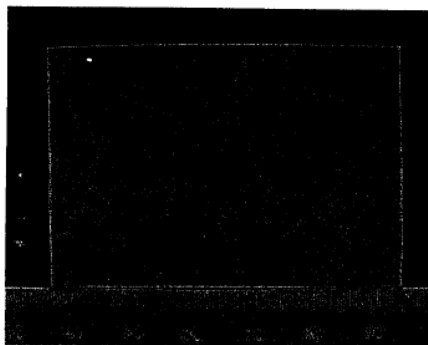
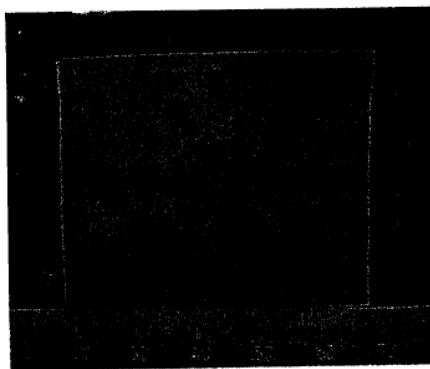


Figure 6



4/6

Figure 7

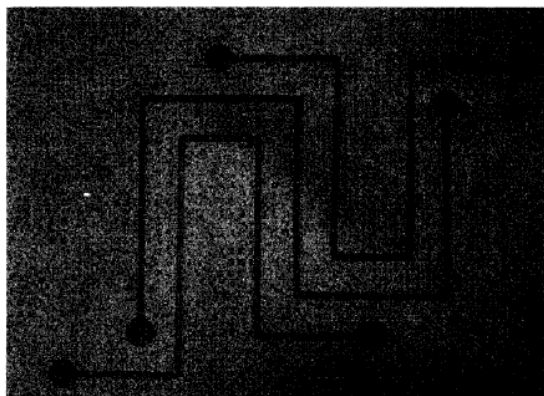


Figure 8

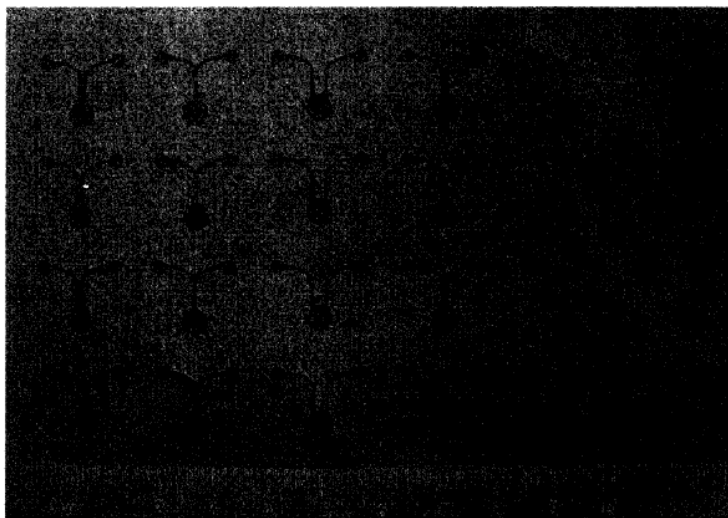


Figure 9



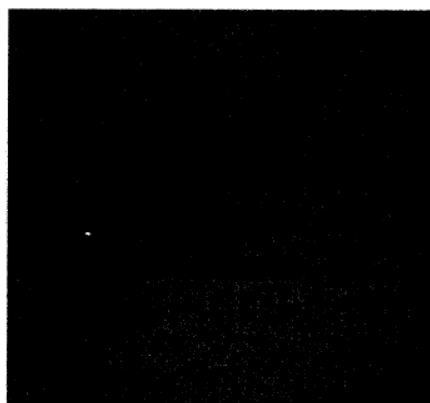
Figure 10



Figure 11



Figure 12



This page is intentionally blank

---

# Appendix D

---

Awards

---

**Award:**

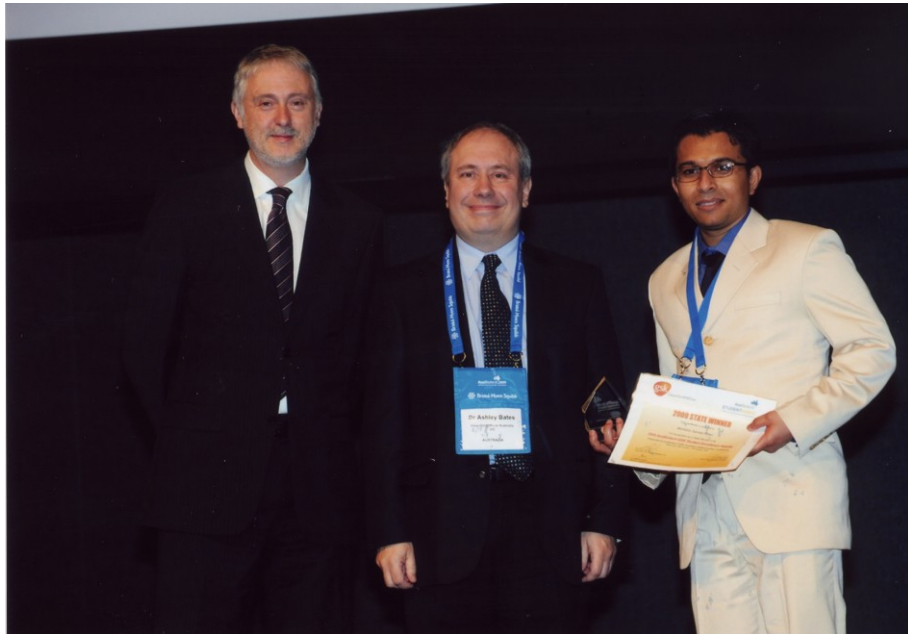
State Winner (VIC) in the AusBiotech-GSK Student Excellence Awards 2009.

**Organisers/Sponsors:**

Australian Biotechnology Organisation (AusBiotech Ltd.) and GlaxosmithKline (GSK). AusBiotech Ltd. is the national body of the biotechnology and life science industry in Australia.

**Award Objective:**

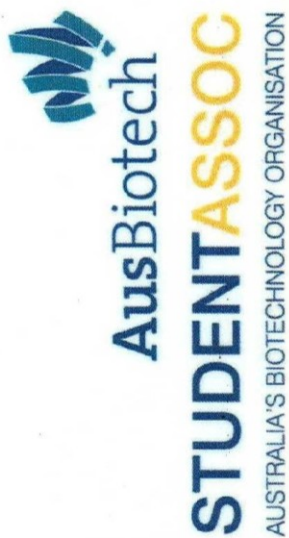
AusBiotech-GSK Student Excellence Award is a national award program aims to encourage and recognize Australia's promising student life-scientists and bio-entrepreneurs. This award supports the innovation work that will be the basis of Australia's biotechnology industry in the future.



Award presentation; from left, the Hon. *Gavin Jennings* MLC, Minister for Environment, Climate Change and Innovation; *Dr. Ashley Bates*, Head, Discovery Research, GlaxoSmithKline and *Mohidus Samad Khan*.



State winners with the organizer; from left, *Colin William Bignell* (Tasmania), *Matthew Cook* (Queensland), *Lidia Matestic* (New South Wales), *Dr. Anna Lavelle* (CEO, AusBiotech), *Mohidus Samad Khan* (VIC) and *Tony Carlisle* (South Australia).



# 2009 STATE WINNER

This certificate is awarded to

**Mohidus Samad Khan**

For recognition as a State Winner in the

## 2009 AusBiotech-GSK Student Excellence Awards

Presented at AusBiotech 2009, Australia's Biotechnology Conference  
Melbourne, 26th October – 30<sup>th</sup> October 2009

Dr Anna Lavelle,  
Chief Executive Officer, AusBiotech Ltd

Dr Ashley Bates,  
Head of R&D Alliances Australia/NZ,  
GlaxoSmithKline Australia

Dr Olgatina Bushi,  
National AusBiotech Student Association Coordinator



This page is intentionally blank

---

# Appendix E

---

Enzymatic Papers: Effect  
of Paper Structure and  
Composition

---

This page is intentionally blank

**Monash University**

**Declaration for Thesis Appendix E**

**Declaration by candidate**

In the case of Appendix E, the nature and extent of my contribution to the work was the following:

Nature of contribution	Extent of contribution (%)
Initiation, key ideas, experimental and analysis works, development and writing up of the paper	70

The following co-authors contributed to the work. Co-authors who are students at Monash University must also indicate the extent of their contribution in percentage terms:

Name	Nature of contribution	Extent of contribution (%) for student co-authors only
Gil Garnier	Initiation, key ideas, reviewing and editing of the paper	Supervisor
Sharon B. M. Haniffa	Initiation and experimental work	10
Alison Slater	Initiation and experimental work	10

Candidate's  
Signature

	Date <i>17/12/09</i>
--	-------------------------

**Declaration by co-authors**

The undersigned hereby certify that:

- (1) the above declaration correctly reflects the nature and extent of the candidate's contribution to this work, and the nature of the contribution of each of the co-authors.
- (2) they meet the criteria for authorship in that they have participated in the conception, execution, or interpretation, of at least that part of the publication in their field of expertise;
- (3) they take public responsibility for their part of the publication, except for the responsible author who accepts overall responsibility for the publication;
- (4) there are no other authors of the publication according to these criteria;
- (5) potential conflicts of interest have been disclosed to (a) granting bodies, (b) the editor or publisher of journals or other publications, and (c) the head of the responsible academic unit; and
- (6) the original data are stored at the following location(s) and will be held for at least five years from the date indicated below:

**Location(s)**

Bioresource Processing Research Institute of Australia (BioPRIA), Department of Chemical Engineering, Monash University, Clayton, VIC 3800, Australia.
--

**Signature 1**

	Date <i>22/12/09</i>
--	-------------------------

**Signature 2**

	Date
--	------

**Signature 3**

	Date
--	------

*Undergraduate student*  
*11 11 }*

# Enzymatic Papers: Effect of Paper Structure and Composition

Mohidus Samad Khan, Alison Slater, Sharon B. M. Haniffa and Gil Garnier\*

Bioresource Processing Research Institute of Australia (BioPRIA),  
Department of Chemical Engineering,  
Monash University, Clayton, VIC 3800, Australia.

\*Corresponding author: Gil.Garnier@eng.monash.edu.au

Appendix E	A71
Enzymatic Papers: Effect of Paper Structure and Composition	A71
1. Introduction	A74
2. Experimentals	A76
2.1. Materials	A76
2.2. Methods	A76
3. Results	A79
3.1. Paper Composition	A79
3.2. Enzymes Adsorption	A80
3.3. Thermal Stability and Aging of Enzymatic Papers	A81
4. Discussion	A86
6. Conclusion	A87
Acknowledgment	A88
References	A89

## 1. INTRODUCTION

Bioactive paper is an emerging technology offering many new applications in biotechnology, health and environmental which have been restricted by the high cost and the limited availability of tests (1-5). Paper is highly wettable when untreated, easy to functionalise, biodegradable, sterilisable, biocompatible and cheap. It has long being used for analysis in chromatography (6). Paper can easily be engineered for new applications. Thin coatings of polymers and inorganics can be achieved through conventional wet-end addition and by surface treatments such as surface sizing and coating (3). Paper is a natural material of choice for the production of disposable bioassay and micro-fluidic devices. However, the biotechnology industry has a limited understanding of the effect of paper structure and chemical composition on the transport of fluids.

Paper allows, through capillarity, the controlled transport of liquids and offers a substrate to retain biomolecules. This has led to microfluidic bioactive papers pioneered by Whitesides and further refined by other groups (1-2, 7-8). Pelton recently presented two critical reviews of bioactive paper (9-10).

Filter paper has been the substrate of choice for most bioactive and microfluidic paper research and development. This is in part because of convenience, wide availability, high absorbance, high purity and standard properties of filter paper, but also in part by lack of understanding of the paper technology. However, from a material perspective, filter paper is an archaic material with the most basic structure and chemistry; it is also relatively expensive. There is little knowledge available on the effect of paper structure and composition on the bioactive performance or on the ideal properties of paper as a substrate for biological applications. The current paper technology can enable the large scale and low cost manufacturing of very advanced materials. Fiber orientation can be engineered in 3 dimensions. While fibers are currently layered mostly in parallel x-y planes (9), their composition and orientation can be designed. To control fibers distribution in the z direction, pulp fibers can be layered into a sheet with a multi-section headbox; three layers are usual in the tissue industry. An alternative process, common for linerboard production, is to press two or more wet-lies together prior to pressing. Fibers orientation in the x-y plane- or in the MD-CD directions- is affected by the jet to wire velocity difference, with rushing ( $V_{jet} > V_{wire}$ ) and dragging ( $V_{jet} < V_{wire}$ ) producing preferential fiber alignment in the CD and MD direction, respectively. Paper can benefit from surface treatments creating concentration gradients- or interphases – of organic or inorganic materials that can be beneficial to biological applications.

The product life time is a critical requirement of bioactive papers as they must sustain the often harsh conditions of shipping and provide a reasonable shelf-life. Immobilizing enzyme on paper by simple physisorption was shown to decrease the enzyme reaction rate by two to three orders of magnitude (11), but also to increase its thermal resistance and aging performance by two to three orders of magnitude (5). It is of interest to investigate whether paper chemistry, such as filler, lignin, and sizing, affect enzyme activity or aging of enzymatic papers.

The aim of this study is to analyze the effect of paper structure and composition on the activity, stability and aging of enzymes immobilized on different types of paper. A secondary objective is to define the requirements of the ideal substrate for bioactive

paper. The bioactive performance of a newsprint and a fine paper were compared to Whatman #4 filter paper. An enzyme, alkaline phosphatase was chosen as model biomolecule. The enzymatic activity on paper was measured by quantifying the intensity of the enzyme-substrate colour product by image analysis. Paper samples were immersed into an excess solution of enzyme. The enzymatic papers were aged at different temperatures for different periods, and their relative enzymatic activities were measured by depositing an excess of liquid substrate system, allowing the reaction to proceed to completion, and measuring the resulting product concentration. Thermal treatment was designed to accelerate the aging of enzymatic papers.

## **2. EXPERIMENTALS**

### **2.1. Materials**

Alkaline phosphatase (ALP) from bovine intestinal mucosa, was purchased from Aldrich and used as received. ALP was dissolved to a concentration of 0.5 mg/mL in 1 M diethanolamine buffer with 0.50 mM magnesium chloride and 5 M HCl to maintain pH at 9.7. Water (Millipore, 18M $\Omega$ ) was used for making all dilutions. The 5-bromo-4-chloro-3-indolyl phosphate/nitroblue tetrazolium (BCIP/NBT) liquid substrate system, purchased from Aldrich, was selected to quantify the enzymatic activity of ALP on paper. The biochemical reaction of ALP with BCIP/NBT results in a blue-purple complex; its intense colour can be observed visually, is very stable and does not fade upon exposure to light [24].

Whatman #4 filter paper (England, 96 g/m<sup>2</sup>), newsprint (Nornews, Norske Skog, Boyer, Australia; 48.8 g/m<sup>2</sup>) and Reflex copy paper (Australian Paper, Maryvale, Australia, 80 g/m<sup>2</sup>) were chosen as substrate to immobilize the biomolecules.

### **2.2. Methods**

#### **2.2.1. Enzyme on Paper**

Enzyme aqueous solutions were applied onto paper following TAPPI (T 205 sp-95) standard. Paper samples (d = 16 cm) were immersed into the ALP enzymatic solution contained in a large Petri-dish (Figure 1). The well-soaked paper samples were then blotted using standard blotting papers (Drink Coster Blotting, 280 GSM) to remove any extra solution. A polyethylene sheet (3M, PP2500, d = 16 cm) was deposited

underneath each blotted sample. Paper and polyethylene sheet were placed into a drying ring. The paper samples were kept horizontal while being removed from the stock solutions and placed into drying ring to ensure a uniform enzyme concentration on paper. The samples were left to dry in a dark chamber at 23°C and 50% relative humidity (RH), for 24 hours. The enzymatic paper samples were then used for further deactivation experiment and this time was defined as  $t = 0$ . Analyses of the surface profiles and histogram distribution of gray values are described elsewhere (5).

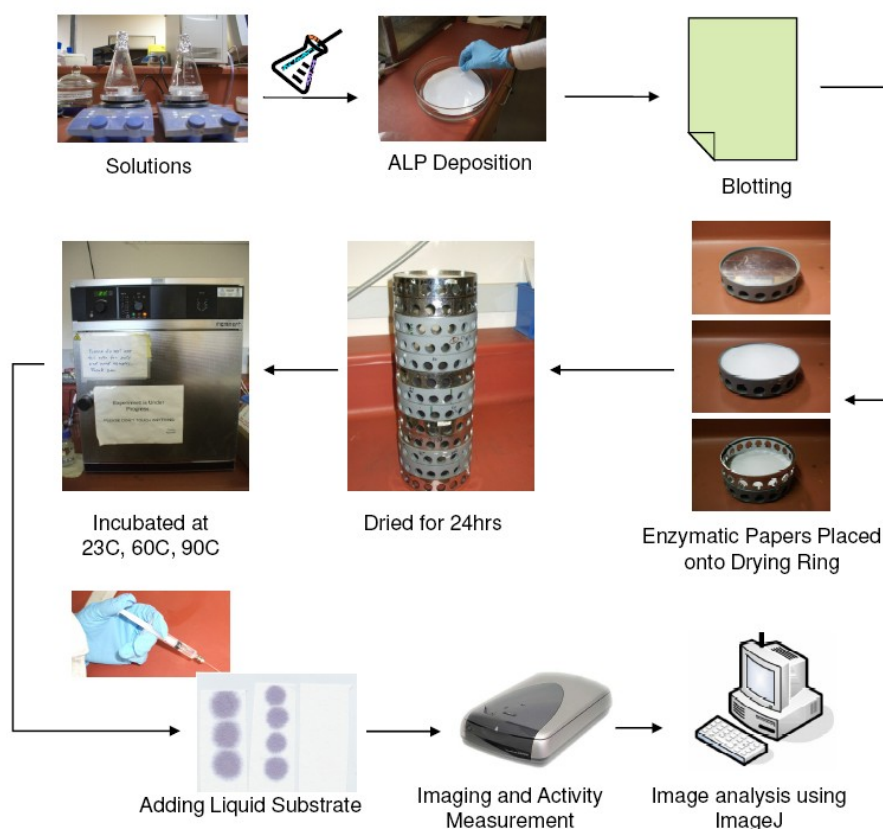


**Figure 1:** Experimental system to prepare ALP enzymatic papers.

### 2.2.2. Thermal Stability of Enzymatic Papers

The enzymatic papers were cut into small samples (6 cm × 2 cm) and aged at different temperatures. The ALP enzymatic paper samples were treated at 23°C, 60°C or 90°C for various periods. For 23°C, the samples were treated in a temperature and humidity controlled lab (23°C and 50% RH). Two ovens (Memmert Universal Oven, Schwabach, Germany) were used to treat samples at 60°C and 90°C. A digital humidity and temperature indicator (VAISALA Humidity and Temperature Indicator, Finland;

operating range: -20°C to +60°C) were used to measure the relative humidity (RH) in the ovens. At 60°C, the RH was in range of 6.5-7.0%. For the second oven, the limiting RH reading was 5-5.5% for 65°C, which indicates even dryer conditions at 90°C.

After the aging treatment, the liquid substrate was applied onto the enzymatic papers. This was done as follow: small droplets of fresh liquid substrates were applied onto the aged enzymatic papers using a 1.0 mL syringe equipped with a stainless steel flat-tipped needle (0.21 mm outer diameter). The enzyme-substrate (E-S) reaction was allowed to proceed in a dark chamber for half an hour at standard condition, 23°C and 50% RH; this insures complete enzymatic reaction (5, 11). From the colour intensity of enzyme-substrate reaction, the relative activity of the enzymatic paper was measured. Each measurement reported results from the average of 6 to 8 full replicates.

### 2.2.3. Activity Measurement:

The colour resulting from the E-S reaction on enzymatic papers was measured at 1200 dpi using a standard scanner (EPSON PERFECTION 2450 PHOTO) (Figure 1). The scanned images were analyzed using ImageJ software (ImageJ 1.41o). ImageJ calculates the gray values of RGB (red-green-blue) images. For any selected area, the ImageJ software calculates the weighted average gray value within the selection, which can be related to the activity of enzymatic paper. From the gray value analysis, the relative activity of enzymatic papers was measured as described elsewhere (5, 11). Activity corresponding to the gray value at  $t = 0$  hr was considered as 100%. The relative activity at different time intervals was measured and normalized by the activity at  $t = 0$  hr, i.e. relative activity,  $[Ea]_t/[Ea]_0 = I/I_0$ . The colour intensity increases with enzyme concentration on paper is described elsewhere (5).

### 3. RESULTS

#### 3.1. Paper Composition

The activity of a model enzyme, alkaline phosphatase (ALP), on three commercial papers varying in structure and composition was investigated. A high grade newsprint was first investigated (Nornews). Mostly made of mechanical (65%+), recycled (10-30%) and sometimes high yield chemical pulp (up to 25%), newsprint is the cheapest grade of paper thanks to its low basis weight (40-50 g/m<sup>2</sup>) and inexpensive fibers. The newsprint chemical composition is close to that of wood, which raises issues on the effect lignin, a network polymer of propyl phenol, might have on enzyme activity. Newsprint is often self-sized from the redistribution of its natural resin and fatty acids (wood extractive) on the fibers. The second model paper was a fine paper (Reflex) selected because of its exceptional print quality and permanence. High printing resolution is critical to achieve fine patterns of biomolecules and optimize micro-fluidic systems. Made exclusively from chemical pulp fibers, fine paper is almost pure cellulose fibers which are partially covered with inorganic filler (10-20% precipitated calcium carbonate) and hydrophobic colloids (internal and surface size). Fine paper is an ideal substrate to test the effect of hydrophobicity and inorganics (PCC) on enzyme activity. Last is the high basis weight and high absorbency Whatman filter paper made from cotton linters randomly oriented.

Table I shows the paper basis weight, pulp composition and water droplet adsorption time on the different papers. The 3 papers widely vary in structure, basis weight, chemical composition and absorption.

**Table I: Paper characteristics and composition**

	Filter paper	Newsprint paper	Reflex paper
Basis weight (g/m <sup>2</sup> )	96	48.8	80
Pulp composition	Cotton lint	Eucalypt cold caustic soda (26%), thermal mechanical pulp (pine) (64%), recycle fibre (10%)	Bleached eucalypt pulp (80%), bleached pine pulp (20%)
Wet end additives	Wet strength	Retention aid brighteners	Internal sizing, surface sizing, PCC fillers, retention aid, dyes, brighteners
Paper sizing: Droplet adsorption time	2-3sec	25-27sec	30-35min

### **3.2. Enzymes Adsorption**

ALP was adsorbed by immersing papers in an excess of ALP enzymatic solution. The extra enzymatic solution was removed using standard blotting paper. After the papers were dried ( $t = 0\text{hr}$ ) and aged, the liquid substrate for the enzyme was deposited on the various enzymatic papers and the product colour intensity was quantified by image analysis. Paper samples with and without enzyme are illustrated on Figure 2. Enzyme immobilization on filter paper and Reflex paper did not add any extra colour contribution. However, newsprint turned yellow after been soaked into the enzymatic solution and dried (Figure 2b). The higher colour intensity observed for enzymatic Reflex paper indicated a higher product concentration caused by a higher initial enzyme density on paper (Figure 2c). The enzyme-substrate product colour intensity was the lowest for the enzymatic newsprint paper (Figure 2c).

The colour pattern revealing product formation from the droplet of substrate/dye reacting with the enzyme on paper varied among papers. On filter paper, the pattern was big and perfectly circular with diffuse boundaries. On newsprint, the pattern tends to be elliptic with numerous fiber wicking/featuring. For fine paper, the product pattern was small, circular, of intense colour with a few important feather defects and very sharp boundaries.

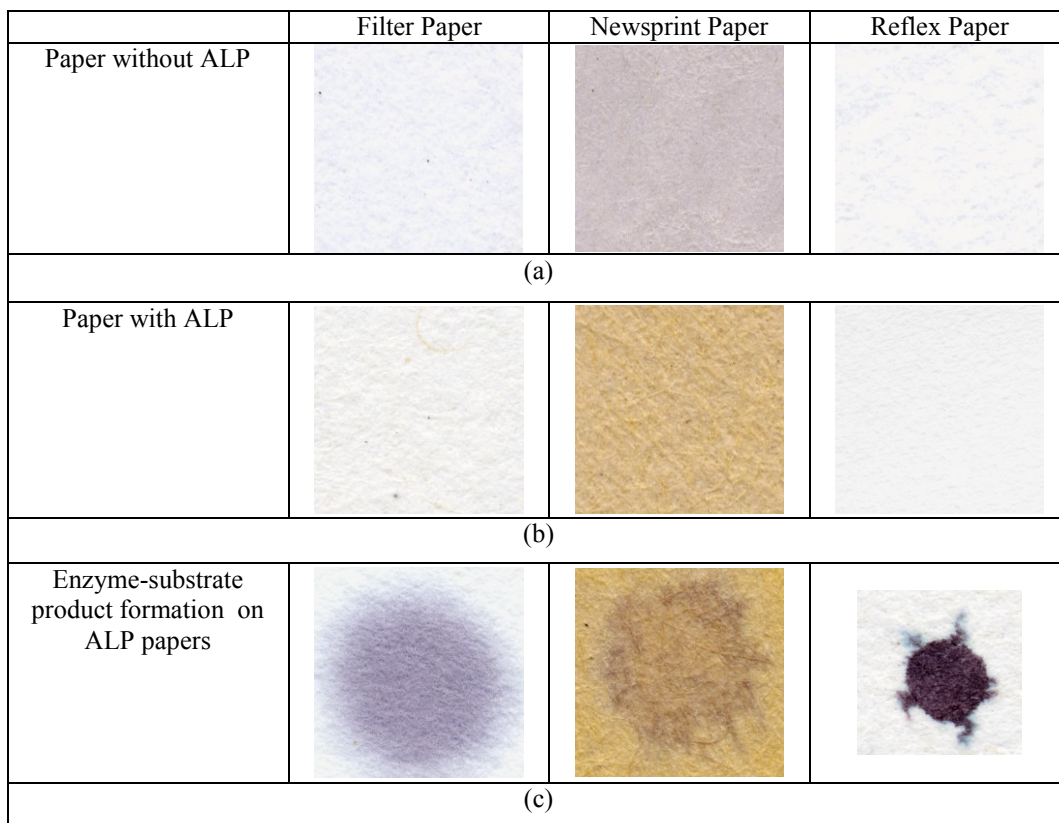


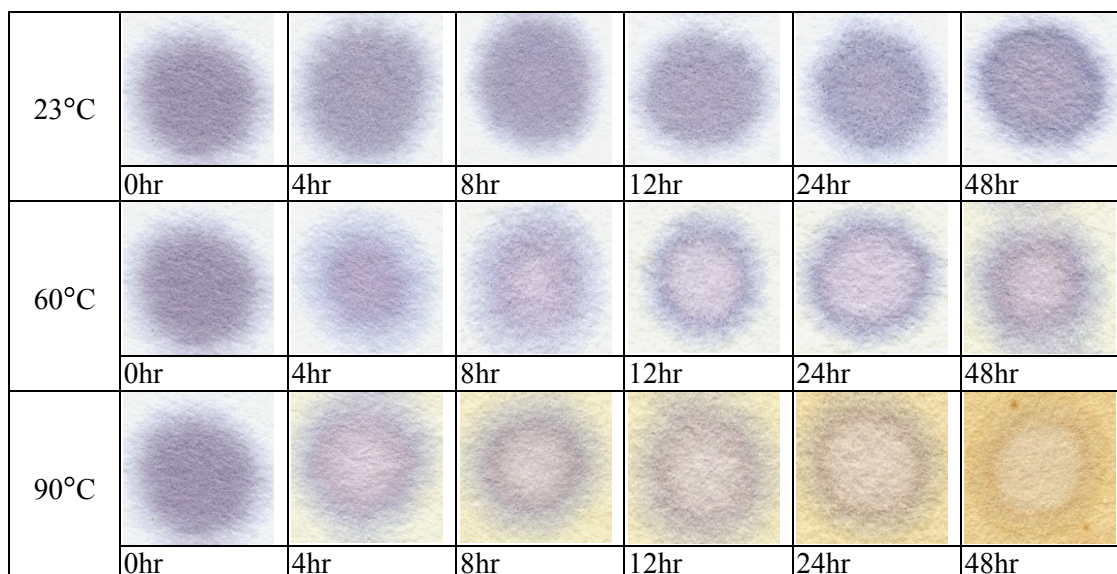
**Figure 2:** ALP enzymatic papers; 23°C, t = 0hr. (a) Paper without ALP, (b) ALP active papers, (c) enzyme-substrate product formation on enzymatic paper samples; The blue purple colour reveals the enzyme (ALP) - substrates (BCIP/NBT) reaction.

### 3.3. Thermal Stability and Aging of Enzymatic Papers

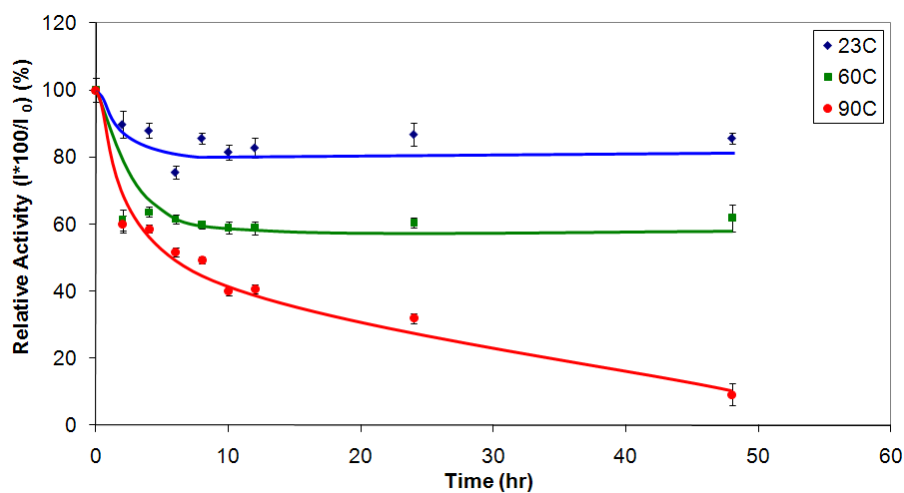
Samples of the enzymatic paper were aged at 23°C, 60°C and 90°C, respectively, for various periods. This was to accelerate aging. After applying the liquid substrate to the aged enzymatic paper and letting the E-S reaction proceed to completion, the paper samples were scanned. The relative activities of the enzymatic filter and newsprint papers were calculated from the weighted mean gray value of the images. The relative activity is defined as the ratio of the enzyme product generated on paper aged ( t hours at a temperature T) normalised by the product concentration generated on the initial paper before any aging treatment; it allows to compare the activity of paper having different initial concentration of enzyme.

Figure 3 shows typical images of enzymatic filter papers heated at 23°C, 60°C and 90°C for periods of up to 48 hrs. The product colour intensity decreased with the

aging enzymatic paper at different temperatures. Paper yellowing became visible for enzymatic filter papers treated at the higher temperature and longer periods ( $\geq 4$  hr) catalyzed by the alkaline enzyme buffer (pH 9.7).



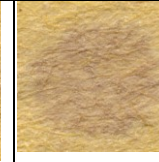
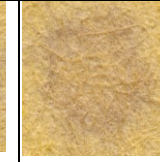
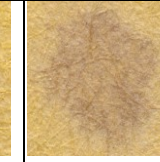
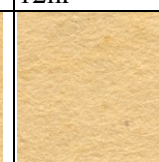
**Figure 3:** Aging of enzymatic filter paper treated at 23°C, 60°C and 90°C for various periods. The blue purple colour reveals the enzyme (ALP) - substrates (BCIP/NBT) reaction.



**Figure 4:** Relative activity of enzymatic filter papers at 23°C, 60°C and 90°C for various periods.

The effect of aging temperature and time on the relative activity of enzymatic filter papers is illustrated in Figure 4. The thermal deactivation rate of enzymatic filter papers was faster in the early hours of thermal treatment at high temperature (90°C) and then gradually decreased at a slower rate. At 23°C the enzymatic filter papers retained most of their activity and exhibited only a moderate loss of activity when exposed at 60°C.

Figure 5 shows images of enzyme active newsprint treated at different temperatures for periods up to 52 hrs. Initially (t = 0), the E-S product colour intensity on enzymatic newsprint paper was moderate; it decreased with aging treatment at 23°C and 60°C. At higher temperature (90°C) the activity of enzymatic newsprint paper dropped to zero within 4 hrs (Figure 5).

23°C						
	0hr	4hr	9hr	12hr	24hr	52hr
60°C						
	0hr	4hr	9hr	12hr	24hr	52hr
90°C						
	0hr	4hr	9hr	12hr	24hr	52hr

**Figure 5:** Aging of enzymatic newsprint paper treated at 23°C, 60°C and 90°C for various periods. The blue purple colour reveals the enzyme (ALP) - substrates (BCIP/NBT) reaction.

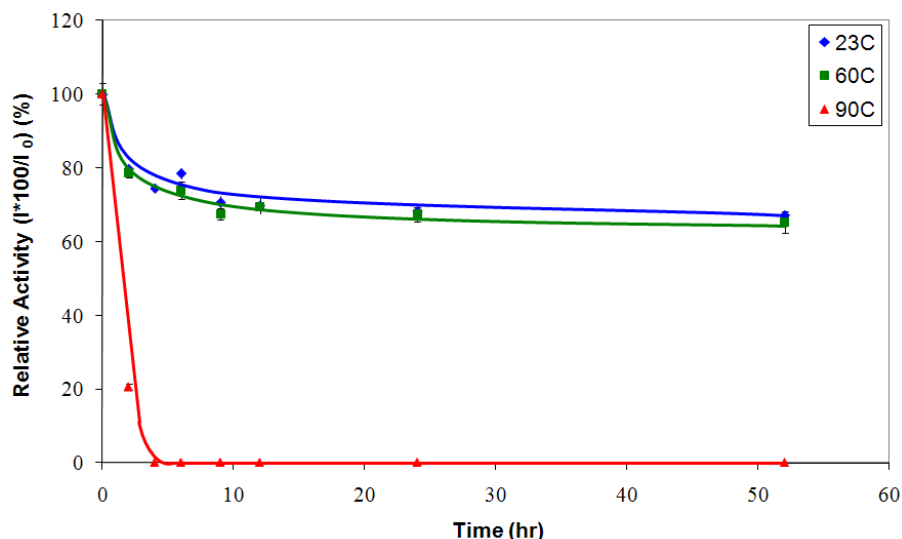
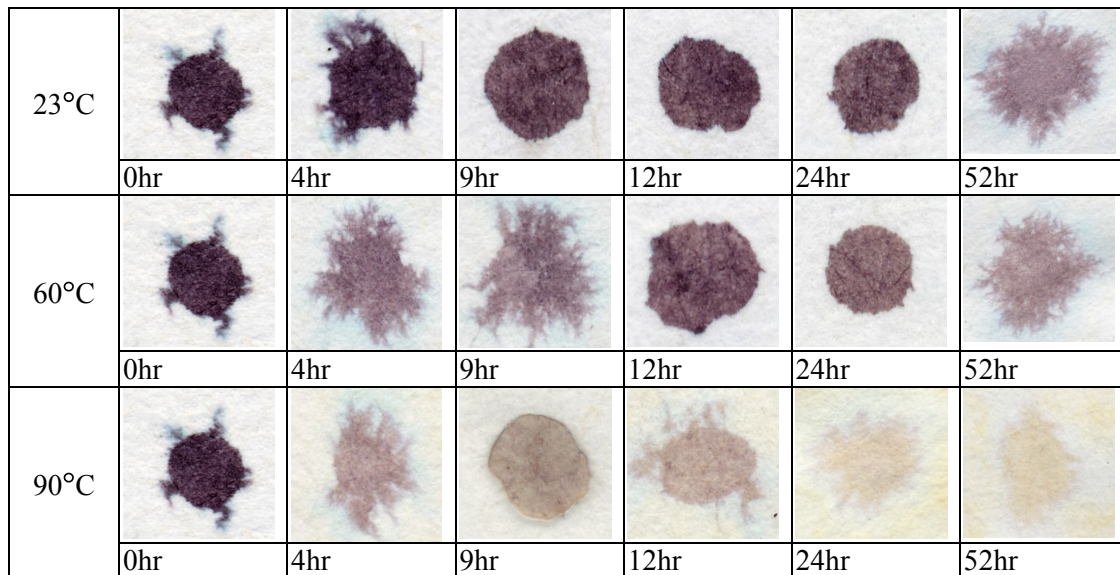


**Figure 6: Relative activity of enzymatic newsprint papers at 23°C, 60°C and 90°C for various periods.**

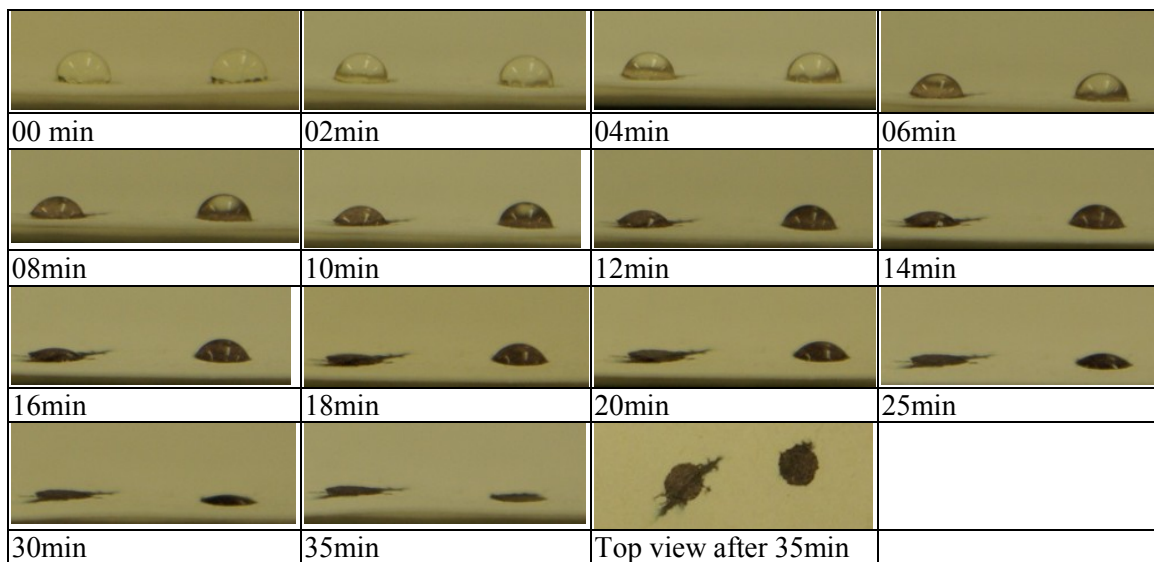
The relative activities of enzymatic newsprint papers at different aging conditions are illustrated in Figure 6. At 23°C and 60°C, the thermal deactivation rates reduced moderately and then gradually decreased at a slower rate. At 90°C the enzymatic activity sharply reduced to zero within four hours (Figure 6).

Figure 7 presents images of E-S product formation on enzymatic Reflex paper aged at 23°C, 60°C and 90°C for various periods. The product colour intensity initially very intense ( $t = 0$  hr), because of a high initial surface density of product/enzyme, moderately reduced when heated at 23°C or 60°C. At higher temperatures (90°C) the product colour intensity reduced significantly with time (Figure 7). The spreading and adsorption of the liquid substrate on the enzymatic Reflex paper was uneven and irregular; this affected the image analysis technique and the relative activity measurement. The liquid wicking and the E-S product formation on the enzymatic Reflex paper varied randomly and formed circular shape spot on the paper or wicked along the paper fibres (Figure 7). At high temperature treatment (90°C) for the longer periods ( $\geq 4$  hr), some paper yellowing became visible. Figure 8 illustrates the liquid substrate spreading and adsorption onto enzymatic Reflex paper. Liquid adsorption on the hydrophobic surface of the enzymatic Reflex paper was very slow (30-35min) (Table I, Figure 8) and the liquid spreading/wicking area on paper was limited. While dispensing on the hydrophobic surface of enzymatic Reflex paper, the substrate droplet

sat on the surface and slowly reacted with the immobilized enzymes. The product from enzymatic reaction created a puddle on paper which either stayed within the droplet radius or wicked along some fibres or paper defects (Figure 8).



**Figure 7:** Aging of enzymatic newsprint paper treated at 23°C, 60°C and 90°C for various periods. The blue purple colour reveals the enzyme (ALP) - substrates (BCIP/NBT) reaction.



**Figure 8:** BCIP/NBT drop spreading and adsorption on enzymatic Reflex paper. The blue purple colour reveals the enzyme (ALP) - substrates (BCIP/NBT) reaction.

## 4. DISCUSSION

The structure and chemical composition of the commercial papers selected varied significantly. From the structure aspect, fiber orientation increased from random to MD orientated from filter paper, fine paper and newsprint; Basis weight decreased in the same order. Filler content and hydrophobicity decreased from Reflex, to newsprint and filter paper.

Liquid adsorption controls the initial enzyme concentration in paper. The liquid fraction is affected by paper structure and chemical composition. However, no beneficial effect of PCC was observed with newsprint. Pore volume, directly linked to paper basis weight, is an important variable. A second variable is the concentration and distribution of hydrophobic sizing domains. Liquid absorption- and enzyme initial concentration-decreases from filter paper, newsprint and Reflex paper. The type of pulp had an important effect on the aging of enzymatic paper activity. The first effect was paper yellowing. Important yellowing was observed on newsprint. This was expected and results from the yellowing of lignin (12-14). Filter paper yellowed to a lesser extent for the longer aging treatments at high temperatures; this is due to cellulose degradation catalysed by high alkalinity and high temperature (13, 15). Reflex paper yellowed to a lesser extend and only under the harshest conditions (90°C, 4 h) revealing the beneficial effect of PCC.

Pulp also had an important effect on enzyme activity. Newsprint enzymatic paper, the only grade containing mechanical pulp, showed a drastic enzyme deactivation when aged at 90°C; the newsprint enzymatic paper became completely inactive after being heated 4 hours at 90°C. This was unexpected. We raise the hypothesis that this is due to some heat activated interaction with lignin. Whether this desactivation is specific to ALP, all enzymes or biomolecules in general is unknown and requires further attention. Newsprint - and therefore lignin- had no detrimental effect on ALP enzyme reactivity as enzymatic newsprint behaved similarly to the enzymatic filter paper at low temperatures (up to 60°C).

No relationship between filler content and enzyme activity was observed. Pelton et al. reported important antimicrobial activity from paper containing titanium dioxide (TiO<sub>2</sub>). Upon light exposure, TiO<sub>2</sub> produces UV by photo catalysis. While no such photo catalysis or antimicrobial activity has been reported for precipitated calcium

carbonate (PCC), it can act as buffer in paper and significantly increase the local pH. Calcium carbonate is also reported to increase the activity of some enzymes. Furthermore, PCC has a high surface area available for enzyme adsorption, therefore increasing the potential loading. PCC was expected to increase ALP activity or to prevent aging; this was not observed as the important sizing hydrophobization might have obscured the PCC effect.

Paper hydrophobicity is critical. As tested, the liquid absorption of fine paper was inefficient to absorb any significant enzyme solution in a reasonable time (less than 30 min). The important sizing contributed to feathering default as the liquid followed and penetrated paper through the few structure/sizing defects.

The current newsprint and fine paper are inadequate as substrate for enzyme, and filter paper remains the best choice commercially available. This was somewhat expected as newsprint and fine paper were optimized for contact and non-contact printing; not liquid absorption. However, the cost of filter paper remains prohibitive for most common application. Specific paper for biological support and bioactive paper need to be engineered. A first requirement is a high liquid absorption; this means no sizing and a relatively high basis weight (50-100 g/m<sup>2</sup>). A second requirement is minimal fiber orientation to allow uniform wicking in all directions and uniform liquid distribution. Precipitated calcium carbonate had no visible effect on ALP activity. Any effect of PCC might have been obscured by another dominating variable: lignin inhibition for newsprint, hydrophobicity for fine paper. However, a drastic reduction in enzyme stability was observed on newsprint enzymatic paper treated at high temperatures. This is likely due to a heat catalysed interaction between lignin and ALP enzyme. Whether this deactivation is specific to ALP enzyme, most enzymes or to biomolecules in general is unknown and requires further investigation.

## **6. CONCLUSION**

The performance of three commercial papers: a fine paper, a newsprint and a filter paper- as support for an enzyme- alkaline phosphates (ALP)- was compared. Paper samples were soaked in an excess of enzyme solution, blotted, dried and aged at different temperatures and periods. A solution containing the enzyme substrate with a selective dye was then deposited on the enzymatic papers and the colour intensity

directly proportional to the product concentration was measured by image analysis. The effect of aging on enzyme was reported in terms of relative activity.

Whatman filter paper performed best in terms of wettability, enzyme uniform absorption and enzyme thermal stability. The current newsprint and fine paper are inadequate as substrate for ALP enzymatic paper. Newsprint strongly inhibited ALP activity when aged at high temperatures (90°C); this is probably due to some heat activated interaction with lignin. However, lignin or newsprint did not desactivated ALP enzyme at low temperatures. No effect of PCC filler on enzyme aging was recorded. Fine paper was too strongly sized to allow proper enzyme absorption. The ideal substrate for bioactive paper needs to be absorbent and made of high purity cellulose to avoid any side reaction that might affect the often sensitive biomolecules. Papermaking offers tremendous potential to engineer optimized grade by controlling fiber orientation and surface composition.

## **ACKNOWLEDGMENT**

Many thanks to Dr. W. Bachelor **from** APPI for supplying the newsprint paper samples with the technical information; R. Jones (from Australian Paper) and J. Sestanovich (from GE Healthcare) for providing technical information on Reflex and filter paper composition, respectively. MSK would like to thank Monash University for postgraduate scholarships.

## REFERENCES

- (1) Martinez, A. W., Phillips, S. T., Butte, M. J., Whitesides, G. M. - Patterned Paper as a Platform for Inexpensive, Low-Volume, Portable Bioassays. *Angewandte Chemie International Edition*. **46**(8):1318-1320, 2007.
- (2) Martinez, A. W., Phillips, S. T., Carrithe, E., Thomas III, S. W., Sindi, H., Whitesides, G. M. - Simple Telemedicine for Developing Regions: Camera Phones and Paper-Based Microfluidic Devices for Real-Time, Off-Site Diagnosis. *Analytical Chemistry*. **80**(10):3699-3707, 2008.
- (3) Khan, M. S., Tian, J., Xu, L., Shen, W., Garnier, G. Bioactive Enzymatic Papers. In: l'Anson, S. J., editor. **Advances in Pulp and Paper Research, Oxford 2009**: The Pulp & Paper Fundamental Research Society. p. 1149-1166. 2009
- (4) Khan, M. S., Fon, D., Li, X., Tian, J., Forsythe, J., Garnier, G., Shen, W. - Biosurface Engineering through Ink Jet Printing. *Colloids and Surfaces B: Biointerfaces*. **75**(2):441-447, 2010.
- (5) Khan, M. S., Xu, L., Shen, W., Garnier, G. - Thermal Stability of Bioactive Enzymatic Papers. *Colloids and Surfaces B: Biointerfaces*. **75**(1):239-246, 2010.
- (6) Lepri, L., Cincinelli, A. Tlc Sorbents. In: Cazes, J., editor. **Encyclopedia of Chromatorgrahpy**. (ed 2): CRC Press. p. 1-5. 2004
- (7) Voss, R., Brook, M. A., Thompson, J., Chen, Y., Pelton, R. H., Brennan, J. D. - Non-Destructive Horseradish Peroxidase Immobilization in Porous Silica Nanoparticles. *Journal of Materials Chemistry*. **17**:4854-4863, 2007.
- (8) Li, X., Tian, J., Nguyen, T., Shen, W. - Paper-Based Microfluidic Devices by Plasma Treatment. *Analytical Chemistry*. **80**(23):9131-9134, 2008.
- (9) Pelton, R. - Bioactive Paper Provides a Low-Cost Platform for Diagnostics. *Trends in Analytical Chemistry*. **28**(8):925-942, 2009.
- (10) Pelton, R. Bioactive Paper - a Paper Science Perspective. In: l'Anson, S. J., editor. **Advances in Pulp and Paper Research, Oxford 2009**: The Pulp & Paper Fundamental Research Society. p. 1096-1145. 2009
- (11) Khan, M. S., Slater, A., Haniffa, S. B. M., Garnier, G. - Reaction Kinetics of Alkaline Phosphatase Immobilized on Papers. *Langmuir*. **Submitted**, 2009.
- (12) Fengel, D., Wegener, G. - **Wood: Chemistry, Ultrastructure, Reactions**. Berlin; New York, Walter De Gruyter Inc, 1984.
- (13) Hon, D. N.-S. Yellowing of Modern Papers. In: Williams, J. C., editor. **Preservation of Paper and Textiles of Historic and Artistic Value, Volume 2**: American Chemical Society. p. 119-141. 1981
- (14) Li, C., Ragauskas, A. J. - Brightness Reversion of Mechanical Pulps. Part Xvii: Diffuse Reflectance Study on Brightness Stabilization by Additives under Various Atmospheres. *Cellulose*. **7**(4):369-385, 2000.
- (15) Carter, H. A. - The Chemistry of Paper Preservation Part 2. The Yellowing of Paper and Conservation Bleaching. *Journal of Chemical Education*. **73**(11):1068-1073, 1996.